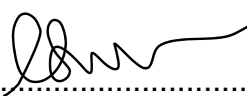


Applications of Transition metal dichalcogenides and Transition metal dioxides for renewable technologies

Submitted by Edward Allery David Baker, to the University of Exeter as a thesis
for the degree of Doctor of Philosophy in Physics, September 2023.

This thesis is available for Library use on the understanding that it is copyright
material and that no quotation from the thesis may be published without proper
acknowledgement.

I certify that all material in this thesis which is not my own work has been
identified and that any material that has previously been submitted and approved
for the award of a degree by this or any other University has been acknowledged.

(Signature).....

Edward Allery David Baker

Abstract

In this thesis, we have studied many different two-dimensional materials for their use as either devices for photoelectrolysis or as Li-ion battery electrodes. Both of which are key technologies for the future of the human race and the planet as a whole. The first 3 chapters provide the background and methods used within this thesis. In chapter 4 we investigate MoS_2 and PdSe_2 for their potential use as photoelectrolysis devices, finding that their performances are unaffected by the presence of another material in a heterostructure, indicating that layered materials can be selected for different properties and combined into a heterostructure that would benefit from all these properties. In chapter 5, ScS_2 is investigated for use as a Li-ion battery electrode and shows great potential as a Li-ion cathode. The upper and lower intercalation limits are investigated and it is found that this material possesses a remarkably large window of stability when compared to that of other TMDCs with a capacity of 182.99 mAhg^{-1} , high average voltage of 3.977 V and has minimal volumetric expansion. In chapter 6, nine different TMDC-graphene superlattices are investigated for their use as Li-ion intercalation electrodes. We find that ScS_2 -graphene in both T- and R- phases possess voltages nearing 3 V , while the other seven lie in the range of 0 V to 1.5 V . Most of these show little volumetric expansion in the range of 5% to 10% , comparable to that of NMC at 8% . We also assess the capacities of these superlattices, finding that ScS_2 -T, ScS_2 -R and TiS_2 -T possess large capacities of 306.77 mAh/g for both ScS_2 phases and 310.84 mAh/g respectively, with MoS_2 -T possessing a capacity of 121.99 mAh/g . In chapter 7, we identify the region $0.6 \leq x \leq 0.625$, $0.2 \leq y \leq 0.25$ and $0.083 \leq 1 - x - y \leq 0.125$ in $\text{Ni}_x\text{Mn}_y\text{Co}_{1-x-y}\text{O}_2$ as being the most likely within the NMC phase space to offer the highest capacities.

Acknowledgements

The work within this thesis is the culmination of four years of work that would not have been possible without the help from friends and colleagues alike. I would like to extend my thanks to a number of people who have aided me with both my work and supported me through this time: Conor Jason Price, Frank Huw Davies, Joe Pitfield, Ned Thaddeus Taylor, Quinton Chan, Shane Graham Davies, Steven Paul Hepplestone and William Borrows. I would like to give particular thanks to Ned Thaddeus Taylor for his extensive knowledge of both Linux and Density Functional Theory that he shared with me and the rest of the Hepplestone Research Group, to Joe Pitfield for his friendship through out the duration of our PhDs and to Conor Jason Price for his in depth knowledge of both batteries and water splitting.

I would like to thank my supervisor Dr Steven Paul Hepplestone, without whom this project would not exist, for constantly pushing me for more results and for always being available for discussions on any topic. I would also like to thank him for calling me, and the rest of the Hepplestone Research Group, "weak" ¹ during our weekly group meetings.

¹This may have been him simply asking us how our week had been.

Funding Acknowledgements

I would like to thank the University of Exeter's Center for Doctoral Training (CDT) (now known as the Centre for Metamaterials Research and Innovation or CMRI), the Engineering and Physical Sciences Research Council (EPSRC) and my PhD sponsor Anaphite for funding my PhD and the research that I have conducted throughout my doctorate (Grant number EP/L015331/1). The work within this thesis also made use of the UK national supercomputers Archer and Archer 2 *via* our membership to the UK's HEC Materials Chemistry Consortium, which is funded by the EPSRC (Grant numbers EP/L000202 and EP/R029431), the tier 2 supercomputer Isambard *via* the University of Exeter's involvement in the GW4 group, the University of Exeter's High-Performance Computing facility ISCA and the Physical Sciences Data-science Service hosted by the University of Southampton and STFC (Grant number EP/S020357/1).

Table of Contents

List of Tables	ix
List of Figures	xi
List of Publications	xii
Author's Declaration	xiii
1 Introduction	1
1.1 The Energy Crisis	1
1.1.1 What Is It	1
1.1.2 How We Can Tackle It	3
1.2 Structure Stability and Energetics	5
1.3 Baseline Structures	6
1.3.1 Transition metal dichalcogenides	6
1.3.2 Oxide structures	11
1.4 The Challenge	16
1.5 Outline of Thesis	17
2 Density Functional Theory	18
2.1 Periodic Materials	19
2.1.1 The Born-von Karman boundary conditions	20
2.1.2 Bloch's theorem	21
2.2 Variational principle	22
2.2.1 The ground state energy	24
2.3 Many body systems	26
2.4 The Born-Oppenheimer approximation	28
2.4.1 Solving the zeroth and first orders: Equilibrium of the Nuclei	32
2.4.2 Solving the second and third orders: Nuclear Vibration . . .	33
2.5 Hartree-Fock Method	35
2.6 Hohenberg-Kohn Theorem	36
2.7 Kohn-Sham Theorem	39
2.8 Exchange-Correlation and Functionals	43
2.8.1 The PBE functional	46

2.8.2	The HSE functional	49
2.9	Pseudopotentials	49
2.9.1	Projector Augmented Wave method (PAW)	51
2.10	Ewald Summation	54
2.11	Brillouin zone sampling	59
2.12	Van der Waals corrections	60
2.13	Geometric relaxation	61
3	Background Theory	64
3.1	How Batteries work	64
3.1.1	History of Batteries	64
3.1.2	Li-ion Batteries	66
3.2	State of the art Li-ion battery cathodes	71
3.2.1	Alloyed Transition metal dioxides	73
3.2.2	Stability	75
3.3	How water splitters work	77
3.3.1	History and Basics of Water Splitters	77
3.3.2	Photoelectrolysis	80
3.4	State of the art Photoelectrolysis Devices	84
3.4.1	Single Electrode Photoelectrolysis	85
3.4.2	Degradation and Photocorrosion	87
4	Computational Analysis of the Enhancement of Photoelectrolysis using Transition Metal Dichalcogenide Heterostructures	89
4.1	Introduction	89
4.2	Methods	92
4.2.1	Density Functional Theory Parameters	92
4.2.2	Energetics of water splitting	94
4.2.3	Adsorption Sites and Phase Diagrams	98
4.3	Results and Discussions	102
4.3.1	Heterostucture Geometric and Electronic Structure	102
4.3.2	Adsorption sites and stability	104
4.3.3	Reaction steps	108
4.4	Conclusion and Chapter Summary	111
4.5	Supporting Information	112
4.5.1	Reaction pathways	112
4.5.2	Adsorbant concentration effects	114
4.5.3	Band Alignment	115

5	First Principles Study of Layered Scandium Disulfide for use as Li-Ion and Beyond-Li-Ion Batteries	117
5.1	Introduction	117
5.2	Methods	120
5.2.1	Density Function Theory Parameters	120
5.2.2	Methods for Material Evaluation	122
5.2.3	Convex Hulls	125
5.3	Results	126
5.3.1	Determination of Structure	126
5.3.2	Properties of ScS ₂ Cathodes	129
5.3.3	Intercalation Beyond a=1	138
5.3.4	Metal Mixing	138
5.4	Conclusion and Chapter Summary	140
5.5	Supporting Information	141
5.5.1	Phase Diagram Derivation	141
5.5.2	Convex Hull for Sc-O and Sc-S Compounds	146
6	A computational study of the enhancement of graphene electrodes for use in Li-ion batteries <i>via</i> forming superlattices with transition metal dichalcogenides	147
6.1	Introduction	147
6.2	Method	150
6.2.1	Density Functional Theory Parameters	150
6.2.2	Voltages and stability	151
6.3	Results	153
6.3.1	General properties	153
6.3.2	Voltages	154
6.3.3	Volumetric Expansion	156
6.3.4	Thermal Stability and Capacity	157
6.3.5	Changing the ratio of carbon to TMDC	159
6.4	Conclusion and Chapter Summary	161
6.5	Supporting Information	162
6.5.1	Derivation of E_{IS}	162
6.5.2	Formation of LiC ₆	165
6.5.3	Supercells	166
6.5.4	Voltages	167
6.5.5	Volumetric expansion	168
6.5.6	Effect of additional Graphene	168

7	First Principles and Empirical potential based study of Delithiated $\text{Ni}_x\text{Mn}_y\text{Co}_{1-x-y}\text{O}_2$ Phase Stability for use in Li-ion Cathodes	172
7.1	Introduction	172
7.2	Method	174
7.2.1	Density Functional Theory Parameters	175
7.2.2	Empirical potentials	176
7.2.3	Phases Investigated	178
7.3	Results and Discussions	179
7.3.1	DFT Convex Hull	179
7.3.2	Properties of the Layered Materials	182
7.3.3	Empirical Convex Hull	183
7.3.4	DFT, GULP and LAMMPS Comparison	185
7.4	Conclusion and Chapter summary	187
8	Conclusions and Outlook	188
8.1	Summary	188
8.2	Future Work	192
8.3	Closing Remarks	193
	Appendices	194
A	Lattice and Basis Vectors for TMDCs	195
B	Jahn-Teller Distortions	197
	Bibliography	201

List of Tables

4.1	Zero point energy corrections and entropy for adsorbed groups and molecules.	95
4.2	OER energetic steps.	114
4.3	HER energetic steps.	114
4.4	Absorption energies on the MoS ₂ monolayer.	114
4.5	Absorption energies on the PdSe ₂ monolayer.	115
4.6	Absorption energies on the MoS ₂ /PdSe ₂ heterostructure.	115
5.1	Comparison table of key lithium-ion electrode properties for ScS ₂ and other presently practiced electrode materials	137
6.1	Strains and Formation energies for TMDC-graphene superlattices.	154
6.2	E_{IS} for the TMDC-graphene superlattices and bulk TMDCs.	165
6.3	Formation energy of Li _{a=1} MS ₂ C _b from LiC ₆ and other compounds.	166
6.4	Formation energy of Li _{a=2} MS ₂ C _b from LiC ₆ and other compounds.	166
6.5	Formation energy of Li _{a=1} MoS ₂ C _b from LiC ₆ and other compounds.	167
6.6	In and out of plane lattice constants for TMDC-graphene superlattices.	167
6.7	In plane lattice constants for bulk TMDCs and graphene supercells.	168
6.8	Strains and Formation energies for TMDC-graphene superlattices.	169
6.9	Voltages for TMDC-Graphene superlattices and bulk TMDCs.	169
6.10	Volumetric expansion for TMDC-Graphene superlattices and bulk TMDCs.	170
6.11	Voltage, E_{IS} and volumetric expansion for MoS ₂ -T superlattice as the number of graphene layers is varied.	170
6.12	Average atomic charges in MoS ₂ -T superlattices without lithium.	171
6.13	Average atomic charges in MoS ₂ -T superlattices with lithium.	171

List of Figures

1.1	Monthly mean carbon dioxide in the atmosphere.	2
1.2	Side-on view showing the different components in a single TMDC layer.	7
1.3	Side-on and top-down view of H-phase TMDCs.	8
1.4	Side-on and top-down view of T-phase TMDCs.	9
1.5	Different stacking orders of TMDCs in H- and T-phases.	10
1.6	Example of a transition metal dioxide alloy and heterostructure . .	11
1.7	Energy diagram of degenerate d -shell orbitals in transition metal dioxides.	12
1.8	Side-on and angled view of the Rutile structure.	13
1.9	Side-on and angled view of the delithiated Spinel structure.	14
1.10	Side-on and angled view of the Anatase structure.	15
2.1	Jacob's Ladder of functionals.	44
2.2	A schematic of the local Pseudopotential and wavefunction smoothing.	50
2.3	The irreducible Brillouin zone for a crystal with hexagonal symmetry.	59
3.1	Charging and discharging process of Li-ion batteries.	67
3.2	Relative energy levels within Li-ion batteries.	69
3.3	The voltage curve for lithium cobalt oxide as the lithium content is varied.	72
3.4	A plot of how the energy levels of the HER and OER vary with pH.	80
3.5	A schematic of the OER and HER.	82
3.6	Energy of the valence and conduction bands relative to the HER and OER.	83
3.7	Energy levels in different types of photoelectrolysis devices.	85
4.1	a schematic showing the potential adsorption sites considered. . .	98
4.2	Schematic of the MoS ₂ /PdSe ₂ Heterostructure, its DOS and absorption spectra.	103
4.3	Phase diagrams for MoS ₂ and PdSe ₂ monolayers.	105
4.4	Phase diagram for the MoS ₂ /PdSe ₂ heterostructure.	107
4.5	Energy diagram for the OER and HER steps on the monolayers. . .	108

4.6	Energy diagram for the OER and HER steps on the heterostructure.	111
4.7	Schematic of the electronic transport within the heterostructure. . .	116
5.1	Schematic of a convex hull.	125
5.2	Structure of Li_aScS_2 with varying lithium content.	126
5.3	Nudged elastic band results for lithium movement through T- and αScS_2	127
5.4	Voltages, volumetric expansion and E_{IS} for ScS_2 with Li, Na, K and Mg.	130
5.5	Phonon band structures for $\alpha\text{-ScS}_2$ and $\alpha\text{-LiScS}_2$	133
5.6	Elastic properties of T- ScS_2 in its pristine and intercalated forms. .	134
5.7	Electronic band structure and orbital-decomposed density of states for pristine $\alpha\text{-ScS}_2$	136
5.8	Formation energy of substituting scandium with different metal species.	139
5.9	Convex hulls for Sc-O and Sc-S compounds.	146
6.1	Schematic of ScS_2 -graphene superlattice with and without lithium.	151
6.2	Voltages, volumetric expansion and lattice expansion for TMDC-graphene superlattices with lithium intercalation.	155
6.3	E_{IS} for TMDC-graphene superlattices as the amount of lithium is varied.	158
6.4	Voltages, E_{IS} and volumetric expansion for MoS_2 -T superlattice with varying amounts of graphene.	160
6.5	Structure of a TMDC-graphene superlattice at $a = 1$	168
7.1	A schematic of the workflow and the layered structure of NMC. . .	175
7.2	The eight different phases considered and the convex hull generated from these.	180
7.3	The DFT convex hull with formation energies.	181
7.4	Bader charge analysis of the atoms within the layered NMC structures.	183
7.5	Bond lengths of the layered NMC structures.	184
7.6	Fitted potential and the LAMMPS convex hull.	185
7.7	DFT, GULP and LAMMPS energy comparison for NMC.	186
B.1	Jahn-Teller Distortion.	197
B.2	d -shell orbital filling for $d1$ to $d5$	199
B.3	d -shell orbital filling for $d6$ to $d10$	200

List of Publications

Chapter 4

- Edward Allery David Baker, Joe Pitfield, Conor Jason Price, Steven Paul Hepplestone, *Computational analysis of the enhancement of photoelectrolysis using transition metal dichalcogenide heterostructures*, Journal of Physics: Condensed Matter, **34**(37), (2022), p. 375001.
DOI: [10.1088/1361-648X/AC7D2C](https://doi.org/10.1088/1361-648X/AC7D2C)

Chapter 5

- Conor Jason Price, Joe Pitfield, Edward Allery David Baker, Steven Paul Hepplestone, *First principles study of layered scandium disulfide for use as Li-Ion and beyond-Li-Ion batteries*, Physical Chemistry Chemical Physics, **25**(3), (2023), p. 2167.
DOI: [10.1039/D2CP05055B](https://doi.org/10.1039/D2CP05055B)

Chapter 6

- Edward Allery David Baker, Conor Jason Price, Steven Paul Hepplestone, *Computational Study of the Enhancement of Graphene Electrodes for Use in Li-Ion Batteries via Forming Superlattices with Transition Metal Dichalcogenides*, Journal of Physical Chemistry C, **128**(2), (2024), p. 723.
DOI: [10.1021/acs.jpcc.3c06300](https://doi.org/10.1021/acs.jpcc.3c06300)

Additional work

- Conor Jason Price, Edward Allery David Baker, Steven Paul Hepplestone, *First principles study of layered transition metal dichalcogenides for use as electrodes in Li-Ion and Mg-Ion batteries*, Journal of Materials Chemistry A, **11**(23), (2023), p. 12354.
DOI: [10.1039/D3TA00940H](https://doi.org/10.1039/D3TA00940H)
- Conor Jason Price, Edward Allery David Baker, Steven Paul Hepplestone, *Properties of Layered TMDC Superlattices for Electrodes in Li-Ion and Mg-Ion Batteries*, Journal of Physical Chemistry C, **128**(5), (2024), p 1867.
DOI: [10.1021/acs.jpcc.3c05155](https://doi.org/10.1021/acs.jpcc.3c05155)

Author's Declaration

The curation of data and its analysis that are presented within this thesis were performed by Mr Edward Allery David Baker, Mr Joe Pitfield, Mr Conor Jason Price and Dr Steven Paul Hepplestone. Useful discussions of these works was had with Dr Ned Thaddeus Taylor, Dr Francis Huw Davies and Mr Shane Graham Davies.

The work in chapter 4 was a collaborative effort between Mr Pitfield and Mr Baker with assistance from Mr Price. Mr Pitfield and Mr Baker jointly investigated adsorptions onto the surfaces of MoS₂, PdSe₂ and a heterostructure of the two. Mr Price assisted in the calculation of absorption spectra for these materials.

The work in chapter 5 was a collaborative effort between Mr Price, Mr Pitfield and Mr Baker. Mr Price was the largest contributor to this work, having contributed to the conceptualisation, data curation, the formal analysis and methodology of this work. Mr Pitfield contributed to data curation, the formal analysis and methodology and Mr Baker contributed to data curation and the formal analysis.

The work in chapter 6 was motivated by discussions with the company sponsoring my PhD, Anaphite, to explore how two-dimensional battery electrodes are affected by the introduction of graphene. Mr Baker and Mr Hepplestone carried out all the calculations and analysis of these results. Mr Price helped with formal analysis and the methodology.

The work in chapter 7 was motivated by discussions with the company sponsoring my PhD, Anaphite, to explore the group of alloyed transition metal dioxides known as NMC (Ni_xMn_yCo_{1-x-y}O₂) for their use as battery cathodes. Mr Baker and Mr Hepplestone carried out all the calculations and analysis of these results.

Chapter 1

Introduction

"The first principle is that you must not fool yourself and you are the easiest person to fool."

– Richard Feynman

1.1. The Energy Crisis

1.1.1 What Is It

With an ever increasing demand for power, combined with our heavy reliance on fossil fuels, the need for cleaner fuels and energy sources is growing rapidly. Current sources of clean energy, such as wind turbines and photo voltaic panels, produce power intermittently requiring some way of storing the power for when it is needed. This is mainly done using batteries. Unfortunately, our current batteries are short lived and have insufficient capacities, leaving more to be desired from them.

Currently, fossil fuels make up roughly 80 to 85% of the worlds energy generation [1]. Due to this use, carbon dioxide levels have reached ≈ 422 ppm as of July 2023 as shown in Figure 1.1. This is higher than the highest known historical carbon dioxide level from the past 800,000 years of ≈ 300 ppm [2]. Numerous studies have linked the rise in atmospheric carbon dioxide levels to climate change, this being the rise in the average global temperature since the mid-20th century, as well as the link between this and humanities use of carbon dioxide producing fossil fuels.

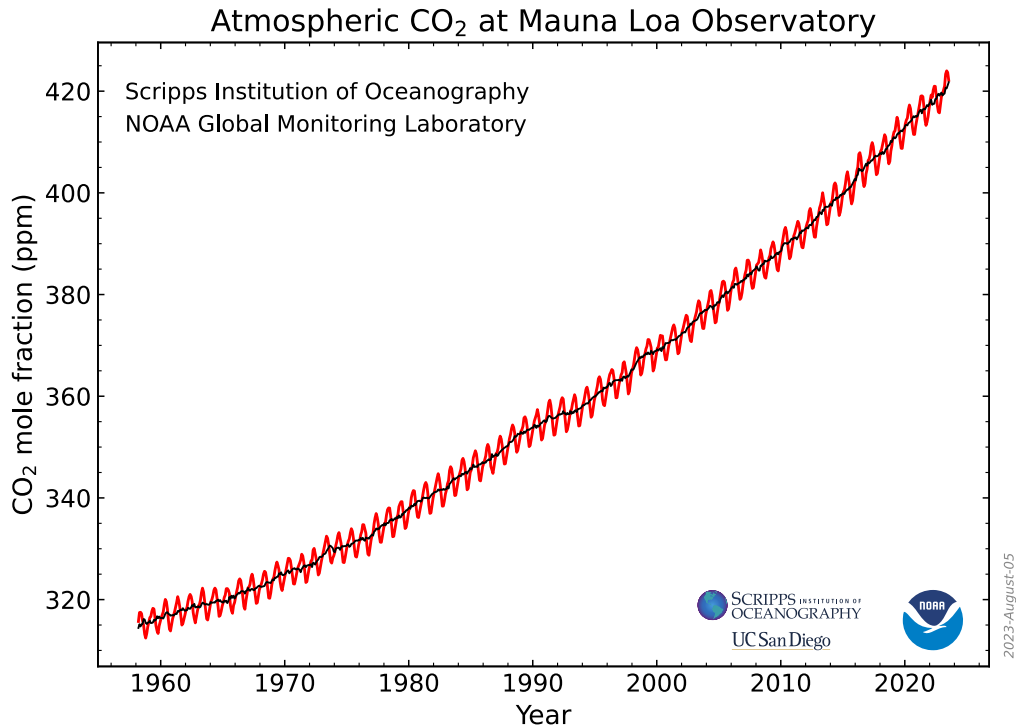


Figure 1.1: A graph showing monthly mean carbon dioxide measured at Mauna Loa Observatory, Hawaii. The Red line represents the monthly mean values, and the Black line represents the same data after correction for the average seasonal cycle.[3, 4].

All our electricity produced in power plants could, in theory, be replaced with solar and wind power. However, for use in transportation, current batteries will not suffice. Lighter batteries or an alternative, green, fuel is required.

Present Li-ion batteries are limited by the low energy density of cathode materials, with the highest capacity in present commercially available cathode materials at ≈ 200 mAh/g [5, 6]. If the energy density of batteries was higher, this would lead to fully electric vehicles with ranges closer to that of their fossil fuel using counterpart, which would require cathode capacities closer to 500 mAh/g [7, 8]. The challenge is finding Li-ion cathode materials with sufficient capacities. However, current high capacity cathode materials break down quickly with use, presenting another challenge to be solved.

An alternative to both fossil fuels and batteries is hydrogen as an alternative fuel. Hydrogen is a fuel that can be stored and transported in a similar manner to fossil fuels, but when it undergoes combustion with oxygen, only water is

produced as a byproduct, meaning it is a clean fuel. Unfortunately, present methods of producing hydrogen are inefficient with electrolysis having a maximum efficiency of 61%, however this does not take into account the efficiency of generating the energy used to make the hydrogen that will pull the overall efficiency down [9]. Other sources, such as steam-methane reforming, even produce carbon monoxide and carbon dioxide as byproducts, essentially making the benefit of producing hydrogen as an alternative fuel completely null [10]. However, another process can be used to produce hydrogen from water with only oxygen as a byproduct that has the potential to have higher efficiencies than electrolysis, this process is called photoelectrolysis. Photoelectrolysis uses energy from the sun to directly split water into hydrogen and oxygen by making use of a catalyst [11, 12].

1.1.2 How We Can Tackle It

The nature of both of the solutions outlined above are a combination of Physics, Chemistry, Engineering and Materials Science. In order to solve them, an understanding of the culmination of these fields in the four following areas is required.

1. Electronic properties.
2. Chemical energetics.
3. Structural and geometric forms of the materials involved.
4. Thermal stability.

Each of these in turn requires accurate knowledge of how electrons interact with, and within, an atomic lattice which needs to be determined. This can be done *via* experimental investigations, but with such a wide range of different possible material candidates, this can be both very costly and very time consuming. However, a theoretical approach could be used instead, and cost much less while providing more insight into the materials properties. These four challenges can be solved using a few different theory based tools such as Density Functional Theory (DFT), the use of Analytical Methods and Molecular Dynamics.

Density Functional Theory, or DFT for short, is a constantly evolving area of physics and chemistry. Essentially, DFT is an *ab initio* method for almost exactly solving a many body variant of the Schrödinger equation for a system of atoms and electrons. This solution is found as a function of the electron density within the system, this is where DFT gets its name. As mentioned, an exact solution cannot be found, this is due to a form of electron-electron interaction called exchange-correlation not having a known exact solution, leading to the use of approximations that are either computationally low cost but less accurate, or computationally expensive but very accurate. DFT can be used to calculate the energy, electronic band structure and phononic properties of an atomic system. From these, the system's light absorption properties, whether it is an insulator, conductor or semi-conductor and its vibrational properties can be determined. Other properties can also be found but these are of most importance to these works [13].

Analytical methods [14] such as the Tight Binding model or the empirical pseudopotential model can also be used to obtain the electronic properties of atomic systems. Unlike DFT which is derived from first principles, TB uses parameterisation and simulates electrons as being tightly bound to atoms, meaning they have limited interaction with other atoms. On the other hand, the empirical pseudopotential model can be used to simulate electrons as being nearly free or as atomic orbitals by using either planewaves or Gaussians. These can both be used to get the same properties as DFT, such as energetics and electronic band structures.

Molecular Dynamics (MD) is usually used in conjunction with DFT and Analytical methods for getting correct lattice constants, bond lengths and bond angles within systems, so that the electronic properties derived from DFT or Analytical methods are more realistic. MD is a way of simulating and analysing how atoms and molecules in a system will move within a time frame, normally measured in picoseconds. As MD mainly uses interatomic potentials, instead of solving for electron densities and forces, it can be used for much larger systems than DFT. Alternatively, MD can also use the force fields calculated *via* DFT or Analytical

solutions to move the atoms around into more favourable configurations, this is normally referred to as relaxation [15].

These tools can be used to understand the electronic, energetic, catalytic and geometric properties, among others, of a wide range of materials, giving a deep understanding of them without the need to physically make them. They can also be used to discover new materials that have never been seen before, as well as potential routes to their synthesis.

1.2. Structure Stability and Energetics

Structural stability is how favourable a given atomic arrangement is relative to other possible arrangements of the same set of atoms. This can be assessed in a few different ways using the tools outlined above. The simplest of which is a simple energetics based approach, if you take two different structures with the exact same composition, the one with the lowest energy is more stable. This is quite useful but does not tell you the whole story, a good example of this is diamond and graphite. Both diamond and graphite are known stable polymorphs of carbon, but graphite is the lower energy structure. In this situation, the energetics alone would tell you that only graphite would form, meaning that extra approaches need to be considered.

MD can be used on top of an energetics argument, in some cases, to determine if a structure will "collapse" (if the atomic structure is not dense enough) or "explode" (if the atomic structure is too dense) under normal conditions. The energetics of a system can also change with temperature and pressure, changing either of these can change what the lowest energy polymorph is. One way of modeling how the energetics of a system changes with temperature is *via* phonon calculations that can be done with DFT. Modeling vibrational modes within a crystalline system can tell you if these vibrations are stable, or if they will lead to non-restorative forces that force the structure into a different morphology. The entropy of a system can be derived from the phononic vibrational modes to then calculate

the relation between the temperature and energy of a system and thus assess the phase stability at different temperatures.

This section gives a general outline on how to determine whether a structure is stable or not and will be described in more depth later in these works, but the most important thing is to start with a structure that you already know to be stable, and modify it to be suitable for the intended use. For these works, there are a few baseline structures that will be investigated and modified for use as either photoelectrolysis devices or Li-ion battery cathodes.

1.3. Baseline Structures

In this section, the baseline structures that will be investigated are outlined. These consist of transition metal dichalcogenides [16], that have had a lot of attention within many different semiconductor fields including water splitting and photoelectrolysis, and transition metal oxides, which are currently used in the state of the art battery cathodes. These structures will be described here, but their properties will be explored in depth later in these works.

1.3.1 Transition metal dichalcogenides

Transition metal dichalcogenides, TMDCs for short, are a group of materials consisting of one part transition metal and two parts chalcogen with a general formula of MX_2 where: M is the transition metal and X are chalcogens which are elements in IUPAC group 16 such as oxygen and sulphur. These atoms are arranged into two-dimensional sheets consisting of three atomic layers separated but held together by the weak van der Waals force, the two outer layers are chalcogen atoms and the middle layer is transition metal atoms, see Figure 1.2. The TMDC group is made of multiple sub groups based on the coordination of the transition metal atoms. The most common of these are groups are called H and T, whether a TMDC is more favourable in H or T coordination is determined by the arrangement and number of the transition metal's *d*-shell electrons and their interaction

with the chalcogen atoms. Stress and strain applied to TMDCs or even the intercalation of other species in the van der Waals gap can also change which coordination is more favourable, e.g. intercalating lithium between layers of H-phase MoS₂ changes it to T-phase [17, 18, 19].

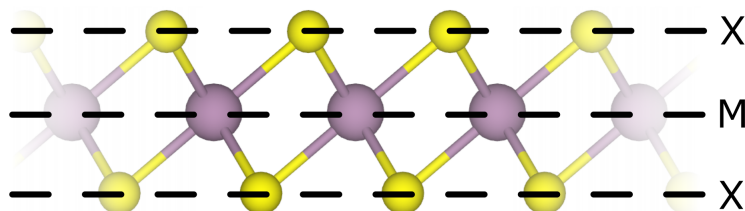


Figure 1.2: A side-on view showing the different components in a single TMDC layer. The dashed lines indicate which atoms are in which layer. M denotes the transition metal layer and X denote the chalcogenide layers.

Given the wide range of combinations of transition metals and chalcogenides, along with the H and T coordination groups, there are many different TMDCs with varying electronic properties. On top of this, TMDCs can be separated into few layers or even single layers, giving them greater band gaps than their bulk counterparts, further diversifying the group's electronic properties.

Molybdenum disulphide (MoS₂) is the most common of the TMDCs, having been used as a solid lubricant [20] and a catalyst in the hydrosulphurisation reaction [21] in the petroleum industry, but both of these use bulk (many layer) MoS₂. Single layers of TMDCs can be made using exfoliation: single layers of MoS₂ were exfoliated into monolayers by the intercalation (between the layers) of lithium followed by a reaction with water in 1986 by Per Joensen *et al.* [22]

MoS₂ is one of the few TMDCs that are naturally occurring, found in the mineral molybdenite as bulk MoS₂, but the majority of the possible TMDCs have to be synthesised. The wide range of properties that TMDCs display, along with the possibility to combine them together, has led to them being investigated for a number of different applications including use as transistors, flexible electronic devices, photovoltaics, photodetectors and molecular sensing applications just to name a few [23].

1.3.1.1 TMDC H Coordination

TMDCs with H coordination refer to those where a transition metal atom is surrounded by six chalcogenides in the trigonal prismatic geometry. This means that the three chalcogens bonded to the bottom of the transition metal mirror the three above. Overall, this leads to a graphene like honeycomb structure, where ever other site is two stacked atoms instead of one, see Figure 1.3. The lattice and basis vectors for this is given in Appendix A.

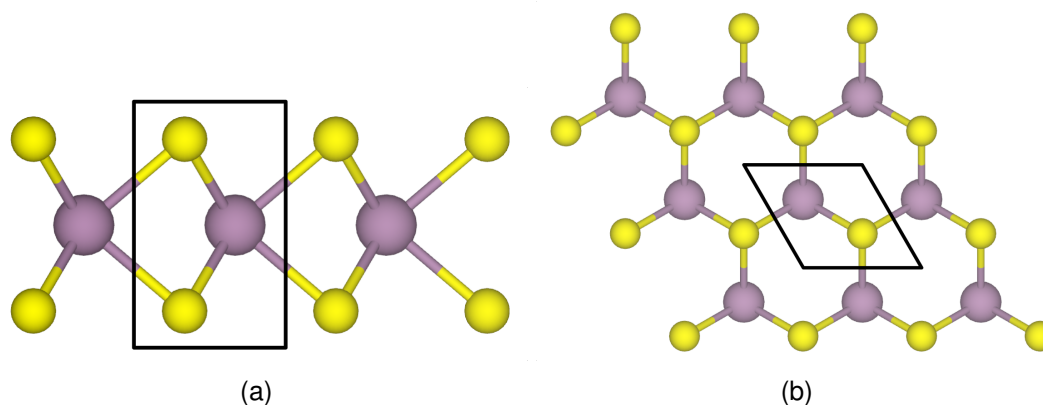


Figure 1.3: A side-on and top-down view of a TMDC with H coordination. (a) is the side-on view and (b) is the top-down view. The black outline denotes the unit cell / repeat unit.

H coordinated TMDCs have three degenerate sets of d -shell orbitals according to Ligand Field Theory, denoted $d_{xz, yz}$, $d_{x^2-y^2, xy}$ and d_{z^2} from highest energy to lowest energy. The filling of these orbitals will determine the electronic properties of the TMDC, be it metallic, semi-conducting or insulating. Group 5 and 6 transition metals are known to form H coordinated TMDCs more favourably than T coordination [24].

1.3.1.2 TMDC T Coordination

TMDCs with T coordination refer to those where a transition metal atom is surrounded by six chalcogenides in the octahedral geometry. This means that the three chalcogens bonded to the bottom of the transition metal are rotated 60° along the vertical axis with respect to the three above. Overall, this leads to a honeycomb structure that has chalcogen atoms in the centre of the hexagons as

well as on half of the vertices, see Figure 1.4. The lattice and basis vectors for this is given in Appendix A.

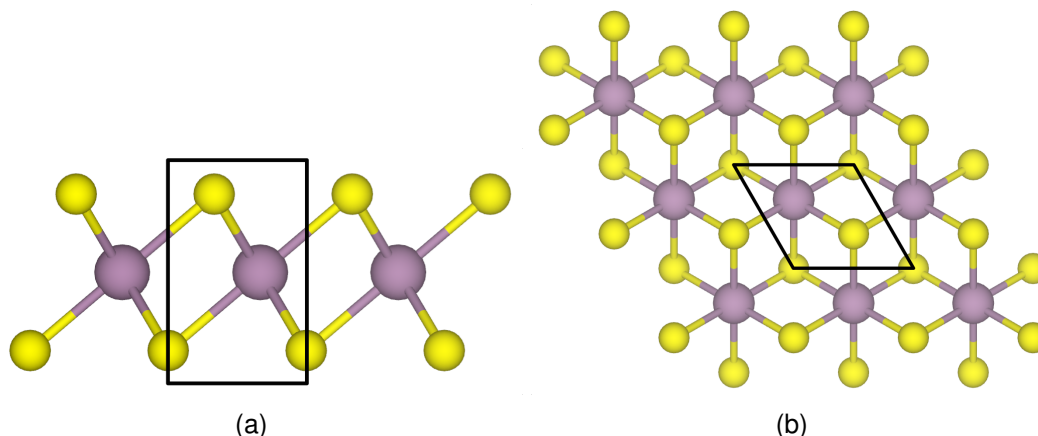


Figure 1.4: A side-on and top-down view of a TMDC with T coordination. (a) is the side-on view and (b) is the top-down view. The black outline denotes the unit cell / repeat unit.

T coordinated TMDCs form two non-bonding degenerate sets of d -shell orbitals according to Ligand Field Theory, one higher in energy and one lower in energy denoted d_{z^2, x^2-y^2} and $d_{yz, xz, xy}$ respectively. The filling of these orbitals will determine the electronic properties of the TMDC, be it metallic, semi-conducting or insulating. Group 4, 7 and 10 transition metals are known to form T coordinated TMDCs more favourably than H coordination [24].

1.3.1.3 TMDC Stacking

On top of coordination, stacking order also affects the electronic properties of TMDCs. Stacking order is coordination dependent, with all H coordinated TMDCs requiring two layers per unit cell, rotated 60° relative to each other, in order to create multi layer structures. Whereas, T coordinated TMDCs can be a single repeated layer, or three layers slightly offset from each other. These stacking orders are shown in Figure 1.5, additional stacking orders exist but have been omitted.

For the TMDCs with H coordination, the three different stacking orders are labeled: 2Ha where the transition metal atoms in the two layers line up along the vertical axis (aba cbc), 2Hb where the chalcogenide atoms in the two layers line

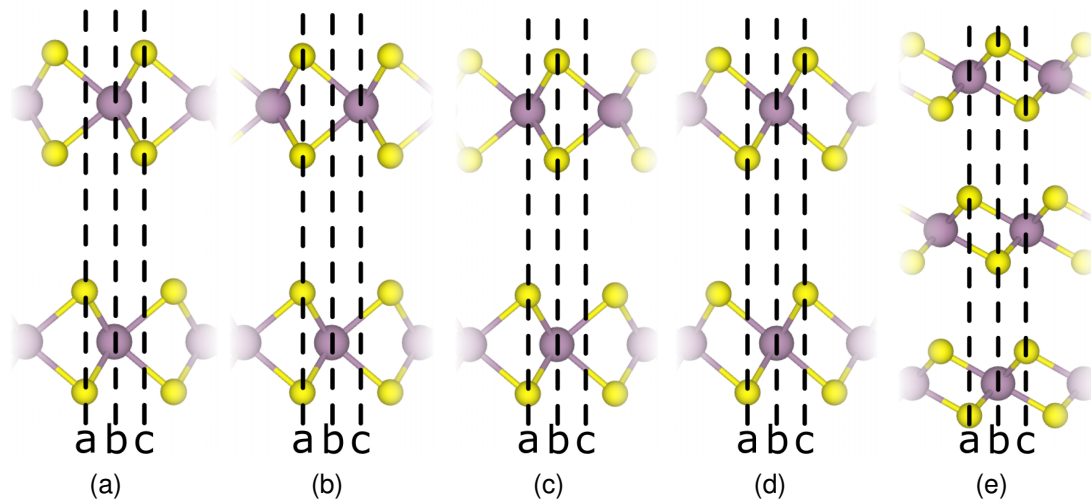


Figure 1.5: Five different stacking orders of TMDCs. (a), (b) and (c) are all H coordination stacking orders, requiring two layers for a repeat unit that are rotated by 60° relative to each other. The only different between these is how the layers line up, (a) has only the transition metals lining up (2Ha), (b) has only the chalcogens lining up (2Hb) and (c) has the chalcogens from one layer line up with the transition metal of the other (2Hc). (d) and (e) are both T coordination stacking orders. (d) requires only a single layer for a repeat unit as all atoms in one layer line up with those in the next (1T). (e) requires three layers for a repeat unit as every layer is shifted by over one atom each layer (R3m).

up along the vertical axis (aba aca), and 2Hc where the transition metal atoms in one layer line up along the vertical axis with the chalcogenide atoms in the adjacent layers (aba bab).

For the TMDCs with T coordination, the two different stacking orders are labeled: 1T where all like atoms from a layer line up along the vertical axis with those in all other layers (abc), and R3m where each layer is offset from the next requiring three layers for a repeat unit (abc bca cab).

1.3.1.4 Alloying and Hetero structuring

On top of the different coordinations and stacking orders observed in TMDCs, there are two other ways to modify these structures to expand their properties and potential applications: alloying and heterostructuring.

Alloying means mixing a metal together with one or more other metals. For example mixing copper with tin to make bronze. Within these works, alloying will refer to exchanging a portion of the transition metals within these structures

with a different transition metal leading to composition in the form $M_aN_bX_2$, where M and N represent two different transition metals, $a + b = 1$, and X represents a chalcogenide [6]. An example of this with three different transition metals is shown in Figure 1.6 (a).

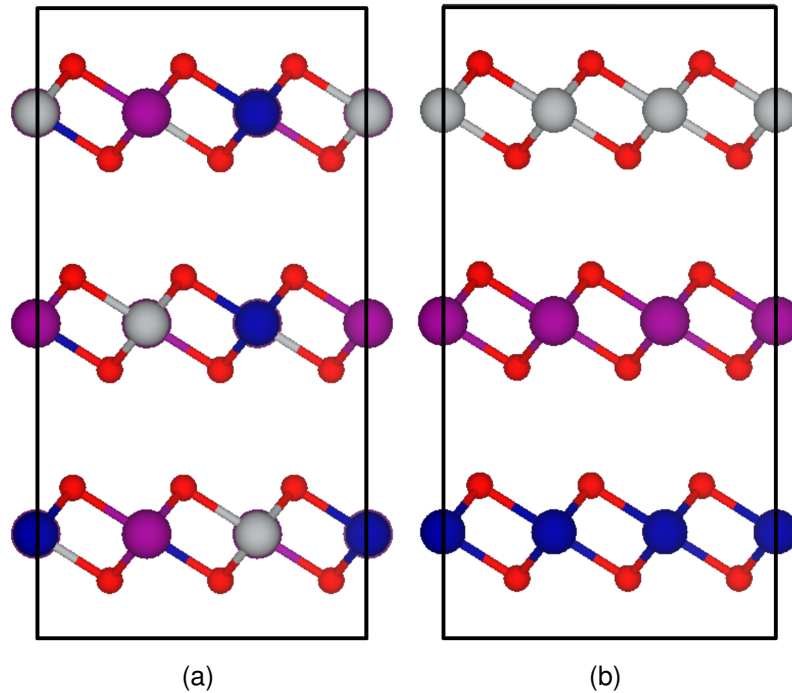


Figure 1.6: (a) an example of a transition metal dioxide alloy that has a mixing of three different transition metals. (b) an example of a transition metal dioxide heterostructure that is made up of three different layers.

Heterostructuring involves taking single layers of two or more different TMDCs and stacking them together, giving a combination of two different TMDCs, without the mixing of transition metals seen in alloying. This also allows for different chalcogenides to be used in different layers, not just transition metals. TMDCs can also be combined with other two-dimensional materials in heterostructures such as graphene and hexagonal boron nitride [25]. An example of this with three different layers is shown in Figure 1.6 (b).

1.3.2 Oxide structures

Transition metal oxides, or oxides for short, consist of any stoichiometry of transition metal to oxygen but the main ones considered throughout these works are

of the stoichiometry 1:2 transition metal atoms to oxygen atoms, alloying is also considered for these structures.

Within many of the oxide systems considered, six bonds are formed in an octahedral complex around the transition metals just like T-phase TMDCs. In octahedral complexes, the d -shell orbitals are split into two degenerate sets: the lower energy set is labeled t_{2g} and consists of orbitals d_{xy} , d_{xz} and d_{yz} , the higher energy set is labeled e_g and consists of orbitals d_{z^2} and $d_{x^2-y^2}$. These degenerate sets can be further split *via* different interactions. Uneven filling of these orbitals can lead to Jahn-Teller distortions, as shown in Figure 1.7, which either elongates or compresses a pair of the octahedral bonds relative to the other four, this is discussed in more depth in Appendix B. The overlap between these orbitals and those in the bonded ligands can also lead to distortions with different magnitudes depending on the different species involved. Discussed below are some of the transition metal dioxides considered within these works.

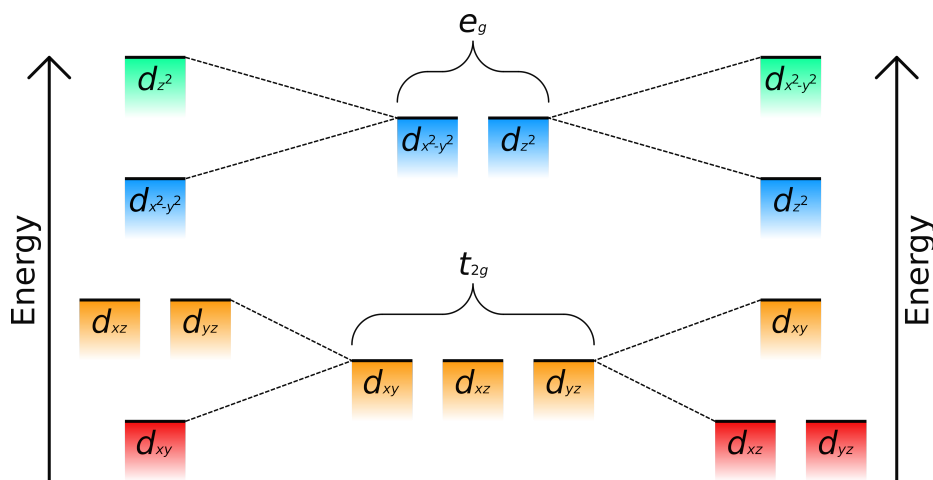


Figure 1.7: A energy diagram showing the splitting of degenerate orbitals within the d -shell of an octahedrally bonded transition metal. Different fillings can lead to different splitting of the degenerate e_g and t_{2g} orbitals, which leads to slightly different crystal structures.

1.3.2.1 Rutile

Rutile is a common form of Titanium dioxide (TiO_2) with a tetragonal crystal structure. Like the T-phase TMDCs, the transition metal atoms are bonded to six oxygen atoms in an octahedral complex, but they are arranged into a grid of offset pillars that are interconnected by the oxygen atoms, see Figure 1.8.

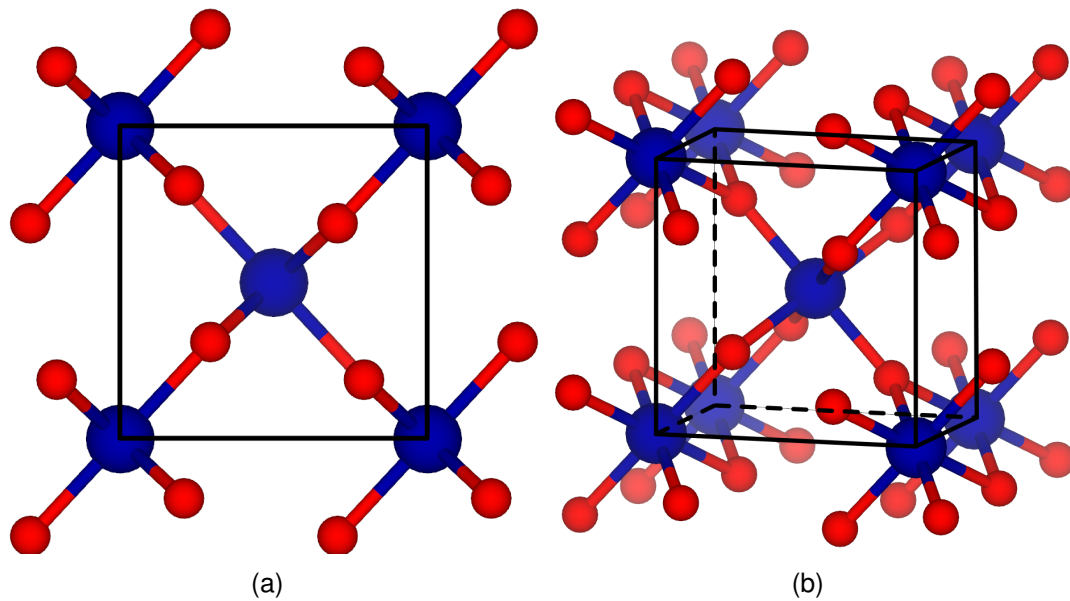


Figure 1.8: A side-on and angled view of the Rutile structure. (a) is the side-on view and (b) is the angled view. The black outline denotes the unit cell / repeat unit.

Within Rutile TiO₂, due to the transition metal octahedral sharing edges along the z axis and vertices in the x - y plane, the t_{2g} set is split, with the d_{xy} orbital higher in energy than the degenerate d_{xz} and d_{yz} orbitals. The t_{2g} set of orbitals around the transition metal overlap with the p -shell orbitals in the oxygen atoms sharing electrons. The symmetry of these orbitals is what leads to the octahedral coordination, but the t_{2g} splitting causes bonds in the z axis direction to be shorter, this shows d_1 like Jahn-Teller distortions. The shared electrons localize closer to the oxygen atoms than the transition metal atoms, giving the oxygen atoms a charge of 2^- and the transition metal atoms a charge of 4^+ [26, 27].

1.3.2.2 Spinel

Spinel is a cubic crystal with formula MgAl₂O₄, Spinel can also refer to the larger Spinel group, consisting of multi transition metal oxides with general formula AB₂X₄ where A is a metal, B is a transition metal and X is oxygen. In this work, Spinel refers to the delithiated structure of LiMn₂O₄, e.g. Mn₂O₄ as shown in Figure 1.9. In this crystal structure, the transition metal atoms are bonded to six oxygen atoms with a octahedral coordination. These transition metal atoms are

in four groups of four, per unit cell, with overlap in the centre and corners of the unit cell and large gaps in between, leading to a cubic unit cell with lots of gaps.

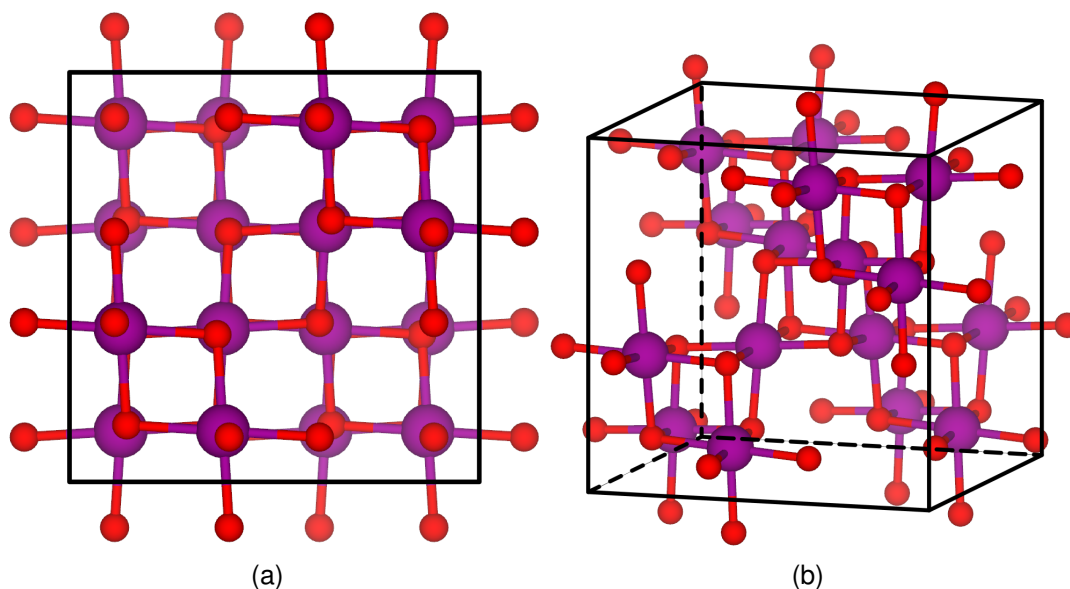


Figure 1.9: A side-on and angled view of the delithiated Spinel structure of LiMn_2O_4 . (a) is the side-on view and (b) is the angled view. The black outline denotes the unit cell / repeat unit.

Within this Spinel structure, there can be two different transition metal orbital configurations. When there is no lithium present, the average manganese atom has a valency of $4+$, but when lithium is introduced half of the manganese gain an electron to become Mn^{3+} . For Mn^{4+} , the electrons are spin polarised across the degenerate t_{2g} orbitals, having one electron in each of d_{xy} , d_{xz} and d_{yz} orbitals, showing no Jahn-Teller distortions. For Mn^{3+} that appear in the lithiated structure, the electrons are spin polarised, having one electron in each of d_{xy} , d_{xz} , d_{yz} and d_{z^2} orbitals. The d_{xz} and d_{yz} are degenerate while the d_{xy} is higher in energy, the d_{z^2} orbital is the highest filled orbital in this system. This leads to the bonds in the z direction to be elongated, more so than any elongation seen in either Rutile or Anatase TiO_2 because the d_{z^2} orbital has a greater overlap with the orbitals of the oxygen atoms in the Spinel structure leading to a strong d_4 Jahn-Teller distortion [28].

1.3.2.3 Anatase

Anatase is a metastable form of Titanium dioxide (TiO_2) also with a tetragonal crystal structure. The transition metal atoms are each bonded to six oxygen atoms in a distorted octahedral coordination, these transition metals are arranged into layers of square grids with the oxygen atoms connecting to two transition metal atoms in the same layer, and another in a layer above or below, see Figure 1.10.

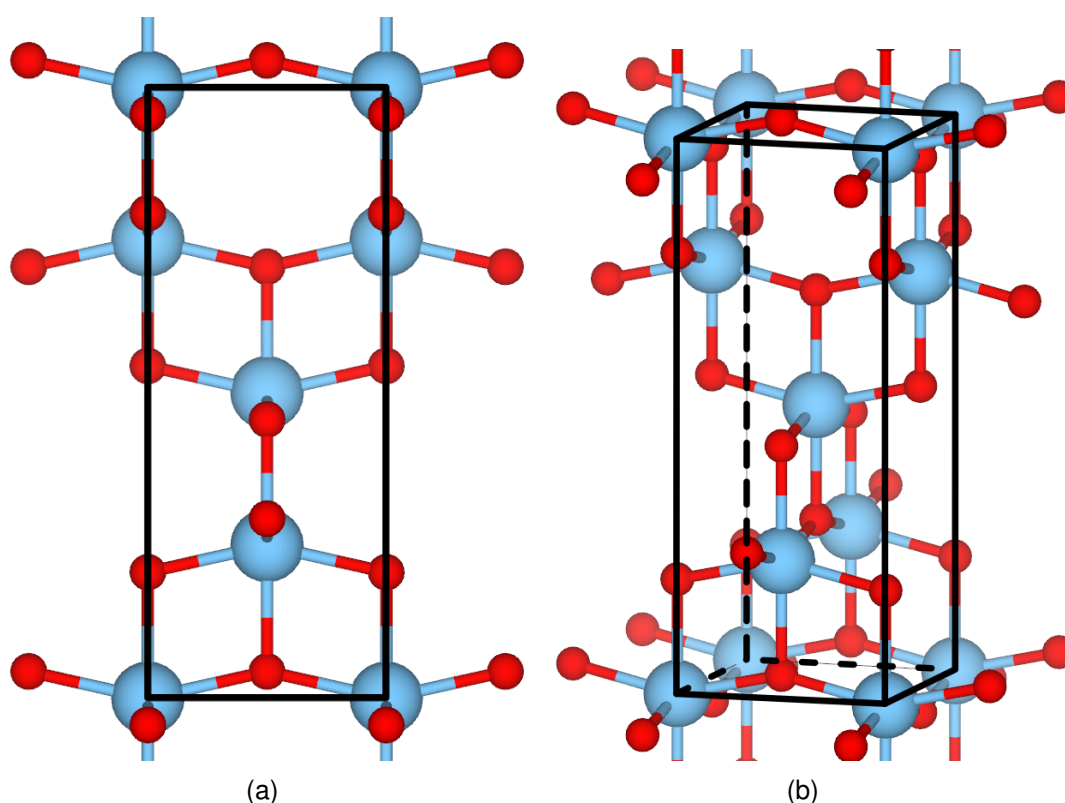


Figure 1.10: A side-on and angled view of the Anatase structure. (a) is the side-on view and (b) is the angled view. The black outline denotes the unit cell / repeat unit.

Within this Anatase structure, the e_g orbitals are split with the $d_{x^2-y^2}$ orbital higher in energy than the d_{z^2} orbital, the t_{2g} orbitals are also split with the d_{xy} orbital higher in energy than the degenerate d_{xz} and d_{yz} orbitals. The t_{2g} set of orbitals around the transition metal overlap with the p -orbitals in the oxygen atoms sharing electrons. The symmetry of these orbitals is what leads to the octahedral coordination, but this does not have perfect symmetry due to the aforementioned splitting showing d_2 like Jahn-Teller distortion, elongating the z direction bonds.

The shared electrons localize closer to the oxygen atoms than the transition metal atoms, giving the oxygen atoms a charge of 2^- and the transition metal atoms a charge of 4^+ [26, 29].

1.4. The Challenge

In this work, a theoretical investigation into the properties of transition metal dichalcogenides and oxides for the use as either photoelectrolysis devices or as battery cathodes for the intercalation of Li-ions is conducted. In particular, we look to develop tools, based on DFT and additional methods, that can be used to gain a better understanding of these materials entirely from a theoretical standpoint.

The investigation into transition metal oxides will consist of looking at different oxide structures and alloys to optimise their stability for use as Li-ion battery cathodes. This requires finding an oxide with the right stoichiometry of alloyed transition metals that is not only stable when lithium is added and removed, but also retains a high capacity and voltage with extended use.

The TMDC family will be investigated for their surface adsorption, stability in water environments and light absorption properties. This requires finding a TMDC that has optimal catalytic energetics for the steps involved in photoelectrolysis, an optimal band gap and is stable in water. This could also be achieved by finding multiple TMDCs that are optimal for different aspects of photoelectrolysis and heterostructuring them together, hopefully preserving the properties they had when separate.

There will also be an overlap, with some TMDCs being investigated for use as Li-ion battery cathodes as the layered structure is favourable for the intercalation and deintercalation of lithium in the van der Waals gap. Many current state of the art battery cathodes in use today have the same structure as TMDCs such as lithium cobalt oxide and NMC.

1.5. Outline of Thesis

In the next chapter, density functional theory will be discussed, being the main method used in these works. In the third chapter, the history of batteries and the basic theory of how Li-ion batteries operate will be discussed, along with the background physics and chemistry of how they work and relevant equations. The current state of the art battery materials will also be presented. Water splitting and photoelectrolysis are discussed in this same chapter, with relevant background physics, chemistry and the guiding reaction pathways, the current state of the art photoelectrolysis devices are also presented. A lot of terminology used throughout the thesis will be defined in these two chapters. In the fourth chapter, we present the development of a method looking at the use of TMDC heterostructures as photoelectrolysis devices. This includes a description of phase diagrams and how they are constructed. In the fifth chapter, the TMDC ScS_2 is investigated for use as a Li-ion and beyond Li-ion battery cathode material. This includes a description of convex hulls and the derivation for a new metric of stability for these materials. In the sixth chapter, TMDC-graphene heterostructures are investigated as a way to improve the capacity of graphene as a Li-ion battery anode. In chapter seven, the alloyed transition metal dioxides $\text{Ni}_x\text{Mn}_y\text{Co}_{1-x-y}\text{O}_2$ (NMC) are analysed in their delithiated state to build an understanding of the lower Li-ion intercalation limit in these materials. This includes a description of empirical potentials that are used within this work. Finally, in chapter eight, we will summarise the work done in this thesis and outline any future work that could be built off of it.

Chapter 2

Density Functional Theory

"In fact, the mere act of opening the box will determine the state of the cat, although in this case there were three determinate states the cat could be in: these being Alive, Dead, and Bloody Furious."

– Terry Pratchett, *Lords and Ladies*

Electrons, nuclei and the way they interact with each other determines the properties of materials that we use every day. Understanding the way these properties come from the arrangements of electrons and nuclei is, therefore, fundamental to our understanding of the world as a whole.

There are multiple different approaches to this within the field of condensed matter physics, such as the tight-binding model, Hartree-Fock, perturbation theory, configuration interaction methods and density functional theory. Density functional theory (DFT) is used within this thesis, it is a powerful and widely used tool in computational and condensed matter physics that allows for the exploration of the properties of materials. This chapter aims to provide an exploration of the fundamental principles and theorems that DFT uses and is built upon.

This will begin with the Schrödinger equation, which can be used to get the energy, forces and wavefunctions, among other important information, of an arrangement of particles, and how this can be applied to periodic structures. Almost all crystalline materials can be described by a small set of atoms with a specific arrangement that can be repeated *ad infinitum*, meaning that if we can understand this small repeating unit, we can understand the material as a whole.

The main theorems that DFT arises from are the Hohenberg-Kohn theorems, the first of which states that for a given external potential, there is a unique electron density that is the ground state electron density, and the second states that a

unique function for the energy can be defined in terms of the the electron density, the minimum of which is the ground state electron density and energy. These are where the Density part of DFT come from. Another key part of DFT are the Kohn-Sham equations, which are based on a set of non-interacting electron-like particles that behave like the interacting electrons, which are also pivotal to making DFT calculable in a reasonable amount of time.

All of this and more are explained in this section to give a broad understanding of DFT and how important it is to the field of condensed matter physics.

2.1. Periodic Materials

We will start from the basics of crystals, where repeating units can be used to make up a larger whole [30, 31, 32]. From the standard definition for the real space translation vector \mathbf{T} and reciprocal space translation vector \mathbf{G}

$$\mathbf{T} = n_1 \mathbf{a}_1 + n_2 \mathbf{a}_2 + n_3 \mathbf{a}_3, \quad (2.1)$$

$$\mathbf{G} = m_1 \mathbf{b}_1 + m_2 \mathbf{b}_2 + m_3 \mathbf{b}_3, \quad (2.2)$$

where $\mathbf{a}_{(1,2,3)}$ and $\mathbf{b}_{(1,2,3)}$ are the real and reciprocal space primitive lattice vectors respectively, $n_{(1,2,3)}$ and $m_{(1,2,3)}$ are integers. These are related to each other *via*

$$\mathbf{a}_j \cdot \mathbf{b}_l = 2\pi \delta_{jl}, \quad (2.3)$$

$$\mathbf{T} \cdot \mathbf{G} = 2p\pi \rightarrow e^{i\mathbf{T} \cdot \mathbf{G}} = 1, \quad (2.4)$$

where δ_{jl} is the Kronecker delta (equal to 1 when $j = l$ and 0 when $j \neq l$) and p is an integer. If a potential $V(\mathbf{r})$ is periodic in real space, it can be defined in reciprocal space as a Fouier series

$$V(\mathbf{r}) = V(\mathbf{r} + \mathbf{T}) = \sum_{\mathbf{G}} V_{\mathbf{G}} e^{i\mathbf{G} \cdot \mathbf{r}}, \quad (2.5)$$

where $V_{\mathbf{G}}$ are Fourier coefficients of $V(\mathbf{r})$. This periodicity of the potential imposes restrictions on the motion of electrons and the form of their wavefunctions. This can be described using the Born-von Karman boundary conditions.

2.1.1 The Born-von Karman boundary conditions

The Born-von Karman boundary conditions impose the restriction that the wavefunction of an electron in a periodic potential must have the same periodicity [30, 33, 34, 35]. If we assume the wavefunction has the form of a planewave

$$\psi(\mathbf{r}) = e^{i(\mathbf{k}\cdot\mathbf{r}-\omega t)}, \quad (2.6)$$

if we make this periodic, with period \mathbf{T} (the real space translation vector), this implies that

$$\psi(\mathbf{r}) = \psi(\mathbf{r} + \mathbf{T}), \quad (2.7)$$

which can also be stated as

$$\psi(\mathbf{r}) = \psi(\mathbf{r} + N_1\mathbf{a}_1) = \psi(\mathbf{r} + N_2\mathbf{a}_2) = \psi(\mathbf{r} + N_3\mathbf{a}_3), \quad (2.8)$$

where N_i are the integer number of unit cells in each direction of the lattice vectors, meaning that the whole crystal is $N_1 \times N_2 \times N_3$ unit cells. We can represent this, like we did for the potential, in reciprocal space by a Fourier transform which then means that

$$e^{jN_1\mathbf{k}\cdot\mathbf{a}_1} = e^{jN_2\mathbf{k}\cdot\mathbf{a}_2} = e^{jN_3\mathbf{k}\cdot\mathbf{a}_3} = 1. \quad (2.9)$$

This restricts the allowed values of the wavevector to satisfy $N_{(1,2,3)}\mathbf{k}\cdot\mathbf{a}_{(1,2,3)} = 2\pi p$, where p is an integer.

2.1.2 Bloch's theorem

If in a periodic system, the wavefunction is periodic. This means that the operators that act on it also need to be periodic [30]. If we take the Schrödinger equation

$$\hat{H}\psi(\mathbf{r}) = \left[-\frac{\hbar^2}{2m}\nabla^2 + V(\mathbf{r}) \right] \psi(\mathbf{r}) = E\psi(\mathbf{r}), \quad (2.10)$$

we can rewrite it using Fourier series for all the operators and the wavefunction to get

$$\begin{aligned} \hat{H}\psi(\mathbf{r}) &= \hat{H} \sum_{\mathbf{k}} C_{\mathbf{k}} e^{i\mathbf{k}\cdot\mathbf{r}} = \\ \sum_{\mathbf{k}} \frac{\hbar^2 k^2}{2m} C_{\mathbf{k}} e^{i\mathbf{k}\cdot\mathbf{r}} + \left[\sum_{\mathbf{G}} V_{\mathbf{G}} e^{i\mathbf{G}\cdot\mathbf{r}} \sum_{\mathbf{k}} C_{\mathbf{k}} e^{i\mathbf{k}\cdot\mathbf{r}} \right] &= E \sum_{\mathbf{k}} C_{\mathbf{k}} e^{i\mathbf{k}\cdot\mathbf{r}}, \end{aligned} \quad (2.11)$$

where $C_{\mathbf{k}}$ are the Fourier coefficients of $\psi(\mathbf{r})$. Given that the potential term is summed over all \mathbf{G} and all \mathbf{k} , \mathbf{k} in this can be replaced with $\mathbf{k} - \mathbf{G}$ and rearranged to get

$$\sum_{\mathbf{k}} e^{i\mathbf{k}\cdot\mathbf{r}} \left[\left(\frac{\hbar^2 k^2}{2m} - E \right) C_{\mathbf{k}} + \sum_{\mathbf{G}} V_{\mathbf{G}} C_{\mathbf{k}-\mathbf{G}} \right] = 0, \quad (2.12)$$

Because the Born-von Karman planewaves are an orthogonal set of functions, we can reduce this to

$$\left(\frac{\hbar^2 k^2}{2m} - E \right) C_{\mathbf{k}} + \sum_{\mathbf{G}} V_{\mathbf{G}} C_{\mathbf{k}-\mathbf{G}} = 0. \quad (2.13)$$

We know that the first Brillouin zone contains all the information about reciprocal space so we can write $\mathbf{k} = (\mathbf{q} - \mathbf{G}')$, where \mathbf{q} lies in the first Brillouin zone and \mathbf{G}' is another reciprocal lattice vector. This leads to

$$\left(\frac{\hbar^2 (\mathbf{q} - \mathbf{G}')^2}{2m} - E \right) C_{\mathbf{q}-\mathbf{G}'} + \sum_{\mathbf{G}} V_{\mathbf{G}} C_{\mathbf{q}-\mathbf{G}'-\mathbf{G}} = 0. \quad (2.14)$$

We can make one finally change of variable, $\mathbf{G}'' \rightarrow \mathbf{G} + \mathbf{G}'$, to get

$$\left(\frac{\hbar^2(\mathbf{q} - \mathbf{G}')^2}{2m} - E \right) C_{\mathbf{q}-\mathbf{G}'} + \sum_{\mathbf{G}''} V_{\mathbf{G}''-\mathbf{G}'} C_{\mathbf{q}-\mathbf{G}''} = 0. \quad (2.15)$$

This equation specifies the $C_{\mathbf{k}}$ which are used to make up the wavefunction $\psi(\mathbf{r})$. If we choose a particular value of \mathbf{q} , then all $C_{\mathbf{k}}$ are of the form $C_{\mathbf{q}-\mathbf{G}}$, therefore, for each distinct value of \mathbf{q} there is a wavefunction $\psi_{\mathbf{q}}(\mathbf{r})$ of form

$$\begin{aligned} \psi_{\mathbf{q}}(\mathbf{r}) &= \sum_{\mathbf{G}} C_{\mathbf{q}-\mathbf{G}} e^{i(\mathbf{q}-\mathbf{G})\cdot\mathbf{r}} \\ &= e^{i\mathbf{q}\cdot\mathbf{r}} \sum_{\mathbf{G}} C_{\mathbf{q}-\mathbf{G}} e^{-i\mathbf{G}\cdot\mathbf{r}} \\ &= e^{i\mathbf{q}\cdot\mathbf{r}} u_{\mathbf{q}}(\mathbf{r}). \end{aligned} \quad (2.16)$$

This is Bloch's theorem [36], where $u_{\mathbf{q}}(\mathbf{r})$ is a function with the same periodicity as the lattice. It can be used to describe the motion of not only electrons, but any particle, which satisfies Schrödinger's equation, propagating in a lattice. The potential used here is local, but a similar process can be done for a non-local potential given by $\int V(\mathbf{r}, \mathbf{r}') \psi(\mathbf{r}') d\mathbf{r}'$ as these still have the same periodicity as the crystal. The local potential form can be extracted from this by setting $V(\mathbf{r}, \mathbf{r}') = V(\mathbf{r})\delta(\mathbf{r} - \mathbf{r}')$ [37].

2.2. Variational principle

The most common method of solving the Schrödinger equation is by using the variational principle [37], we start by showing that the expectation value of the Hamiltonian $\langle \psi | \hat{H} | \psi \rangle$ is made stationary (meaning it is a minima) over all differentiable wavefunctions $\psi(\mathbf{r})$ that satisfy Bloch's theorem with a wave vector \mathbf{k} with wavefunction $\psi_{\mathbf{k}}(\mathbf{r})$. By letting $\psi(\mathbf{r})$ be close to $\psi_{\mathbf{k}}(\mathbf{r})$ such that

$$\psi(\mathbf{r}) = \psi_{\mathbf{k}}(\mathbf{r}) + \delta\psi(\mathbf{r}), \quad (2.17)$$

where $\delta\psi(\mathbf{r})$ is a small variation or perturbation. As $\psi(\mathbf{r})$ satisfies Bloch's theorem, $\delta\psi(\mathbf{r})$ also does, meaning that

$$\langle \psi | \hat{H} | \psi \rangle = \langle \psi_{\mathbf{k}} | \hat{H} | \psi_{\mathbf{k}} \rangle + \delta \langle \psi | \hat{H} | \psi \rangle. \quad (2.18)$$

Given that we can't assume the wavefunctions to be normalised, we can write the expectation value as

$$\langle \psi | \hat{H} | \psi \rangle = \frac{\int \psi^* \hat{H} \psi dv}{\int \psi^* \psi dv}, \quad (2.19)$$

where v represents any integration coordinates. Rephrasing this in terms of our variation $\delta\psi(\mathbf{r})$ we get

$$\begin{aligned} \langle \psi_{\mathbf{k}} | \hat{H} | \psi_{\mathbf{k}} \rangle + \delta \langle \psi | \hat{H} | \psi \rangle &= \frac{\int (\psi_{\mathbf{k}}^* + \delta\psi^*) \hat{H} (\psi_{\mathbf{k}} + \delta\psi) dv}{\int (\psi_{\mathbf{k}}^* + \delta\psi^*) (\psi_{\mathbf{k}} + \delta\psi) dv}, \\ &= \frac{\int \psi_{\mathbf{k}}^* \hat{H} \psi_{\mathbf{k}} dv + \int \delta\psi^* \hat{H} \psi_{\mathbf{k}} dv + \int \psi_{\mathbf{k}}^* \hat{H} \delta\psi dv}{\int \psi_{\mathbf{k}}^* \psi_{\mathbf{k}} dv + \int \delta\psi^* \psi_{\mathbf{k}} dv + \int \psi_{\mathbf{k}}^* \delta\psi dv}, \end{aligned} \quad (2.20)$$

where terms of the order $\delta\psi^2$ have been excluded due to $\delta\psi(\mathbf{r})$ being defined as small. We then use the approximation $\frac{1}{1+x} \simeq 1 - x$ for $x \ll 1$ and where $x = \frac{\int \delta\psi^* \psi_{\mathbf{k}} dv}{\int \psi_{\mathbf{k}}^* \psi_{\mathbf{k}} dv} + \frac{\int \psi_{\mathbf{k}}^* \delta\psi dv}{\int \psi_{\mathbf{k}}^* \psi_{\mathbf{k}} dv}$ to get

$$\begin{aligned} \langle \psi_{\mathbf{k}} | \hat{H} | \psi_{\mathbf{k}} \rangle + \delta \langle \psi | \hat{H} | \psi \rangle &= \left(\int \psi_{\mathbf{k}}^* \hat{H} \psi_{\mathbf{k}} dv + \int \delta\psi^* \hat{H} \psi_{\mathbf{k}} dv + \int \psi_{\mathbf{k}}^* \hat{H} \delta\psi dv \right) \times \\ &\quad \frac{1}{\int \psi_{\mathbf{k}}^* \psi_{\mathbf{k}} dv} \left(1 - \frac{\int \delta\psi^* \psi_{\mathbf{k}} dv}{\int \psi_{\mathbf{k}}^* \psi_{\mathbf{k}} dv} - \frac{\int \psi_{\mathbf{k}}^* \delta\psi dv}{\int \psi_{\mathbf{k}}^* \psi_{\mathbf{k}} dv} \right). \end{aligned} \quad (2.21)$$

From this we can rearrange for the expectation value of the perturbation $\delta \langle \psi | \hat{H} | \psi \rangle$

$$\begin{aligned} \delta \langle \psi | \hat{H} | \psi \rangle &= \frac{\int \delta\psi^* \hat{H} \psi_{\mathbf{k}} dv}{\int \psi_{\mathbf{k}}^* \psi_{\mathbf{k}} dv} + \frac{\int \psi_{\mathbf{k}}^* \hat{H} \delta\psi dv}{\int \psi_{\mathbf{k}}^* \psi_{\mathbf{k}} dv} \\ &\quad - \langle \psi_{\mathbf{k}} | \hat{H} | \psi_{\mathbf{k}} \rangle \left(\frac{\int \delta\psi^* \psi_{\mathbf{k}} dv}{\int \psi_{\mathbf{k}}^* \psi_{\mathbf{k}} dv} + \frac{\int \psi_{\mathbf{k}}^* \delta\psi dv}{\int \psi_{\mathbf{k}}^* \psi_{\mathbf{k}} dv} \right), \end{aligned} \quad (2.22)$$

where the four additional terms that arise have been omitted due to them being of the order $\delta\psi^2$. If we now choose $\psi_{\mathbf{k}}$ so that $\langle\psi_{\mathbf{k}}|\hat{H}|\psi_{\mathbf{k}}\rangle$ is stationary, meaning $\delta\langle\psi|\hat{H}|\psi\rangle = 0$, we get

$$\int \delta\psi^* [\hat{H} - \langle\psi_{\mathbf{k}}|\hat{H}|\psi_{\mathbf{k}}\rangle] \psi_{\mathbf{k}} d\nu + \int \psi_{\mathbf{k}}^* [\hat{H} - \langle\psi_{\mathbf{k}}|\hat{H}|\psi_{\mathbf{k}}\rangle] \delta\psi d\nu, \quad (2.23)$$

where, as defined, $\delta\psi$ is a small variation leading to

$$[\hat{H} - \langle\psi_{\mathbf{k}}|\hat{H}|\psi_{\mathbf{k}}\rangle] \psi_{\mathbf{k}} = 0, \quad (2.24)$$

which returns us to the solution of the Schrödinger equation

$$\hat{H}\psi_{\mathbf{k}} = E\psi_{\mathbf{k}}, \quad (2.25)$$

meaning that $\psi_{\mathbf{k}}(\mathbf{r}) = \psi(\mathbf{r})$ within a small perturbation from the minima. Using this principle we can now find the ground state wavefunction and energy for a given system.

2.2.1 The ground state energy

Starting from a normalised trial wavefunction ψ , the variational principle has shown that the ground state energy, E_0 , of the system described by this is always less than or equal to the expectation value using this trial wavefunction

$$E_0 \leq \langle\psi|\hat{H}|\psi\rangle. \quad (2.26)$$

If we vary ψ until this expectation value is minimised, we can obtain the wavefunction and energy of the ground state for a given system. In order to prove this, we start with a system with wavefunction ψ_n and energy E_n that are the eigenstates and eigenvalues of \hat{H}

$$\hat{H}\psi_n = E_n\psi_n, \quad (2.27)$$

where $E_0 < E_1 < \dots$, meaning that ψ_0 is the ground state wavefunction, ψ_1 is the first excited state and so on. If all ψ_n are assumed to be orthonormal, $\langle \psi_n | \psi_m \rangle = \delta_{nm}$, we can write a trial wavefunction as

$$\psi = \sum_n c_n \psi_n, \quad (2.28)$$

where $\sum_n |c_n|^2 = 1$. We can now expand the expectation value of the Hamiltonian to get

$$\begin{aligned} \langle \psi | \hat{H} | \psi \rangle &= \left\langle \sum_n c_n \psi_n \left| \hat{H} \right| \sum_m c_m \psi_m \right\rangle \\ &= \sum_{n,m} c_n^* c_m \langle \psi_n | \hat{H} | \psi_m \rangle \\ &= \sum_n c_n^* c_n E_n \langle \psi_n | \psi_n \rangle \\ &= \sum_n E_n |c_n|^2, \end{aligned} \quad (2.29)$$

if we pull out the $n = 0$ term from this summation we get

$$\langle \psi | \hat{H} | \psi \rangle = |c_0|^2 E_0 + \sum_{n,n>0} |c_n|^2 E_n. \quad (2.30)$$

We can now write

$$\langle \psi | \hat{H} | \psi \rangle = E_0 + \sum_{n,n>0} |c_n|^2 (E_n - E_0), \quad (2.31)$$

from which we can see that the second term is always greater than zero, resulting in the variation principle

$$\langle \psi | \hat{H} | \psi \rangle \geq E_0. \quad (2.32)$$

This same method can be applied to get approximations to wavefunctions of excited states, but as the errors in this method are cumulative for higher and

higher excited states, the variation principle is generally used only for ground states.

2.3. Many body systems

So far we have only considered the wavefunction and Hamiltonian for a single particle, in order to describe any real system we will need to solve the Hamiltonian for many interacting particles. The Hamiltonian operator \hat{H} for the Schrödinger equation is

$$\hat{H}\psi(\mathbf{r}) = \left[-\frac{\hbar^2}{2m} \nabla^2 + V(\mathbf{r}) \right] \psi(\mathbf{r}) = E\psi(\mathbf{r}), \quad (2.33)$$

where \hbar is the reduced Planck constant, m is mass, \mathbf{r} is a position vector, ∇^2 is the Laplace operator, $V(\mathbf{r})$ is an external potential field, E is the energy and $\psi(\mathbf{r})$ is the wavefunction. This can be seen to be made up of two terms, a kinetic energy term and a potential energy term, and can be used to find the energy of a particle that is either moving or is stationary in a external potential $V(\mathbf{r})$.

The kinetic energy term can be expanded into a summation due to it being independent for each particle

$$-\frac{\hbar^2}{2m} \nabla^2 \rightarrow \sum_i \left[-\frac{\hbar^2}{2m_i} \nabla_i^2 \right], \quad (2.34)$$

where i indexes each particle. The potential term, if we consider this as a simple coulomb interaction, will be directly related the position of ever other particle in a system. This means that the potential term must have a form similar to

$$V(\mathbf{r}) \rightarrow V(\mathbf{r}_1, \dots, \mathbf{r}_n) = \sum_{i,j} \left[\frac{q_i q_j}{4\pi\epsilon_0 |\mathbf{r}_i - \mathbf{r}_j|} \right], \quad (2.35)$$

where q_i is the charge on particle i and ϵ_0 is the permittivity of free space. Lastly we have to expand the wavefunction from single particle to many particle by simple changing it to

$$\psi(\mathbf{r}) \rightarrow \psi(\vec{r}_1, \dots, \vec{r}_n). \quad (2.36)$$

Combining all these back into the Schrödinger equation we get the many-body Schrödinger equation that can be used to describe a many-body system of interacting particles

$$\begin{aligned} \hat{H}\psi(\vec{r}_1, \dots, \vec{r}_n) &= \left[\sum_i \left(-\frac{\hbar^2}{2m_i} \nabla_i^2 \right) + \sum_{i,j} \left(\frac{q_i q_j}{4\pi\epsilon_0 |\vec{r}_i - \vec{r}_j|} \right) \right] \psi(\vec{r}_1, \dots, \vec{r}_n) \\ &= E\psi(\vec{r}_1, \dots, \vec{r}_n). \end{aligned} \quad (2.37)$$

This can be split further, starting with the kinetic energy term being split into an ionic kinetic energy term and an electronic kinetic energy term, denoted as T_{ion} and T_{elec} respectively. The potential term is also split into three terms, an ion-ion interaction term, an electron-electron interaction term and an electron-ion interaction term, denoted as $V_{ion-ion}$, $V_{elec-elec}$ and $V_{elec-ion}$ respectively. The Schrödinger equation now has the form

$$\begin{aligned} \hat{H}\psi(\vec{R}_1, \dots, \vec{R}_N, \vec{r}_1, \dots, \vec{r}_n) &= (T_{ion} + T_{elec} + V_{ion-ion} + V_{elec-elec} + V_{elec-ion}) \times \\ &\psi(\vec{R}_1, \dots, \vec{R}_N, \vec{r}_1, \dots, \vec{r}_n) \\ &= E\psi(\vec{R}_1, \dots, \vec{R}_N, \vec{r}_1, \dots, \vec{r}_n), \end{aligned} \quad (2.38)$$

where

$$\begin{aligned}
T_{ion} &= -\frac{\hbar^2}{2} \sum_i^N \left(-\frac{1}{M_i} \nabla_i^2 \right), \\
T_{elec} &= -\frac{\hbar^2}{2m_e} \sum_i^n \nabla_i^2, \\
V_{ion-ion} &= \frac{1}{4\pi\epsilon_0} \sum_{i,j \neq i}^{N,N} \left(\frac{q_i q_j}{|\vec{R}_i - \vec{R}_j|} \right), \\
V_{elec-elec} &= \frac{e^2}{4\pi\epsilon_0} \sum_{i,j \neq i}^{n,n} \left(\frac{1}{|\vec{r}_i - \vec{r}_j|} \right), \\
V_{elec-ion} &= \frac{e}{4\pi\epsilon_0} \sum_{i,j}^{n,N} \left(\frac{q_j}{|\vec{r}_i - \vec{R}_j|} \right),
\end{aligned} \tag{2.39}$$

for a system of N ions and n electrons where ion i has mass M_i , charge q_i and position R_i and the electrons have mass m_e and charge e , with electron i having position r_i .

2.4. The Born-Oppenheimer approximation

Now that we have split the Hamiltonian into five different terms, we want to split the wavefunction into an ionic and an electronic part, the goal of this is to end up with a Schrödinger equation for just the electrons that is dependent on the positions of the electrons, r , the relative positions between ions, ξ , and the orientation of the ions, Θ , in Eulerian angles (θ, ϕ, ψ)

$$\hat{H}_{elec} \phi_n = (\hat{T}_{elec}(r) + \hat{V}_{elec-elec}(r) + \hat{V}_{elec-ion}(r; \xi, \Theta)) \phi_n. \tag{2.40}$$

where ϕ_n is the normalised electronic wavefunction for the n^{th} electron.

The Born-Oppenheimer approximation is a method of splitting the Schrödinger equation into terms which each contain less and less energy of the system of ions and electrons being described [38]. This is done by introducing a new variable that is related to the mass of the electrons and ions, κ , that is equal to

$$\kappa = \left(\frac{m_e}{\bar{M}} \right)^{1/4}, \tag{2.41}$$

where m_e is the mass of an electron and \bar{M} is the average mass of the ions. This can be used to get a natural order of the energy terms, with κ^2 terms relating to nuclear vibrations (second order) and κ^4 terms relating to nuclear rotations (fourth order), while the κ^1 and κ^3 terms disappear (first and third order). Higher order terms do exist, corresponding to coupling between the three basic types of motion, but the amount of energy contributed from these is so small that they will be ignored.

If we start from equation 2.38, we can write the electronic and ionic kinetic energy terms as

$$T_{elec} = -\frac{\hbar^2}{2m_e} \sum_r \sum_k \frac{\partial^2}{\partial r_k^2}, \quad (2.42)$$

$$T_{ion} = -\kappa^4 \frac{\hbar^2}{2m_e} \sum_R \sum_l \mu_l \frac{\partial^2}{\partial R_l^2}, \quad (2.43)$$

where \sum_r is over the position coordinates of the electrons and \sum_R is over all coordinates of the ions, this also includes the rotation of the ions. μ_l has been introduced as dimensionless numbers defined by $M_l = \bar{M}/\mu_l$ where M_l is the mass of a single ion. We then represent the total energy operator by

$$H = H_0 + \kappa^4 H_1, \quad (2.44)$$

where

$$T_{elec} + V_{ion-ion} + V_{elec-elec} + V_{elec-ion} = H_0 \left(r, \frac{\partial}{\partial r}; R \right), \quad (2.45)$$

$$T_{ion} = \kappa^4 H_1 \left(\frac{\partial}{\partial R} \right), \quad (2.46)$$

where all coulomb interactions between all electrons and all ions rely only on the relative positions of the particles. This means that if we consider the zeroth order approximation (κ^0 terms), we do not include any ionic kinetic energy in any form.

For higher orders of the approximation, we will need to split the ionic coordinates into two sets, the first is a set of relative positions between ions

$$\xi_i = \xi_i(R), \quad (2.47)$$

and the second is the positions and orientations of the ions, with the orientations being in the form of Eulerian angles (θ, ϕ, ψ)

$$\Theta_i = \Theta_i(R). \quad (2.48)$$

With these we can split the ionic kinetic energy term into

$$H_1 = H_{\xi\xi} + H_{\xi\Theta} + H_{\Theta\Theta}, \quad (2.49)$$

where $H_{\xi\xi}$ depends on ξ_i and $\frac{\partial^2}{\partial\xi_i\partial\xi_j}$, $H_{\xi\Theta}$ depends on ξ_i , Θ_i , $\frac{\partial}{\partial\xi_i}$ and $\frac{\partial}{\partial\Theta_i}$ and $H_{\Theta\Theta}$ depends on ξ_i , Θ_i , $\frac{\partial}{\partial\Theta_i}$ and $\frac{\partial^2}{\partial\Theta_i\partial\Theta_j}$.

If we now expand out the energy operator from equation 2.44, and apply it to the wavefunction we get

$$(H_0 + \kappa^4(H_{\xi\xi} + H_{\xi\Theta} + H_{\Theta\Theta}) - E)\psi = 0. \quad (2.50)$$

We now introduce a perturbation to the relative positions of the nuclei, $\xi_i = \xi_i + \kappa\zeta_i$ and use this to do a Taylor's expansion on all terms in the above function

$$H_0(r, \frac{\partial}{\partial r}; \xi + \kappa\zeta, \Theta) = H_0^{(0)} + \kappa H_0^{(1)} + \kappa^2 H_0^{(2)} + \dots, \quad (2.51)$$

where

$$\begin{aligned}
(a) \quad H_0^{(0)} &= H_0\left(r, \frac{\partial}{\partial r}; \xi\right), \\
(b) \quad H_0^{(1)} &= \sum_i \zeta_i \frac{\partial H_0}{\partial \xi_i}, \\
(c) \quad H_0^{(2)} &= \frac{1}{2} \sum_{i,j} \zeta_i \zeta_j \frac{\partial^2 H_0}{\partial \xi_i \partial \xi_j}, \\
&\dots
\end{aligned} \tag{2.52}$$

and using $\frac{\partial}{\partial \xi} = \frac{1}{\kappa} \frac{\partial}{\partial \zeta}$

$$\begin{aligned}
\kappa^4 H_1\left(X, \frac{\partial}{\partial X}\right) &= \kappa^4 \left(\frac{1}{\kappa^2} H_{\zeta\zeta} + \frac{1}{\kappa} H_{\zeta\Theta} + H_{\Theta\Theta} \right), \\
&= \kappa^2 H_{\zeta\zeta}^{(0)} + \kappa^3 (H_{\zeta\Theta}^{(0)} + H_{\zeta\zeta}^{(1)}) + \kappa^4 (H_{\Theta\Theta}^{(0)} + H_{\zeta\Theta}^{(1)} + H_{\zeta\zeta}^{(2)}) + \dots,
\end{aligned} \tag{2.53}$$

where each $H_a^{(n)}$ is related to $H_a^{(n-1)}$ is the same way as H_0 . A Taylor's expansion is used on both the energy and the wavefunction to get

$$\begin{aligned}
\psi &= \psi^{(0)} + \kappa \psi^{(1)} + \kappa^2 \psi^{(2)} + \dots, \\
E &= E^{(0)} + \kappa E^{(1)} + \kappa^2 E^{(2)} + \dots,
\end{aligned} \tag{2.54}$$

Putting these into equation 2.50 we can group the terms that have the same power of κ to get a series of approximation equations

$$\begin{aligned}
(a) \quad & (H_0^{(0)} - E^{(0)})\psi^{(0)} = 0, \\
(b) \quad & (H_0^{(0)} - E^{(0)})\psi^{(1)} = (E^{(1)} - H_0^{(1)})\psi^{(0)}, \\
(c) \quad & (H_0^{(0)} - E^{(0)})\psi^{(2)} = (E^{(1)} - H_0^{(1)})\psi^{(1)} + (E^{(2)} - H_0^{(2)} - H_{\zeta\zeta}^{(0)})\psi^{(0)}, \\
(d) \quad & (H_0^{(0)} - E^{(0)})\psi^{(3)} = (E^{(1)} - H_0^{(1)})\psi^{(2)} + (E^{(2)} - H_0^{(2)} - H_{\zeta\zeta}^{(0)})\psi^{(1)} + \\
& (E^{(3)} - H_0^{(3)} - H_{\zeta\theta}^{(0)} - H_{\zeta\zeta}^{(1)})\psi^{(0)} \\
(e) \quad & (H_0^{(0)} - E^{(0)})\psi^{(4)} = (E^{(1)} - H_0^{(1)})\psi^{(3)} + (E^{(2)} - H_0^{(2)} - H_{\zeta\zeta}^{(0)})\psi^{(2)} + \\
& (E^{(3)} - H_0^{(3)} - H_{\zeta\theta}^{(0)} - H_{\zeta\zeta}^{(1)})\psi^{(1)} + (E^{(4)} - H_0^{(4)} - H_{\theta\theta}^{(0)} - H_{\zeta\theta}^{(1)} - H_{\zeta\zeta}^{(2)})\psi^{(0)}. \\
& \dots
\end{aligned} \tag{2.55}$$

These correspond to the zeroth to fourth order Born-Oppenheimer approximations. Higher orders approximate equations can be found but each higher order contributes roughly 15% of the previous if we use the simple approximation that the mass of an ion is 2000 times larger than the mass of an electron ($\kappa = (m_e/m_p)^{1/4} \approx 0.153$ where m_p is the mass of a proton).

2.4.1 Solving the zeroth and first orders: Equilibrium of the Nuclei

The zeroth and first order equations are equivalent to thinking of the nuclei as stationary in their average positions. The general solution to the zeroth order takes the form

$$\psi_n^{(0)} = \chi_n^{(0)}(\zeta, \Theta)\phi_n^{(0)}(r; \xi, \Theta), \tag{2.56}$$

where $\chi_n^{(0)}$ is an arbitrary function of ξ_i and Θ_i , which is included to allow higher orders to be solved, and $\phi_n^{(0)}$ is a normalised eigenfunction.

Solving equation 2.55b

$$(H_0^{(0)} - E^{(0)})\psi^{(1)} = (E^{(1)} - H_0^{(1)})\psi^{(0)}, \quad (2.57)$$

can only be done when the right-hand side is orthogonal to $\psi_n^{(0)}$, this requirement gives the condition

$$\left\{ \left(H_0^{(1)} \right)_{nn} - E^{(1)} \right\} \chi_n^{(0)}(\zeta, \Theta) = 0, \quad (2.58)$$

where $\left(H_0^{(1)} \right)_{nn}$ is the diagonal matrix element of $H_0^{(1)}$ relative to x_k and, due to the way $H_0^{(1)}$ has been defined, is a homogeneous linear function of ζ_i . This means that, if we do not consider a wavefunction that vanishes, we get

$$E^{(1)} = 0, \quad \left(H_0^{(1)} \right)_{nn} = 0. \quad (2.59)$$

This leads to a solution to the first order approximation of

$$\psi_n^{(1)} = \chi_n^{(0)}(\zeta, \Theta)\phi_n^{(1)}(r; \xi, \Theta) + \chi_n^{(1)}(\zeta, \Theta)\phi_n^{(0)}(r; \xi, \Theta). \quad (2.60)$$

Yet again, we have another arbitrary function $\chi_n^{(1)}$, the form of which can be determined by solving higher orders.

2.4.2 Solving the second and third orders: Nuclear Vibration

When equations 2.59 and 2.60 are substituted back into equation 2.55c we get the second order approximation as

$$(H_0^{(0)} - E^{(0)})\psi^{(2)} = -H_0^{(1)}\chi_n^{(0)}\phi_n^{(1)} + (E^{(2)} - H_0^{(2)} - H_{\zeta\zeta}^{(0)})\chi_n^{(0)}\phi_n^{(0)} - H_0^{(1)}\chi_n^{(1)}\phi_n^{(0)}, \quad (2.61)$$

which can be solved to eventually get the second order solution

$$\psi_n^{(2)} = \chi_n^{(0)}(\zeta, \Theta)\phi_n^{(2)}(r; \xi, \Theta) + \chi_n^{(1)}(\zeta, \Theta)\phi_n^{(1)}(r; \xi, \Theta) + \chi_n^{(2)}(\zeta, \Theta)\phi_n^{(0)}(r; \xi, \Theta). \quad (2.62)$$

The third order approximation solution follows this same pattern, but we will only be using up to the second order approximation solution. Taking up to the second order approximation solution (up to terms with κ^2), the wavefunction from equation 2.54 becomes

$$\begin{aligned}\psi &= \psi_n^{(0)} + \kappa\psi_n^{(1)} + \kappa^2\psi_n^{(2)} + \dots \\ &= \chi_n^{(0)} \left(\phi_n^{(0)} + \kappa\phi_n^{(1)} + \kappa^2\phi_n^{(2)} + \dots \right) \\ &\quad + \kappa\chi_n^{(1)} \left(\phi_n^{(0)} + \kappa\phi_n^{(1)} + \dots \right) + \kappa^2\chi_n^{(2)} \left(\phi_n^{(0)} + \dots \right) + \dots,\end{aligned}\tag{2.63}$$

which can be reduced down to

$$\psi = \left(\chi_n^{(0)}(\zeta, \Theta) + \kappa\chi_n^{(1)}(\zeta, \Theta) + \kappa^2\chi_n^{(2)}(\zeta, \Theta) \right) \phi_n(r; \xi, \Theta).\tag{2.64}$$

This wavefunction has a simple interpretation, the first order describes the motion of the nuclei and the second order shows that during nuclear motion, the electrons move with them almost as if the nuclei were stationary from their frame of reference. This second order approximation is often referred to as the adiabatic approximation as the motion of the electrons as they follow the nuclei is adiabatic.

Because this wavefunction is an electronic wavefunction multiplied by a Taylor's series of ionic wavefunctions, we can remove the ionic part from both sides of the Schrödinger equation. This electronic wavefunction is not acted upon by the ionic kinetic energy term T_{ion} or the ion-ion interaction term $V_{ion-ion}$ meaning that they can be dropped, leaving us with

$$\hat{H}_{elec}\phi_n = \left(\hat{T}_{elec}(r) + \hat{V}_{elec-elec}(r) + \hat{V}_{elec-ion}(r; \xi, \Theta) \right) \phi_n.\tag{2.65}$$

Many methods for solving the Schrödinger equation for multi-electron and ion systems use the Born-Oppenheimer approximation such as the Hartree-Fock method and density functional theory. It is also the starting point for many electron-phonon interaction calculations among other areas of condensed matter research [37].

2.5. Hartree-Fock Method

One of the first standard methods for solving many-body quantum systems is the Hartree-Fock method [37, 39, 40], this involves first writing a properly anti-symmetric determinant wavefunction for N electrons, called a Slater determinant

$$\Phi((\mathbf{r}_1, \sigma_1), \dots, (\mathbf{r}_N, \sigma_N)) = \frac{1}{\sqrt{N!}} \begin{vmatrix} \psi_1(\mathbf{r}_1, \sigma_1) & \cdots & \psi_1(\mathbf{r}_N, \sigma_N) \\ \vdots & \ddots & \vdots \\ \psi_N(\mathbf{r}_1, \sigma_1) & \cdots & \psi_N(\mathbf{r}_N, \sigma_N) \end{vmatrix} \quad (2.66)$$

which includes the electronic spin σ_i in each single-particle "spin-orbital" $\psi_i(\mathbf{r}_j, \sigma_j)$. This Slater determinant also satisfies the Pauli exclusion principle as when $\psi_1 = \psi_2$, the determinant is zero. We will first consider a case with no spin-orbit interactions $\psi_i(\mathbf{r}_j, \sigma_j) = \psi_i^\sigma(\mathbf{r}_j)\alpha_i(\sigma_j)$, which introduces the spin variable $\alpha_i(\sigma_j)$ (it is of note that in a closed-shell cases, the position function, $\psi_i^\sigma(\mathbf{r}_j)$, is independent of spin). If the Hamiltonian is independent of spin, the energy is given by

$$\begin{aligned} E_{HF} = \langle \Phi | \hat{H} | \Phi \rangle &= \sum_{i,\sigma} \int \psi_i^{\sigma*}(\mathbf{r}) \left[-\frac{1}{2} \nabla^2 + V_{ext}(\mathbf{r}) \right] \psi_i^\sigma d\mathbf{r} + E_{II} \\ &+ \frac{1}{2} \sum_{i,j,\sigma_i,\sigma_j} \int \psi_i^{\sigma_i*}(\mathbf{r}) \psi_j^{\sigma_j*}(\mathbf{r}') \frac{1}{|\mathbf{r} - \mathbf{r}'|} \psi_i^{\sigma_i}(\mathbf{r}) \psi_j^{\sigma_j}(\mathbf{r}') d\mathbf{r} d\mathbf{r}' \\ &- \frac{1}{2} \sum_{i,j,\sigma} \int \psi_i^{\sigma*}(\mathbf{r}) \psi_j^{\sigma*}(\mathbf{r}') \frac{1}{|\mathbf{r} - \mathbf{r}'|} \psi_j^\sigma(\mathbf{r}) \psi_i^\sigma(\mathbf{r}') d\mathbf{r} d\mathbf{r}'. \end{aligned} \quad (2.67)$$

The first term of this equation groups together all single-body expectation values that involve sums over orbitals, the second term is the electron-ion interaction energy, the third and fourth terms are the direct and exchange interaction terms between electrons. Hartree units are used for this to shorten the equation ($\hbar = m_e = e^2 = 1$).

The Hartree-Fock method is to minimise the total energy with respect to all degrees of freedom in the wavefunction of the same form as equation 2.66 which gives the Hartree-Fock equation,

$$\left[-\frac{1}{2}\nabla^2 + V_{ext}(\mathbf{r}) + \sum_{j,\sigma_j} \int \psi_j^{\sigma_j*}(\mathbf{r}')\psi_j^{\sigma_j}(\mathbf{r}')\frac{1}{|\mathbf{r}-\mathbf{r}'|}d\mathbf{r}' \right] \psi_i^\sigma(\mathbf{r}) - \sum_j \int \psi_j^{\sigma_j*}(\mathbf{r}')\psi_i^\sigma(\mathbf{r}')\frac{1}{|\mathbf{r}-\mathbf{r}'|}\psi_j^\sigma(\mathbf{r})d\mathbf{r}' = \epsilon_i^\sigma \psi_i^\sigma(\mathbf{r}). \quad (2.68)$$

The first term of this is the kinetic energy of an electron and the second term is the potential between an electron and an ion. The third term is called the Hartree term and is the potential between an electron and the average charge distribution of all the other electrons. The final term is the exchange term which is essentially the Pauli exclusion principle and acts to separate electrons of the same spin.

The main limitation of the Hartree-Fock method is that it only includes exchange effects but not correlation effects which is the interaction between electrons of different spin and is very important for capturing all properties of electronic systems. Even when solving the Hartree-Fock equations exactly (which can only be done for spherically symmetric atoms and the homogeneous electron gas), the Schrödinger equation has not been solved, instead an approximate wavefunction is obtained. Methods exist that can be used to get better approximations to the wavefunctions that extend Hartree-Fock; however, these come with the limitation of poor scaling with an increase in the number of atoms ($\mathcal{O}(N^4)$) [37].

2.6. Hohenberg-Kohn Theorem

The adiabatic approximation gives us a simplified Schrödinger equation that we can solve to get the energy of a many-body system, but this is still a very complex problem to solve. This theorem and the ones that follow it are the crux of Density functional theory, namely the density part. In this subsection we will go through the Hohenberg-Kohn theorems to show how electron density can be used to get all the properties of a system [37, 41].

The first Hohenberg-Kohn theorem states that *'the external potential $V_{ext}(\mathbf{r})$ is (to within a constant) a unique functional (a function of a function) of $\rho(\mathbf{r})$; since, in turn $V_{ext}(\mathbf{r})$ fixes \hat{H} we see that the full many particle ground state is a unique functional of $\rho(\mathbf{r})$ '*. In order to prove this, we consider two systems that have identical electron densities, $\rho(\mathbf{r})$, but with different external potentials $V_{ext}(\mathbf{r})$ and $V'_{ext}(\mathbf{r})$. The Hamiltonians for these are

$$\begin{aligned}\hat{H} &= \hat{T}(\mathbf{r}) + \hat{V}_{elec-elec}(\mathbf{r}) + V_{ext}(\mathbf{r}), \\ \hat{H}' &= \hat{T}(\mathbf{r}) + \hat{V}_{elec-elec}(\mathbf{r}) + V'_{ext}(\mathbf{r}).\end{aligned}\tag{2.69}$$

These different Hamiltonians belong to two different ground state wavefunctions Ψ and Ψ' and have corresponding ground state energies E_0 and E'_0 , respectively, where $E_0 \neq E'_0$. As Ψ and Ψ' are different, applying Ψ' to \hat{H} will result in a energy greater than the ground state,

$$E_0 = \langle \Psi | \hat{H} | \Psi \rangle < \langle \Psi' | \hat{H} | \Psi' \rangle = \langle \Psi' | \hat{H}' | \Psi' \rangle + \langle \Psi' | \hat{H} - \hat{H}' | \Psi' \rangle.\tag{2.70}$$

The two Hamiltonians can be expanded out, making the last term dependent on the difference of the external potentials,

$$E_0 < E'_0 + \langle \Psi' | V_{ext}(\mathbf{r}) - V'_{ext}(\mathbf{r}) | \Psi' \rangle = E'_0 + \int \rho(\mathbf{r}) [V_{ext}(\mathbf{r}) - V'_{ext}(\mathbf{r})] d\mathbf{r}.\tag{2.71}$$

By swapping the primed and unprimed quantities and repeating the previous steps we obtain

$$E'_0 < E_0 - \int \rho(\mathbf{r}) [V_{ext}(\mathbf{r}) - V'_{ext}(\mathbf{r})] d\mathbf{r}.\tag{2.72}$$

From adding these together we get a contradiction, $E_0 + E'_0 < E'_0 + E_0$. This means that these two systems cannot have the same ground state electron den-

sity, meaning that $V_{ext}(\mathbf{r})$ is a unique functional of $\rho(\mathbf{r})$, and thus so is the Hamiltonian \hat{H} .

The second Hohenberg-Kohn Theorem states that 'A universal function for the energy $E[\rho]$ in terms of the density $\rho(\mathbf{r})$ can be defined, valid for any external potential $V_{ext}(\mathbf{r})$. For any particular $V_{ext}(\mathbf{r})$, the exact ground state energy of a system is the global minimum value of this functional, and the density $\rho(\mathbf{r})$ that minimises the functional is the exact ground state density $\rho_0(\mathbf{r})$ '. In order to prove this, we note that since the external potential is uniquely determined by the density which then uniquely determines the wavefunction, all other observables must be uniquely determined. Thus we can write the energy of a system purely in terms of the electron density as

$$\begin{aligned} E[\rho]_{HK} &= T[\rho] + E_{elec-elec}[\rho] + \int \rho(\mathbf{r})V_{ext}(\mathbf{r})d\mathbf{r} + E_{ion-ion} \\ &\equiv F_{HK} + \int \rho(\mathbf{r})V_{ext}(\mathbf{r})d\mathbf{r} + E_{ion-ion}, \end{aligned} \quad (2.73)$$

where $E_{ion-ion}$ is the interaction energy of the ions and F_{HK} is the internal energies related to the interacting electron system which contains the kinetic and the electron-electron interaction energies,

$$F_{HK} = T[\rho] + E_{elec-elec}[\rho]. \quad (2.74)$$

In the ground state, the energy is defined by a unique ground state density, $\rho_0(\mathbf{r})$,

$$E = E[\rho_0] = \langle \psi | \hat{H} | \psi \rangle. \quad (2.75)$$

By using the variational principle, we know that a different electron density ρ' will give a higher energy

$$E = E[\rho_0] = \langle \psi | \hat{H} | \psi \rangle < \langle \psi' | \hat{H} | \psi' \rangle = E[\rho'] = E'. \quad (2.76)$$

Given this, it follows that if the total energy of a system written as a function of electron density is minimised with respect to the electron density, the ground state will be found.

Pulling both these theorems together, we can show how the Hohenberg-Kohn functional is equal to the expectation value of the Hamiltonian in a unique ground state. If we consider a system with external potential $V_{ext}(\mathbf{r})$ with ground state electron density $\rho(\mathbf{r})$, the ground state wavefunction of the system is Ψ

$$E = E_{HK}[\rho] = \langle \Psi | \hat{H} | \Psi \rangle . \quad (2.77)$$

If we put in a different electron density, which will not be this system's ground state, $\rho'(\mathbf{r})$. The energy of this state E' must be greater than the ground state energy E and relates to the ground state electron density as

$$E = \exp \{ \hat{H} \} \Psi \leq \langle \Psi' | \hat{H} | \Psi' \rangle . \quad (2.78)$$

This shows that the energy in terms of the Hohenberg-Kohn functional evaluated at the ground state density $\rho_0(\mathbf{r})$ is lower than the energies obtained by evaluating this at any other density $\rho(\mathbf{r})$.

2.7. Kohn-Sham Theorem

The Kohn-Sham theorem takes this many-body system of ions and interacting electrons, and replaces the electrons with non-interacting electron-like particles. Two assumptions are used to say that this new system of non-interacting electrons has the same energy as the interacting one [37, 42].

The first assumption is that the exact ground state electron density can be represented by the ground state density of an auxiliary system of non-interacting particles, this is called the '*non-interacting-V representability*'. There is no rigorous proof for this assumption, but we assume it is valid.

The second assumption is that the auxiliary Hamiltonian is chosen to have the same kinetic operator and effective local potential $V_{eff}(\mathbf{r})$ acting on an electron at point \mathbf{r} .

The Hamiltonian of this auxiliary system of non-interacting electron-like particles would look like (using Hartree atomic units)

$$\hat{H}_{aux}^{\sigma} = -\frac{1}{2}\nabla^2 + V_{eff}^{\sigma}(\mathbf{r}), \quad (2.79)$$

where σ is spin. We have not yet defined the form of the potential $V_{eff}^{\sigma}(\mathbf{r})$ that acts on this system, meaning that this method should apply to any form of $V_{eff}^{\sigma}(\mathbf{r})$. We begin by stating that this auxiliary system of non-interacting electron-like (Kohn-Sham) particles has the same charge density $\rho(\mathbf{r})$ as the real system of real electrons

$$\rho(\mathbf{r}) = \sum_{\sigma} \rho^{\sigma}(\mathbf{r}) = \sum_{\sigma} \sum_{i=1}^{N^{\sigma}} |\psi_i^{\sigma}(\mathbf{r})|^2, \quad (2.80)$$

where i is the index for orbitals, N^{σ} is the total number of orbitals for a given spin σ . ψ_i^{σ} are the single-electron wavefunctions called the Kohn-Sham orbitals. From this, the Kohn-Sham particles kinetic energy T_s is given by

$$T_s = -\frac{1}{2} \sum_{\sigma} \sum_{i=1}^{N^{\sigma}} \langle \psi_i^{\sigma} | \nabla^2 | \psi_i^{\sigma} \rangle = -\frac{1}{2} \sum_{\sigma} \sum_{i=1}^{N^{\sigma}} \int |\nabla \psi_i^{\sigma}(\mathbf{r})|^2 d\mathbf{r}. \quad (2.81)$$

We will introduce a coulomb interaction term to account for the electron density, $\rho(\mathbf{r})$, interacting with itself, this will take the form of the Hartree coulomb interaction term

$$E_H[\rho] = \frac{1}{2} \int \frac{\rho(\mathbf{r})\rho(\mathbf{r}')}{|\mathbf{r} - \mathbf{r}'|} d\mathbf{r}d\mathbf{r}'. \quad (2.82)$$

We can now rewrite the Hohenberg-Kohn energy from equation 2.73 as the Kohn-Sham energy

$$E_{KS} = T_s[\rho] + \int V_{ext}(\mathbf{r})\rho(\mathbf{r})d\mathbf{r} + E_H[\rho] + E_{ion-ion} + E_{xc}[\rho]. \quad (2.83)$$

where $V_{ext}(\mathbf{r})$ is the external potential due to the ions (this can include any additional external fields and is assumed to be independent of spin), $E_{ion-ion}$ is the energy due to ion-ion interaction and E_{xc} is the energy due to exchange-correlation related effects. By comparing equations 2.73 and 2.83 we can see that the exchange-correlation term is

$$\begin{aligned} E_{xc}[\rho] &= F_{HK}[\rho] - (T_s[\rho] + E_H[\rho]), \\ &= \langle \hat{T} \rangle - T_s[\rho] + \langle \hat{V}_{elec-elec} \rangle - E_H[\rho], \end{aligned} \quad (2.84)$$

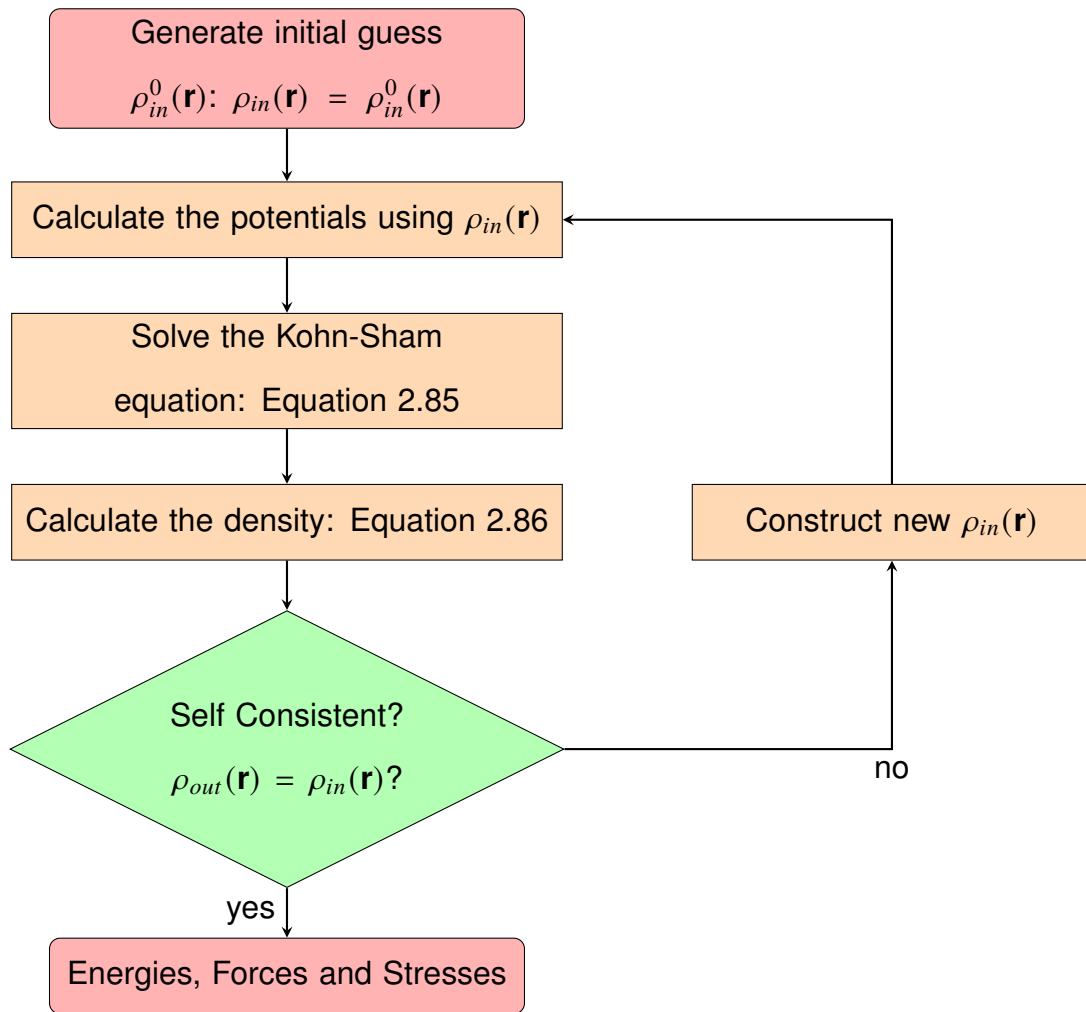
where $\hat{V}_{elec-elec}$ is the electron-electron interaction term. We can see from this that the exchange-correlation energy term is the difference between the kinetic energy and interaction energies of the real system and the same energies for the Kohn-Sham auxiliary system with Hartree electron-electron interaction energy.

From all of this we can write the full Kohn-Sham equations, the first of which is a single electron wavefunction equation

$$\left[-\frac{1}{2}\nabla^2 + V_{ext}[\rho(\mathbf{r})] + V_H[\rho(\mathbf{r})] + V_{xc}[\rho(\mathbf{r})] \right] \psi_i^\sigma(\mathbf{r}) = \epsilon_i^\sigma \psi_i^\sigma(\mathbf{r}), \quad (2.85)$$

$$\sum_i^N |\psi_i^\sigma(\mathbf{r})|^2 = \rho(\mathbf{r}). \quad (2.86)$$

In order to solve this, a self-consistent method is used where an initial guess to the electron density is input. From this initial guess the potentials are calculated (V_{ext} , V_H and V_{xc}). The potentials can then be used to solve for the wavefunction using equation 2.85 which can then, in turn, be used to get back a density using equation 2.86. If the initial guess differs from the output density then a modified density is used as the new input density. These steps are then continued iteratively until the input density is the same as the output density, or converges, to within a defined limit. This process is shown below.



This is the general method of solving the Kohn-Sham equations self consistently, with the goal being to minimise the energy. In this scheme, either the effective potential or the wavefunction can be used as the variable for minimisation. There are many different methods for doing this minimisation with the most currently used ones being based off of the method of Bendt and Zunger [43] which has been refined and sped up over the year, such as through the use of Broyden's method of self-consistent field convergence acceleration as highlighted by G P Srivastava [44]. Within this thesis, the blocked-Davidson algorithm is used to achieve self-consistency [45, 46].

The Kohn-Sham method was initially shown to work for a homogeneous electron gas. However, solving an auxiliary system of non-interacting Kohn-Sham particles has not been proven to work for the general case, it is however used on the basis of proof by exhaustion, or in other words, it has been shown to work for all cases it has been tested on.

2.8. Exchange-Correlation and Functionals

Using the three above theorems we have gone through the foundation which density functional theory is built on. All the terms in equation 2.83, except the exchange-correlation term $E_{xc}[\rho]$ (and the ion-ion interaction energy but this is still trivial to solve), can be solved exactly using charge density $\rho(\mathbf{r})$. The exact form of $E_{xc}[\rho]$ is generally unknown, however many approximations have been made with varying degrees of success for different types of systems [37]. The exchange part of this is related to the Pauli exclusion principle and is effectively the energy to exchange two electrons with the same spin. The correlation part, on the other hand, encompasses all spin difference related effects and electron-electron interactions.

The many different approximations to $E_{xc}[\rho]$ are often illustrated figuratively using an analogous Jacob's ladder, where functionals at the bottom of the ladder are the least accurate but also cost the least computation power, and as you move up the ladder the functionals get more accurate at the cost of more computational power. This is shown in figure 2.1.

Hartree-Fock has no Coulomb correlation and has only the Hartree energy to describe the interaction between electrons, this is known as the Fermi correlation (or exchange) and is insufficient to describe the many-body effects of a real system. Because of this, Hartree-Fock is near the bottom of the ladder as it is only accurate in a limited amount of cases.

The next rung up the ladder is LDA, or the local density approximation, aptly named as the exchange-correlation term is reliant on the local electron density at a given position within the system. The charge density is assumed to be similar to that of a homogeneous electron gas and $\rho(\mathbf{r})$ is slowly varying with position. This can be expressed as

$$E_{xc}^{LDA}[\rho(\mathbf{r})] = \int \epsilon_{xc}^{LDA}[\rho(\mathbf{r})]\rho(\mathbf{r})d\mathbf{r}, \quad (2.87)$$

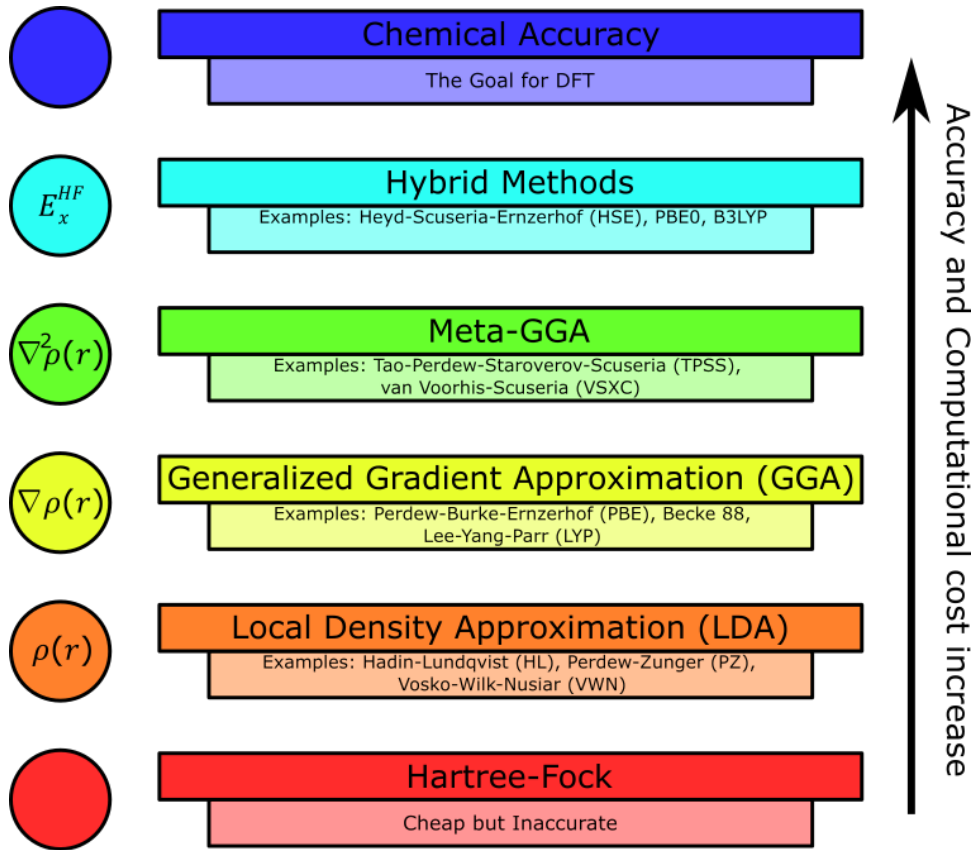


Figure 2.1: Jacob's Ladder showing the different levels of functionals in increasing accuracy and computational cost.

where $\epsilon_{xc}^{LDA}[\rho(\mathbf{r})]$ is the calculated LDA exchange-correlation energy per electron for a uniform electron gas with density $\rho[\mathbf{r}]$, essentially assuming that the density is constant. This gives a potential

$$V_{xc}^{LDA}(\mathbf{r}) = \frac{d}{d\rho} \{ \epsilon_{xc}^{LDA}[\rho(\mathbf{r})] \rho(\mathbf{r}) \}. \quad (2.88)$$

Because of the slowly varying electron density, we can redefine ρ as simply a mean electron density using the inter-electronic spacing r_s

$$\rho^{-1} = \frac{4\pi}{3} r_s^3, \quad (2.89)$$

which then allows us to rewrite the exchange-correlation potential as

$$V_{xc}^{LDA}(\mathbf{r}) = \epsilon_{xc}^{LDA} - \frac{r_s}{3} \frac{d\epsilon_{xc}^{LDA}}{dr_s}. \quad (2.90)$$

As we have used the approximation that the density is slowly varying, we shall use the mean electron density. LDA leads to errors due to over-binding, giving higher binding energies and smaller lattice parameters for crystals.

GGA, or the generalised gradient approximation, extends LDA by making the exchange-correlation energy dependent on the gradient of the charge density $\nabla\rho(\mathbf{r})$ as well as the charge density $\rho(\mathbf{r})$. This is written as

$$E_{xc}^{GGA}[\rho(\mathbf{r})] = \int \epsilon_{xc}^{GGA}[\rho(\mathbf{r}), \nabla\rho(\mathbf{r})] \rho(\mathbf{r}) d\mathbf{r}, \quad (2.91)$$

where $\epsilon_{xc}^{GGA}[\rho(\mathbf{r}), \nabla\rho(\mathbf{r})]$ is the calculated GGA exchange-correlation energy per electron. The GGA exchange-correlation potential has the general form

$$V_{xc}^{GGA}(\mathbf{r}) = \left[\epsilon_{xc}^{GGA} + \rho \frac{\partial \epsilon_{xc}^{GGA}}{\partial \rho} + \nabla \left(\rho \frac{\partial \epsilon_{xc}^{GGA}}{\partial \nabla \rho} \right) \right]. \quad (2.92)$$

The GGA functional can take many forms, unlike LDA which has a single universal form. One of the most commonly used forms of GGA is one proposed by Perdew, Burke and Ernzerhof (PBE) in 1996 in the paper titled '*Generalized gradient approximation made simple*' (having accrued well over 100,000 citations). Due to the use of $\nabla\rho(\mathbf{r})$, GGA is typically more accurate than LDA but is also more computationally expensive. GGA offers reduced errors in bond dissociation energies, improved transition-state barriers and band gap values closer to experimental values. It is also known to typically overestimate lattice parameters by about 5%.

The next obvious step for improving the accuracy of GGA is to introduce dependence on the second derivative of the density $\nabla^2\rho(\mathbf{r})$ (sometimes referred to as $\tau(\mathbf{r})$), this is exactly what Meta-GGAs do. Obviously, adding more and more derivatives will lead to better and better accuracy but the computational cost will skyrocket, instead a different approach is taken for higher rungs on the ladder. Hybrid functionals mix in different amounts of the Hartree-Fock exchange energy, which perfectly estimates the real exchange energy. This is normally mixed in with a GGA level exchange-correlation energy which means that this is more costly than just a GGA alone.

2.8.1 The PBE functional

The vast majority of the work carried out in this thesis has been done so using the PBE functional [37, 47], here we show how this is defined. We begin by splitting the exchange-correlation energy term into two parts, the exchange energy and the correlation energy. To solve the correlation part of this we begin with the correlation functional in the form

$$E_c^{GGA}[\rho_\uparrow, \rho_\downarrow] = \int d^3r \rho [\epsilon_c^{unif}(r_s, \zeta) + H(r_s, \zeta, t)], \quad (2.93)$$

where r_s is the local Wigner-Seitz radius ($\rho = 3/4\pi r_s^3$), $\zeta = (\rho_\uparrow - \rho_\downarrow)/\rho$ is the relative spin polarization and $t = |\nabla\rho|/2\phi k_s \rho$ is a dimensionless density gradient where $\phi(\zeta) = [(1 + \zeta)^{2/3} + (1 - \zeta)^{2/3}]/2$ is a spin-scaling factor and $k_s = \sqrt{4k_F/\pi a_0}$ is the Thomas-Fermi screening wave number ($a_0 = \hbar^2/me^2$) and $H(r_s, \zeta, t)$ is a function that is dependent on the gradient. The functional form of $H(r_s, \zeta, t)$ is constructed using three conditions:

(a) In the limit of slowly varying density ($|\nabla\rho| \rightarrow 0$ thus $t \rightarrow 0$), H is given by its second-order gradient expansion

$$H(r_s, \zeta, t) \rightarrow \frac{e^2}{a_0} \beta \phi^3 t^2, \quad (2.94)$$

where $\beta \simeq 0.066725$. This is a high density limit ($r_s \rightarrow 0$) of the weakly r_s -dependent gradient coefficient for the correlation energy, this emerges naturally from numerical GGA solutions.

(b) In the rapidly varying limit ($|\nabla\rho| \rightarrow \infty$ thus $t \rightarrow \infty$),

$$H(r_s, \zeta, t) \rightarrow -\epsilon_c^{unif}, \quad (2.95)$$

meaning that the GGA correlation becomes equal to zero. This is because, in the tail of an electron density of a finite system, the exchange energy density and potential dominate over the correlation part.

(c) Under uniform scaling to the high-density limit ($\rho(\mathbf{r}) \rightarrow \lambda^3 \rho(\lambda \mathbf{r})$ and $\lambda \rightarrow \infty$ meaning $r_s \rightarrow 0$ and $t \rightarrow \infty$) the correlation energy must scale to a constant. $H(r_s, \zeta, t)$ must cancel out the logarithmic singularity of $\epsilon_c^{unif}(r_s, \zeta) \rightarrow (e^2/a_0)\phi^3[\gamma \ln(r_s/a_0) - \omega]$, where γ and ω are weak functions of ζ which are replaced by their values at $\zeta = 0$ for simplicity ($\gamma = (1 - \ln 2)/\pi^2 \simeq 0.031091$ and $\omega \simeq 0.046644$)

$$H(r_s, \zeta, t) \rightarrow \frac{e^2}{a_0} \gamma \phi^3 \ln(t^2). \quad (2.96)$$

These three conditions are satisfied by the ansatz

$$H(r_s, \zeta, t) = \frac{e^2}{a_0} \gamma \phi^3 \times \ln \left\{ 1 + \frac{\beta}{\gamma} t^2 \left[\frac{1 + At^2}{1 + At^2 + A^2 t^4} \right] \right\}, \quad (2.97)$$

where

$$A = \frac{\beta}{\gamma} \left[\exp \left\{ \frac{-\epsilon_c^{unif} a_0}{\gamma \phi^3 e^2} \right\} - 1 \right]^{-1}. \quad (2.98)$$

The exact form of the correlation energy per electron is, in general, impossible to determine but for an unpolarized gas ($\zeta = 0$) forms are available for the high density ($r_s \rightarrow 0$) and the low density case ($r_s \gg 1$)

$$\epsilon_c^{unif}(r_s, 0) = \begin{cases} 0.311 \ln(r_s) - 0.048 + r_s(A \ln(r_s) + C) + \dots & r_s \rightarrow 0 \\ \frac{a_1}{r_s} + \frac{a_2}{r_s^{3/2}} + \frac{a_3}{r_s^2} + \dots & r_s \gg 1 \end{cases} \quad (2.99)$$

where A , C , and a_i are all parameters. The simplest form of this is one by Perdew-Zunger (PZ) and is a simple interpolation between the high and low density cases

$$\epsilon_c^{unif}(\rho, \zeta) = \epsilon_c^{unif}(\rho, 0) + [\epsilon_c^{unif}(\rho, 1) - \epsilon_c^{unif}(\rho, 0)] f_x(\zeta), \quad (2.100)$$

where $f_x(\zeta) = ((1 + \zeta)^{4/3} + (1 - \zeta)^{4/3} - 2)/(2(2^{1/3} - 1))$ is an interpolation function.

A similar process is followed for the exchange energy with four further conditions:

(d) Under the uniform density scaling in condition (c), E_x scales such that, for $\zeta = 0$ everywhere, we must have

$$E_x^{GGA} = \int d^3r \rho \epsilon_x^{unif}(\rho) F_x(s), \quad (2.101)$$

where $\epsilon_x^{unif} = -3e^2 k_F / 4\pi$. This recovers the correct uniform gas limit $F_x(0) = 1$.

(e) The exact exchange energy obeys the spin-scaling relationship

$$E_x[\rho_\uparrow, \rho_\downarrow] = \frac{E_x[2\rho_\uparrow] + E_x[2\rho_\downarrow]}{2}. \quad (2.102)$$

(f) For small density variations around a uniform density electron gas, a linear response is recovered (as $s \rightarrow 0$)

$$F_x(s) \rightarrow 1 + \mu s^2, \quad (2.103)$$

where $\mu = \beta(\pi^2/3) \simeq 0.21951$, the effective coefficient for exchange cancels that of correlation.

(g) The Lieb-Oxford bound, which is effectively the lower bound associated with indirect coulomb interactions,

$$E_x[\rho_\uparrow, \rho_\downarrow] \geq E_{xc}[\rho_\uparrow, \rho_\downarrow] \geq -1.679e^2 \int d^3r \rho^{4/3}, \quad (2.104)$$

will be satisfied if the spin-polarized enhancement factor $F_x(\zeta = 1, s) = 2^{1/2} F_x(s/2^{1/3})$ grows gradually with s to a maximum value ≤ 2.273 ($F_x(s) \leq 1.804$).

These ((f) and (g)) are satisfied by

$$F_x(s) = 1 + \kappa - \frac{\kappa}{1 + (\mu s^2 / \kappa)}, \quad (2.105)$$

where $\kappa = 0.804$.

Overall this leads to a exchange-correlation energy functional of form

$$E_{xc}^{PBE} = \int d^3r \rho \epsilon_x^{unif}(\rho) F_x(s) + \int d^3r \rho [\epsilon_c^{unif}(r_s, \zeta) + H(r_s, \zeta, t)]. \quad (2.106)$$

This is the form of the exchange-correlation functional that we have used throughout this thesis, being a GGA level functional it is a good balance between accuracy and computational expense.

2.8.2 The HSE functional

Alongside the PBE functional, a hybrid functional has been used for comparison in some specific cases. The hybrid functional used is that of Heyd, Scuseria and Ernzerhof, referred to as HSE06 [48, 49]. Here we give a brief description of this specific hybrid functional. As mentioned earlier, hybrid functionals mix in Hartree-Fock exchange energy with the exchange from a DFT functional (LDA or GGA for example) using

$$E_{xc}^{Hybrid} = \alpha E_x^{HF} + (1 - \alpha)E_x^{DFT} + E_c^{DFT}, \quad (2.107)$$

where E_x and E_c are the exchange and correlation energy functionals respectively and α is the Hartree-Fock screening variable. Different hybrid functionals use different fixed values of α or allow it to vary. The HSE06 functional uses $\alpha = 0.25$ meaning that it uses 25% Hartree-Fock exchange energy and 75% DFT exchange, this is normally a GGA function such as PBE and is the one used within this thesis. Because this requires solving the Kohn-Sham equations fully using the PBE functional and then also solving the Hartree-Fock equations fully for the exchange component, this is far more computationally intense than just solving for either on their own.

2.9. Pseudopotentials

Pseudopotentials are used to simplify electronic structure calculations by replacing the strong coulomb potential from atomic nuclei and tightly bound core electrons with an effective ionic potential, reducing the number of bodies in a many body system, and thus reducing the computational cost. This is called the pseudopotential (frozen-core) method and can be done because the tightly bound core

electrons are nearly unchanged in molecules and solids, this fact means that many different types of pseudopotentials can be created to capture a different number of "core" electrons, either to increase accuracy or decrease computational cost [37]. These pseudopotentials modify the many-body electronic potential into two parts: local and non-local, that sum to the normal potential. The local part becomes finite at short ranges and returns to that of a Coulomb like potential ($\propto -1/r$) at long range, this occurs above a cutoff radius (r_{cutoff}). The non-local part is short ranged only, being non-zero below r_{cutoff} , and is made up of multiple angular momentum dependent potentials, which can be thought of as different atomic orbitals. An example of the local pseudopotential and a normal potential is shown in Figure 2.2. The non-local part would make up the difference in these in the region below r_{cutoff} .

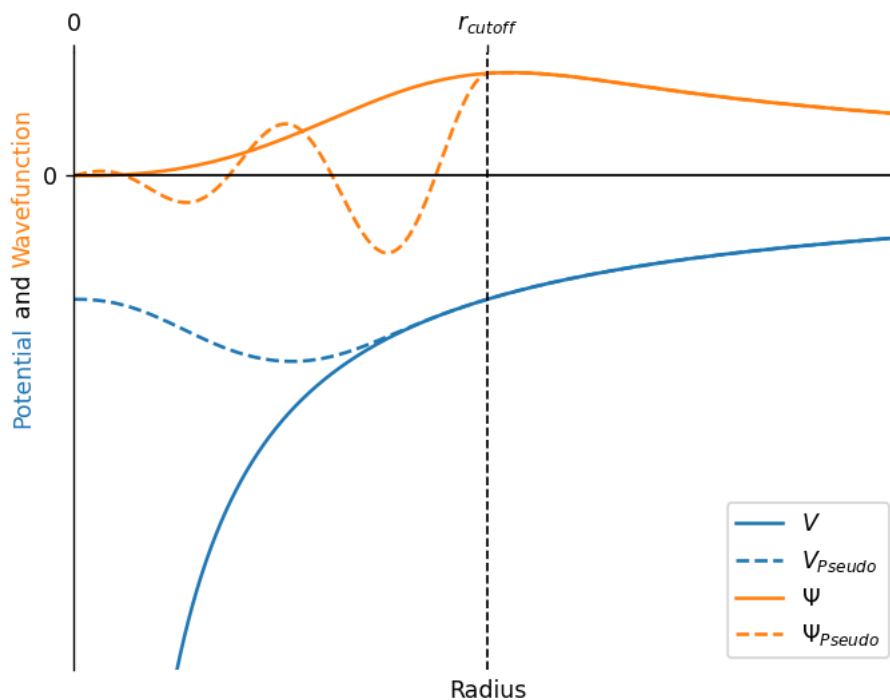


Figure 2.2: A schematic showing how a local pseudopotential and a pseudo wavefunction differ from the all-electron potential and wavefunction respectively.

Many of the different types of pseudopotentials are build off of ideas that originated in the orthogonalized planewave (OPW) approach which turns the eigenvalue problem into two parts, a smooth valance function and a core function. We begin by defining an orthogonalized planewave

$$\chi_{\mathbf{k}}^{OPW}(\mathbf{r}) = \frac{1}{\Omega} \left[e^{i\mathbf{k}\cdot\mathbf{r}} - \sum_j \mu_{\mathbf{k}j} u_j(\mathbf{r}) \right], \quad (2.108)$$

where Ω is volume and

$$\mu_{\mathbf{k}j} = \int e^{i\mathbf{k}\cdot\mathbf{r}} u_j(\mathbf{r}) d\mathbf{r}. \quad (2.109)$$

This means that $\chi_{\mathbf{k}}^{OPW}(\mathbf{r})$ is orthogonal to every $u_j(\mathbf{r})$ function, which are simply required to be localized around each atomic nuclei. The OPWs $\chi_{\mathbf{k}}^{OPW}(\mathbf{r})$ have the following characteristics of valence level wavefunctions: it is orthogonal to all core levels, rapidly oscillates in the core region and because these core levels are localized around atomic cores, the summation term in $\chi_{\mathbf{k}}^{OPW}(\mathbf{r})$ is small outside the core. The electronic wavefunction is a linear combination of these OPWs

$$\psi_{\mathbf{k}}(\mathbf{r}) = \sum_{\mathbf{K}} c_{\mathbf{K}} \chi_{\mathbf{k}}^{OPW}(\mathbf{r}), \quad (2.110)$$

where $c_{\mathbf{K}}$ are coefficients and \mathbf{K} are the reciprocal lattice vectors. If $u_j(\mathbf{r})$ are chosen well, equation 2.108 is split into a smooth component plus a localized part, the smooth part can be easily represented as a summation of planewaves and the localized part can obey a wave equation

$$\frac{1}{2} \nabla^2 u_j + (E_j - V_j) u_j = 0. \quad (2.111)$$

Given such a broad definition for these wavefunctions, it is clear why many pseudopotentials followed this formalization.

2.9.1 Projector Augmented Wave method (PAW)

The PAW method of pseudopotential generation follows the approach of OPW by using the all-electron wavefunction in the same form as equation 2.108 [50]. To begin we will define a smooth part of a valence wavefunction $\tilde{\psi}_i^v(\mathbf{r})$ and a linear transformation \mathcal{T} that relates the set of all-electron valence functions $\psi_j^v(\mathbf{r})$ to the smooth function $\tilde{\psi}_i^v(\mathbf{r})$ via $\psi^v = \mathcal{T}\tilde{\psi}^v$. This transformation is assumed to be

equal to unity except within a sphere centred on the nucleus $\mathcal{T} = \mathbf{1} + \mathcal{T}_0$. In Bra-Ket notation, each smooth function can be expanded in partial waves m within spherical harmonics

$$|\tilde{\psi}^v\rangle = \sum_m c_m |\tilde{\psi}_m^v\rangle, \quad (2.112)$$

with the all-electron function taking a similar form

$$|\psi^v\rangle = \mathcal{T} |\tilde{\psi}^v\rangle = \sum_m c_m |\psi_m^v\rangle. \quad (2.113)$$

This means that the full wavefunction can be written as

$$|\psi^v\rangle = |\tilde{\psi}^v\rangle + \sum_m c_m \left[|\psi_m^v\rangle - |\tilde{\psi}_m^v\rangle \right]. \quad (2.114)$$

Given the transformation \mathcal{T} is linear, the coefficients c_m must be given by a projection in each sphere

$$c_m = \langle \tilde{p}_m | \tilde{\psi}_m^v \rangle \quad (2.115)$$

where \tilde{p} is a set of projection operators (smooth, non norm-conserving) which are only non-zero inside a defined pseudopotential cutoff radius. If these satisfy the biorthogonality condition $\langle \tilde{p}_m | \tilde{\psi}_{m'}^v \rangle = \delta_{mm'}$ then the one-centre expansion

$$\sum_m |\tilde{\psi}_m^v\rangle \langle \tilde{p}_m | \tilde{\psi}^v \rangle = \tilde{\psi}. \quad (2.116)$$

In the same way that there are many forms that pseudopotentials can take, the same can be said for these projector operators, however their transformation still involves the full-electron wavefunction

$$\mathcal{T} = \mathbf{1} + \sum_m \left[|\psi_m^v\rangle - |\tilde{\psi}_m^v\rangle \right] \langle \tilde{p}_m |. \quad (2.117)$$

The general form of the PAW equations can be expressed in terms of this transformation

$$\tilde{A} = \mathcal{T}^\dagger \hat{A} \mathcal{T} = \hat{A} + \sum_{mm'} |\tilde{p}_m\rangle \left[\langle \psi_m^v | \hat{A} | \psi_{m'}^v \rangle - \langle \tilde{\psi}_m^v | \hat{A} | \tilde{\psi}_{m'}^v \rangle \right] \langle \tilde{p}_{m'} |, \quad (2.118)$$

where \hat{A} is any operator in an all-electron problem and \tilde{A} operates on the smooth part of the wavefunction. The expressions for physical quantities in this approach also follow the same form, the density $\rho(\mathbf{r})$ can be written as

$$\rho(\mathbf{r}) = \tilde{\rho}(\mathbf{r}) + \rho^1(\mathbf{r}) - \tilde{\rho}^1(\mathbf{r}) \quad (2.119)$$

which can be written with eigenstates i with occupations f_i

$$\tilde{\rho}(\mathbf{r}) = \sum_i f_i |\tilde{\psi}_i^v(\mathbf{r})|^2, \quad (2.120)$$

$$\rho^1(\mathbf{r}) = \sum_i f_i \sum_{mm'} \langle \tilde{\psi}_i^v | \tilde{\psi}_m^v \rangle \psi_m^{v*}(\mathbf{r}) \psi_{m'}^v(\mathbf{r}) \langle \tilde{\psi}_{m'}^v | \tilde{\psi}_i^v \rangle, \quad (2.121)$$

and

$$\tilde{\rho}^1(\mathbf{r}) = \sum_i f_i \sum_{mm'} \langle \tilde{\psi}_i^v | \tilde{\psi}_m^v \rangle \tilde{\psi}_m^{v*}(\mathbf{r}) \tilde{\psi}_{m'}^v(\mathbf{r}) \langle \tilde{\psi}_{m'}^v | \tilde{\psi}_i^v \rangle. \quad (2.122)$$

where $\tilde{\rho}(\mathbf{r})$ is the density due to the smooth functions evaluated in Fourier space or on a grid that extends throughout space, $\tilde{\rho}^1(\mathbf{r})$ is the same as $\tilde{\rho}(\mathbf{r})$ evaluated only in the spheres on radial grids and $\rho^1(\mathbf{r})$ the density in the spheres with the full function. Note that ρ^1 contains the contributions of the core states and that $\tilde{\rho}^1$ and $\tilde{\rho}$ contain pseudo core states. In essence, this means that the density of an all-electron system minus the density of the core electrons for the same all-electron is equal to the same for the system made up of the augmented system.

Due to equation 2.118 being valid for any operator in an all-electron system, the same fact will be true for any quantity of a system. This is the strength of pseudopotentials, describing a many-electron system with less electrons due to how unchanging core electrons are.

2.10. Ewald Summation

The ion-ion interaction energy term within Kohn-Sham DFT, while important, has been ignored thus far. This interaction energy is from a coulomb interaction between positively charged particles which only decays to have no effect at infinite distance. As we are using periodic conditions, this introduced an issue were an ion in a unit cell interacts with its own periodic image, effectively interacting with itself an infinite amount of times. Ewald summation [51] solves this issue and removes the need for an infinite sum of coulomb interactions at the same time.

If we consider N ions in a vacuum with positions $\mathbf{R}_1, \mathbf{R}_2, \dots, \mathbf{R}_N$ each with charges q_1, q_2, \dots, q_N respectively, for now ignoring any periodicity. The coulomb interaction energy is

$$E_{ion-ion} = \frac{1}{4\pi\epsilon_0} \sum_{i,j} \frac{q_i q_j}{|\mathbf{R}_i - \mathbf{R}_j|}, \quad (2.123)$$

where the summation is over all pairs of ions with a total of $N(N-1)/2$ total pairs. If we now introduce a periodic boundary condition with real space lattice vectors $\mathbf{a}_1, \mathbf{a}_2$ and \mathbf{a}_3 . This means that for every ion with position \mathbf{R}_i and charge q_i there are also ions at positions $\mathbf{R}_i + n_1\mathbf{a}_1 + n_2\mathbf{a}_2 + n_3\mathbf{a}_3$, where $n_{(1,2,3)}$ are integers. If we make $\mathbf{nL} = n_1\mathbf{a}_1 + n_2\mathbf{a}_2 + n_3\mathbf{a}_3$, we can rewrite equation 2.123 to include the interactions between periodic images, we will also split the sum over (i, j) into two summations with a factor 1/2 in front to remove double counting,

$$E_{ion-ion} = \frac{1}{4\pi\epsilon_0} \frac{1}{2} \sum_{\mathbf{n}} \sum_{i=1}^N \sum_{j=1}^N ' \frac{q_i q_j}{|\mathbf{R}_i - \mathbf{R}_j + \mathbf{nL}|}. \quad (2.124)$$

The ' symbol is used to indicate that if $\mathbf{n} = 0$, the $i = j$ term should be excluded. Because of the nature of the coulomb interaction, this sum converges very slowly but with some special transformations we can change this to converge rapidly.

We now introduce the potential $\phi_{[i]}(\mathbf{R})$

$$\phi_{[i]}(\mathbf{R}) = \phi(\mathbf{R}) - \phi_i(\mathbf{R}) = \frac{1}{4\pi\epsilon_0} \sum_{\mathbf{n}} \sum_{j=1}^N ' \frac{q_j}{|\mathbf{R}_i - \mathbf{R}_j + \mathbf{nL}|}, \quad (2.125)$$

which is the difference between the potential due to all N ions with all their periodic images ($\phi(\mathbf{R})$) and the potential due to just ion i ($\phi_i(\mathbf{R})$). This can be used to restate equation 2.124 as

$$E_{ion-ion} = \frac{1}{2} \sum_{\mathbf{n}} \sum_{i=1}^N q_i \phi_{[i]}(\mathbf{R}). \quad (2.126)$$

Now we will consider the form of the charge distribution of these ions. The charge density of a single ion, i , can be written as a delta function

$$\rho_i(\mathbf{R}) = q_i \delta(\mathbf{R} - \mathbf{R}_i). \quad (2.127)$$

we can split this into two terms by adding and subtracting a Gaussian distribution component

$$\begin{aligned} \rho_i(\mathbf{R}) &= \rho_i^S(\mathbf{R}) + \rho_i^L(\mathbf{R}), \\ \rho_i^S(\mathbf{R}) &= q_i \delta(\mathbf{R} - \mathbf{R}_i) - q_i G_\sigma(\mathbf{R} - \mathbf{R}_i), \\ \rho_i^L(\mathbf{R}) &= q_i G_\sigma(\mathbf{R} - \mathbf{R}_i), \end{aligned} \quad (2.128)$$

where $G_\sigma(\mathbf{R})$ is a standard Gaussian distribution. We can use this to split the potential due to ion i into two terms

$$\begin{aligned} \phi_i(\mathbf{R}) &= \phi_i^S(\mathbf{R}) + \phi_i^L(\mathbf{R}), \\ \phi_i^S(\mathbf{R}) &= \frac{q_i}{4\pi\epsilon_0} \int \frac{\delta(\mathbf{R} - \mathbf{R}') - G_\sigma(\mathbf{R} - \mathbf{R}')}{|\mathbf{R} - \mathbf{R}'|} d^3\mathbf{R}', \\ \phi_i^L(\mathbf{R}) &= \frac{q_i}{4\pi\epsilon_0} \int \frac{G_\sigma(\mathbf{R} - \mathbf{R}')}{|\mathbf{R} - \mathbf{R}'|} d^3\mathbf{R}'. \end{aligned} \quad (2.129)$$

We can split the potential field of all ions except ion i in the exact same way

$$\phi_{[i]}(\mathbf{R}) = \phi_{[i]}^S(\mathbf{R}) + \phi_{[i]}^L(\mathbf{R}), \quad (2.130)$$

which allows us to rewrite the energy, $E_{ion-ion}$, as

$$E_{ion-ion} = \frac{1}{2} \sum_{i=1}^N q_i \phi_{[i]}^S(\mathbf{R}_i) + \frac{1}{2} \sum_{i=1}^N q_i \phi_{[i]}^L(\mathbf{R}_i). \quad (2.131)$$

This is then further split such that the second term includes the effect of ion i and a self interaction term is subtracted

$$E_{ion-ion} = E^S + E^L - E^{self}, \quad (2.132)$$

where

$$E^S = \frac{1}{2} \sum_{i=1}^N q_i \phi_{[i]}^S(\mathbf{R}_i), \quad (2.133)$$

$$E^L = \frac{1}{2} \sum_{i=1}^N q_i \phi_i^L(\mathbf{R}_i), \quad (2.134)$$

$$E^{self} = \frac{1}{2} \sum_{i=1}^N q_i \phi_i^L(\mathbf{R}_i). \quad (2.135)$$

This gives us three terms, a short range coulomb energy for ions close to ion i that does not include ion i (E^S), a long range coulomb energy for ions far from i (E^L) and a self interaction coulomb energy term (E^{self}).

The Gaussian parts of these can be found by solving the Poisson's equation

$$\nabla^2 \phi_\sigma(\mathbf{R}) = -\frac{G_\sigma(\mathbf{R})}{\epsilon_0}, \quad (2.136)$$

to get

$$\phi_\sigma(\mathbf{R}) = \frac{1}{4\pi\epsilon_0 R} \operatorname{erf}\left(\frac{R}{\sqrt{2}\sigma}\right). \quad (2.137)$$

Given that $\operatorname{erfc}(z) = 1 - \operatorname{erf}(z)$, we can write

$$\begin{aligned} \phi_i^S(\mathbf{R}) &= \frac{1}{4\pi\epsilon_0} \frac{q_i}{|\mathbf{R} - \mathbf{R}_i|} \operatorname{erfc}\left(\frac{|\mathbf{R} - \mathbf{R}_i|}{\sqrt{2}\sigma}\right), \\ \phi_i^L(\mathbf{R}) &= \frac{1}{4\pi\epsilon_0} \frac{q_i}{|\mathbf{R} - \mathbf{R}_i|} \operatorname{erf}\left(\frac{|\mathbf{R} - \mathbf{R}_i|}{\sqrt{2}\sigma}\right). \end{aligned} \quad (2.138)$$

This leads to the short range energy having the final form

$$\begin{aligned}
E^S &= \frac{1}{2} \sum_{i=1}^N q_i \phi_{[i]}^S(\mathbf{R}_i) \\
&= \frac{1}{4\pi\epsilon_0} \frac{1}{2} \sum_{\mathbf{n}} \sum_{i=1}^N \sum_{j=1}^N \frac{q_i q_j}{|\mathbf{R}_i - \mathbf{R}_j + \mathbf{nL}|} \operatorname{erfc} \left(\frac{|\mathbf{R}_i - \mathbf{R}_j + \mathbf{nL}|}{\sqrt{2}\sigma} \right),
\end{aligned} \tag{2.139}$$

which has the same form as equation 2.124, except for the complimentary error function that truncates this at long range, allowing this to be computed as a sum in real space. The self interaction energy term can also be computed using $\lim_{z \rightarrow 0} \operatorname{erf}(z) = 2z/\sqrt{\pi}$ to get

$$\begin{aligned}
\phi_i^L(\mathbf{R}_i) &= \frac{q_i}{4\pi\epsilon_0} \sqrt{\frac{2}{\pi}} \frac{1}{\sigma}, \\
E^{self} &= \frac{q_i}{4\pi\epsilon_0} \frac{1}{\sqrt{2\pi}\sigma} \sum_{i=1}^N q_i^2.
\end{aligned} \tag{2.140}$$

Finally, we need to deal with the long range energy term. This cannot be computed by a sum in real space and thus Ewald transformed this into a sum in reciprocal space. $\phi^L(\mathbf{R})$ can be thought of as an infinite periodic array of ions, and thus can undergo a Fourier transformation

$$\hat{\phi}^L(\mathbf{k}) = \int_V \phi^L(\mathbf{R}) e^{-i\mathbf{k}\cdot\mathbf{R}} d^3\mathbf{R}, \tag{2.141}$$

where V is the volume of the supercell. To find a solution to this we use the Poisson's equation

$$\nabla^2 \phi^L(\mathbf{R}) = -\frac{\rho^L(\mathbf{R})}{\epsilon_0}, \tag{2.142}$$

which we can use the Fourier transform on to get

$$k^2 \hat{\phi}^L(\mathbf{k}) = \frac{\hat{\rho}^L(\mathbf{k})}{\epsilon_0}, \tag{2.143}$$

where $k = |\mathbf{k}|$.

Taking the charge density to be a collection of periodic Gaussians in real space, we can Fourier transform it to solve for the charge density in reciprocal space

$$\begin{aligned}\rho^L(\mathbf{R}) &= \sum_{\mathbf{n}} \sum_{j=1}^N q_j G_{\sigma}(\mathbf{R} - \mathbf{R}_j + \mathbf{nL}), \\ \hat{\rho}^L(\mathbf{k}) &= \int_V \sum_{j=1}^N q_j G_{\sigma}(\mathbf{R} - \mathbf{R}_j + \mathbf{nL}) e^{-i\mathbf{k}\cdot\mathbf{R}} d^3\mathbf{R}, \\ &= \sum_{j=1}^N q_j e^{-i\mathbf{k}\cdot\mathbf{R}_j} e^{-\sigma^2 k^2/2},\end{aligned}\tag{2.144}$$

this gives us the long range potential in reciprocal space

$$\hat{\phi}^L(\mathbf{k}) = \frac{1}{\epsilon_0} \sum_{j=1}^N q_j e^{-i\mathbf{k}\cdot\mathbf{R}_j} \frac{e^{-\sigma^2 k^2/2}}{k^2}.\tag{2.145}$$

Applying an inverse Fourier transform to this we get

$$\phi^L(\mathbf{R}) = \frac{1}{V\epsilon_0} \sum_{\mathbf{k}\neq 0} \sum_{j=1}^N \frac{q_j}{k^2} e^{-i\mathbf{k}\cdot(\mathbf{R}-\mathbf{R}_j)} e^{-\sigma^2 k^2/2},\tag{2.146}$$

which allows us to state the long range energy term as

$$E^L = \frac{1}{2V\epsilon_0} \sum_{\mathbf{k}\neq 0} \sum_{i=1}^N \sum_{j=1}^N \frac{q_i q_j}{k^2} e^{-i\mathbf{k}\cdot(\mathbf{R}_i-\mathbf{R}_j)} e^{-\sigma^2 k^2/2}.\tag{2.147}$$

Combining equations 2.139, 2.140 and 2.147 we get the full form for the ion-ion interaction energy

$$\begin{aligned}E_{ion-ion} &= \frac{1}{4\pi\epsilon_0} \frac{1}{2} \sum_{\mathbf{n}} \sum_{i=1}^N \sum_{j=1}^N \frac{q_i q_j}{|\mathbf{R}_i - \mathbf{R}_j + \mathbf{nL}|} \text{erfc}\left(\frac{|\mathbf{R}_i - \mathbf{R}_j + \mathbf{nL}|}{\sqrt{2}\sigma}\right) \\ &+ \frac{1}{2V\epsilon_0} \sum_{\mathbf{k}\neq 0} \sum_{i=1}^N \sum_{j=1}^N \frac{q_i q_j}{k^2} e^{-i\mathbf{k}\cdot(\mathbf{R}_i-\mathbf{R}_j)} e^{-\sigma^2 k^2/2} \\ &- \frac{q_i}{4\pi\epsilon_0} \frac{1}{\sqrt{2\pi}\sigma} \sum_{i=1}^N q_i^2.\end{aligned}\tag{2.148}$$

This gives us our three terms: a term that is short ranged in real space, a term that is short ranged in reciprocal space and a self interaction term to remove double counting. It is of note that as $\sigma \rightarrow 0$, the Gaussians used in this approximate delta functions. This can also be used for more than just the ion-ion interaction energy. The Ewald summation method can also be used for any periodic charge with a Gaussian like distribution.

2.11. Brillouin zone sampling

Many of the calculations of crystal properties require integrating periodic functions over the entire Brillouin zone or over specific special points. This integration can be captured with a discrete set as long as sufficient points are sampled where the integrand varies rapidly, which is very important when dealing with metals as we need to capture the region in reciprocal space where the electronic bands cross from being filled to unfilled. But this is also important for insulators as an incorrect choice of points may lead to a metallic material appearing as an insulator. The symmetry of materials can be used to reduce information of a system into the irreducible Brillouin zone and looking at the vertices and the edges that link them can often provide all of the important information needed to get the properties of a material [30]. An example of the irreducible Brillouin zone for a crystal with hexagonal symmetry is shown in figure 2.3.

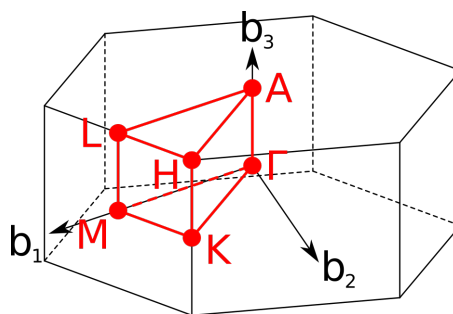


Figure 2.3: The irreducible Brillouin zone for a crystal with hexagonal symmetry, it contains all the information of the Brillouin zone while being 24 times smaller than the repeat unit.

For an integrand $f_i(\mathbf{k})$, with eigenfunctions $\psi_{i,\mathbf{k}}$ and eigenvalues $\epsilon_{i,\mathbf{k}}$, that smoothly varies and is periodic, we can expand it in Fourier components to get

$$f_i(\mathbf{k}) = \sum_{\mathbf{T}} f_i(\mathbf{T}) e^{i\mathbf{k}\cdot\mathbf{T}}, \quad (2.149)$$

where \mathbf{T} is the translation vector. This can be truncated into a finite sum if the rapidly varying terms at large \mathbf{T} decreases exponentially. Special points are chosen to integrate this smooth periodic function efficiently.

The most commonly used method proposed by Monkhorst and Pack [52] is to define a uniform set of points in reciprocal space using a formula that works for any crystal

$$\mathbf{k}_{n_1, n_2, n_3} \equiv \sum_i^3 \frac{2n_i - N_i - 1}{2N_i} \mathbf{b}_i, \quad (2.150)$$

where \mathbf{b}_i are the primitive reciprocal lattice vectors and $n_i = 1, 2, \dots, N_i$. With this grid in place, Monkhorst and Pack proposed to reduce this down to only points contained within the irreducible Brillouin zone by applying weights to each to capture how many of each point would be in the full Brillouin zone (if a point would appear four times in the Brillouin zone it would be given a weighting of four time). This is commonly called a Monkhorst-Pack grid and can be defined with any amount of points along the primitive reciprocal lattice vectors, with a offset in these directions to capture any important features of a system.

2.12. Van der Waals corrections

Many functionals are unable to capture the effects of Van der Waals interactions that are caused by London dispersion. In order to compensate for this, the energy from Kohn-Sham DFT can be offset by a dispersion correction energy term E_{disp} which can, in turn, be used to get a potential caused by a Van der Waals interaction. A common form of this correction, and the one that has been used throughout this thesis is the DFT-D3 method of Grimme *et al.* [53] with the form

$$E_{DFT-D3} = E_{KS} - E_{disp}, \quad (2.151)$$

where

$$E_{disp} = E^{(2)} + E^{(3)}. \quad (2.152)$$

This is made up of two parts, a two-body interaction term $E^{(2)}$ and a three-body interaction term $E^{(3)}$, these are applied to all atomic pairs and triples respectively. The two-body term is given by

$$E^{(2)} = \sum_{AB} \sum_{n=6,8,10,\dots} s_n \frac{C_n^{AB}}{r_{AB}^n} f_{d,n}(r_{AB}), \quad (2.153)$$

where C_n^{AB} is the average isotropic n th-order dispersion coefficient for atom pair AB and r_{AB} is their internuclear distance. s_n are scaling factors and $f_{d,n}(r_{AB})$ are damping functions that account for singularities when r_{AB} is small and avoids double-counting. The three-body term is given by

$$E^{(3)} = \sum_{ABC} f_{d,(3)}(\bar{r}_{ABC}) E^{ABC}, \quad (2.154)$$

where \bar{r}_{ABC} is the a geometrically averaged radii, $f_{d,(3)}(\bar{r}_{ABC})$ is another damping function and E^{ABC} is the Axilrod-Teller-Muto (triple dipole) dispersion term. Within DFT, the two-body term is often taken for $n = 6$ and $n = 8$ but no further, while the three-body term is dropped altogether as these terms are very small.

2.13. Geometric relaxation

Being able to get the properties of a system of fixed atoms is very useful within the field of materials research but so far we have not considered if the arrangement of atoms is the most favourable, geometric relaxation algorithms can use the potential fields calculated withing normal DFT to predict local atomic arrangements that would result in a lower energy (more favourable). There are a few different methods for doing this but within this thesis we have used two methods, the conjugate gradient algorithm [54, 37] and the RMM-DIIS method [55].

The conjugate gradient algorithm is similar to steepest descent methods in that it tries to minimise energies by following the direction of steepest decent (along the direction of the forces on the ions), but the conjugate gradient algorithm also takes into account the direction taken in the previous relaxation step. This can be used to choose a more optimal direction for energy minimisation and leads to conversion faster, for a quadratic function in N dimensions, the conjugate gradient algorithm is guaranteed to reach the minimum in N steps. Consider a quadratic functional

$$F(\{x_i\}) \equiv F(\mathbf{x}) = \frac{1}{2} \mathbf{x} \cdot \mathbf{H} \cdot \mathbf{x}, \quad (2.155)$$

with gradients

$$\mathbf{g} = -\frac{\partial F}{\partial \mathbf{x}} = -\mathbf{H} \cdot \mathbf{x}. \quad (2.156)$$

The first relaxation step follows the steepest decent method as there are no previous steps to consider, so the minimisation of F is along a line $\mathbf{x}^1 = \mathbf{x}^0 + \alpha^1 \mathbf{d}^0$, where $\mathbf{d}^0 = \mathbf{g}^0$. For all steps the minimisation occurs for

$$\mathbf{d}^n \cdot \mathbf{g}(\mathbf{x}^{n+1}) = 0. \quad (2.157)$$

For the $n+1$ step, the fastest minimisation occurs if we move in the direction where the gradient along the previous direction \mathbf{d}^n remains zero. The change in gradient in the new direction \mathbf{d}^{n+1} is $\Delta \mathbf{g} = \alpha^{n+1} \mathbf{H} \cdot \mathbf{d}^{n+1}$, meaning that the condition is met if

$$\mathbf{d}^n \cdot \mathbf{H} \cdot \mathbf{d}^{n+1} = 0. \quad (2.158)$$

This equation defines the "conjugate direction" and if it is satisfied for each step then it is satisfied for all steps.

The RMM-DIIS method is a combination of the residual minimisation method (RMM) and the discrete inversion in the iterative subspace method (DIIS), this method minimises the norm of a residual vector instead of the energy directly

and uses previous steps similar to the conjugate gradient algorithm. If we start from

$$\psi^{n+1} = c_0\psi^0 + \sum_{j=1}^{n+1} c_j\delta\psi^j, \quad (2.159)$$

where the set c_j is chosen to minimise the norm of the residual R^{n+1} which is given by $(\mathbf{H} - \epsilon^n)|\psi^n\rangle = |R[\psi^n]\rangle$, $|\psi^n\rangle$ and ϵ^n are the approximate eigenvectors and eigenvalues and $|R[\psi^n]\rangle$ is the residual vector. The c_j coefficients can be obtained by diagonalising the Hamiltonian in the iterative subspace $\{\psi^0, \psi^1, \dots, \psi^n\}$. The DIIS part of this method involves the construction of a full matrix of the size of the subspace as long as all these can be stored (in computer memory) and can be used to solve equations such as the Kohn-Sham equations.

This chapter provides an in-depth exploration of Density functional theory and the principles upon which it is built, which serves as the foundation for much of computational materials science. DFT is a powerful tool capable of predicting the electronic structure and properties for systems of atoms that can be described either as an infinitely repeating unit (if planewave wavefunctions are used) or as molecules (if gaussian wavefunctions are used). The Hohenberg-Kohn theorems eloquently show how all the properties of a system can be functionalised in terms of density while Kohn-Sham built upon this, by reducing the computational cost dramatically by mapping the original interacting system of electrons onto a system of non-interacting electron-like particles. Understanding the founding principles of DFT is paramount to using it to its fullest capabilities.

Chapter 3

Background Theory

"We can't solve problems by using the same kind of thinking we used when we created them."

– Albert Einstein

In this chapter, we explore the ever evolving fields of batteries and water splitting devices, both of which are key players in the venture for sustainable green energy solutions. To be able to appreciate the current state of the art materials and devices in both fields of research, we begin by going back to their roots and the governing principles behind them. Batteries are vital for storing energy and water splitters are crucial for generating hydrogen, a clean fuel source, both of these rely heavily on intricate electrochemical principles. This chapter serves as a foundation for understanding the fields moving into the future, overcoming the challenges of current materials.

3.1. How Batteries work

3.1.1 History of Batteries

Over the centuries, batteries have evolved and improved to store and provide more energy, with the first potential battery being constructed roughly 2000 years ago. The Baghdad battery is a device that was discovered in modern day Khujut Rabu, Iraq. Although this device is called a battery by those who discovered it, its true purpose is unknown. The Baghdad battery consists of a terracotta pot, a copper sheet rolled into a cylinder and a iron rod, corrosion of these metals indicates the presence of either wine or vinegar. This combinations of materials is capable of generating an electric charge but we know that it wasn't in this case.

In 1745, a device capable of storing high-voltage electric charge was discovered by two separate people, Ewald Georg von Kleist and Pieter van Musschenbroek of Leiden, the second being where its name comes from: the Leyden jar. The Leyden jar consists of a glass jar with metal foil on the inside and outside surfaces acting as a capacitor. The foil on the outside of the jar was grounded and the foil on the inside was connected to a conductor in the lid of the jar. This device could be charged using an electrostatic generator and was used for many early experiments with electric charges.

In 1749, Benjamin Franklin linked capacitors together for his experiments with electricity, this was when the term "battery" was first used for electrochemical cells. Its meaning was "multiple devices working together", due to this, all electrochemical cells are called batteries today.

The first true battery was invented by Alessandro Volta in 1800, called the Voltaic pile, it consisted of alternating zinc and copper plates connected by a layer of cloth soaked in brine as an electrolyte and stacked on top of each other. This device was capable of producing constant electrical current unlike all the previous devices. The Voltaic pile did have a few problems: due to the stacking, the brine used as an electrolyte could leak out and short the device. The current would also electrolyse the brine electrolyte used, producing hydrogen gas bubbles that increased the resistance of the battery with use and short-circuits within the zinc plates caused by impurities, called Local action.

The next big development in battery technology was the invention of the Lead-Acid battery. In 1859, Gaston Planté invented the Lead-Acid battery that, unlike all previous true batteries, could be recharged and reused by passing a current through it in reverse. This battery consists of a lead anode and a lead dioxide cathode immersed in sulphuric acid. The electrodes in this system react with the acid to produce lead sulphate. In this context, an anode is the electrode that conventional current enters the battery system and has a positive charge, a cathode is where the conventional current leaves the battery system and has a negative

charge. This battery design was very bulky, but was capable of producing large currents and could be used to power multiple devices at one.

In 1899, Waldemar Jungner invented the nickel-cadmium battery that used nickel and cadmium electrodes in a potassium hydroxide solution, this was the first alkaline battery. In the 1950s a cheaper version of the alkaline battery was invented, consisting of a manganese dioxide cathode and a powdered zinc anode in an alkaline electrolyte. This powdered zinc was used to increase the surface area of the anode.

The most recent, and of the most interest in these works, is the Li-ion battery. Lithium is a metal with a low atomic weight making it perfect for an intercalation battery. This is a type of battery that moves an intercalatant from one material to another *via* an electrolyte and electron transfer. Intercalation means the insertion of ions or molecules into a layered structure. The first lithium based battery, called the lithium-iodine battery, was not an intercalation battery but, thanks to multiple discoveries in the 1980s a rechargeable Li-ion battery was developed. The first of these discoveries was made in 1980 by John B. Goodenough, who discovered the potential of lithium cobalt oxide (LiCoO_2) as a Li-ion battery cathode material, being a layered material similar to TMDCs that can store lithium between its layers [56]. In 1983, Rachid Yazami discovered the graphite anode, also capable of storing lithium between its layers like LiCoO_2 [57]. These discoveries, along with a few others, lead Akira Yoshino to build a LiCoO_2 and graphite Li-ion battery not long after, which went on to be commercialised by Sony in 1991. John B. Goodenough, Akira Yoshino and M. Stanley Whittingham, who discovered the concept of intercalation batteries, were awarded the 2019 Nobel Prize in Chemistry for this work in the development of Li-ion batteries [58].

3.1.2 Li-ion Batteries

Li-ion batteries are complex chemical structures made up from a few key components: these are the electrodes, the electrolyte, the contacts, the separator and the binder. The most important of these are the electrodes and electrolyte as

these determine the capacity, voltage, energy density and stability of the battery as a whole. However the other components are used to improve the lifetime and efficiency of these batteries.

There are two types of electrode, the anode and cathode. These are where the Li-ions are intercalated and deintercalated. Li-ions within the anode are in a high energy state, this is where the Li-ions sit when the battery is in the charged state. Whereas, Li-ion within the cathode are in a lower energy state, being where the Li-ions sit when the battery is discharged. When the battery is being charged, electrons are moved from the cathode to the anode, being driven by an external power source, this gives the anode a negative charge and the cathode a positive charge. This difference in charge drives the Li-ions, that have a positive charge, from the cathode to the anode *via* interacting with the electrolyte in order to make both the anode and cathode neutral in charge. When the battery is being used to power another device, this whole process gets reversed, electrons from the anode pass to the cathode, powering a connected device, giving the anode a positive charge, and the cathode a negative charge. This difference in charge is yet again balanced by the positive Li-ions moving from the anode to the cathode. These processes are shown in Figure 3.1.

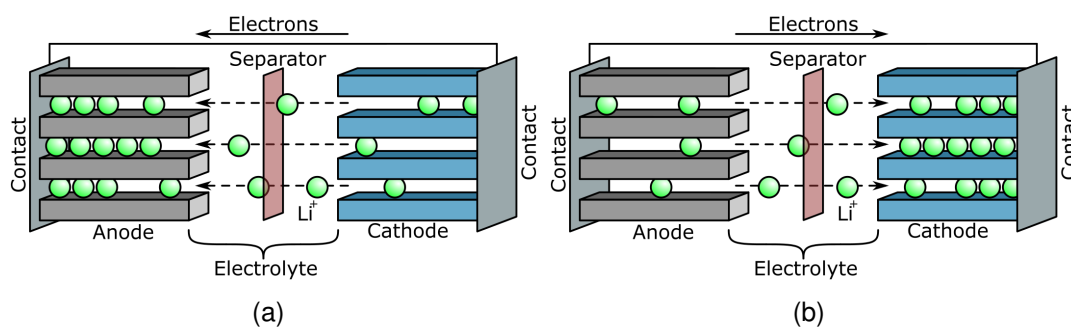


Figure 3.1: A schematic of the (a) charging and (b) discharging process in a Li-ion battery.

The electrolyte in Li-ion batteries is different to those in other types of batteries but serves the exact same purpose. The electrolyte is a solution composed of multiple different molecules, some of which are used to transport Li-ions, but this solution does not conduct electrons, otherwise the battery would immediately

short itself. A good electrolyte needs to have a large band gap (be insulating) and not undergo decomposition at high voltages.

The separator is a permeable membrane between the anode and cathode, its purpose is to prevent any growths on the anode (cathode) from growing through the electrolyte to the cathode (anode) and shorting the battery, while simultaneously allowing the transport of ions between the electrodes. The contacts provide a route for electrons in either the anode or cathode to escape when the battery is being charged or discharged, they are normally made of different conductive metals for each electrode.

3.1.2.1 Electrochemical Potentials

The relationship between the electron energies in the anode, cathode and electrolyte are what determine the voltage produced by a battery. The difference in the Fermi energy, or chemical potential, between the anode and cathode is what determines the maximum potential difference achievable by the battery when there is no load, which is known as the open circuit voltage, V_{OC} [59]

$$V_{OC} = \frac{\mu_A - \mu_C}{e}, \quad (3.1)$$

where μ_A is the Fermi energy of the anode, μ_C is the Fermi energy of the cathode and e is the magnitude of the elementary charge. This open circuit voltage is limited by the band gap of the electrolyte used, μ_C must be greater than the highest occupied molecular orbital (HOMO) of the electrolyte and μ_A must be less than the lowest unoccupied molecular orbital (LUMO) of the electrolyte, meaning that both μ_A and μ_C need to lie within the band gap of the electrolyte, this is shown in Figure 3.2.

If either μ_A or μ_C lie outside of the band gap of the electrolyte, they will react forming solid passivating films, called solid electrolyte interphase (SEI). These SEI layers can be beneficial to a batteries chemistry in some cases but will always increase the internal resistance of a battery and reduce the overall capacity and power.

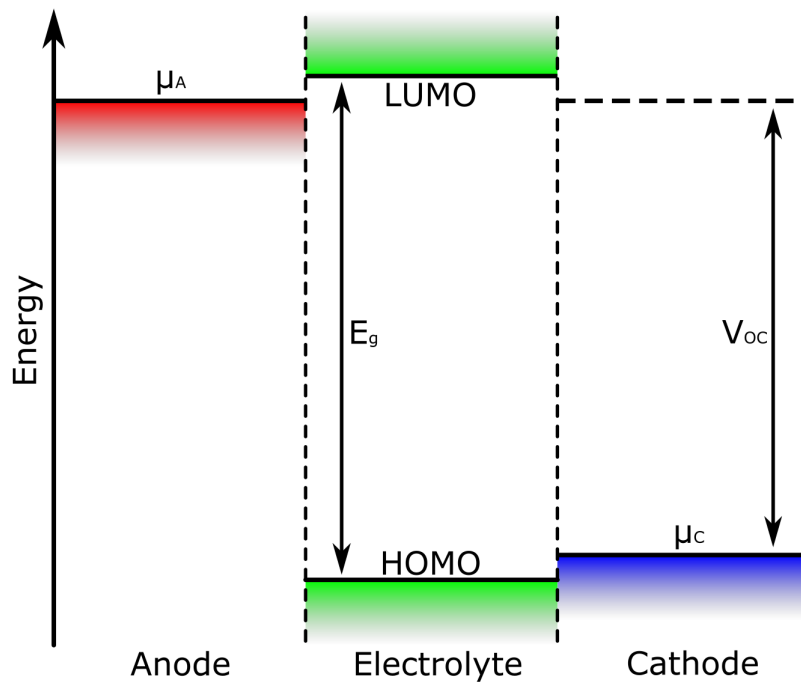


Figure 3.2: A schematic showing the relative energy levels within a Li-ion battery. μ_A and μ_C are the Fermi energies of the Anode and Cathode respectively and V_{OC} is the open circuit voltage. HOMO is the highest occupied molecular orbital of the electrolyte, LUMO is its lowest unoccupied molecular orbital and E_g is its band gap. This shows that μ_A and μ_C lie between the HOMO and LUMO of the electrolyte.

This would suggest that batteries have a constant voltage, independent of how charged they are. However this is not the case. The voltage of a Li-ion battery generally decreases as it is discharged, the more Li-ions are intercalated into the cathode, the lower the voltage. The voltage is also different when charging and discharging, requiring a higher voltage to charge a battery than is output when discharged. This is due to polarization resistance that is caused by the transition from one material to another, which decreases the discharge voltage below V_{OC} and increases the charge voltage above this by the same amount [60]. Calculating the voltage of a system requires knowing the change in the system's Gibbs free energy between the charged and discharged states. The change in the Gibbs free energy ΔG is given by [61]

$$\Delta G = \Delta H - T\Delta S = \Delta U + P\Delta V - T\Delta S, \quad (3.2)$$

where ΔH is the change in enthalpy of the system, ΔS is the change in entropy, ΔU is the change in internal energy and ΔV is the change in volume. T and P

are temperature and pressure respectively. The chemical potentials in Equation 3.1 are correlated with the partial molar quantity of the change in the Gibbs free energy ΔG . Equations 3.1 and 3.2 can be combined to get the real voltage of a system, more commonly referred to as the equilibrium voltage V_E

$$V_E = \frac{-\Delta G}{(x_2 - x_1)F}, \quad (3.3)$$

where x_1 and x_2 indicate the solid solubility limits of the intercalation reaction, and F is the Faraday constant. For use with density functional theory, this equation is modified for integer changes to the number of lithium atoms and to account for the use of electron volts instead of joules

$$V_E = -\frac{E(Li_{x_2}A) - (E(Li_{x_1}A) + (x_2 - x_1)E(Li))}{(x_2 - x_1)e}, \quad (3.4)$$

where the numerator is the Gibbs free energy still, but in electron volts. x_1 and x_2 now represent an integer number of Li-ions ≥ 0 and $E(Li_{x_1}A)$ and $E(Li_{x_2}A)$ represent the Gibbs free energy of a system A with quantities x_1 and x_2 of lithium per unit. $E(Li)$ is the energy of bulk lithium. This will give the voltage of either the anode or cathode, relative to the chemical potential of lithium.

3.1.2.2 Capacity

The capacity of a battery is far simpler than the voltage: it is a measure of how much charge the battery can store. In Li-ion batteries, this is measured either per unit volume or per unit mass as mAh/cm³ or mAh/g (or in equivalent units) and is determined by the amount of lithium that can be reversibly intercalated into either the anode or cathode per unit volume or per unit mass. There is both a minimum and maximum limit to this that is determined by the stability of the host material. Some host materials become unstable and break down when all the intercalated lithium is removed, leading to a lower limit. For the other limit, too much lithium can be added to a system, leading to unwanted, irreversible, side reaction to occur. These limits can also change as the battery is cycled due to

the movement of lithium fundamentally changing the host structure, among other causes.

The capacity of a battery per gram can be calculated using

$$C = \frac{(x_2 - x_1)eN_A}{M_{Sx_2}} = \frac{(x_2 - x_1)eN_A}{(x_2 - x_1)M_{Li} + M_{Sx_1}}, \quad (3.5)$$

where x_2 and x_1 are the molar fractions of lithium at the maximum and minimum intercalation limits respectively. M_{Li} , M_{Sx_2} and M_{Sx_1} are the molar masses of lithium and the system at the maximum and minimum intercalation limits respectively, meaning $M_{Sx_2} = (x_2 - x_1)M_{Li} + M_{Sx_1}$. This gives the capacity in the units of C/g, to convert into mAh/g it is simply divided by 3.6 as a coulomb is an ampere second.

For use with density functional theory calculations, very little modification is required to equation 3.5 to get

$$C = \frac{N_e e N_A}{M_{Li} N_e + M_{Sx_1}}, \quad (3.6)$$

where N_e is the number of electrons (equivalent to the amount of lithium that can be cycled). However, determining what the upper and lower limits of intercalation are is relatively difficult. We can choose to have the upper limit be when the voltage drops below zero, meaning that said lithium would prefer to form bulk lithium, or we could choose to look at all possible side reactions, which involve the breakdown of the host material, to determine if side products such as Li_2O or Li_2S are more favourable. For the lower limit we can look at the stability of the host material as its lithium content is decreased. For this case this means whether or not a different phase of the host material is more favourable or if lithium is simple more stable when not intercalated.

3.2. State of the art Li-ion battery cathodes

Layered materials with van der Waals gaps have been used within many different formulations of Li-ion battery electrodes due, in part, to this gap being able to

easily accommodate the insertion and removal of Li-ions. As mentioned earlier, lithium cobalt oxide (LiCoO_2) was one of the first layered transition metal oxides used showing great promise as a cathode [56]. When going from LiCoO_2 to $\text{CoO}_2 + \text{Li}$, this material boasts a high average voltage of $\approx 3.92 \text{ V}$ (from the density functional theory result shown in Figure 3.3, the experimental voltage is extrapolated from the original paper by Goodenough *et al.* [56]) and a capacity of 984.5 C/g (273.5 mAh/g) which is equivalent to an energy density of 3854.4 J/g .

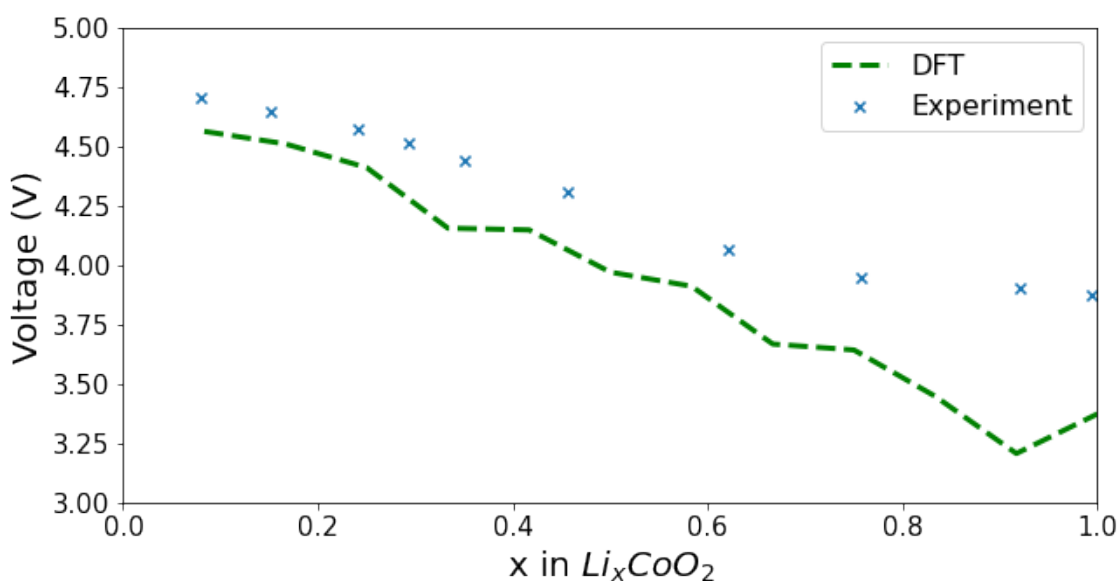


Figure 3.3: The voltage curve for lithium cobalt oxide as the lithium content is varied. The blue crosses show the experimental result for x in Li_xCoO_2 reproduced from work by Goodenough *et al.* [56] and the green dashed line is the results from a density functional theory calculation.

Unfortunately, this is not the full picture. Just like many other Li-ion battery materials, LiCoO_2 suffers from draw backs such as: all the lithium not being able to be removed which effectively halves the capacity and energy density [62], capacity reducing with each and every charge-discharge cycle due to Co dissociation [63], oxygen release at high voltages [64], and the high cost of Co metal. Alternatives have been investigated such as LiNiO_2 and LiMnO_2 but these suffer from similar problems, with the former having poor thermal stability and breaking down into more favourable Ni-oxides upon lithium removal [65], and the latter undergoes a phase transition from layered to spinel [66] while also having a lower capacity and undergoes Mn dissociation [67]. Transition metals from Ti to Ni have been

investigated in the past, but all possessed experimental voltages lower than that of LiCoO_2 , and therefore were not investigated further [68].

This has led to a search for alternative layered transition metal oxides that overcome some or all of these problems, one route of research is that of alloying different transition metals together such as NCA ($\text{Ni}_x\text{Co}_y\text{Al}_{1-x-y}\text{O}_2$) and NMC ($\text{Ni}_x\text{Mn}_y\text{Co}_{1-x-y}\text{O}_2$) where x and y can be tuned to change the properties of these materials. A few different stoichiometries of both NMC and NCA are currently in use in commercial batteries, however there is still ongoing research into improving these materials for next generation batteries.

3.2.1 Alloyed Transition metal dioxides

Alloying different transition metals together in these materials allows us to take advantage of their different properties, such as the voltages at which redox occurs. This was one of the reason why nickel was alloyed to LiCoO_2 as it undergoes both $\text{Ni}^{4+} \rightarrow \text{Ni}^{3+}$ and $\text{Ni}^{3+} \rightarrow \text{Ni}^{2+}$ at similar voltages, which can be used in tandem with manganese, which is far more stable in this layered structure when it is in its 2+ valence state. This lead to the first formulation of NMC with equal parts nickel, manganese and cobalt ($\text{LiNi}_{1/3}\text{Mn}_{1/3}\text{Co}_{1/3}\text{O}_2$ called NMC-111). The material has been reported to have a capacity between 150 and 200 mAh/g with a voltage window from 2.5 to 4.6 V [62, 69, 70]. This is a clear improvement over LiCoO_2 with a similar voltage, higher capacity and better stability but unfortunately, it still suffers from similar problems to the component layered mono transition metal dioxides: the release of oxygen can still occur at high voltages and the transition metals still dissociate, both of which lead to capacity fade with repeated cycling [71, 72, 73]. Additionally, due to the ionic radii of lithium and nickel being similar, disordering can occur where nickel migrates to the lithium layers and *vice versa*, effectively blocking the lithium transport layer, reducing the capacity [74, 75].

Varying the stoichiometry of nickel, manganese and cobalt in NMC materials has been investigated to reduce some of these issues and increase the capacity, with Ni-rich stoichiometries being the most popular as higher nickel content

allows for higher levels of lithium extraction at set voltage limits [76]. However, an increase in nickel content also leads to an increase in Li/Ni disordering [74, 75]. Popular Ni-rich NMC stoichiometries include NMC-433 ($\text{LiNi}_{2/5}\text{Mn}_{3/10}\text{Co}_{3/10}\text{O}_2$), NMC-622 ($\text{LiNi}_{3/5}\text{Mn}_{1/10}\text{Co}_{1/10}\text{O}_2$) and NMC-811 ($\text{LiNi}_{4/5}\text{Mn}_{1/10}\text{Co}_{1/10}\text{O}_2$), all of which have equal parts cobalt and manganese. NMC-622 and NMC-811 show large theoretical capacities close to ≈ 275 mAh/g but practically can only achieve ≈ 190 and 200 mAh/g respectively, with both showing voltages of ≈ 3.25 V, with NMC-811 being slightly lower than NMC-622 [77]. This shows that there is some trade off between voltage and capacity when varying the nickel content.

In general, increased nickel content increases the capacity by allowing for more lithium to be removed from the structure. Increased cobalt content improve the capacity retention, meaning that lithium can be inserted and removed more before capacity is lost due to degradation. Finally, increased manganese content increases the stability at higher temperatures, allowing for use in hotter environments or at increased charging and discharge rates that often leads to loss of energy in the form of heat [78].

Another method often used to increase the capacity of these materials is to replace some of the transition metals with additional lithium resulting in materials with the formula $\text{Li}_{1+z}(\text{Ni}_x\text{Mn}_y\text{Co}_{1-x-y})_{1-z}\text{O}_2$. These Li-rich NMCs can have capacities up to 270 mAh/g due to heavy transition metals being removed and replaced with lithium, but suffer from voltage fade with repeated cycling [78, 79, 80, 81, 82, 83, 84].

Alternatively, replacing some of the transition metals with entirely different metals can lead to increased stability, one of the most popular of these is the introduction of aluminium to get NCA ($\text{LiNi}_x\text{Co}_y\text{Al}_{1-x-y}\text{O}_2$) [85] or NMA ($\text{LiNi}_x\text{Mn}_y\text{Al}_{1-x-y}\text{O}_2$) [86]. In these cases, aluminium is used in very small amounts (< 0.1) as it is not redox active. Doping is often shown to stabilise NMC with many different metals having been investigated such as titanium, niobium, tungsten and molybdenum [87, 88, 89], but these, like aluminium, are redox inactive.

3.2.2 Stability

While there has been a lot of development into the improvement of these materials, they all suffer from instability, either when at low lithium concentrations, during extended cycling or due to high temperatures. Clearly, understanding the root causes of these issues is key to improving these materials.

3.2.2.1 Phase Stability

These materials are often formed with lithium in a fully lithated state, e.g. LiMO_2 , meaning that the first problem that could be encountered is if a phase other than the layered is more favourable. These could include, but are not limited to, the spinel phase where the transition metals form a three dimensional lattice instead of layers, and disorder rock-salt phase where the transition metals and lithium sites are mixed randomly. Normally, these phases begin forming after lithium removal, with spinel phases $\text{Li}_2\text{NiMn}_3\text{O}_8$, LiCoNiO_4 and LiNi_2O_4 and rocksalt phase NiO being predicted to form theoretically [90] and observed experimentally [91]. These phases become more and more favourable compared to a layered structure as the lithium content is decreased or the nickel content is increased.

The spinel structures can form favourably from a 50% (dis)charged state as they have the same stoichiometry but the rocksalt phase such as NiO require the removal of oxygen. As mentioned earlier oxygen release can occur when charging to high voltages, the reason for this is that electron removal at high levels of delithiation creates holes that become trapped in oxygen 2p orbitals [92, 93]. This causes the formation of O_2 molecules that can then be released from NMC leaving it with an oxygen deficiency, making the formation of NiO and other rocksalts possible.

When lithium is fully removed, a handful of other transition metal dioxide phase could become more favourable than the layered phase, such as rutile, anatase or delithiated spinel. However, these all require significant reordering from the layered structure, limiting where these phases could form to areas where the atoms are less confined, such as surfaces and grain boundaries.

3.2.2.2 Surface Stability

The surface can react with, or effectively catalyse reactions of, the electrolyte such as ethylene carbonate [94] forming a new material on the surface. This new material on the surface is called the solid-electrolyte interphase (SEI) and is known to be one of the causes of voltage and capacity fade over time. The formation of the SEI can also be expedited by imperfections in the surface such as cracks and grain boundaries. These can allow for phase transitions as there is more room to reorganise, as well as allowing for reactions with other compounds present to occur, such as H₂O, CO₂, LiPF₆ [95] and sulphides [5], which can lead to the redox of the transition metals. Adsorptions of these compounds can also effectively block lithium pathways into the van der Waals gap reducing the capacity of NMC materials. Oxygen dissociation can occur more readily at the surface [96, 93] leading to the formation of rocksalt phases, which also block off the van der Waals gap.

3.2.2.3 Thermal Stability

Many of the previously mentioned reactions and phase changes can be expedited by an increase in temperature [91, 73], with higher temperatures giving each and every atom additional energy according to $k_B T$, which is the internal energy of an atom at a given temperature (for room temperature, 298 K, this equates to ≈ 25.2 meV). It has been shown that an increase in nickel content leads to less stability at higher temperatures [76]. This can be attributed to the energy required to remove oxygen atoms from the NMC structure, oxygen atoms that have high nickel coordination are less stable than those with less neighbouring nickel atoms [73].

Despite the high voltages and capacities that these alloyed transition metals oxides have, there is a clear need to stabilize them, either *via* optimising their stoichiometries or other means such as doping, in order to design the next generation of cathodes. Mitigating the causes of degradation is at the forefront of the

ongoing research into alloyed transition metal oxides and overcoming it will allow for the more exotic chemistries to become commercialised.

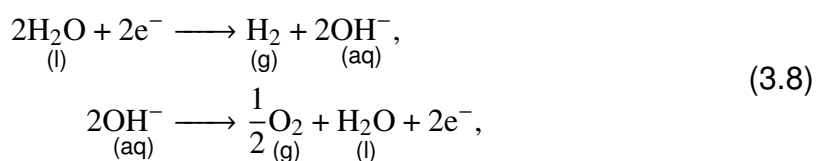
3.3. How water splitters work

3.3.1 History and Basics of Water Splitters

Not long after the invention of the voltaic pile by Alessandro Volta in 1800, the continuous current it produced was used by William Nicholson and Anthony Carlisle to break water into its base components *via* electrolysis, which follows the reaction

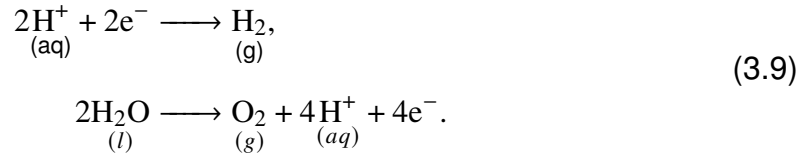


where energy is added to water to split it into hydrogen and oxygen gases. Current flows from one electrode to another, one that takes electrons from the voltaic pile to reduce water into H_2 and aqueous OH^- ions, and the other oxidises these OH^- ions to make O_2 , some water and electrons. These occurs *via* the half reactions



called the hydrogen evolution reaction (HER) and the oxygen evolution reaction (OER) which occur at the cathode and anode respectively. The overall reaction is reversible, with water and energy in the form of heat being generated. However, it wasn't till 1869 that the generation of hydrogen *via* electrolysis became cheaper thanks to the invention of the Gramme machine by Zénobe Gramme. The Gramme machine was an electrical generator that produces a direct current, allowing for continuous current for a far longer duration than the voltaic pile (essentially for as long as work is done on the machines crank).

The HER and OER half reactions stated above are only one possible route of electrolysis that occurs in a basic solution (high pH), another set of half reactions exist for an acidic solution (low pH)



These, like the basic solution equations, occur at the cathode and anode respectively. These reactions require a potential difference of at least 1.23 V to occur due to the relative change in Gibbs free energy require for the two half reactions. These can be compared to each other by first considering the change in Gibbs free energy for each half reaction under standard conditions (298.15 K, 101.325 kPa, 0 pH) relative to the standard hydrogen electrode per electron, called the standard electrode potential (E°). This means that the reaction $2\text{H}^+ + 2\text{e}^- \longrightarrow \text{H}_2$ is said to have zero change in Gibbs free energy per electron. From this, the standard electrode potential energy for the other half reaction is $E^\circ = 1.23 \text{ eV}$ [97], meaning that four times this amount is required for the reaction $2\text{H}_2\text{O} \longrightarrow \text{O}_2 + 4\text{H}^+ + 4\text{e}^-$.

3.3.1.1 The Nernst Equation

These potentials will change when the conditions are changed, be it temperature, pressure or pH. This change can be calculated according to the Nernst equation which is derived from a few different expressions. Starting with

$$E^\circ = E^\circ_{reduction} - E^\circ_{oxidation},
 \tag{3.10}$$

which means that an oxidation reaction must be reversed when calculating the reaction quotient which is introduced later, reduction reactions do not. This can be related to the change in Gibbs free energy under standard conditions, ΔG° , by

$$\Delta G^{\circ} = -nFE^{\circ}, \quad (3.11)$$

where n is the number of electrons transferred in the reaction and F is the Faraday constant. If we change the standard conditions to general conditions we get

$$\Delta G = -nFE, \quad (3.12)$$

where ΔG is the change in the Gibbs free energy and E is the potential difference. These can be related to one another using

$$\begin{aligned} \Delta G &= \Delta G^{\circ} + RT \ln Q, \\ -nFE &= -nFE^{\circ} + RT \ln Q, \end{aligned} \quad (3.13)$$

where R is the molar gas constant, T is temperature and Q is the reaction quotient. When rearranged, we get the Nernst equation [97]

$$E = E^{\circ} - \frac{RT}{nF} \ln Q. \quad (3.14)$$

For the standard hydrogen electrode, $E^{\circ} = 0$ for all temperatures and the reaction quotient is $Q = [\text{H}_2]/[\text{H}^+]$, meaning that $\ln Q = \ln[\text{H}_2] - \ln[\text{H}^+]$, which allows us to relate this to the pH of the solution through $\ln[\text{H}^+] = -2.303 \cdot \text{pH}$. As such, an increase in pH leads to the potential of the HER reaction, $2\text{H}^+ + 2\text{e}^- \longrightarrow \text{H}_2$, decreasing and ΔG increasing.

On the other hand, the OER reaction, $2\text{H}_2\text{O} \longrightarrow \text{O}_2 + 4\text{H}^+ + 4\text{e}^-$, first needs to be reversed as it is an oxidation reaction. This means $Q = 1/[\text{H}^+][\text{O}_2]$ (H_2O is not included in the reaction quotient) and $\ln Q = -\ln[\text{H}^+] - \ln[\text{O}_2]$ such that for this reaction, as pH is increased, the potential decreases and ΔG increases.

Given that these reaction happen in tandem, they are both affected by changes in pH in the same way such that the difference in their potentials is always 1.23 eV, as shown in Figure 3.4.

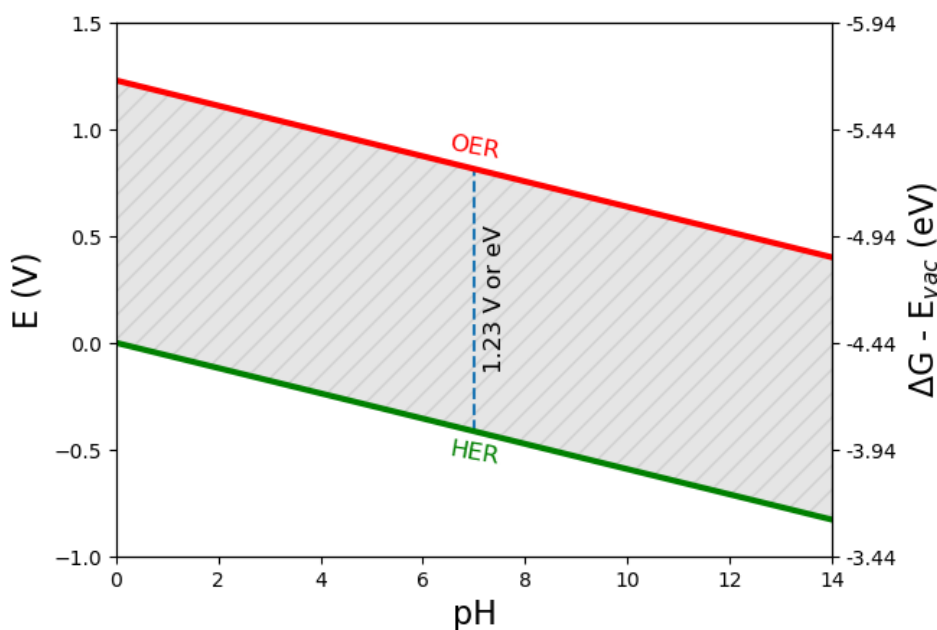
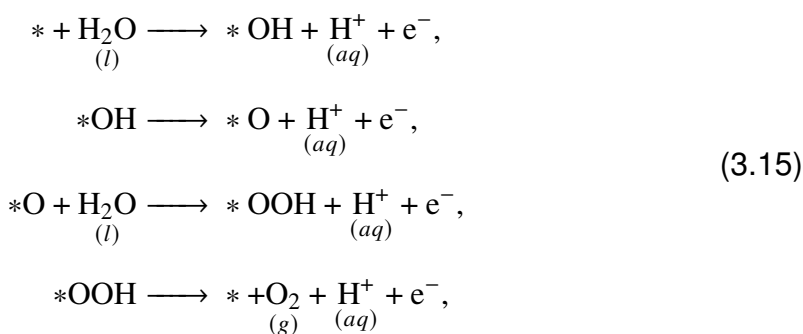


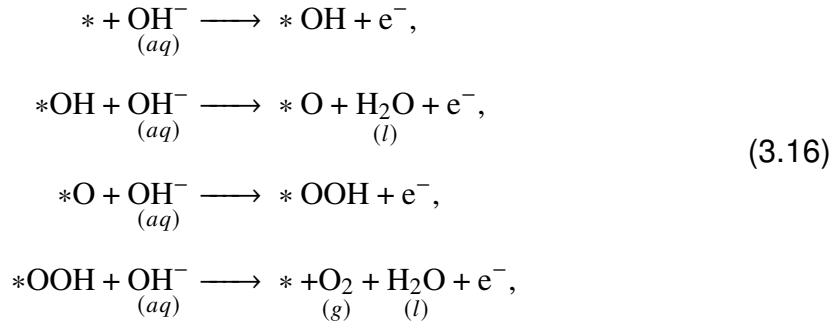
Figure 3.4: How pH affects the potential of the HER and OER half reaction for splitting water. The left axis shows the potential difference relative to the standard hydrogen electrode and the right axis shows the change in the Gibbs free energy in eV relative to the vacuum level (the energy of a stationary free electron outside of a material).

3.3.2 Photoelectrolysis

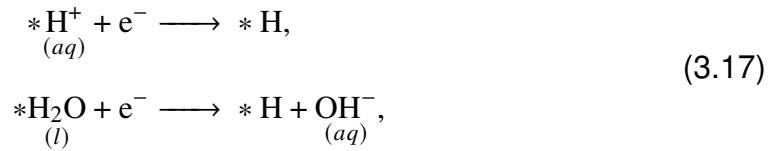
Within water splitting *via* electrolysis, the energy the electrons carry is supplied by an external circuit. However, this energy could instead come from the excitation of electrons *via* the absorption of photons. This process occurs naturally in photosynthesis where the hydrogen in the water forms other organic molecules with carbon and oxygen, with the byproduct being oxygen. Both photosynthesis and photocatalytic water splitting, sometimes called photoelectrolysis, require four electron excitations for a complete reaction meaning that four photons need to be absorbed. This is because the OER half reaction occurs *via* four subreactions



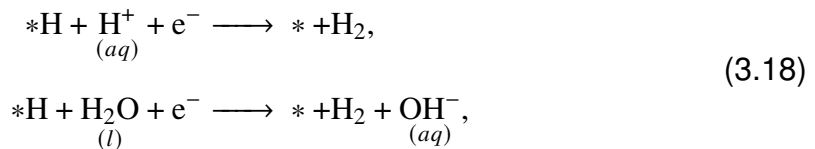
which occur in an acidic solution. Here * represents the surface of the photocatalyst, meaning that *OH is an OH group adsorbed onto the surface of the photocatalyst. A similar set of subreactions can be written for a basic solution



In both sets of subreactions, four electrons are produced meaning that two lots of the respective HER half reaction can occur, which also occur *via* subreactions. These are split into three separate reaction for an acidic and basic solution. The first of these reactions is called the Volmer reaction



which are the acidic and basic reactions respectively. This reaction can then be followed by the Heyrovsky reaction



which are the acidic and basic reactions respectively. Alternatively, the Volmer reaction can occur twice, resulting in two separate hydrogen adsorptions. These two adsorbed hydrogen atoms can then react together *via* the Tafel reaction



There is only one version of the Tafel reaction as it does not involve H^+ or OH^- . This does, however, require that the two hydrogen adsorptions are close to one another. A schematic of the OER and HER (following the Volmer and Heyrovsky reactions) is shown in Figure 3.5 for the acidic case.

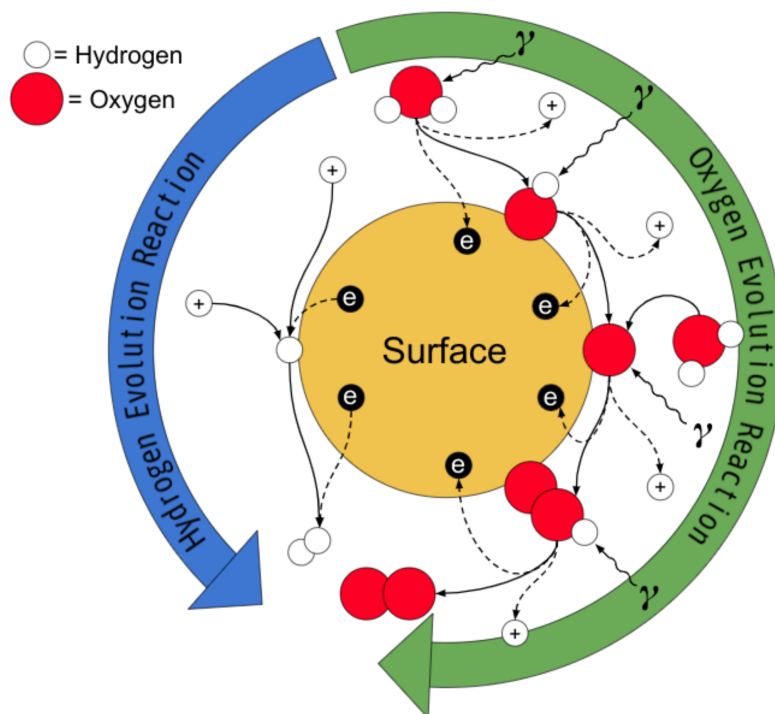


Figure 3.5: A schematic of the OER and HER (following the Volmer and Heyrovsky reactions) in acidic conditions.

3.3.2.1 Electronic Band Interactions

Now that we understand the reactions that occur, we can move onto the interaction of the catalyst's electrons and light. This requires an understanding of the electronic bands within the catalyst.

In order for electrons to have enough energy for the HER reactions, they need to be excited by absorbing light with at least 1.23 eV of energy (equivalent to roughly 1000 nm). For this to occur, the catalyst needs to be able to absorb light of this energy and therefore possess a bandgap equal to 1.23 eV. Electrons are excited from the valence band to the conduction band, they then drop down

in energy and react in the HER subreactions. Electrons produced by the OER subreactions also drop down in energy to the valence band, filling up the empty states produced by the initial electronic excitation. In order for the electrons to be able to drop down in energy, the band gap of the catalyst actually needs to be greater than 1.23 eV for this to be both favourable and probable. Each of the OER and HER subreactions will have an associated activation energy that will need to be overcome *via* the electrons having even more energy, meaning that the band gap needs to be even larger. Additionally, while the ideal energy for each of the OER subreaction is 1.23 eV, every single possible different catalytic surface will change the energy of each step, making them require more or less than the ideal 1.23 eV. They will, however, always sum to four times 1.23 eV (4.92 eV).

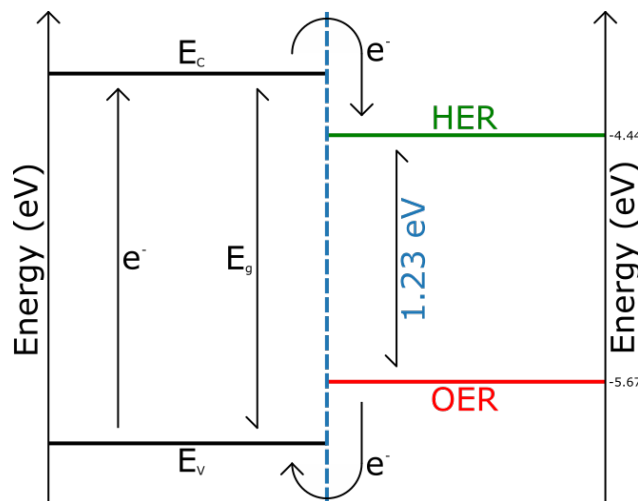


Figure 3.6: The energy levels of the valence and conduction bands of a material used for photoelectrolysis compared to the energy level at which the OER and HER occur at a pH of 0.

Figure 3.4 shows the relative positions of the OER and HER reaction with respect to the vacuum level. This is the energy of a stationary free electron outside of a material. Electronic bands within a material lie relative to this same vacuum level. In order for electrons to drop down in energy from the conduction band of the material to the HER the conduction band needs to be higher than the HER relative to the vacuum level. This is true also for electrons to drop down from the OER to the valence band, i.e. the valence band needs to be lower than the OER. This means that the valence and conduction bands need to straddle the HER and OER in energy, which is shown in Figure 3.6 for a pH of 0.

3.4. State of the art Photoelectrolysis Devices

Unlike battery cathodes, there are many different types of materials that are of current interest in the field of photoelectrolysis due to different sought after properties, the most important of these are the efficiencies of the different processes that occur in order to split water. There are a few main factors that can be used to determine the overall performance of a photoelectrolysis device, these are light absorption, charge generation, charge separation, charge transportation and finally charge extraction into the HER and OER reaction [98]. These are all parts of the solar to hydrogen (STH) efficiency of a given material or materials. Some materials are more efficient at different parts of this leading to high efficiency in one or more steps but a low STH efficiency.

While it is easy to see how a single material can be used to absorb light and do both the OER and HER, the strict requirements of the band alignment means that it is far easier to find two or more materials that can work in tandem, each responsible for a separate part of this. One form of these are photoanodes combined with a cathode, the photoanode is responsible for the absorption of light and as a catalyst for the OER while the electrically linked cathode is responsible for the HER, this is shown in Figure 3.7 (a). Some examples of photoanodes currently under investigation are α -Fe₂O₃, TiO₂, ZnO, WO₃, SnO₂, BiVO₄ and PbBi₂Nb₂O₉ [98, 99, 100]. However these systems suffer from low STH efficiency due to the recombination of electrons and holes, as well as the additional energy that is required for charges to be transported through a wire from the photoanode to the cathode. It has been shown that nanostructuring these materials, in order to increase their surface area to volume ratio and shorten the distance that the charges have to travel, or heterostructuring, dopant control and the attachment of quantum dots, in order to provide more favourable routes for charges to be transported *via*, can improve their overall STH efficiency [98].

Photocathodes have also been investigated in depth as an alternative to photoanodes. These photocathodes act as light absorbers and the site where the HER occurs and a normal anode is used for the OER, this is shown in Figure

3.7 (b). Materials that are being investigated for this use include perovskites like MAPbI_3 (where MA is methylammonium), CsPbBr_3 and CsFAMA (where FA is formamidinium) [101], and transition metal oxides such as Cu_2O , CuO , Cu_3VO_4 , NiO and Co_3O_4 [99, 102]. Just like the photoanodes, these photocathodes suffer from low STH efficiencies that can be improved upon *via* nanostructuring and heterostructuring.

There is also another form of photoelectrolysis device that uses both a photoanode and a photocathode. Within these systems, electrons are excited in the photoanode and then de-excite, either directly or *via* an intermediate material, to the valence band of the photocathode where the electrons undergo an additional excitation before catalysing the HER, this is shown in Figure 3.7 (c). These are called Z-scheme photoelectrolysis devices and while they gain the benefit of having two materials that are efficient at the HER and OER respectively, the requirement of two excitation events increases the chances of recombination and thus lowers the STH efficiency [103].

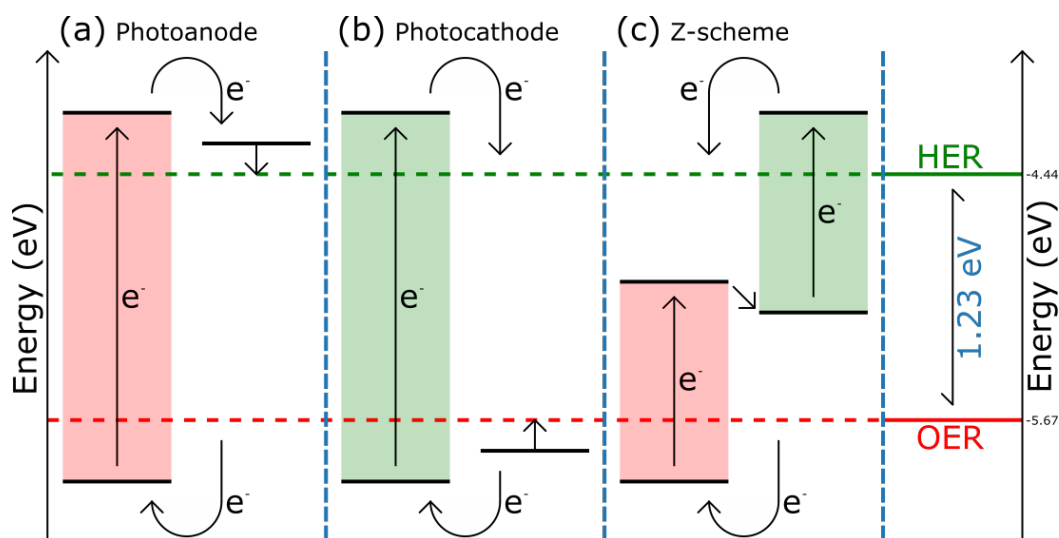


Figure 3.7: The energy levels of the (a) photoanode with cathode, (b) photocathode with anode and (c) photoanode with photocathode in the Z-scheme setup compared to the energy levels at which the OER and HER occur.

3.4.1 Single Electrode Photoelectrolysis

While there are many materials that have appropriately sized and positioned bandgaps for catalysing both the HER and the OER, finding a material that is

efficient at both is a challenge. There are materials that are far better at the OER than the HER due to having a large OER overpotential (Where there is a large difference in energy between the OER and the valence band), such as SrTiO₃, Ta₂O₅, Bi₂MoO₆, BiVO₄, TiO₂ and ZnO, while other materials are the opposite and are far better at the HER due to having a large HER overpotential (Where there is a large difference in energy between the HER and the conduction band), such as C_xFe₂O₄, InVO₄, In₂O₃, Ce₂O₃ and Cu₂O [100]. For photoelectrolysis, an overpotential means that the position of the band is either significantly higher than the HER or significantly lower than the OER. Other materials that are equally capable of both reactions exist [103, 104, 105], based off either transition metal oxides, such as ZrO₂, KTaO₃, ZrO₂, WO₃, Fe₂O₃ SnO₂, or general semiconducting materials, such as ZnS, SiC, CdS, InP, GaP and GaAs [99, 102, 104]. These generally have higher STH efficiencies than multiple electrode setups due to there being less steps where electron-hole recombination can occur.

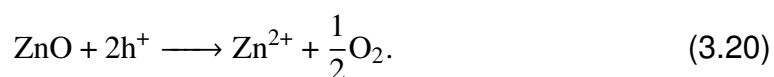
These materials can also be improved by similar means as the multiple electrode setups mentioned before. The addition of noble metal nanoparticles, such as Pt, Ru, Ir or Ni, to the surface can help with the HER reaction but also allows the reverse OER (oxygen reduction reaction) to occur more readily [100]. Heterostructuring can help with charge separation, such as TiO₂ / α -Fe₂O₃, α -Fe₂O₃ / SrTiO₃, Fe₂O₃ / ZnFe₂O₄, TiO₂ / ZnFe₂O₄, TiO₂ / WO₃, WO₃ / BiVO₄ and TaON / CaFe₂O₄, reducing the probability of electron-hole recombination [98] by spatially separating the electron and hole.

While having a large HER or OER overpotential, or both, leads to less overall recombination, it also means more of the energy absorbed does not end up as hydrogen. For this reason there has been lots of attention on visible light active (VLA) materials that have bandgaps that only just straddle the HER and OER. One of the most recent of these are the d⁰ (Ta⁵⁺ and Nb⁵⁺) and d¹⁰ (Ge⁴⁺ and Ga³⁺) metal (oxy)nitrides which have some of the highest STH efficiencies possible. Unfortunately these materials are difficult to produce, often having defects

which can act as recombination sites on top of the low bandgap allowing for recombination to occur more readily [100].

3.4.2 Degradation and Photocorrosion

Once the electrons in a material are excited by light they can give up their energy in many different ways, the most common of which is recombination but said electron and hole can instead go on to react in adverse ways. The holes in a system can reduce the catalyst instead of water, for the catalyst ZnO this follows the reaction



While this does create oxygen just like the OER reaction does, this does not produce the H^+ required by the acidic HER and breaks down the catalyst. These side reactions can be reduced by the use of hole scavengers or electron accepters. Hole scavengers such as alcohol and sulphide ions react with holes in the valence band so that they can't adversely react with the catalyst itself, however this means that the hole can no longer be used in the OER. Electron accepters such as Ag^+ or Fe^{3+} have a similar issues, while they remove electrons from the conduction band, they prevent them from reacting in the HER [104].

The current state of the art photoelectrolysis devices show great promise for producing sufficient quantities of clean hydrogen, there has been significant progress in device improvement *via* nanostructuring and heterostructuring leading to higher STH efficiencies. However, there are still several challenges that need to be overcome before practical large scale use. Limiting losses *via* recombination and improving material stability to photocorrosion is the current focus of ongoing research.

In this chapter we have covered the intricacies of batteries and photoelectrolysis devices, going over the historical context, theoretical foundations and the

current state of the art in both fields. A clear set of challenges has been outlined that need to be overcome in order to advance these fields of research. In the following chapters we hope to address some of these.

Chapter 4

Computational Analysis of the Enhancement of Photoelectrolysis using Transition Metal Dichalcogenide Heterostructures

"This is an obvious wrong."

– A comment by a reviewer

In this chapter, individual TMDCs MoS₂ and PdSe₂ and a heterostructure of these have been investigated for their potential use as photoelectrolysis devices. The energetic steps of both the HER and OER have been looked at on these monolayers and the heterostructure to determine whether or not they are suitable and to see the effect of heterostructuring. We will begin with a brief introduction to this area of research and the methods used within this chapter. The adsorption of different species involved in the HER and OER have been compared to one another through the use of phase diagrams, these are described along with the different investigated adsorption sites, the energetics of the water splitting reactions and the DFT parameters used within this chapter.

4.1. Introduction

The need to reduce CO₂ levels [106] has resulted in increased demand for clean alternative fuels such as hydrogen. Hydrogen can be obtained via photocatalytic breakdown of water, often termed "water-splitting" [107], which offers a potentially cheap and renewable method of producing clean hydrogen gas [11, 12].

The critical factor in the photocatalytic reactions associated with the water splitting reactions is the surface involved; each has different energetics associated with enabling the process. The search for the ideal surface is thus crucial to utilisation of photocatalytic water splitting. The desired decomposition reaction is comprised of two reactions known as the hydrogen (HER) and oxygen evolution reactions (OER).

Two dimensional (2D) materials, such as the transition metal dichalcogenides (TMDCs) are good candidates for water splitting catalysts [108, 109, 16] due to their desirable electronic [110, 111] and catalytic properties [12, 112]. Molybdenum disulphide (MoS_2) is prolific among the TMDCs, as it is naturally occurring and finds use as a solid lubricant [20] as well as for the hydrosulphurisation reaction [21] as a catalyst in the petroleum industry. PdSe_2 has shown potential for a wide array of electronic applications, including photovoltaics [113], solar cells [114] and thermoelectrics [115].

Heterostructuring and overlayers are increasingly attractive approaches to tailoring properties for photocatalysis [116, 117, 118, 119, 120, 121, 122, 123, 124, 125]. Two-dimensional materials are ideal for heterostructuring, due to the comparative ease with which they can be made (such as via exfoliation [126]) and has been applied to TMDCs [127, 128, 129, 130, 131]. For water splitting, predicting the band alignment of various TMDCs heterostructures from their components is relatively easy [111] due to the weak interaction between the layers. For solar energy harvesting, the focus of heterostructuring has been on Type II band alignment heterojunctions, which have shown gains in optimising band edge positions [128], improving the carrier mobility [132] and the resultant electric field causing a reduction in electron-hole recombination [116]. Type I (straddling) heterojunctions have seen some consideration as photocatalysts [133, 134, 135, 117]. Type I heterojunctions drive both electrons and holes towards the straddled layer, which can promote spontaneous recombination and lower efficiency of Type I compared to Type II. In particular, in some cases Type I has been shown to be more robust to conditions where the water is mixed with

other components (such as acid)[135]. PdSe₂ has been considered for water splitting and for Type I approaches, Song *et al.* [136] have indicated that PdSe₂ has a low intrinsic recombination rate, which is highly suitable for photocatalysis.

Previous explorations of monolayer MoS₂ and P-PdSe₂ have shown agreement for properties such as lattice constant and structure with first principles results using the GGA functional [112]. The optical gaps of these two structures are experimentally observed as 1.89 eV [112] and 1.3 eV [137] respectively, with the corresponding GGA values being 1.79 eV to 1.88 eV [138, 112] and 1.37 eV [139], again respectively. MoS₂ is well known to exist in the H- and T-phases [140, 141], whilst PdSe₂ has only recently been fabricated and is observed to form the T- [142, 113, 114] and a two-dimensional phase which includes Se-Se bonds often called P-phase [143, 114], with the T-phase having been made in nanotube form with a band gap of 0.7 eV [142].

The photocatalytic potential of MoS₂ for water splitting has attracted considerable attention [144] due to its good absorbance of light [145], though its other properties have been shown to be less desirable, in particular its poor electrical conductivity [146] and required overpotential for water splitting of at least 170 mV [147, 148]. An additional issue for MoS₂ is that the basal plane S-sites show a reduced reaction rate compared to edge and defect sites [149]. To circumvent these issues, several approaches focus on combining MoS₂ with a second system aiming to improve these properties. Combination of MoS₂ with oxygenated graphene and C₃N₄ by Xu *et al.* [150] showed MoS₂ could reach a hydrogen evolution rate of 1841.72 μmol h⁻¹ g⁻¹, with external quantum efficiency of 7.11%. Xiang *et al.* [151] showed that a TiO₂/MoS₂/graphene composite could reach hydrogen evolution rate of 165.3 μmol h⁻¹, corresponding to a quantum efficiency of 9.7% at a wavelength of 365 nm, even without a cocatalyst. Hou *et al.* [146] used MoS₂ as part of a carbon nanocage, where the improved surface area increased the photocatalytic activity, but notably increased the required overpotential for the HER to 530 mV. Approaches such as tailoring the porosity of the nanosheets [152] have been found to improve the activity of HER catalysts.

The band gap of T-PdSe₂ is reported to be 0.77 eV (1.3 eV) with the GGA-PBE (HSE06) functional, with an in plane lattice constant of 3.56 Å [114]. The suitability of this phase of PdSe₂ for photovoltaic applications is postulated by Lei *et al.* [153]. Given this suggestion, among others [154, 155], we consider it for use as a photocatalyst in conjunction with monolayers of the well studied MoS₂, with potential applications for this heterojunction extending beyond water splitting [114].

Photoelectrolysis of water involves three key processes; photon absorption by a photocatalyst, the resultant electron excitation, and the subsequent reaction at the boundary of the photocatalyst [156]. Despite this simplified overview, many different factors dictate the suitability of a photocatalyst [157], and the complexity of the design [158] increases possible permutation options.

Here we present theoretical calculations of the electronic and energetic properties of 2H-MoS₂ and 1T-PdSe₂ individually and as a heterostructure for application in water splitting. These are investigated using density functional theory (DFT). The band alignment of the heterostructure with respect to the OER and HER is discussed and the different functional groups involved in the water splitting reactions are added to these structures to determine their energetics. The phase diagrams of these systems and their adsorptions are investigated to determine their relative stability in an air environment. We present the reaction pathways for water splitting on both monolayers and the heterostructure comparing the results. Finally, we describe a robust methodology for developing TMDCs for water splitting.

4.2. Methods

4.2.1 Density Functional Theory Parameters

First principles DFT calculations were performed using the Projector augmented wave (PAW) [159, 160] method implemented in the Vienna Ab initio Simulation Package (VASP) [161, 162, 45, 46]. The calculations utilizes Perdew-Burke-

Ernzerhof electron exchange correlation functions [163, 164]. The blocked-Davidson algorithm is used to achieve self-consistency for all calculation done in this piece of work [45, 46]. The plane wave energy cutoff was set at 900 eV, as it was found that lower values could not correctly capture the vacuum gap that was included, with a Γ -centred Monkhorst-pack grid [165] of at least $6 \times 6 \times 1$ for the two individual constituents and $3 \times 3 \times 1$ for the heterostructure supercells. Van der Waals interactions were included using the DFT-D3 method of Grimme [53] to account for the weak interactions between the 2D layered materials. The structures were geometrically relaxed until the forces between the atoms were less than $0.01 \text{ eV}/\text{\AA}$ using a combination of the conjugate gradient algorithm [54] and a quasi-Newtonian relaxation algorithm, RMM-DIIS [55]. For all monolayers and the heterostructure, a vacuum gap of 15 \AA in the [001] direction was used to remove spurious layer interactions and all layers were aligned to the (001) Miller plane. PAW pseudopotentials were used for the electrons. The electrons that have been treated as valence are: Mo $4d5s$, Pd $4d$, S $3s3p$, Se $4s4p$, O $2s2p$ and H $1s$. The experimental lattice constants for H-Phase [166] MoS_2 are 3.16 \AA and 12.30 \AA (for a and c respectively), compared to the PBE GGA lattice constants 3.19 \AA and 12.44 \AA . For both MoS_2 and PdSe_2 , a 2×2 supercell of either TMDC was used as a reference.

The absorption spectra presented are calculated following the approach of Tsai [167], using the energy eigenvalues obtained from density functional theory. The matrix elements necessary to account for selection rules are not evaluated due to the large number of plane waves required to construct the wave functions described for each k -point, spin and band (This was a limitation in the method that we used, requiring far more memory than we had access to for the systems investigated). The number of plane waves required to build the wave functions in these cases was significantly higher than typical systems due to the vacuum region introduced to model the surface. It has also been shown that the absorption spectra of TMDC heterostructures is simply a superposition of their constituent TMDC, at least for two layers [168].

MoS₂ and PdSe₂ supercells of varying sizes were used to simulate different concentrations of oxygen (O), hydrogen (H), hydroxyl (HO) and hydroperoxyl (HOO) groups using the PBE functional. The HSE06 functional has not been used as it overestimate the band gap of monolayer TMDCs such as MoS₂ (with HSE06 giving a band gap of 2.12 eV or more [169, 170], experimentally measured value of 1.89 eV [112]). Similarly, energetics related to the adsorption of atoms/molecules assessed using the HSE06 functional have been shown to be similar to those for the PBE functional [171]. The heterostructure was made using the ARTEMIS [172] package, which carries out a series of rotation matchings of the two layers and produces a unit cell with the minimal strain, alongside estimating the interlayer distance. The resulting structure consists of 16 unit cells of MoS₂ overlaid by a 12 unit cells of PdSe₂, with an angle mismatch of 30°, corresponding to 0.43% tensile strain on the MoS₂ layer and 1.52% compressive strain on the PdSe₂ layer. The structure and electronic properties of this heterostructure are discussed in more depth later in the paper.

4.2.2 Energetics of water splitting

Chemical potentials play an important role in how the reactions of the water splitting process occur. The chemical potential of H₂ gas can be related to temperature and pressure via [173]:

$$\mu_{H_2(g)} = \mu_{H_2(g)}^0 + k_B T \ln(p_{H_2}), \quad (4.1)$$

where p_{H_2} is the partial pressure of H₂ gas and $\mu_{H_2(g)}^0$ is the chemical potential of H₂ gas at standard conditions (1 atmosphere and 298.15 K). The value of $\mu_{H_2(g)}^0$ is equivalent to the Gibbs free energy and can be calculated from the enthalpy and entropy,

$$G(T, p)_{H_2} = H(T, p)_{H_2} - TS(T, p)_{H_2}, \quad (4.2)$$

which is equivalent to

$$\mu_{H_2}^0 = E_{DFT, H_2} + E_{ZPE, H_2} - TS_{H_2}^0, \quad (4.3)$$

where E_{DFT, H_2} is the energy obtained from DFT of a H_2 molecule in isolation (a single H_2 molecule with a large vacuum gap on all sides) and E_{ZPE, H_2} is the zero-point energy (ZPE) correction. These two terms are equivalent to the enthalpy of H_2 , $H(T, p)_{H_2}$. Table 4.1 shows the ZPE corrections for adsorptions, which are similar for varying surfaces, and the standard entropies, S^0 .

Table 4.1: The ZPE, obtained from the literature [173, 174, 175], and entropy values (at standard conditions) which are obtained from standard tables [173, 175].

Species	E_{ZPE} (eV)	TS^0 (eV)
HOO*	0.461	0.138
HO*	0.307	0.007
H*	0.05	0.2
O*	0.075	0.051
O _{2(g)}	0.10	0.64
H _{2(g)}	0.265	0.41
H ₂ O _(l)	0.55	0.67

Following the approach of Man *et al* [173, 176], the calculations performed in DFT are at 0 K. As this is done under the adiabatic approximation [177], the motions of the ions are not included in the total energy. In order to better model the energetics of water splitting, the contribution to the ground state energy from the ionic motion needs to be included, i.e. the ZPE term. This ZPE term accounts for the ionic motion of the molecule at zero Kelvin. The final term ($TS_{H_2}^0$) is to include the effects of vibrational modes at finite temperature. Adding these terms creates a more accurate approximation [173] to conditions at 298.15 K.

The reactions that form the water splitting process occur at two energy levels; the hydrogen and oxygen evolution reaction (HER and OER respectively) potentials. These levels are calculated with respect to the standard hydrogen electrode, which is defined by the following reaction,



This can be expressed in terms of the chemical potentials as

$$\mu_{H^+} + \mu_{e^-} = \frac{1}{2}\mu_{H_2(g)}. \quad (4.5)$$

This relation can be further broken down into the chemical potentials of protons and electrons,

$$\mu_{H^+} = \mu_{H^+}^0 - 2.303 k_B T \text{ pH}, \quad (4.6)$$

and

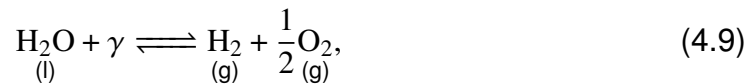
$$\mu_{e^-} = \mu_{e^-}^0 - eU, \quad (4.7)$$

where eU is the shift in the electron energy due to an electric potential and $\mu_{H^+}^0$ and $\mu_{e^-}^0$ represent the chemical potentials under standard conditions. These conditions allow equation (4.5) to be restated as

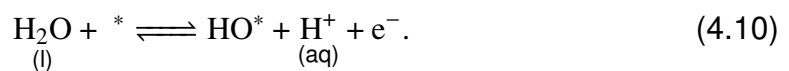
$$\mu_{H^+}^0 + \mu_{e^-}^0 = \frac{1}{2}\mu_{H_2(g)}^0. \quad (4.8)$$

At a pH of 0, the HER and OER occur at -4.44 eV [178] and -5.67 eV respectively, in reference to the vacuum level. The HER is 1.23 eV above the OER. The position of the HER and OER can either be adjusted via a change in pH (upwards) or via an applied potential (i.e. the overpotential).

The overall water splitting reaction is given as



where γ represents the photon's energy. This expression can be further decomposed into the constituent reactions involving the catalytic surface, each of which have an associated energy and set of reactants and products. The first step in the process, within which the catalytic surface reacts with water at the OER, is as follows [173]



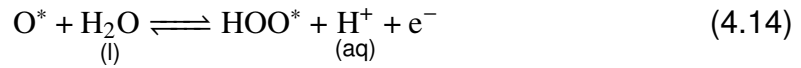
where * represents the surface of the structure. Similarly, HO* is a surface with HO adsorbed. From this, the change in the Gibbs free energy is expressed as

$$\Delta G_1 = \Delta G_{HO^*} - \Delta G_* - \Delta \mu_{H_2O} + \mu_{H^+} + \mu_{e^-}. \quad (4.11)$$

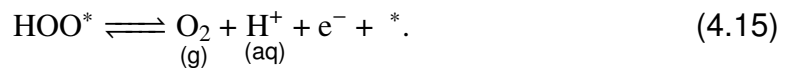
This can be expanded using equations (4.3), (4.6), (4.7) and (4.8) as

$$\begin{aligned} \Delta G_1 = & (E_{DFT} + E_{ZPE} - TS^0)_{HO^*} - (E_{DFT} + E_{ZPE} - TS^0)_* \\ & - (E_{DFT} + E_{ZPE} - TS^0)_{H_2O} + \frac{1}{2}(E_{DFT} + E_{ZPE} - TS^0)_{H_2} \\ & - 2.303 k_B T \text{ pH} - eU. \end{aligned} \quad (4.12)$$

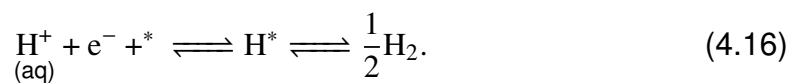
A similar process can be followed for the remaining steps of each reaction, as seen in Man *et al* [173].



and



The free energy diagrams are taken with respect to the standard hydrogen electrode (pH = 0 and U = 0) indicating that there is an abundance of hydrogen and there is no energy difference between H⁺ + e⁻ and H₂. This latter point means that, instead of considering the full Volmer-Heyrovsky or Volmer-Tafel equations [176], the HER can be reduced to



As the start and end stages are equivalent only the intermediate step of ΔG_{H^*} is necessary as a the descriptor of the HER activity for a wide variety of

catalysts. Further details are available at the end of this chapter 4.5. The H^+ ions used during the HER steps balance with the ions produced during the OER steps.

In the ideal case, the optimum energy involved in each step of the OER reaction pathway would be the same, 1.23 eV (the separation of the HER and OER potentials [179]). However, as previously demonstrated [176, 173, 175, 180, 181], surfaces can alter the energies of these reactions such that an additional potential (the overpotential) is required for the reaction step to occur. This overpotential can either be created by a larger band gap or via an external field and can lower the theoretical efficiency of a semiconducting water splitting device.

4.2.3 Adsorption Sites and Phase Diagrams

For both MoS_2 and $PdSe_2$ monolayers, three different adsorption sites have been considered: above a chalcogen atom (S, Se), above a transition metal atom (Mo, Pd) and above the ring site. These sites are shown in figure 4.1 for the H-phase structure of MoS_2 .

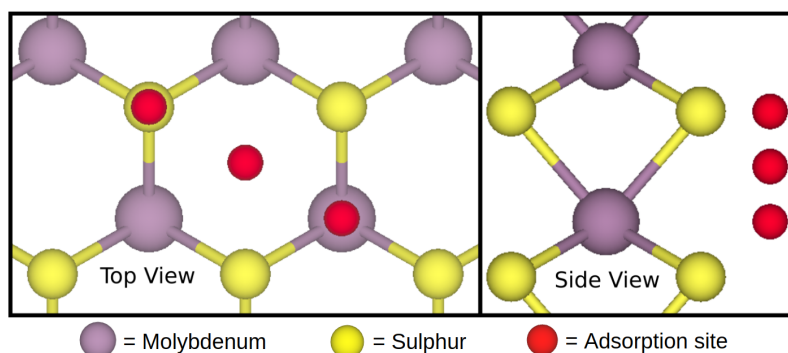


Figure 4.1: a schematic showing the potential adsorption sites considered. The red atoms are the potential adsorption sites for the H-phase structure of MoS_2 .

These three sites have been studied with each of the different species involved in the HER and OER steps: H, O, HO and HOO. For the heterostructure, these same sites have been considered and no interstitial sites are investigated. For each of these species, the relaxed structure with the lowest Gibbs free energy is the most energetically favourable. Other sites may support metastable adsorptions at a slightly higher energy, which can result in better photoelectrolysis properties because increasing the energy of one step will lead to the next step requiring less

energy. However for the purposes of this work, we have only considered the most favourable site for further analysis. In order to compare the adsorption of different species, phase diagrams are made following the approach of Heifets *et al.* [182], and many others within the DFT community [183, 184, 185, 186, 187, 188, 189, 190, 191].

Phase diagrams are used to show how the structure, phase or morphology of a material changes as conditions within a system vary. These could be pressure, temperature, volume and concentration. These are constructed from distinct regions where a certain phase of a material is the most thermodynamically favourable for given conditions. These regions are bounded by lines of equilibrium, these are lines where both phases can coexist under the same conditions, e.g. both phases are equally favourable. Where multiple lines meet, three or more phase can coexist under the same conditions. These diagrams do not show metastable phases of materials, without modification, as these are never the most favourable form of a material.

In order to construct a phase diagram we will start from the standard definition of the Gibbs free energy, G ,

$$G = H - TS = U + PV - TS, \quad (4.17)$$

where H is enthalpy, T is temperature, S is entropy, U is internal energy, P is pressure and V is volume. A small change in the Gibbs free energy is

$$dG = dH - TdS - SdT = VdP - SdT + (dq - TdS), \quad (4.18)$$

where dq is a change in heat energy. Enthalpy H and a small change in it dH are defined as

$$H = U + PV, \quad (4.19)$$

$$dH = dU + PdV + VdP. \quad (4.20)$$

A small change in the entropy dS is defined by

$$dS \geq dq/T. \quad (4.21)$$

We consider two species, A and B, which can occur both separately or as a single solid solution A_nB_m made up of n A per m B. When this solid solution is made from the two species there is an associated change in both enthalpy ΔH and entropy ΔS which contribute to a total change in the Gibbs free energy ΔG

$$\Delta G = \Delta H - T\Delta S. \quad (4.22)$$

For ΔH it is assumed that only the potential energy of the system changes significantly due to the interactions between atoms A and B having a different associated energy than A - A and B - B interactions. If the combination of A and B is more energetically favourable than A and B separated, ΔH will be negative. If A and B are more favourable as separate compounds, ΔH will be positive. ΔH for forming A_nB_m , $\Delta H(A_nB_m)$, from n A and m B is given by

$$\Delta H(A_nB_m) = H(A_nB_m) - nH(A) - mH(B). \quad (4.23)$$

where $H(A)$ is the enthalpy of A. If, for now, we consider the zero temperature case ($T = 0$ K) we get a change in Gibbs free energy of

$$\Delta G = H(A_nB_m) - nH(A) - mH(B). \quad (4.24)$$

We can relate the enthalpy to the energy calculated for a system using DFT using

$$\begin{aligned} H(A) &= E_{DFT}(A) + E_{corr}(A) \\ &= E(A), \end{aligned} \quad (4.25)$$

where $E_{DFT}(A)$ is the energy of A as calculated in DFT, $E_{corr}(A)$ is any correction to this energy and $E(A)$ is the energy of A at zero Kelvin. We can restate equation 4.24 as

$$\begin{aligned}\Delta G &= E(A_n B_m) - nE(A) - mE(B) \\ &= E_{Form}(A_n B_m),\end{aligned}\tag{4.26}$$

where $E_{Form}(A_n B_m)$ is the formation energy of $A_n B_m$, that is, the energy required to make $A_n B_m$ from A and B at 0 Kelvin. Comparing the formation energy of different composition of A and B, the composition with the lowest formation energy is the most favourable structure, e.g. if $E_{Form}(A_3 B_4) < E_{form}(AB_2)$ then $A_3 B_4$ will form over AB_2 .

In order to see how the most favourable structure changes as the conditions are changed we can reintroduce the $T\Delta S$ term, however, we will do this *via* the introduction of chemical potential μ . We will use the definition of chemical potential at constant internal energy and volume of

$$\mu = -T \left(\frac{\partial S}{\partial N} \right)_{U,V},\tag{4.27}$$

which is dependent on temperature and how entropy changes is the number of particles in the system changes. If the number of particles in a system is varied, which will vary μ , the energy gained from forming a compound from said particles will change, in the case of the above system we have two particles, A and B, thus we have a chemical potential associated with both of these, μ_A and μ_B respectively. These are the variables that we change in order to construct a chemical potential phase diagram which we will label as $\Delta\mu_{A/B}$. Within this work we vary the chemical potentials of O_2 and H_2 gases using the following relation

$$E_i = E_{TMDCO_n H_m} - E_{TMDC} - n(E_O - \Delta\mu_O) - m(E_H - \Delta\mu_H),\tag{4.28}$$

where E_i is the relative energy of phase i for a particular combination of chemical potentials. $E_{TMDCO_nH_m}$ is the energy of a structure with an adsorbed species, E_{TMDC} is the energy of the TMDC structure without the respective adsorbed species, $E_{O/H}$ is half the energy of O_2 and H_2 gases respectively. $\Delta\mu_{O/H}$ are defined as the change in chemical potentials of oxygen and hydrogen gases, referenced to $E_{O/H}$ respectively. n and m denote the stoichiometry of the systems investigated, with n being the number of adsorbed oxygen atoms and m the number of adsorbed hydrogen atoms. We compare the value of E_i for all structures considered and the structure that has the lowest value for E_i at given values of $\Delta\mu_O$ and $\Delta\mu_H$ is the most favourable. This is an adsorption energy that is then shifted by changing the chemical potentials, as such, the adsorption energy, E_{Ad} , is defined as E_i when $\Delta\mu_O = \Delta\mu_H = 0$. The gradient between regions is given by $d(\Delta\mu_H)/d(\Delta\mu_O) = -(n_1 - n_2)/(m_1 - m_2)$, where the subscripts on n and m are for the two different structures that meet at the boundaries of regions. It is of note that due to the shift of these diagrams, all positive values of $\Delta\mu_{O/H}$ are regions in which the formation of O_2/H_2 gases are more favourable than the adsorptions shown.

4.3. Results and Discussions

4.3.1 Heterostructure Geometric and Electronic Structure

To evaluate the suitability of the $MoS_2/PdSe_2$ heterostructure as a photocatalyst, one needs to evaluate the electronic and absorption properties of the heterostructure. The $MoS_2/PdSe_2$ heterostructure shows minimal reconstruction under relaxation with the two constituent layers maintaining their individual geometries, shown in figure 4.2(a). The MoS_2 layer has a tensile strain of 0.42% and the $PdSe_2$ layer has a compressive strain of 1.52%, this strain was minimised by rotating the layers by 30° relative to one another. The interlayer distance is 6.07 Å. Forming the heterostructure from a monolayer of MoS_2 (H-Phase) and $PdSe_2$ (T-phase) is an exothermic process, with a formation energy of $-0.0245 \text{ eV}/\text{Å}^2$.

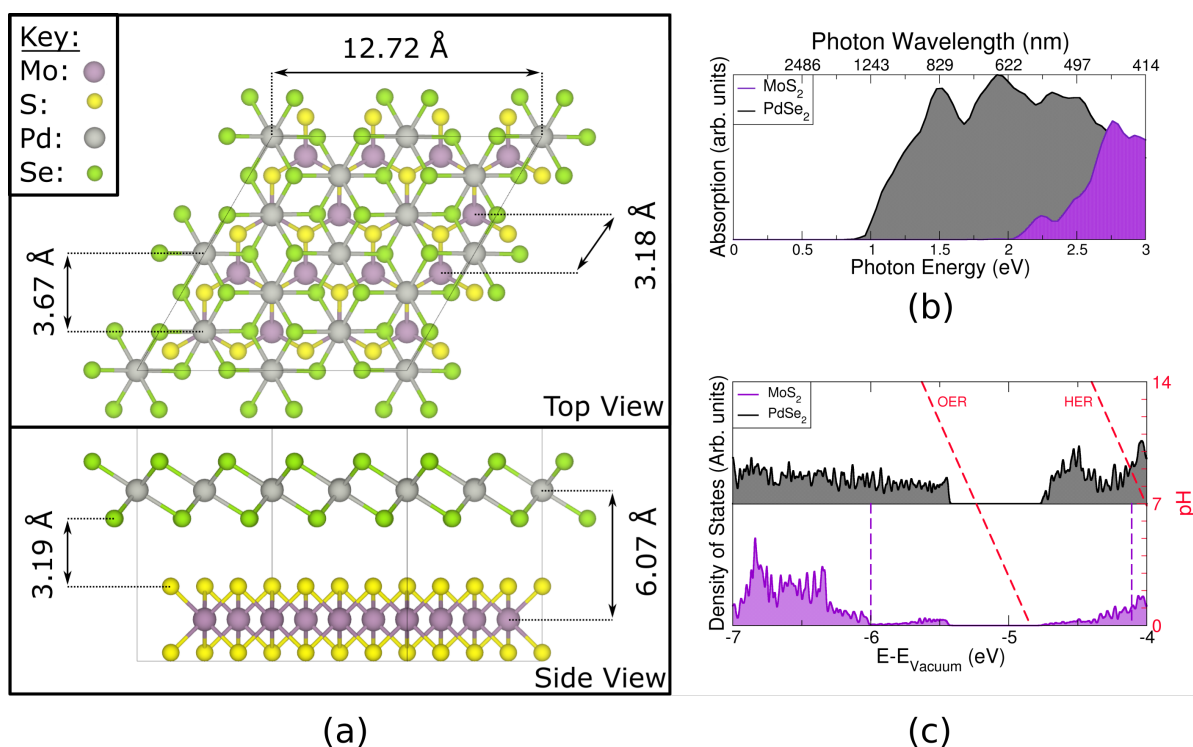


Figure 4.2: (a) a schematic showing the MoS₂/PdSe₂ Heterostructure with the lattice constants and interlayer distances labelled. (b) the absorption spectra for the two monolayers, MoS₂ in purple and PdSe₂ in black. (c) the layer-projected density of states for the Heterostructure calculated with respect to the vacuum, MoS₂ in purple and PdSe₂ in black. The OER and HER are indicated by the red dashed lines and the band gap of MoS₂ is indicated by the dashed purple lines. The zeros for graphs (b) and (c) are where the shaded regions end (at the x-axis for those that touch the bottom of the graph area)

For comparison, forming bulk MoS₂ and PdSe₂ from their respective monolayers is also exothermic, with corresponding formation energies of $-0.014 \text{ eV}/\text{\AA}^2$ and $-0.025 \text{ eV}/\text{\AA}^2$. This indicates that the heterostructure is likely to be stable when formed from these constituents. As these structures show minimal interlayer interaction, both electronically and geometrically, one can consider the absorption spectra of the system as being a composition of the two individual spectra, forming a Type I heterojunction. As can be seen from the theoretical absorption spectra shown in figure 4.2(b), the two constituents absorb strongly at the onset of the band gap, with the PdSe₂ layer absorbing strongly in the 1-2 eV region. This is supported by the layer-projected density of states (layer-PDOS) presented in figure 4.2(c), this decoupling between the monolayers is typical of TMDC heterostructures [111]. These density of state graphs are referenced to the vacuum energy by calculating the monolayer's and heterostructure's electron

affinities which is the energy for an electron to go from the bottom of the conduction band to being free. The dashed purple lines indicate the band gap of the MoS₂ layer. The states that are observed in the gap of the MoS₂ layer correspond to induced gap states occurring due to the decay of PdSe₂ states into the MoS₂ layer. This phenomena is observed in other structures which possess interfaces [176, 192, 193, 194, 195] and is discussed at the end of this chapter in section 4.5. For a pH of 3 and below, the HER aligns with the lowest unoccupied molecular orbital of MoS₂, and for all pH values the OER is higher than the highest occupied molecular orbital of MoS₂. The PdSe₂ layer does not have suitable alignment for the HER but works for the OER at pH of 4 and above. This indicates that the MoS₂ layer can support electron hole pairs with sufficient energy to carry out the water splitting reaction. However, the PdSe₂ layer's band gap is too small for this reaction.

The MoS₂ band gap is larger than the PdSe₂ gap, which creates an electric field that drives electron-hole pairs from the MoS₂ layer to the PdSe₂ layer. However, as the PdSe₂ gap is smaller than the MoS₂, trapping the electron hole pair in the PdSe₂ layer, encouraging recombination in the same layer. This approach to designing a water splitter means one could choose a surface TMDC that has a smaller gap than the bulk substrate and thus engineer the system to trap electron-hole pairs at the surface.

4.3.2 Adsorption sites and stability

In order to determine the appropriate reaction pathway for water splitting for MoS₂ and PdSe₂ several different site adsorptions were considered. Figure 4.3 displays the outcome of this search, showing the most preferential site for the the adsorption of each of the adsorbed species investigated: H, O, HO and HOO, on 2 × 2 supercells of the corresponding TMDCs.

For MoS₂, all the H-sites considered relaxed to the shown adsorption site in figure 4.3(c). It was found that as the concentration of H adsorption was decreased from 1 per 2×2 surface (2.5×10^{14} per cm⁻²) to 1 per 4×4 (6.3×10^{13} cm⁻²),

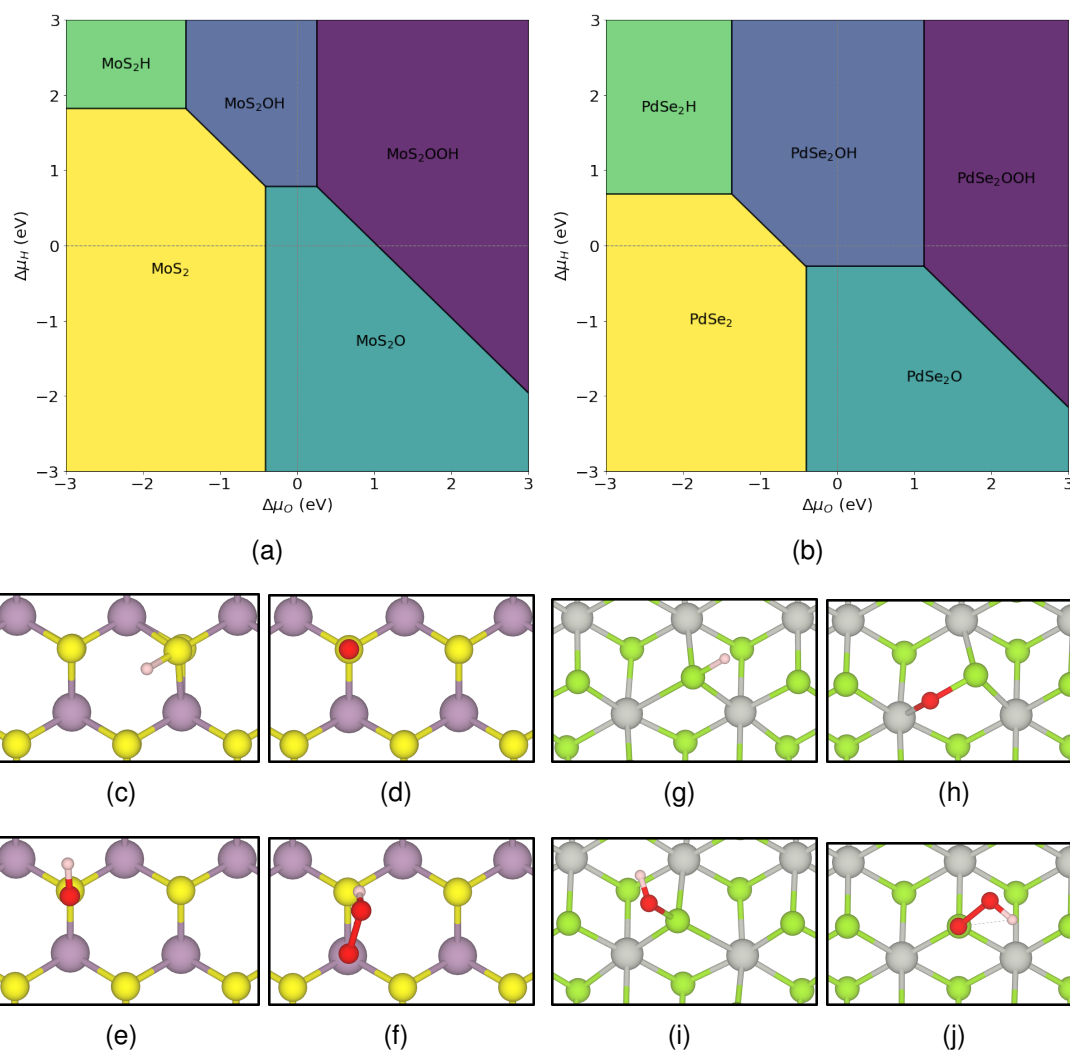


Figure 4.3: The phase diagrams for MoS₂ and PdSe₂ are shown in (a) and (b) respectively. The most thermodynamically favourable adsorption sites on MoS₂ are shown from a top down view in (c - f) for the H, O, OH and OOH adsorptions respectively. The most thermodynamically favourable adsorption sites on PdSe₂ are shown from a top down view in (g - j) for the H, O, HO and HOO adsorptions respectively.

the energy to adsorb H (E_{Ad}) increased by 49 meV, indicating that H prefers to aggregate. The most favourable sites for O and HO was above the sulphur atom and all considered sites relaxed to this configuration. The most favourable site for HOO was the molybdenum site as shown in figure 4.3(f). This means that the adsorption has migrated and it is interesting to note that this migration happened within the relaxation as well, with the HOO starting adsorbed to the S and moving to the Mo. Unlike the H result, it was found that as the concentration of O decreased, E_{Ad} decreased, indicating O prefers to be spread out over the surface instead of aggregating. HO showed the same trend as H, preferring to cluster.

To examine the exact stability of these adsorptions, a phase diagram of the various adsorbed species was constructed, as shown in figure 4.3(a), this shows how these adsorption sites on MoS₂ compare to each other with varying chemical potentials of H₂ and O₂ gases. As one would expect, increasing the chemical potential of the H or O (via either temperature, pressure or concentration) encourages the adsorption of H or O respectively. In standard conditions (corresponding to $\Delta\mu_O = 0$ and $\Delta\mu_H = 0$ in figure 4.3(a)), the oxygen adsorption dominates over the other adsorptions, indicating that under standard conditions oxygen will be preferentially adsorbed to the surface ($E_{Ad} = -0.40$ eV).

For PdSe₂, like MoS₂, the most favourable site for H adsorption was the chalcogen site, i.e the selenium, as shown in Fig. 4.3 (h). Similarly, the HO adsorption on PdSe₂ also preferred the selenium site like in MoS₂. However, unlike in MoS₂, the O adsorption in PdSe₂ forms between the selenium and a palladium. This pathway indicates that O substitution in the selenium site is likely. Finally, the HOO prefers to adsorb on the selenium site rather than the metal site (the opposite of MoS₂). Bader charge analysis [196] of MoS₂ and PdSe₂ monolayers shows that the MoS₂ layer is far more polar (+1.8 and -0.9 |e| for the Mo and S respectively) than the PdSe₂ (+0.3 and -0.15 |e| for the Pd and Se respectively). This effectively means the weak dipole on the OOH is drawn to the metal site in MoS₂ due to coulomb attraction, but substantially less so for PdSe₂. Additionally, in PdSe₂ the selenium site is able to donate charge (due to the high amount of core shielding) and thus the OOH is more likely to be able to form a bond with this site than the corresponding sulphur.

The phase diagram for PdSe₂ shows a similar level of interaction with O, but a significantly higher amount of interaction with H, as shown in figure 4.3(b). This in turn reduces the region where PdSe₂ is stable in isolation. In standard conditions (corresponding to $\Delta\mu_O = 0$ and $\Delta\mu_H = 0$ in figure 4.3(b)), the HO adsorption dominates over the other adsorptions, indicating that under standard conditions HO will be preferentially adsorbed to the surface ($E_{Ad} = -0.68$ eV).

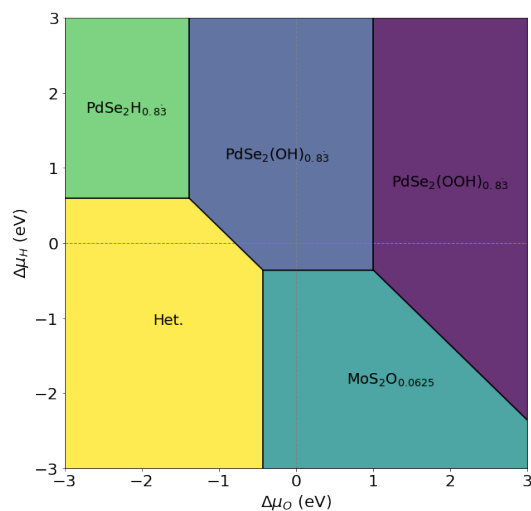


Figure 4.4: The most thermodynamically favourable adsorption sites on the Heterostructure of MoS_2 and PdSe_2 are the same as the monolayers. A phase diagram with regions of stability for the different adsorptions considered in the presence of air. In this phase diagram the prefix of either MoS_2 or PdSe_2 in the legend denotes which surface of the Heterostructure the adsorbed species is on. The O, HO, HOO and H adsorptions on both the MoS_2 and PdSe_2 surfaces have been considered, but those that are unfavourable are absent from the diagram.

For the heterostructure, we used the adsorption sites which were found to be most favourable in the monolayers. These adsorption sites are shown in figure 4.3 (c - j). The phase diagram for the heterostructure shows very similar properties to the phase diagram of PdSe_2 , as is shown in figure 4.4. The exception to this is the O adsorption, which prefers the MoS_2 surface compared to PdSe_2 surface. The reason for this is twofold, firstly, the two energies of absorption on this site (with respect to an O_2 molecule) are $E_{Ad} = -0.43$ eV and $E_{Ad} = -0.33$ eV for the MoS_2 and PdSe_2 surfaces, which are within 0.1 eV of each other. This is within the range of energy differences due to concentration of adsorbants on the surface (see the end of this chapter in section 4.5), indicating that both surfaces are equally likely to adsorb. To fully evaluate the O adsorption region in figure 4.4 requires supercells beyond the current computational limits of this work. In standard conditions ($\Delta\mu_O = \Delta\mu_H = 0$), the PdSe_2 surface dominates, and hence the HO adsorption on the PdSe_2 surface dominates over the other adsorptions ($E_{Ad} = -0.79$ eV). Overall, the adsorption phase diagram for the heterostructure appear very similar to those of the monolayers, in particular the PdSe_2 layer,

indicating that this layer will dominate all the adsorption interactions, particularly in water where the initial steps are the absorption of a H or a OH.

4.3.3 Reaction steps

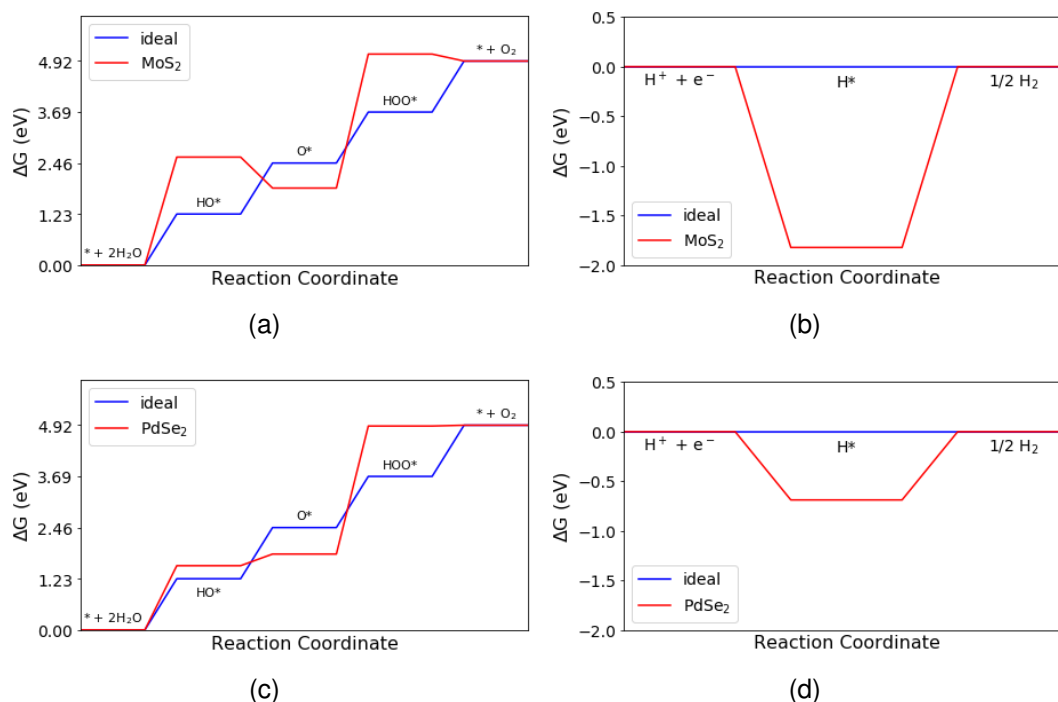


Figure 4.5: The energy diagrams for the potential steps involved in both the OER and HER on MoS₂ and PdSe₂ surfaces at standard conditions (1 atmosphere and 298.15 K). The blue line is the ideal energy and the red is the energy associated with the indicated surface. (a) the energy diagram for the OER on the surface of a pristine MoS₂ monolayer vs the ideal. (b) the energy diagram for the HER on the surface of a pristine MoS₂ monolayer vs the ideal. (c) the energy diagram for the OER on the surface of a pristine PdSe₂ monolayer vs the ideal. (d) the energy diagram for the HER on the surface of a pristine PdSe₂ monolayer vs the ideal.

To effectively evaluate the effect of heterostructuring for water splitting applications, one first needs to understand the reaction pathway on the monolayers as well as the heterostructure. A monolayer of MoS₂ has an electronic band gap of 1.89 eV [112], which is greater than the 1.23 eV an ideal catalyst requires for the four OER steps. In figure 4.5(a) we show the energetic steps for the OER process. The results show that both the HO and HOO adsorption steps require significantly more energy than both the ideal 1.23 eV step height and the direct band gap of MoS₂. The first high barrier of 2.60 eV (over double the energy of ideal 1.23 eV) means that the second step, involving the detaching of the hydrogen (HO to O) is

energetically more favourable, thus happening spontaneously. The comparatively large energetic cost of the first step (2.6 eV) is 0.71 eV greater than the value of the band gap. This will mean that either an external field is applied or that two simultaneous photons are necessary for this reaction step to occur. This is further hindered by the third step of 3.23 eV, which is the rate limiting step and requires an over potential of 2.00 eV. This indicates why MoS₂, in spite of its greater than ideal band gap, is not suitable for the water splitting process.

In comparison to MoS₂, a monolayer of PdSe₂ has better OER energetics as shown in figure 4.5(c). However, we have calculated that the pristine PdSe₂ monolayer has a band gap of 0.77 eV [113], which is less than the required band gap of 1.23 eV meaning an overpotential will be required. The results show that both the HO and HOO adsorption steps need more energy than the ideal case, similar to MoS₂ and that the third reaction step is the rate limiting step. The first reaction step (1.54 eV) and the third reaction step (3.08 eV) require an additional 0.77 eV and 2.31 eV respectively on top of the band gap. The other two steps require less than the band gap of PdSe₂. This indicates that PdSe₂ would be better than MoS₂ for water splitting in terms of energetics as it would require an overpotential of 1.85 V, but due to its lower band gap is not efficient in carrying out the water splitting process.

For the HER process, our results indicate that both monolayer systems will find success, given equation (4.16) (as discussed at the end of this chapter in section 4.5). As can be seen in figures 4.5(d) and 4.5(b), the reaction pathway is lower than the energy of the band gap for either system. However, MoS₂ reaction barrier (± 1.82 eV) is approximately equal to the band gap, meaning that if further energy is required (in the event that $\frac{1}{2}\text{H}_2 \rightleftharpoons \text{H}^+ + \text{e}^-$ is not in balance) then this process will not occur. The PdSe₂ barrier (± 0.69 eV) is much lower, indicating that this reaction pathway would be preferable. In addition, the H₂ production is limited by the production of H⁺ which is controlled by the OER process discussed above, further indicating that PdSe₂ would be better, if it were not for the band gap.

The phase diagrams in figure 4.3(a) (4.3(b)) provide insight into how the reaction process steps in figures 4.5(a) and 4.5(b) (4.5(c) and 4.5(d)) change when the chemical potentials of H and O change. Given that the concentration of H and O are related to the chemical potential, we can comment on how the process changes under differing conditions. For example, in the region where the concentration of O is high, the HOO absorption becomes more likely; this effectively means that this step will become effectively lower in energy.

Both MoS₂ and PdSe₂ would require overpotentials to operate as water splitting devices, but PdSe₂ shows greater promise as the higher of the potential steps involved in both the OER and HER are lower than those in MoS₂. Unfortunately, due to PdSe₂ having a lower band gap than MoS₂, we can expect it to be as unsuitable as MoS₂.

As MoS₂ and PdSe₂ show a more favourable band gap or more favourable energetics respectively, but neither possess both required features, we now discuss the heterostructure. By considering combining the systems, we investigate whether it is possible to design a system using only the favourable properties of each. To fully evaluate this, all reaction pathways including both surfaces of the heterostructure have been considered to see how the energetics change compared to the monolayers.

Our results show that the OER and HER steps for the heterostructures are not significantly modified compared to the monolayers. This is shown in figure 4.6. For adsorptions on the MoS₂ surface, the greatest deviation from the monolayers result is 0.09 eV for OER, which still requires more energy than the band gap of either constituent. Conversely, for PdSe₂ surface, the OER is changed very little, with a maximum deviation of 0.2 eV and the HER has only increased by 0.16 eV, which is still lower than the PdSe₂ band gap. These results show that the surface reaction pathways can be adjusted without need to adjust the underlying material. As such, here the MoS₂ region would present a more suitable bulk and the PdSe₂ layer will be a better reaction surface. As such, a real system could have a significantly thicker MoS₂ region, with a monolayer coating of PdSe₂

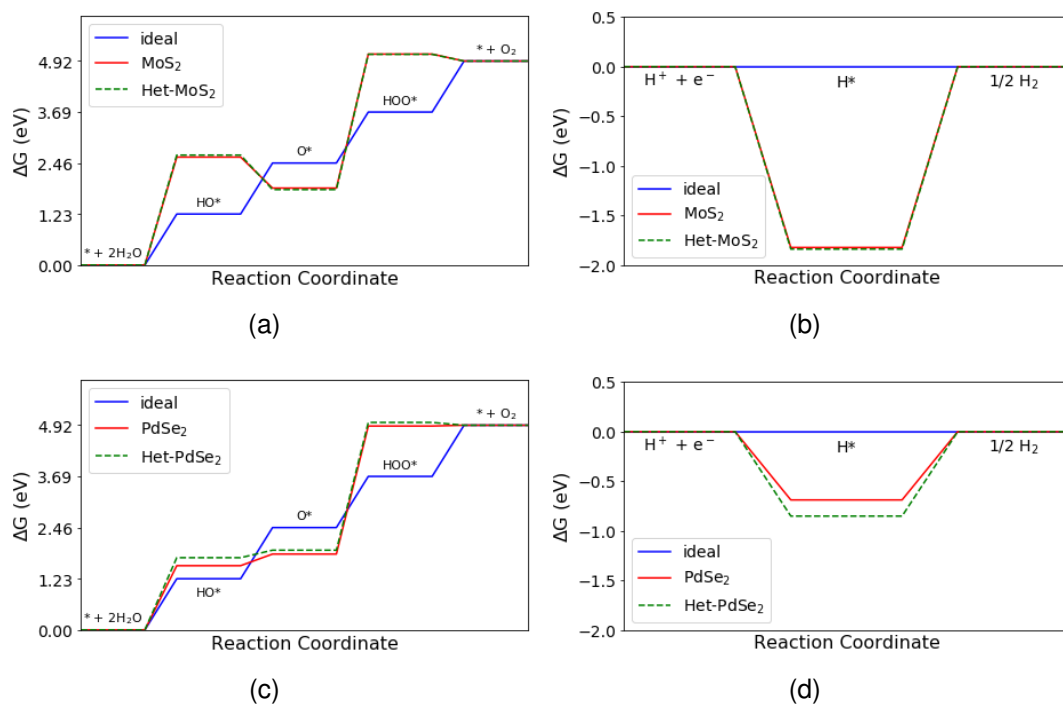


Figure 4.6: The energy diagrams for the potential steps involved in both the OER and HER on MoS₂ and PdSe₂ surfaces of the Heterostructure at standard conditions (1 atmosphere and 298.15 K). The blue line is the ideal energy, the red is the energy associated with the indicated monolayer surface and the green dashed line is the energy associated with the indicated surface of the heterostructure. (a) the energy diagram for the OER on the surface of a MoS₂ surface vs the ideal. (b) the energy diagram for the HER on the surface of a MoS₂ surface vs the ideal. (c) the energy diagram for the OER on the surface of a PdSe₂ surface vs the ideal. (d) the energy diagram for the HER on the surface of a PdSe₂ surface vs the ideal.

which would be the active reaction surface. This combination would allow for bulk adsorption of the photon with appropriate electron-hole pair energies for the reaction process, but with favourable surface energy properties derived from the PdSe₂. Furthermore, the difference in band gap between the bulk MoS₂ region and the PdSe₂ surface layer would create a weak electric field, driving electron-hole pairs to the surface.

4.4. Conclusion and Chapter Summary

The results presented here show that, for MoS₂ and PdSe₂, the water splitting reaction energetics of these TMDC materials are unaffected by the presence of the other in a heterostructure. This indicates that, for van der Waals systems, combinations of materials can be selected to combine materials which can effi-

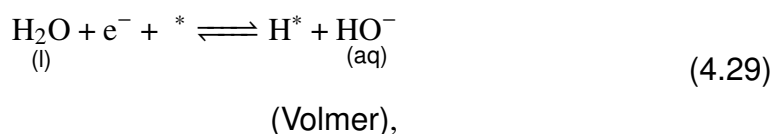
ciently split water, with materials that efficiently absorb. Thus it would be possible to select a lower bandgap TMDC with favourable energetics for the surface, and choose a bulk with good mobility and larger bandgap to enhance the process of water splitting. Further study is required to both confirm whether this occurs under real conditions, and for differing substrates, however it offers an exciting route towards improving water splitting devices.

Our results have shown that the surface of T-phase PdSe₂ requires a smaller overpotential to catalyse the water splitting reaction than the H-phase MoS₂ in all considered cases, whilst the MoS₂ band alignment to the HER and OER is more suitable to water splitting. In both systems, we found that the rate limiting step was the O* to HOO* adsorption step, whereas the H₂ production would occur freely if the overpotential is applied for O₂ production. Our exploration of the heterostructures showed that the surface properties were practically (< 0.2 eV) unchanged when combined. This indicates that using a MoS₂ substrate in conjunction with a PdSe₂ overlayer would be an effective combination. These results indicate that superior water splitting materials could be found through a careful choice of surface and substrate components with complimentary properties, which presents a new avenue of materials research to be explored.

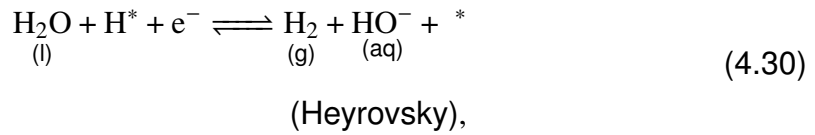
4.5. Supporting Information

4.5.1 Reaction pathways

The HER can be considered in multiple reaction pathways, Volmer Heyrovksy or Volmer Tafel. The first step is called the Volmer reaction[197]



which is then followed by either the Heyrovsky or Tafel reactions[197]



The Heyrovsky reaction occurs when an adsorbed H is isolated from another adsorbed H, whereas the Tafel reaction occurs when two of the adsorbed H are clustered together. In acidic conditions these pathways can be reduced to equation 4.16.

The below tables list all the energies associated with the steps of the OER (table 4.2) and the HER (table 4.3).

For the HER process, three routes were considered: the first two start with the Volmer reaction and then either the Heyrovsky or Tafel, the last is equation (16), which represents the H⁺ rich condition that occurs during the OER process.

In figures 4.5(b) and (d) we show the energetic steps for the HER process with the MoS₂ and PdSe₂ surface respectively, specifically the steps under the H⁺ rich condition. For this process both steps are calculated as the same energy with opposite signs. The energy steps in the H⁺ rich condition are ±1.82 eV for MoS₂ and ±0.69 eV for PdSe₂. For MoS₂, the Volmer, Heyrovsky and Tafel reactions require 4.72 eV, 1.08 eV and -3.64 eV. Similarly, for PdSe₂ the Volmer, Heyrovsky and Tafel reactions require 3.59 eV, 2.21 eV and -1.38 eV. This shows that 2.84 eV and 2.82 eV of additional energy would be required for the Volmer step on top of the bandgaps on MoS₂ and PdSe₂ respectively, effectively making either route involving it far less favourable than the H⁺ rich route.

For the heterostructure, the HER steps show very little change, similar to what is observed for the OER. This indicates that absorption of the photon in the MoS₂ region would be sufficient to carry out the HER process in either the MoS₂ or

PdSe₂ layer. This supports the conclusion presented that MoS₂ will make a suitable substrate with an active PdSe₂ surface layer.

Table 4.2: Summary of the potentials of each step in the OER. Steps 1 through 4 are the reaction in equations (10), (13), (14) and (15) respectively.

TMDC	OER (eV)			
	1	2	3	4
MoS ₂	2.60	-0.75	3.23	-0.17
Het. MoS ₂	2.65	-0.83	3.26	-0.16
PdSe ₂	1.54	0.28	3.08	0.02
Het. PdSe ₂	1.74	0.18	3.07	-0.07

Table 4.3: Summary of the potentials of each step in the HER and the alternate hydrogen reaction. Steps V, H, T and A are the reaction in equations (4.29), (4.30), (4.31) and (16) respectively.

TMDC	HER (eV)			
	V	H	T	A
MoS ₂	4.72	1.08	-3.64	1.82
Het. MoS ₂	4.74	1.06	-3.68	1.84
PdSe ₂	3.59	2.21	-1.38	0.69
Het. PdSe ₂	3.75	2.05	-1.70	0.85

4.5.2 Adsorbant concentration effects

To model the absorption of O, H, OH and OOH on the various systems we have used a supercell approach. Table 4.4 below shows the energies of the various concentrations modelled without the ZPE and TS⁰ corrections (which can be accounted for using the values given in table 4.1).

Table 4.4: Summary of the absorption energies (in eV) for various concentrations of H and O absorbed to the MoS₂ monolayer surface, not including the ZPE and TS⁰ corrections.

Supercell	H	MoS ₂		
		O	OH	OOH
2 × 2	1.50	-0.66	-0.26	-0.29
3 × 3	1.55	-0.68	-0.19	-
4 × 4	1.55	-0.68	-0.19	-

The heterostructure consists of a single layer of MoS₂ (4 × 4 supercell) with a rotated single layer of PdSe₂ (4 × 3 supercell) as shown in figure 4.2. The adsorption energies for the heterostructure are shown in table 4.6 without the ZPE and TS⁰ corrections applied.

Table 4.5: Summary of the absorption energies (in eV) for various concentrations of H and O absorbed to the PdSe₂ monolayer surface, not including the ZPE and TS⁰ corrections.

Supercell	PdSe ₂			
	H	O	OH	OOH
2 × 2	0.37	-0.69	-1.32	-0.48
4 × 3	0.57	-0.62	-	-

Table 4.6: Summary of the absorption energies (in eV) for various concentrations of H and O absorbed to the heterostructure on either the MoS₂ and PdSe₂ surface, not including the ZPE and TS⁰ corrections.

Layer of absorption	Heterostructure			
	H	O	OH	OOH
MoS ₂	1.52	-0.70	-0.21	-0.30
PdSe ₂	0.53	-0.60	-1.13	-0.40

4.5.3 Band Alignment

The layer projected density of states plots seen in figure 4.2(c) are obtained by combining the projected density of states for every ion within each TMDC layer. For the calculation of a projected density of states for an ion, one has to set the limit of volumetric integration around each atom, which is normally parameterised from the bulk interatomic spacing [161, 162, 45, 46]. This is problematic when dealing with interfaces as the charge density does not abruptly stop, and can be considered to have an exponential decay with distance. This means that one will always observe some leakage states (akin to metal induced gap states) regardless of whether these states originate within the layer. These states can be observed in figure 4.7 and in the MoS₂ results in figure 4.2(c). We identify the MoS₂ band gap with thick purple lines. From this alignment, it is clear these states are indeed leakage from the PdSe₂, not only as the band gap of MoS₂ is much larger than that of PdSe₂ (1.89 eV and 0.77 eV respectively), but also as the valence band states have negligible contribution from the MoS₂ atoms. Considering that these states from PdSe₂ are incorrectly attributed to MoS₂, it is then clear that the semiconductor heterojunction formed by the pair is of Type-I band alignment.

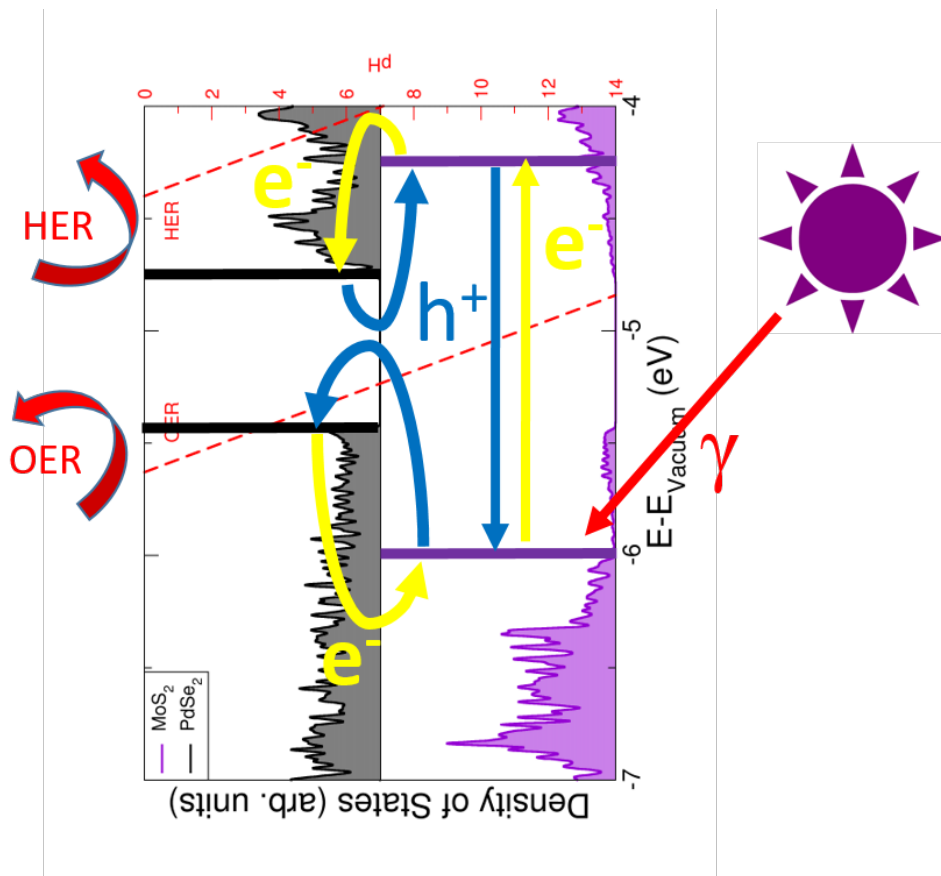


Figure 4.7: The layer-projected density of states for the Heterostructure calculated with respect to the vacuum, MoS₂ in purple and PdSe₂ in black. The OER and HER are indicated by the red dashed lines. The band edge positions of MoS₂ are indicated by the purple lines and the band edge positions of PdSe₂ are indicated by the black lines. Also indicated are the directions the electrons and holes will be driven in these structures.

Chapter 5

First Principles Study of Layered Scandium Disulfide for use as Li-Ion and Beyond-Li-Ion Batteries

"There is a great satisfaction in building good tools for other people to use."

– Freeman Dyson

In this chapter, scandium disulfide is investigated for use as a Li-ion and beyond Li-ion battery cathode, where beyond Li-ion refers to using sodium, potassium and magnesium instead of lithium. Many different properties of this material are investigated from their voltages, volumetric expansion as well as a method for determining the maximum capacity through the use of phase diagrams, this is at the end of this chapter along with convex hulls for Sc-S and Sc-O compounds. We begin with an introduction to this area of research followed by the methods used within this chapter.

5.1. Introduction

As the demand for rechargeable batteries rises, the need for both better and a wider range of cathode materials rises with it. Whereas for anodes there are a wealth of materials available and the key challenge is competing with the abundance of hard carbons, for cathodes the range of materials is much lower with leading contenders being the phosphates [198, 199, 200], the ubiquitous NMC and its variants [201, 76, 202, 203, 204, 205], and spinel oxides such as LiMn_2O_4 [206, 207, 208, 209].

There has been some interest in the use of other intercalant species [210] due to the safety issues associated with lithium, its high cost of production, and the rising concern for the sustainability of lithium deposits. Other Group I elements [211, 212, 213] offer the same chemistry as lithium and so there is hope they would be able to match the performance of lithium. Alternatively, Group II elements have also been considered [214, 215, 216] as they possess two valence electrons and so the available charge transfer (and hence electrode energy storage) should in principle be twice that of the Group I elements.

For intercalation electrodes, layered materials such as the TMDCs [217, 218, 219], NMC [220, 76], and the MXenes [221] are highly attractive as their van der Waals gaps allow for low diffusion barriers and hence fast intercalant transport. Recent works have started to note the potential of scandium, where the doping of metal oxides with scandium has been shown to increase particle size without affecting the crystal structure [222], provide a comparable capacity whilst improve cycling stability [222, 223], and significantly lower the surface energy of nanoparticles [224]. With these clear structural and energetic improvements, as well as the fact that scandium is one of the lightest available metals, it raises the question as to how good scandium-based materials themselves would perform as electrode materials.

Transition metal oxides have been widely investigated and used for intercalation cathodes as they display high voltages and capacities. Lithium scandium dioxide (LiScO_2) has been experimentally verified to exist in only one form, a fractional cationic ordered rock-salt structure, with the $I4_1/amd$ space group [225, 226]. This is similar to the anatase structure of TiO_2 but with lithium filling the voids. However, this material was found to have poor ionic conductivity, requiring substitutional doping with transition metals in place of the scandium atoms [226]. This lack of ionic conductivity prevents its exploitation as a cathode material. Alternative, layered structures have therefore been considered [227, 228], but are unfeasible as the structure is energetically unfavourable compared to the rock-salt phase.

Layered sulfides are closely related to the oxides, and have the added benefit of being compatible with sulfide-electrolytes. Sulfide electrolytes are chemically unstable with high-voltage oxides due to the difference in electronegativity of oxygen and sulfur [229]. Thus, scandium-sulfide materials could offer the optimal properties for cathodes whilst allowing the use of sulfide-electrolytes. The bulk properties of the TMDC T- and H-phases of ScS_2 have been shown to be conducting [230], however, the monolayer form of the H-phase is insulating [231, 230, 232]. For intercalation electrodes, the intercalated form of ScS_2 is of interest. LiScS_2 , NaScS_2 , and KScS_2 have all been synthesised [233, 234], and were found to have the layered $\alpha\text{-NaFeO}_2$ structure with space group $R\bar{3}M$. Unfortunately, theoretical investigations of this structure have been limited to monolayers [235, 236], though these have suggested high capacities of over 400 mAhg^{-1} with lithium intercalation. However, monolayers are significantly more difficult to synthesise compared to their bulk counterpart, and do not provide an accurate representation of the dimensions of electrodes being utilised in functional devices. To the best of our knowledge there are currently no studies investigating the potential of bulk ScS_2 for electrodes, and so the questions of how well the bulk material would perform as an intercalation electrode remains.

In this chapter we explore the potential of intercalated ScS_2 compounds as a cathode material for lithium, sodium, potassium, and magnesium batteries using a range of theoretical techniques built upon first principles calculations. We explore the phase space of these materials to determine the lowest energy structures, determine the relevant properties for cathode performance, and evaluate their dynamic and thermodynamic stabilities to obtain a reversible intercalation capacity. Finally, we consider how the substitution of other metallic species in place of scandium affects these key properties for electrode applications.

5.2. Methods

5.2.1 Density Function Theory Parameters

In this chapter, first principles techniques based on density functional theory were used to determine structural and energetic properties of layered scandium disulfide (ScS_2) intercalated with varying levels of lithium, sodium, potassium, and magnesium. These calculations were done using the Vienna Ab initio Simulation Package (VASP) [161, 162, 45, 46]. The valence electrons included for each species were Sc $3d^24s^1$, S $3s^23p^4$, Li $1s^22s^1$, Na $2p^63s^1$, K $3p^64s^1$, and Mg $2p^63s^2$. All other electrons were effectively contained within the used pseudopotentials. The projector augmented wave method [159] was used to describe the interaction between core and valence electrons, and a plane-wave basis set was used with an energy cutoff of 700 eV, this is lower than what was used in the previous chapter as the structures investigated here do not have large vacuum gaps, thus a lower energy cutoff was found to be sufficient. Van der Waals interactions have been addressed using the zero damping DFT-D3 method of Grimme [53].

Three different phases of the ScS_2 structure were considered: the T-phase, the Hc-phase [237, 238], and the α - NaFeO_2 -like [233, 234] structure which is here referred to as the α -phase. The T- and α -phases have the same in-plane structure but differ in the relative stacking of layers, leading to the α -structure containing three ScS_2 layers in the primitive unit cell, compared to the one in the primitive unit cell of T- ScS_2 . The Hc-phase has a different layer structure, and possesses two layers of ScS_2 in its primitive unit cell. To consider intercalation with the different species, supercells of $(2 \times 2 \times 2)$, $(2 \times 2 \times 1)$, and $(2 \times 2 \times 1)$ were used for the T-, Hc-, and α -phases, respectively. These supercells provided eight different intercalation sites for the T- and Hc- phases, and twelve sites for the α -phase which allow for various filling configurations. Whilst other phases are possible for the TMDCs, such as 3R and distorted T structures, their intercalation environments are similar to that of the T-, Hc-phase, or α -phases, and so have not been explicitly considered here. It was found through two different methods

that the favoured intercalation site in all three phases of ScS_2 is the octahedrally-coordinated site. Consequently, this site has been used in the following study.

All structural relaxations were completed using the Perdew-Burke-Ernzerhof (PBE) [163] functional form of the generalised gradient approximation (GGA), using the conjugate gradient algorithm and converged to a force tolerance of $0.01 \text{ eV}/\text{\AA}$ per atom, while electronic self-consistency is considered to an accuracy of $1 \times 10^{-7} \text{ eV}$. Of these, only the most energetically favourable structures at each level of lithium intercalation were considered. To account for the inaccurate calculation of exchange in GGA functionals, the HSE06 hybrid functional [48, 49, 239] was also used for a selection of systems. Γ -centred Monkhorst-Pack grids [165] of k-points equivalent to a $6 \times 6 \times 6$ grid in the supercells are used throughout.

Phonon band structures were obtained using the frozen-phonon method employed with Phonopy [240]. This is a method of calculating a force constant matrix that can be used to get the phonon modes of a system. For these, the primitive unit cells of the pristine and intercalated structures were geometrically relaxed to a force tolerance of $0.0001 \text{ eV}/\text{\AA}$ per atom, and electronic convergence of $1 \times 10^{-8} \text{ eV}$. From these, the unique displacements were generated in supercells of $6 \times 6 \times 1$. This involved offsetting an atom in this supercell from its relaxed position, calculating the new forces on all atoms due to this displacement, and repeating this for all possible single atom displacements. Elastic properties were determined using these primitive cell for the pristine and intercalated T-phase ScS_2 . The elastic and internal strain tensors were computed from the second order derivatives of the total energy with respect to the position of the ions and changes to the size and shape of the unit cell, as employed in VASP. From the elastic tensor, various elastic moduli were computed.

One possible method commonly used to modify the properties of electrodes is through the introduction of other elements, in particular substitution with transition metals [241, 242, 243] or lithium [209]. We consider the substitution of these metals in place of the scandium, which can be achieved through additional precursor materials. For low quantities of alternative metals this results in a sub-

stitutional doping [201], and for higher concentrations this results in metal mixing akin to how cobalt in lithium cobalt oxide is replaced with nickel and manganese in NMC. Seeing the effects of doping and metal mixing in other materials, it offers the natural question as to whether it can be employed to enhance the properties of ScS_2 . Here, we consider the metals Co, Cr, Fe, Hf, Mn, Nb, Ni, Sn, Ta, Ti, V, and Zr for this substitution, which were chosen to ensure a sufficient spread of species from across the transition metal block. We have also considered lithium as substitutions could occur during synthesis or cycling.

Due to the number of possible concentrations (and the configurations of each of those concentrations) available for metal mixing in the α -phase, we have limited this part of our study to the T-phase. Different concentrations of substitutions were considered, with all unique configurations being considered for each concentration of mixed metals. For $\text{Sc}_{1-x}\text{M}_x\text{S}_2$, concentrations of $\frac{0}{8} \leq x \leq \frac{8}{8}$ in increments of $\frac{1}{8}$ were considered, with $x = \frac{0}{8} = 0$ corresponding to the ScS_2 composition and $x = \frac{8}{8} = 1$ corresponding to the MS_2 composition. The configurations of mixing used are equivalent to the different configurations used for lithium intercalation, with the same indexing being used for the metal species instead of the intercalated lithium. Once the $\text{Sc}_{1-x}\text{M}_x\text{S}_2$ compound is synthesised, the metal species M becomes ‘locked’ in the host structure due to bonding with the sulfur atoms. It is thus more difficult for the metal species to reconfigure into a lower energy configuration than it would be for intercalated species such as lithium. As such, we consider a random configuration of metal mixing by taking the average of the different configurations considered.

5.2.2 Methods for Material Evaluation

To compare ScS_2 intercalated with different amounts of a metal ($\text{M} = \text{Li}, \text{Na}, \text{K}, \text{Mg}$), the voltage, V , can be calculated using [244, 245],

$$\begin{aligned}
V &= -\frac{\Delta G}{\Delta Q} \\
&\approx -\frac{\Delta E}{\Delta Q} \\
&= -\frac{E_{M_{x_2}ScS_2} - \left[E_{M_{x_1}ScS_2} + (x_2 - x_1)E_{Li} \right]}{(x_2 - x_1) \times ze},
\end{aligned} \tag{5.1}$$

with change in Gibbs free energy, ΔG , total metal content $x_2 > x_1$, $E_{M_aScS_2}$ is the energy of the supercell bulk ScS_2 structure with a metal atoms per ScS_2 formula unit, and E_M is the energy of the corresponding metal atom as found in its bulk form [246]. z is the valency of the intercalant, and so $z = 1$ for Group I metals and $z = 2$ for Group II metals.

In some situations, however, taking the difference between two equivalent structures of different lithium contents does not always give the most accurate representation of what happens in reality. For example, intercalants have been found to cluster into domains for some materials rather than distributing evenly throughout the host [247, 248]. In these cases, it is more accurate to consider combinations of different lithium concentrations; for example, it might be favourable for lithium to fill one cell to $LiScS_2$ and leave an adjacent cell empty, rather than filling a single cell to $Li_{0.5}ScS_2$. This would be indicative of clustering/domain separation, and so has been considered in the voltage calculation.

For the following discussion, we will use lithium (Li) as the stand-in for Group I intercalants, and magnesium (Mg) for Group II intercalants. The stability of TMDCs for lithium intercalation depends heavily on the formation of Li_2S . Generally, when this compound forms the reaction becomes difficult to reverse due to the loss of the layered structure and the required separation of the lithium and sulfur. By assessing the relative stability of the Li_2S phase against the intercalated structure, one can construct phase diagrams [249] to indicate the thermodynamic stability of the intercalated structure at different intercalant concentrations. In terms of the chemical potential, we express this limit as,

$$\Delta\mu_{Li} \leq \frac{1}{4-a} \{2\Delta H(Li_2S) - \Delta H(Li_aScS_2) + \Delta\mu_{Sc}\}, \quad (5.2)$$

where $\Delta H(A)$ gives the enthalpy of formation of the compound A with respect to the bulk constituents, and $\Delta\mu_B$ is given by $\Delta\mu_B = \mu_B - \mu_B^0$, with μ_B being the chemical potential of species B in Li_aScS_2 , with B = Li, Sc, S. Due to the different valency between the alkali and alkaline earth metals we consider MgS as a different conversion product for the intercalation of the Group II metals. The equivalent limit is then given as,

$$\Delta\mu_{Mg} \leq \frac{1}{2-a} \{2\Delta H(MgS) - \Delta H(Mg_aScS_2) + \Delta\mu_{Sc}\}. \quad (5.3)$$

Further limits can be considered on the chemical potential, which are expressed as,

$$\Delta\mu_{Li,Mg,Sc,S} \leq 0, \quad (5.4)$$

indicating that the system has not formed the elemental bulks, and

$$\frac{1}{a} \{\Delta H(Li_aScS_2) - \Delta H(ScS_2)\} \leq \Delta\mu_{Li}, \quad (5.5)$$

which indicates that the intercalated TMDC will not spontaneously deintercalate. The origins of these limits are given in the at the end of this chapter in section 5.5.1.

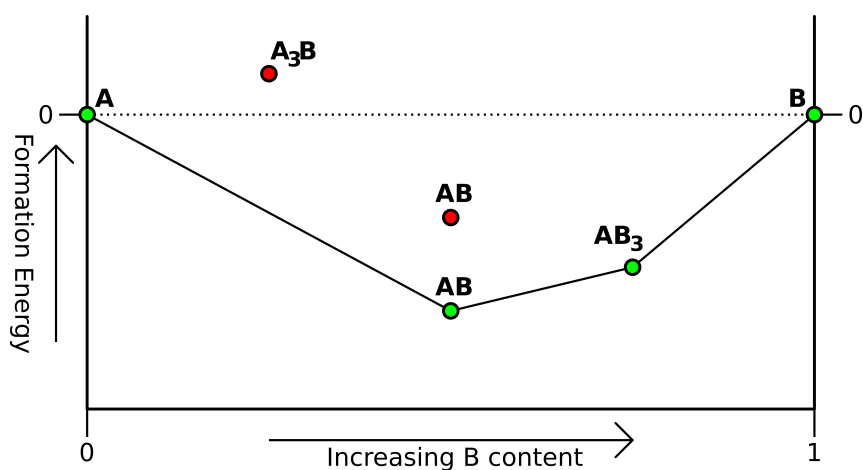


Figure 5.1: A schematic of a convex hull with two species, A and B. The green circles are stable compounds and the red circles are meta stable or unstable compounds.

5.2.3 Convex Hulls

Convex hulls are used, in a similar manner to phase diagrams, to show the most favourable structure for a given set of species under different conditions. In this case, the condition that is varied is the concentration of the different species involved.

In order to construct a phase diagram for two species, A and B, the formation energies of every structure considered is calculated with respect to A and B. These formation energies are then plotted on a set of axes with the formation energy on the y-axis and the ratio of A to B on the x-axis such that A lies at $x = 0$ and B lies at $x = 1$. Lines join together the Structures of the lowest energy with A and B, such that all the considered structures either lie on the hull (are part of the line connected to A and B) or above it. Points that lie on this line are said to be stable while any structure above it are either meta-stable or unstable. Figure 5.1 shows a schematic example of a two species convex hull.

Within this chapter, only two species convex hulls are considered but in later chapters these are expanded to three species convex hulls. In order to represent this, three species convex hulls take the form of a triangular diagram where each of the edges is a two species convex hull viewed from above. In order to show the formation energies of the compounds a colour scale can be used and different symbols can be used to show stable and unstable compounds.

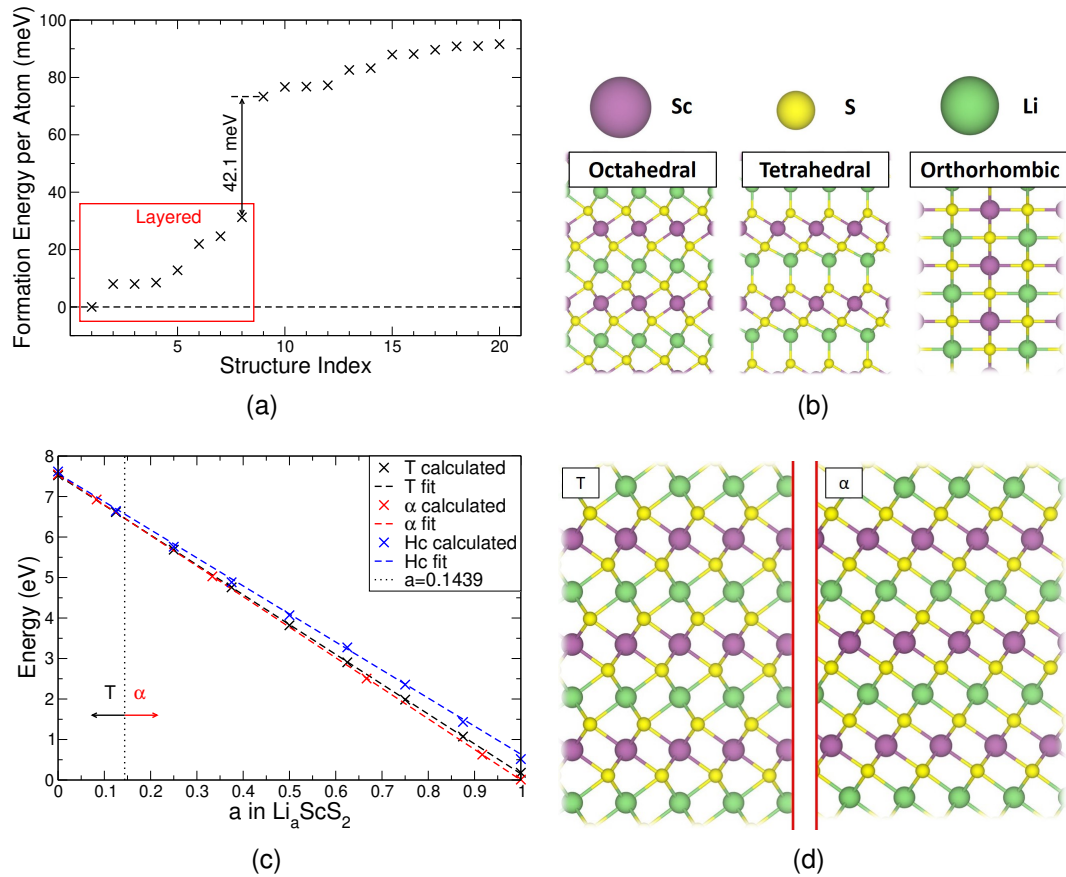


Figure 5.2: 5.2(a) presents the calculated formation energies per atom for the 20 lowest-energy structures of LiScS_2 found using the RAFFLE structural prediction algorithm. The results have been shifted such that the lowest-energy structure has a formation energy of 0 eV/atom. The typical structures obtained from this search are presented 5.2(b), with the layered structures having octahedral or tetrahedral coordination, and the non-layered structure being orthorhombic. 5.2(c) shows the relative energy per formula unit for T-, α - and Hc-phases of Li_aScS_2 , for a range of concentrations a . Linear fits have been presented in each to identify the crossing points. 5.2(d) shows the relation between the T- and α -phases of LiScS_2 .

5.3. Results

5.3.1 Determination of Structure

We explore the phase space of LiScS_2 using our random structure search RAFFLE. Of the over 800 structures generated and structurally relaxed, the 20 lowest-energy systems are presented in 5.2(a). Of these, the eight lowest-energy systems are all T-phase structures with hexagonal symmetry, with the differences in energy arising from different coordination of the lithium with the ScS_2 layers, relative shifts of the ScS_2 layers, and small structural fluctuations arising from the tolerances of the search. These are indicated in 5.2(b), where the structures with

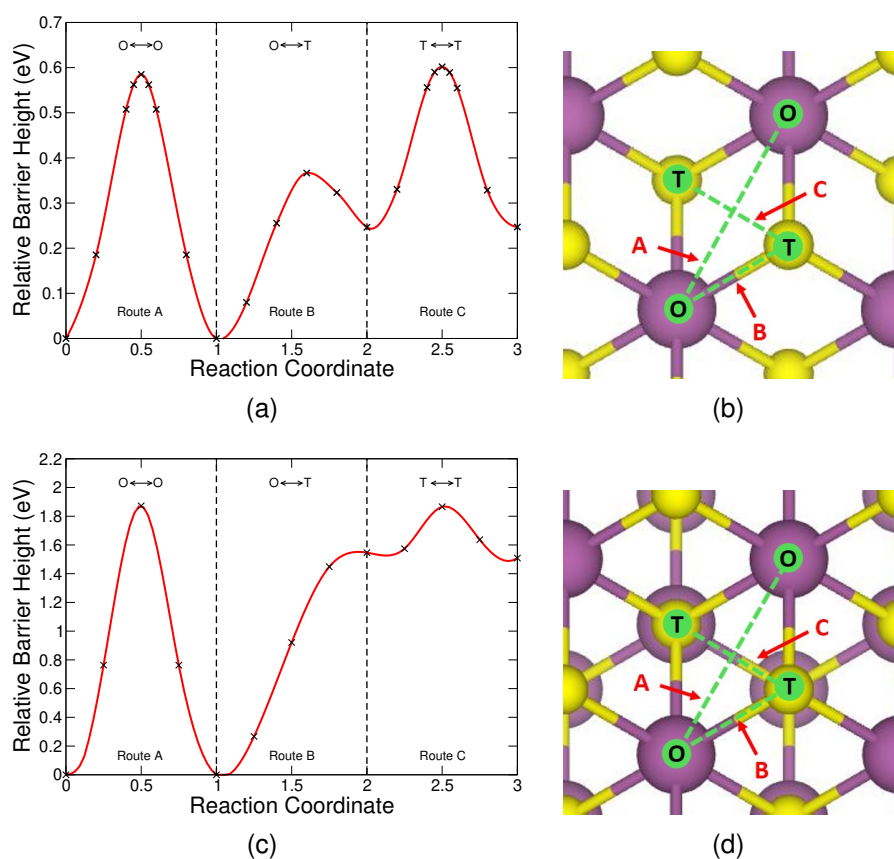


Figure 5.3: Nudged elastic band results used to determine site of intercalation. 5.3(a) shows the results for T-ScS₂ along the routes presented in 5.3(b). Similarly, 5.3(c) shows the results for α -ScS₂ along the routes presented in 5.3(d). The intercalation sites these routes are between, the octahedrally coordinated (O) and tetrahedrally coordinated (T), are also indicated.

octahedrally-coordinated lithium are lower in energy [246, 250, 248, 219] than the equivalent systems with tetrahedrally-coordinated lithium due to the higher coordination between lithium and sulfur. There is then a large jump of 42.1 meV per atom to the next group of structures, which have orthorhombic unit cells. As this energy exceeds typical values associated with thermal energy, it is safe to conclude that the layered structure will preferentially form.

As the structure search shows that layered structures are the most favourable, we explicitly investigate them further. As with all partially heuristic methods of structure searching, the result is never guaranteed to be the true ground state. So, to ensure that we do not limit our investigation to the results of the random structure search, further layered polymorphs of intercalated ScS₂ were also considered. Specifically, we focused on the TMDC 1T-phase (following the results of the random structure search), the TMDC 2Hc-phase, and the α -ScS₂ phase

(following experimental evidence [233, 234]). The results of this are presented in 5.2(c), where we show the energies (per formula unit) of each of the considered phases of Li_aScS_2 . This allows for easy comparison of the different phases and indicates which phases are energetically preferred for different intercalation concentrations. For visual aid we have included a linear fit, which allows us to determine that the T-phase is the lowest in energy for low intercalant concentrations ($a < 0.15$ in Li_aScS_2), whereas for higher concentrations the α -phase is preferred. These two structures are presented in 5.2(d), where the relative shift of the ScS_2 layers can be seen. A similar result was found for other intercalant species.

To further ensure we have not missed the preferred intercalation site we have also carried out nudged elastic band (NEB) calculations with a lithium intercalant. This involved moving a lithium ion along different possible diffusion pathways, allowing it to relax its position perpendicular to this pathway, in order to find an energetic minima. The results of this are shown in 5.3, where we have considered diffusion between two equivalent octahedral sites (Route A), between adjacent octahedral and tetrahedral sites (Route B) and between two equivalent tetrahedral sites (Route C), and are shown in 5.3(b) for the T-phase and 5.3(d) for the α -phase. These results show that the most favourable intercalation site for each of the phases is the octahedral-coordination (O) site, which is the site of intercalation used throughout this work. This is in agreement with other TMDC investigations [246, 250, 248, 219], as well as the results of the structure search.

These NEB results also allow us to comment on the diffusion properties of intercalants in ScS_2 . As the rate of diffusion follows an Arrhenius equation, the height of the activation barriers is a key parameter for characterizing electrode materials. For both T- and α -phases we see that, whilst Route A offers the most direct path between two octahedral sites, diffusion along Route B has a lower activation energy. Route A in the T-phase demonstrates a barrier height of 0.58 eV, and 0.37 eV (0.12 eV) along Route B. These compare very well with the 0.67 eV and 0.34 eV seen for lithium diffusion along monolayer T- ScS_2 [236]. We see the same for the α -phase ScS_2 , though we do note significantly larger barriers of

1.87 eV along Route A and 1.55 eV (0.01 eV) along Route B. These larger barriers are partially caused by the particular methods used for generating these NEB barriers. However a more significant cause is due to the relative layer shift seen for the α -phase compared to the T-phase resulting in an ‘interlocking’ of layers, and hence a sulfur of one layer protrudes into the void space of the next. Thus we see a larger barrier to ionic movement.

We are also interested in the structure of ScS_2 when the intercalants are removed, and so we have investigated a range of Sc-S stoichiometries to determine the stability of ScS_2 . As the data available within literature and on databases such as the ICSD and Materials Project [251] for scandium-sulfide compounds is fairly limited, we have also used the structures of scandium-oxide analogues. The results of this are presented at the end of this chapter in section 5.5.2. For the composition ScS_2 , the layered T-structure is found to be the lowest in energy, though it lies 0.37 eV above the convex hull, and a mixture of Sc_2S_3 and S would be preferred.

5.3.2 Properties of ScS_2 Cathodes

5.3.2.1 Voltages.

ScS_2 has several properties which are attractive as a cathode. In 5.4 we present the voltage, phase stability and volume expansion of ScS_2 for Li, Na, K, and Mg intercalant ions. The voltage profiles of α - ScS_2 intercalated with the considered intercalants are presented in 5.4(a). For ScS_2 intercalated with Group I metals, our calculations show that the voltages at low levels of intercalation reach above 4.5 V. As the concentration of the intercalant increases, the decrease in voltage across the range explored is less than 1.5 V, but remains above 3 V. The α -phase shows for Li, Na and K no change in the voltage for concentrations of $a > 0.4$. Increasing the atomic number of the Group I intercalant results in a small decrease in the average intercalation voltage. Whilst for Li intercalation the average voltage is 3.977 V, this drops to 3.874 V for Na, and to 3.799 V for K. This drop in voltage is due to the reduced charge transfer from the intercalated species

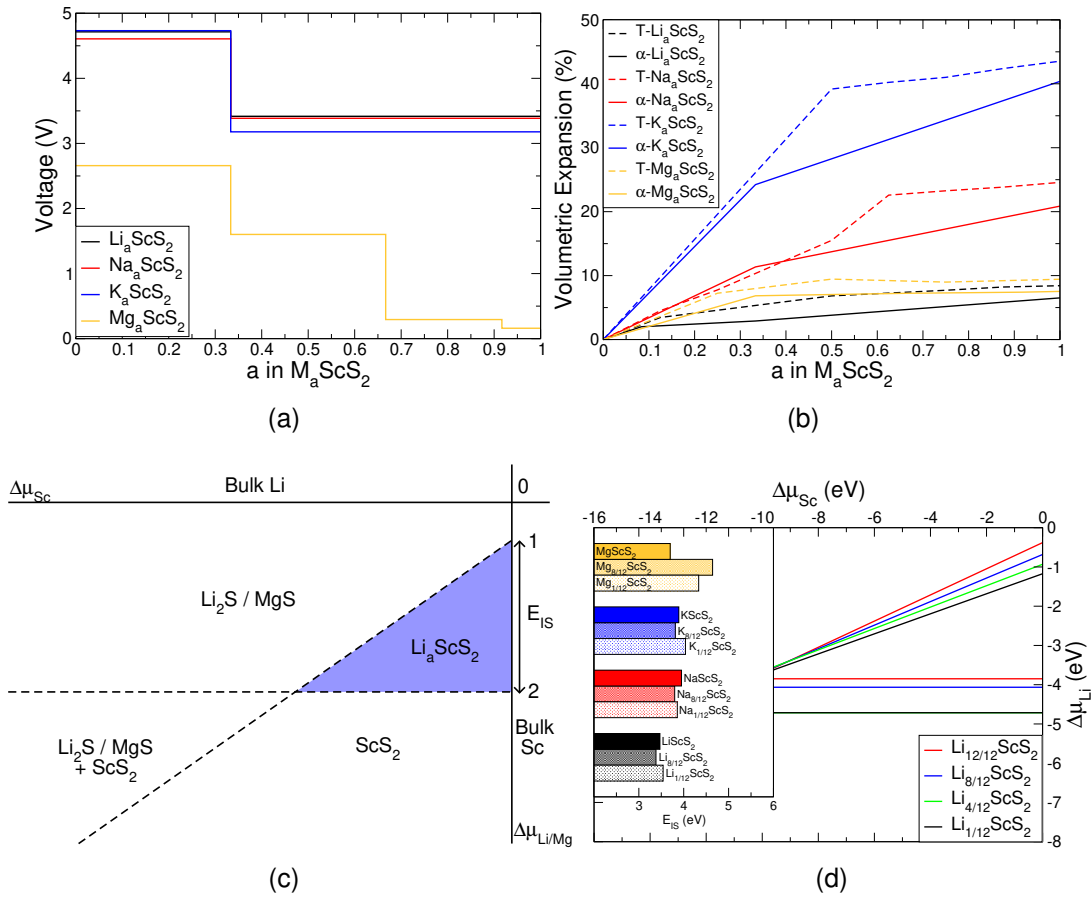


Figure 5.4: 5.4(a) presents the voltage profiles for $\alpha\text{-ScS}_2$ intercalated with Li, Na, K, and Mg. 5.4(b) shows the percentage volume change ($\% = 100 \times \frac{V - V_0}{V_0}$) of T- ScS_2 and $\alpha\text{-ScS}_2$ caused by intercalation. 5.4(c) shows a schematic phase diagram, described by equations 5.2-5.5. 5.4(d) shows the resultant phase diagram for $\alpha\text{-ScS}_2$ intercalated with different concentrations of Li, and the inset presents the values of E_{IS} for $\alpha\text{-ScS}_2$ intercalated with each of the considered intercalants.

to the host material, which was found through the use of Bader analysis, where the lithium charge is 0.88 |e|, the sodium charge is 0.85 |e|, and the potassium charge is 0.80 |e|. These show that there is much less variation in the voltage compared to that for the α -phase for each of the intercalated species. We also see that the voltage obtained from T- ScS_2 is about 0.3 V lower than that obtained from the equivalent $\alpha\text{-ScS}_2$ structure. As the structures of the individual ScS_2 layers are the same in each of these phases, the increase in output voltage must be due to the change in bonding environment arising from the relative shift in the ScS_2 layers. However, for Li, Na and K, irrespective of phase the voltages remain above 3 V for all concentrations considered.

For magnesium intercalation the voltage behaviour is different from that of the Group I elements. The average voltage is 1.474 V for α -ScS₂, but changes considerably by 2.5 V across the range. This is due to the double valency of magnesium allowing for two changes in oxidation state of the host material. This behaviour is also present in the T- and Hc-phases. All phases, when fully intercalated ($a = 1$), decrease to voltages below 0.6 V.

It is important to make a careful choice of exchange-correlation functional in first-principles calculations, as it can lead to discrepancies in the electronic structure [252, 253, 254] and material energetics [255, 256, 257]. We compare our PBE results with those obtained from the HSE06 functional for a limited number of cases to determine the sensitivity of the results to functional choice. Using the hybrid functional we obtain higher voltages of 4.440 V (Li), 4.420 V (Na), 3.953 V (K), and 1.719 V (Mg). These are higher than the PBE voltages by 0.463 V, 0.546 V, 0.154 V, and 0.245 V, respectively. However, the voltage ordering is maintained and thus both functionals indicate that the ScS₂ would be very suitable for a cathode material.

5.3.2.2 Volumetric Expansion.

The volume change of ScS₂ upon cycling needs to remain suitably small for use as an intercalation electrode. 5.4(b) shows the volumetric expansion that arises in T-ScS₂ and α -ScS₂ upon intercalation. This is given as a percentage of the unintercalated bulk material volume, using $\% = 100 \times \frac{V-V_0}{V_0}$, where V_0 is the volume of the unintercalated bulk material. From the figure, we see that as the size of the intercalant is increased from Li to Na to K, the expansion increased by a larger percentage accordingly. For example, the volume change from intercalating with lithium to LiScS₂ is 6.51%, which is comparable to the 8% observed for NMC [258]. However, for NaScS₂ the expansion exceeds 20%, and for KScS₂ is exceeds 40%. Interestingly, intercalation with magnesium leads to a volume expansion of 7.53%, comparable to that arising from intercalation with lithium,

which is due to the larger nuclear charge on the Mg resulting in a reduced ionic radius.

5.3.2.3 Thermodynamic Stability.

One can construct thermodynamic phase diagrams in terms of the chemical potentials of scandium and the intercalated species to determine the stability of the intercalated structure against undesirable conversion reactions. We use this to evaluate the capacity of the material, reasoning that the formation of Li_2S (or equivalent product) will result in irreversible loss of the layered structure and hence cyclability. A schematic of a phase diagram is shown in 5.4(c), where phase boundaries are given by equations 5.2-5.5. Here, we are limited to the quadrant where the chemical potential of the intercalant species and of scandium are both negative, following equation 5.4, which specifies that the elemental bulk forms of the constituent atoms do not form. The diagonal line depicts the boundary described by equations 5.2 and 5.3, above which we would see the intercalated ScS_2 undergo conversion to scandium metal and either Li_2S or MgS . Finally, the horizontal line shows the boundary described by equation 5.5, below which it is not energetically favourable for intercalation to take place, and the pristine ScS_2 would remain. The blue region satisfies equations 5.2-5.5, and indicates a 'window of stability' for which the intercalated structure is stable. To quantify this window of intercalation stability, we use the quantity E_{IS} , which is the difference in the intercepts of the two boundaries with the $\Delta\mu_{\text{Li}/\text{Mg}}$ axis. An expression for this is given at the end of this chapter in section 5.5.1.

The phase diagram for $\alpha\text{-ScS}_2$ intercalated with Li is presented in 5.4(d), and the resultant values of E_{IS} for each of the intercalants is presented in the inset. It is clear to see that, for the range of intercalation concentrations presented here, ScS_2 has a sizeable window of stability with E_{IS} values in excess of 3 eV. This means that ScS_2 has a total capacity of 243.99 mAhg^{-1} (487.98 mAhg^{-1}) at full intercalation for the Group I intercalants (Mg). For the Group I intercalants, E_{IS} remains relatively unchanged with intercalant concentration.

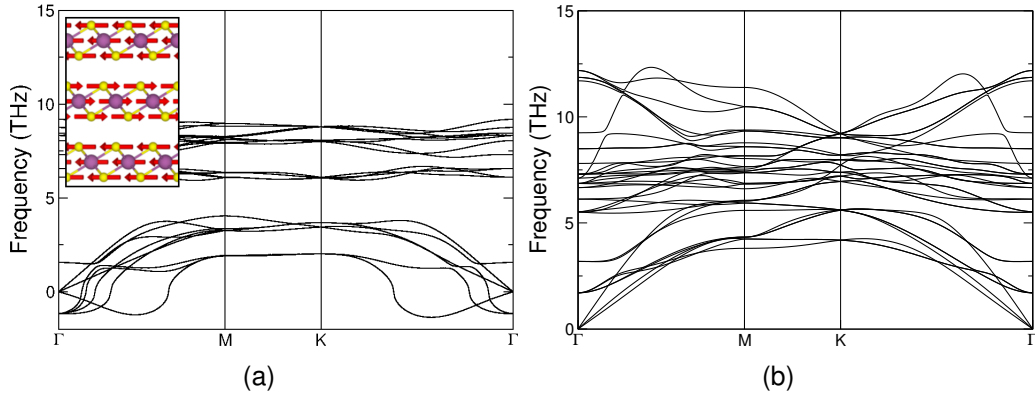


Figure 5.5: Phonon band structures for α -ScS₂ and α -LiScS₂. 5.5(a) shows the phonon band structure for unintercalated α -ScS₂ structure, with the inset showing the atomic structure and motions associated with the imaginary modes at Γ . 5.5(b) shows the phonon band structure for α -ScS₂.

The thermodynamic stability behaviour for magnesium intercalation is different from that of the Group I intercalants. It has very favourable energetics for low intercalation, but for higher concentrations E_{IS} dramatically reduces. This arises from a significant upward shift of the phase boundary between ScS₂ and Mg_aScS₂, given by equation 5.5. This behaviour is not dependent on the phase of the ScS₂. Similar trends were observed for equivalent phase diagrams for the intercalation stability of T-ScS₂ and Hc-ScS₂.

To further validate our approach, we have compared the HSE06 and PBE functionals for this system. We see the value of E_{IS} using HSE06 is a more favourable than compared to PBE. This improvement to E_{IS} arises from a downward shift of the horizontal line described by equation 5.5, and very little change in the diagonal line described by equation 5.2. We see that the stability trends hold for both functionals, and that the more accurate exchange is only important for the comparison between ScS₂ and intercalated ScS₂.

5.3.2.4 Dynamic Stability.

The thermodynamic phase diagrams allowed us to determine the range of concentrations for which the intercalated materials are stable against conversion reactions. However, it is also important to assess whether these materials are dynamically stable by considering their phonon modes. 5.5 presents the phonon band structures for pristine α -ScS₂, and α -ScS₂ intercalated with lithium. As can

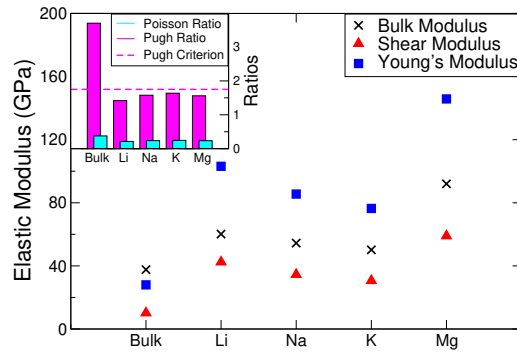


Figure 5.6: Elastic properties of T-ScS₂ in its pristine and intercalated forms. The bulk and shear moduli were calculated using the Voigt scheme.

be seen, the fully intercalated structure is phonon-stable. However, for bulk α -ScS₂, it is clear to see the presence of imaginary phonon modes in the Γ -M path of the Brillouin zone which result in dynamic instability. The motions associated with imaginary modes at -1.16 THz (-38.7 cm⁻¹) correspond to longitudinal in-plane oscillations of the ScS₂ sheets, as indicated in the inset of 5.5(a). This behaviour holds for Na, K, and Mg intercalated into ScS₂.

Our results show that LiScS₂ is phonon stable, and at some point, as the concentration of lithium is decreased, the phonon-stability is lost. The evaluation of the phonon band structures for intermediate lithium concentrations allows us to determine the lowest concentration of lithium we can access before the intercalated layered structure becomes dynamically unstable. For the α -phase, the instability is also seen up to and including Li _{$\frac{2}{12}$} ScS₂. Similarly for T-ScS₂, Li _{$\frac{1}{8}$} ScS₂ is unstable whereas Li _{$\frac{2}{8}$} ScS₂ is not. We can therefore conclude that the lowest concentration of lithium that can be reached (corresponding to the depth of discharge and hence the maximum reversible capacity) in ScS₂ lies in the range $0.125 < a < 0.25$. Taking the range of intercalation to be $0.25 < a < 1$, corresponding to 75% of the theoretical capacity, this gives a charge capacity of 182.99 mAhg⁻¹, which is comparable to the ~200 mAhg⁻¹ of other materials [199, 200, 198, 201, 76, 202, 203, 204, 205]. The 75% of the maximum capacity compares well with the 60%-80% available in NMC materials [76].

5.3.2.5 Elastic Properties.

For stable intercalation cycling it is desirable for the electrode material to be resistant to the associated stresses. One key metric for this is the Pugh ratio, given as the ratio of the bulk modulus and shear modulus, which can be used as an indicator of how ductile or brittle a material is. For Pugh ratios greater than 1.75 materials are usually considered ductile, whereas ratios of less than 1.75 are considered brittle. This ratio, along with other elastic properties [259, 258], for the different intercalants is shown in 5.6 for T-ScS₂. With intercalation, our results show an increase in the bulk, shear and Young's moduli for ScS₂, which follows the results for intercalation of other layered materials [260]. For the Group I intercalants, as the nuclear mass increases we identify a gradual decrease in each of the elastic moduli. However, we note that magnesium intercalation results in a higher stiffness. Whilst the binding energy of Mg into ScS₂ is lower, the higher charge of the intercalant species results in significantly higher Coulomb forces and thus a stiffer system. The inset of 5.6 presents the Poisson ratio, and the Pugh ratio. The Poisson ratio for ScS₂ is 0.38, but drops within the range 0.21-0.25 upon intercalation. We can see that the Pugh ratio for pristine ScS₂ is 3.70, well above the 1.75 Pugh criterion, but drops below 1.75 when fully intercalated. It has been indicated previously [260, 258] that the change in the elastic moduli as a function of concentration is near linear. As such, these materials remain ductile for the majority of concentrations, becoming only slightly brittle when fully intercalated. Compared to other layered materials, such as LiCoO₂ and graphite [260], ScS₂ and its intercalated forms are much more ductile, and so are more attractive for use in flexible electronics.

The elastic stability conditions for specific crystal types have been outlined elsewhere [261], which have been used here to assess the stability of the T- and α -phases. We find that the elements of the elastic tensor for both T- and α -phases break the requirements of $c_{44} > 0$ and $c_{14}^2 < \frac{1}{2}c_{44}(c_{11} - c_{12}) = c_{44}c_{66}$, and so the pristine material is not elastically stable. However, each of the intercalated phases meet all of the conditions, and so are elastically stable.

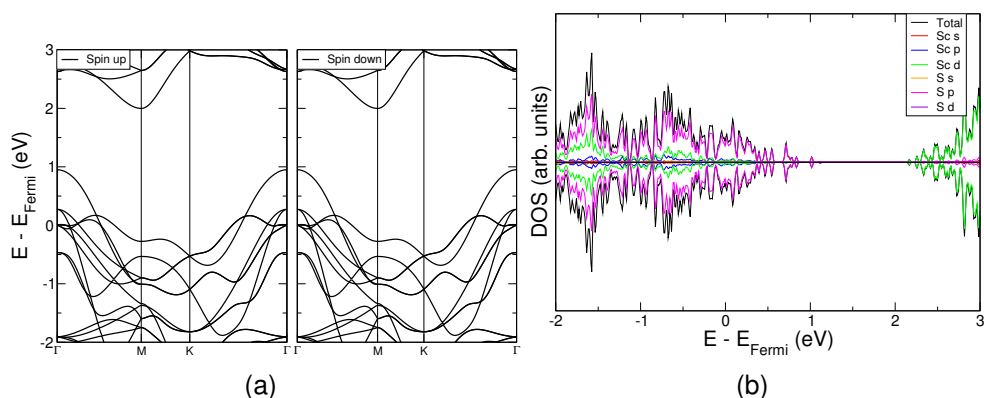


Figure 5.7: Electronic band structure (5.7(a)) and orbital-decomposed density of states (5.7(b)) for pristine α -ScS₂. In each, all data has been normalised such that the highest occupied state (E_{Fermi}) is set to 0 eV. This material is metallic so this zero occurs within the bands.

5.3.2.6 Electronic Structure.

As many electrode materials require conductive additives (such as graphitic carbon) to allow for electronic conduction during cycling of a cell, determining the material electronic structure is also necessary. In the unintercalated form, as shown in 5.7, ScS₂ has a metallic nature with a Fermi level intersecting a band. This was also seen with the other phases considered. The metallic nature of ScS₂ is also seen using the HSE06 functional. This is ideal for electrode materials, as it means that conductive additives are not necessary to facilitate the electron conduction. From the orbital-projected density of states, it can be seen that the valence bands of each of the phases are dominated by sulfur *p*-states and the conduction bands are dominated by scandium *d*-states.

Equivalent data for the intercalated ScS₂ structures showed that the addition of the Group I intercalants provides electrons, filling the previously unoccupied sulfur *p*-orbitals, shifting the Fermi level (located mid-band in ScS₂) upwards. This was also observed within the charge analysis. Upon intercalation to the point of MScS₂ with Group I metals, the intercalated structure develops a semiconducting nature with an occupied valence band separated from the conduction band by an moderate band gap of size ~ 1 eV (PBE). Specifically for LiScS₂, the PBE band gap is 1.36 eV and the HSE06 band gap is 2.32 eV, though we note from previous work that the HSE06 functional generally overestimates the band gap of TMDC

Table 5.1: Comparison table of key lithium-ion electrode properties for ScS₂ and other presently practiced electrode materials

Material	Voltage (V)	Intercalation Capacity (mAhg ⁻¹)	Volume Change (%)
LiScS ₂ (this work)	3.977	182.99	6.51
LiCoO ₂	3.9–4.7 [263]	190-215 [263]	3.25 [264]
NMC	2.85-3.41 [205]	160-189 [205]	8.44 [258]
LiFePO ₄	3.5 [198, 199, 200]	95 [198], 140.9 [199], 156 [200]	6.81 [265]
LiMn ₂ O ₄	4.13, 4.25 [207], 3.9, 4.1 [208]	111.5 [206], 106.3 [207], 105.2 [208]	4.7 [266]

structures [254, 262]. This gives a limit on the intercalation potential obtainable for practical uses: the insulating nature at this point would inhibit electronic conduction during cycling, and any intercalation past this point would require ScS₂ to be mixed with conductive additives to account for the insulating behaviour.

Magnesium intercalated into ScS₂ has different conducting behaviour compared to the group I elements, due to its double valency. Whilst the unintercalated system is conducting, intercalating to Mg_{0.5}ScS₂ fills the unoccupied sulfur *p*-orbitals and results in the structure losing its conductive nature, possessing a band gap of over 1.5 eV using the PBE functional. This would provide a practical limit during cycling, and would require conductive additives to be used to help facilitate intercalation past this point. However, past this the added magnesium provides electrons that begin to fill the unoccupied scandium *d*-states above the band gap.

Of the intercalant metals presented, lithium is the smallest and lightest, presents the highest (average) voltage of nearly 4 V, and has the lowest volumetric expansion. As such, lithium is identified as the best ion for ScS₂ to be used as an intercalation electrode. We summarise the key electrode properties in 5.1, along with the properties of other presently practiced electrode materials for lithium-ion batteries, where it is clear to see that ScS₂ offers a serious competitor to these materials. Below, we focus on lithium for exploring intercalation beyond the LiScS₂ composition, and for considering the effect of substitution of different transition metals for the scandium site in ScS₂.

5.3.3 Intercalation Beyond a=1

The intercalated LiScS_2 structures show both dynamic stability (with no imaginary phonon modes) and thermodynamic stability against conversion (with positive values of E_{IS}), and so the question as to the maximum possible lithium capacity still remains. As each of the octahedral sites is occupied at LiScS_2 , any further addition of lithium results in the occupation of the tetrahedrally-coordinated sites. For the supercell sizes considered, the first step of intercalation past LiScS_2 resulted in a stoichiometry of $\text{Li}_{\frac{13}{12}}\text{ScS}_2$. As this compound still possesses a sizeable value of $E_{IS} = 3.209$ eV, it is still remarkably stable against conversion reactions and demonstrates a robustness in this material to lithium intercalation beyond the usual limit considered for layered materials. However, there is a dramatic decrease in the intercalation voltage (with respect to the LiScS_2 structure) to 0.436 V, which indicates a clear cutoff in the practical uses for ScS_2 as a cathode material. These larger lithium contents align with the lithium concentrations used in the study of monolayer ScS_2 [236], where a drop in the voltage of over 2 V was also seen for concentrations beyond LiScS_2 .

With further intercalation we find the value of E_{IS} to drop, reaching a value of -0.735 eV at Li_2ScS_2 . At these relatively high lithium concentrations the large repulsion between these positively charged ions results in the intercalated structure being destabilised and becoming more susceptible to conversion. A similar drop in E_{IS} could be expected for the monolayer system, along with further instability arising from a separation of the ScS_2 layers.

5.3.4 Metal Mixing

One possible method commonly used to modify the properties of electrodes is through the introduction of other elements (M), in particular transition metals [241, 242] or with excessive lithium [209], resulting in the $\text{LiSc}_{1-x}\text{M}_x\text{S}_2$ compound. We first consider the formation energy of metal mixing, using,

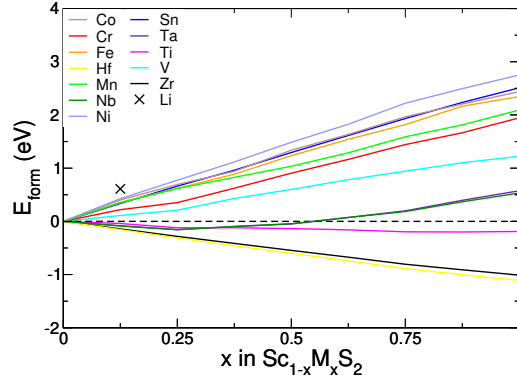


Figure 5.8: Formation energy of substituting scandium with different metal species, given by equation 5.6.

$$E_{form} = [E(\text{Sc}_{1-x}\text{M}_x\text{S}_2) + xE(\text{Sc})] - [E(\text{ScS}_2) + xE(\text{M})]. \quad (5.6)$$

Our results, presented in 5.8, show that for low concentrations ($x < 0.25$), the energetic cost is very low or even negative, with lithium showing the highest formation energy of 0.61 eV at $x = 0.125$. The Group IV metals (Ti, Zr and Hf) have negative formation energies, and so it is energetically favourable to perform this substitution. We also see negative values of E_{form} for Group V elements Nb and Ta for mixing values of $x < 0.5$, whilst the other metals considered here (and $x > 0.5$ for Nb and Ta) demonstrate positive values of formation energy.

In general, our results show that there is a reduction in both the intercalation potential and the values of E_{IS} as the proportion of scandium is reduced. The exception to this is demonstrated with lithium where, for a mixing concentration of $x = 0.125$, the average voltage is increased past the 3.655 V of ScS_2 to 3.668 V. In general, the voltage and E_{IS} values for the mixed materials falls below the weighted average of the two component materials. The greatest difference from the weighted average result is most dramatically show with $\text{Sc}_{0.5}\text{Ta}_{0.5}\text{S}_2$. For voltage, the average of the two components is 2.706 V, whereas the actual voltage obtained is 2.264 V. Similarly for the value of E_{IS} , the average of the ScS_2 and TaS_2 materials is 1.857 eV, whereas the value obtained is 1.381 eV.

The energetic cost of formation of ScS_2 can be reduced by the inclusion of other metals, $\text{Sc}_{1-x}\text{M}_x\text{S}_2$. However, we see that this results in both a decrease

in the obtainable voltage and a decrease in the the thermodynamic stability indicated by E_{IS} . Whilst the mixing of these systems reduces the suitability of ScS_2 as a cathode, the mixing of scandium into other materials for cathodes could be highly beneficial.

5.4. Conclusion and Chapter Summary

In this work, we have presented a thorough first-principles study into the performance of layered ScS_2 as a potential cathode electrode material. We have applied a random structure search to demonstrate that the ground state phase for the intercalated material is a layered structure, agreeing with experimental studies and supporting its use as an electrode. From this, different layered-phases of the material were investigated and intercalated with different metal species. It was found that the T- and α -phases to be energetically preferred, though they are not dynamically stable (determined through analysis of the phonon band structures) for low intercalation concentrations. The lowest achievable intercalant concentration is thus determined to be $a = 0.25$, and so a capacity corresponding to 75% of the theoretical capacity is predicted, corresponding to a charge capacity of 182.99 mAhg^{-1} .

For Group I intercalants, ScS_2 is found to have a high voltage of nearly 3.5 V which is ideal for cathodes. Whilst this is reduced to 1.5 V for intercalation with magnesium (a Group II metal), the double valency offers a larger range of charge transfer and hence a comparable energy density. This low voltage also offers some promise for an anode. Thermodynamic phase diagrams were constructed to evaluate the stability of the layered ScS_2 material against the conversion reaction forming Li_2S (or equivalent compound), a reaction commonly seen for TMDC sulfides when intercalated. ScS_2 was found to have a remarkably large window of stability, particularly when compared to the related TMDC materials. Beyond this, ScS_2 was shown to have a Fermi level which lies within a band, indicating a conductive nature that is convenient for device cycling. It also has a low volumetric

expansion (below 10%) when intercalated with lithium or magnesium, something that is essential for extended device lifetime.

To explore methods that could offer some improvement to the core properties of ScS₂ material, we also considered metal mixing (substitutionally swapping out scandium atoms with transition metal elements, similar to what is done with NMC). With mixing of other metals, we find a gradual drop in both the voltage and the size of the phase diagram window of stability which suggests that this would be detrimental to the performance of a ScS₂ electrode. However, this does highlight the potential advantage scandium could provide if mixed into other layered systems such as the layered transition metal oxides.

Our study highlights that ScS₂ shows potential as a cathode material for lithium-ion batteries, with theoretical estimates of the capacity comparable with NMC and similar materials. We hope that our study encourages further development of this material for lithium-ion batteries.

5.5. Supporting Information

5.5.1 Phase Diagram Derivation

For ScS₂ intercalated with some amount *a* of a metal M, be that a Group I metal (in the following example we use Li) or a Group II metal (in the following example we use Mg), we define the enthalpy of formation of relevant products:

$$\Delta H(\text{Li}_a\text{ScS}_2) = E(\text{Li}_a\text{ScS}_2) - [a\mu_{\text{Li}}^0 + \mu_{\text{Sc}}^0 + 2\mu_{\text{S}}^0] \quad (5.7)$$

$$\Delta H(\text{ScS}_2) = E(\text{ScS}_2) - [\mu_{\text{Sc}}^0 + 2\mu_{\text{S}}^0] \quad (5.8)$$

$$\Delta H(\text{Li}_2\text{S}) = E(\text{Li}_2\text{S}) - [2\mu_{\text{Li}}^0 + \mu_{\text{S}}^0] \quad (5.9)$$

$$\Delta H(\text{MgS}) = E(\text{MgS}) - [\mu_{\text{Mg}}^0 + \mu_{\text{S}}^0] \quad (5.10)$$

where $\Delta H(A)$ gives the enthalpy of formation of the compound A, $E(A)$ gives the energy of the compound A, and $\mu_B^0 = E(B)$ gives the chemical potential of elemental species B when it is in its elemental bulk structure.

The thermodynamic equilibrium condition requires,

$$\Delta H(\text{Li}_a\text{ScS}_2) = a\Delta\mu_{\text{Li}} + \Delta\mu_{\text{Sc}} + 2\Delta\mu_{\text{S}}, \quad (5.11)$$

where we have used the notation $\Delta\mu_B = \mu_B - \mu_B^0$, with μ_B being the chemical potential of elemental species B in Li_aScS_2 . This simply states that the energy of the intercalated structure is the sum of the chemical potentials of the constituent atoms. Rearranging the thermodynamic equilibrium condition gives,

$$\Delta\mu_{\text{S}} = \frac{1}{2} \{ \Delta H(\text{Li}_a\text{ScS}_2) - [a\Delta\mu_{\text{Li}} + \Delta\mu_{\text{Sc}}] \}. \quad (5.12)$$

We require that ScS_2 , Li_2S , MgS , and the bulk forms of the component elements do not form. Therefore,

$$\Delta\mu_{\text{Sc}} + 2\Delta\mu_{\text{S}} \leq \Delta H(\text{ScS}_2), \quad (5.13)$$

$$2\Delta\mu_{Li} + \Delta\mu_S \leq \Delta H(\text{Li}_2\text{S}), \quad (5.14)$$

$$\Delta\mu_{Mg} + \Delta\mu_S \leq \Delta H(\text{MgS}), \quad (5.15)$$

$$\Delta\mu_{Li,Mg,Sc,S} \leq 0. \quad (5.16)$$

Substituting 5.12 into 5.13 and rearranging,

$$\frac{1}{a} [\Delta H(\text{Li}_a\text{ScS}_2) - \Delta H(\text{ScS}_2)] \leq \Delta\mu_{Li}. \quad (5.17)$$

This then gives our first thermodynamic limit on the lithium chemical potential such that the intercalation of the layered ScS_2 structure is preferred to the pristine ScS_2 structure and bulk lithium.

We now substitute 5.12 into 5.14, and rearranging gives,

$$\Delta\mu_{Li} \leq \frac{1}{4-a} [2\Delta H(\text{Li}_2\text{S}) - \Delta H(\text{Li}_a\text{ScS}_2) + \Delta\mu_{Sc}]. \quad (5.18)$$

This gives the limit on the chemical potential of lithium such that the product Li_2S , an experimentally observed product of the conversion reaction of lithium with TMDC sulfides, does not form. We similarly substitute 5.12 into 5.15, giving,

$$\Delta\mu_{Mg} \leq \frac{1}{2-a} [2\Delta H(\text{MgS}) - \Delta H(\text{Mg}_a\text{ScS}_2) + \Delta\mu_{Sc}]. \quad (5.19)$$

The above equations thus describe the boundary conditions for the chemical potential of an intercalated metal, dependent on formation energies of the relevant products, and the chemical potentials of the relevant metals. It should be noted, by considering the equations 5.7-5.10, that the limiting conditions for both the single TMDC and superlattice, equations 5.16-5.19, are independent of μ_S^0 , and hence $\Delta\mu_S$. As a result, the phase diagrams are only dependent on the chemical potentials of the intercalated species and the relevant metals, $\Delta\mu_{Li}$, $\Delta\mu_{Mg}$, and $\Delta\mu_{Sc}$.

Using equations 5.16, 5.17 and 5.18/5.19, we can construct thermodynamic phase diagrams, and a schematic of one is shown in Figure 2c of the main article. We restrict ourselves to the negative-negative quadrant to ensure that the elemental bulks do not form (equation 5.16). Above the diagonal line, labelled "1", the experimentally observed Li_2S crystal is favoured, as opposed to the intercalated ScS_2 . Below the horizontal line, labelled "2", the pristine ScS_2 structure is preferred to intercalation. From this, we show intercalation is favoured for chemical potential combinations that sit within the shaded region indicated in Figure 2c of the main article. Outside of this window, however, the secondary products (as indicated in the figure) are favourable to form. Though a transition to these is not guaranteed, the intercalated ScS_2 structure becomes meta-stable. Whilst other compounds could have their respective boundaries determined to be included in these phase diagrams, such as (for the case of lithium intercalation) Li_2S_2 or ScS , these first require the disintegration of the Li_aScS_2 material into Li_2S and/or elemental bulks. Hence, we only consider the limits outlined above.

To quantitatively compare the phase diagrams for the different concentrations considered, we can evaluate the difference between the intercepts of lines 1 and 2 with the $\Delta\mu_{Li}$ -axis. E_{IS} is then defined as,

$$E_{IS} = \Delta\mu_{Li}^{(1)}(\Delta\mu_{Sc} = 0) - \Delta\mu_{Li}^{(2)}(\Delta\mu_{Sc} = 0), \quad (5.20)$$

where $\Delta\mu_{Li}^{(1/2)}$ ($\Delta\mu_{Sc} = 0$) is the value of the boundary line 1/2 at the point where $\Delta\mu_{Sc} = 0$. For lithium intercalation, using 5.17 and 5.18 this can be written in terms of the relevant values for formation enthalpy,

$$E_{IS}^{Li} = \frac{2}{4-a}\Delta H(Li_2S) + \frac{1}{a}\Delta H(ScS_2) - \frac{4}{4a-a^2}\Delta H(Li_aScS_2), \quad (5.21)$$

and for magnesium intercalation, using 5.17 and 5.19 this can be written as,

$$E_{IS}^{Mg} = \frac{2}{2-a}\Delta H(MgS) + \frac{1}{a}\Delta H(ScS_2) - \frac{2}{2a-a^2}\Delta H(Mg_aScS_2). \quad (5.22)$$

Each of the enthalpy of formation values should be negative for them to be thermodynamically stable with respect to their atomic constituents. When the value of E_{IS} is negative, the first two terms dominate, and line "1" intercepts below line "2" so no stability region exists. When the value of E_{IS}^{Li} is positive, however, $\Delta H(Li_aScS_2)$ dominates and the intercalated ScS_2 material is stable.

Using a similar set of arguments, we can construct equivalent phase diagrams for the systems where transition metal atoms substitutionally replace the scandium atoms of the host ScS_2 structure. Hence, we can also obtain an expression for E_{IS} , as,

$$E_{IS}^{Li} = \frac{2}{4-a}\Delta H(Li_2S) + \frac{1}{a}\Delta H(MSS) - \frac{4}{4a-a^2}\Delta H(LMMS). \quad (5.23)$$

Again, $\Delta H(A)$ gives the enthalpy of formation of the compound A, where MSS indicates the compound $M_bSc_{1-b}S_2$, where metal M has replaced some proportion of scandium, and LMSS the intercalated MSS compound $Li_aM_bSc_{1-b}S_2$. The similarity with equation 5.21 is evident.

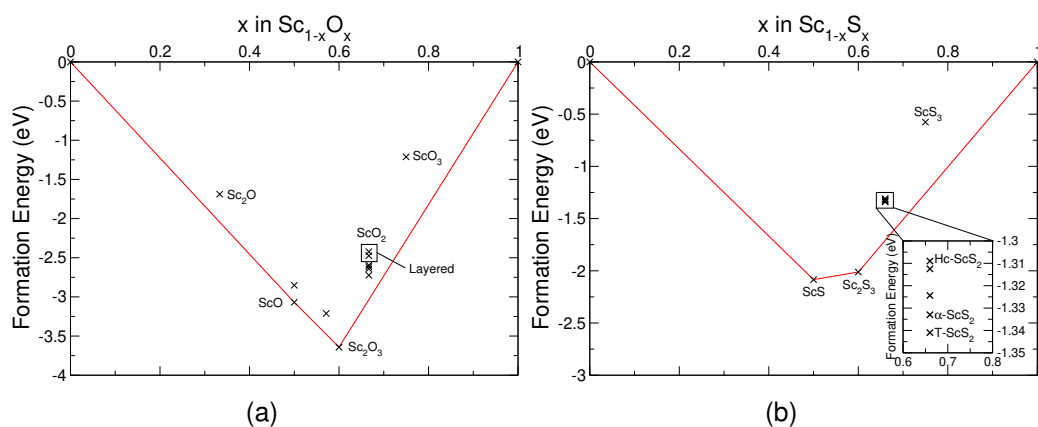


Figure 5.9: Convex hulls for Sc-O (5.9(a)) and Sc-S (5.9(b)) compounds.

5.5.2 Convex Hull for Sc-O and Sc-S Compounds

To investigate other possible structures/compounds that could form upon synthesis of ScS_2 , we have constructed a convex hull. However, as there are a limited number of scandium sulfide compounds that have been presented in the literature and on databases such as the ICSD and Materials Project [251], we have also considered scandium oxide compounds to inform us of potential scandium sulfide analogues.

Figure 5.9(a) presents the generated convex hull for compounds of scandium and oxygen with different stoichiometries. We note that the compounds with stoichiometry ScO_2 do not lie on the hull. Furthermore, the layered structures are the least energetically favourable of the structures considered for that composition, lying 0.62 eV above the hull. Of the structures investigated for the ScO_2 composition, the lowest energy belongs to the monoclinic structure similar to that of Baddeleyite. Clearly, the layered ScO_2 structure would be prone to form the monoclinic structure instead, or a decomposition reaction $2\text{ScO}_2 \rightarrow \text{Sc}_2\text{O}_3 + \frac{1}{2}\text{O}_2$

We find similar results for the scandium sulfide compounds, with the various ScS_2 structures lying above the hull. However, we find for the sulfides that the layered structures are the most favourable, and lie closer to the hull, with T- ScS_2 being ~ 0.37 eV above the hull.

Chapter 6

A computational study of the enhancement of graphene electrodes for use in Li-ion batteries *via* forming superlattices with transition metal dichalcogenides

"It doesn't matter how beautiful your theory is, it doesn't matter how smart you are. If it doesn't agree with experiment, it's wrong."

– Richard Feynman

In this chapter, TMDCs are combined with graphene to form superlattices, which are similar to heterostructures except they repeat, that are investigated for use as Li-ion battery electrodes. Nine different TMDCs were considered with their voltages, volumetric expansions and capacities which were determined using a slight modification to the E_{IS} metric that was used in the previous chapter. A derivation of this is included at the end of this chapter.

6.1. Introduction

Li-ion based batteries are the most widely used energy storage medium for portable electronic devices, seeing use in anything from phones to electric cars and most devices in between. The electrodes of a Li-ion battery are what determine their voltage and capacity, with many different types of material having been used and investigated as Li-ion battery electrodes. These materials mainly consist of layered van der Waals structures following the discovery and use of TiS_2 as a Li-ion intercalation electrode in the 1970's [267, 268, 269], which was followed

by LiCoO_2 in 1980 [56]. From this many other layered materials were investigated such Graphite [57], a non-layered spinel structure LiMn_2O_4 [270, 67] and MoS_2 [271, 272, 273, 274, 275, 276, 277, 278, 279] before the current commercially used NMC [280, 281, 282] and NCA [283] were discovered.

Many electrode materials share the layered structure of transition metal dichalcogenides (TMDCs), which are made of one part transition metal (M) and two parts chalcogen (S, Se or Te denoted as X) with general formula MX_2 [284]. Since the investigations into TiS_2 [267, 268, 269], TMDCs have remained a prevalent electrode [285, 286, 287, 288], with sulphur based TMDCs often being looked at over other TMDCs as they are lighter and have been shown to have higher capacities than selenium and tellurium based TMDCs [289]. The large van der Waals gap of TMDCs allow for the rapid insertion and extraction of intercalants, demonstrated by systems such as VS_2 [290], whilst maintaining relatively low volume changes of 8% for materials such as NMC [291]. This has led to more of these TMDCs to be investigated for use as Li-ion battery electrodes such as WS_2 [292], NbSe_2 [293], ReSe_2 [279], and most recently ScS_2 [294]. Nb- and Ta-based materials [295] have shown to be intercalatable up to ratios of 1:1 Li:MX₂, but their heavier masses result in lower theoretical capacities below 170 mAhg^{-1} . MoS_2 is widely studied [271, 272, 273, 274, 275, 276, 277, 278, 279] in the field of TMDCs and has been the subject of numerous investigations, demonstrating a capacity of 167 mAhg^{-1} but poor conductivity. ScS_2 in particular has recently been suggested as a promising electrode [294], promising an ideal maximum cathode voltage of 4.5 V, a reversible capacity of 183 mAhg^{-1} and a volumetric expansion of 7.5%. In addition, in spite of the ready conversion into Li_2S and Sn, SnS_2 also shows considerable promise as a electrode material [296, 297, 298, 299, 247, 248, 300, 301].

Recent studies have looked at improving many of the properties of TMDCs needed for their use as electrode materials, with the aim of extending device operation, increasing the intercalant capacities, and improving conductivity. Morphology control [271, 302, 303] and composite formation [304, 305, 306, 307,

308, 309, 290], particularly through the inclusion of graphitic carbon [310, 311] or other layered materials, has been used to improve electrical and ionic conductivity, provide mechanical support, and improve the resultant capacity. Carbon is also often used as the anode in Li-ion batteries and can come in multiple forms. The most basic of these is graphite, which can be intercalated up to the LiC_6 limit (equivalent to 339.18 mAh/g) [312]. Graphene has been shown to achieve a higher capacity but this is often suspended monolayers which are unrealistic in a normal battery electrode [313].

Constructing superlattices is an attractive approach for tailoring the properties of two-dimensional materials due to the comparative ease with which they can be made (such as via exfoliation [126]) and has been applied to TMDCs [127, 128, 314, 130, 315]. Given the layered structure of many battery electrodes in use today, such as NMC, NCA, LiCoO_2 and graphite, superlattices could be made from these to modify their voltages, capacities, thermal stability and more in order to improve their overall performance. Some TMDCs-graphene superlattices have already been investigated as intercalation electrodes showing promise as anodes [316, 317, 318], with MoS_2 -graphene superlattices showing voltages of 1.5 V and conversion reactions to Li_2S at 2.3 V [318].

In this chapter, we have investigated the effect that forming superlattices with graphene has on a wide variety of sulphur based transition metal dichalcogenides (TMDCs) using density functional theory (DFT). We have calculated the voltages and capacities by looking at the thermodynamic relation between the TMDCs and bi-products that are often formed when these breakdown in the presence of lithium, Li_2X . We have also investigated the effect that additional graphene layers has on T-phase MoS_2 .

6.2. Method

6.2.1 Density Functional Theory Parameters

First principles DFT calculations were performed using the Projector augmented wave (PAW) [159, 160] method implemented in the Vienna Ab initio Simulation Package (VASP) [161, 162, 45, 46]. The calculations utilizes Perdew-Burke-Ernzerhof electron exchange correlation functions [163, 164]. The plane wave energy cutoff was 500 eV with a Γ -centred Monkhorst-pack grid [165] of at least $3 \times 3 \times 3$ was used for the supercells due to their size, denser grids were used for smaller supercells. Van der Waals interactions were included using the DFT-D3 method of Grimme [53] to account for the weak interactions between the 2D layered materials. The structures were geometrically relaxed until the forces between the atoms were less than 0.01 eV/Å using a combination of the conjugate gradient algorithm [54] and a quasi-Newtonian relaxation algorithm, RMM-DIIS [55]. PAW pseudopotentials were used for core electrons, and the electrons that have been treated as valence are: Mo $4d^55s^1$, W $5d^46s^2$, Sn $5s^25p^2$, Sc $3d^14s^2$, Ni $3d^84s^2$, Mn $3d^54s^2$, Ti $3d^24s^2$, S $3s^23p^4$, C $2s^22p^2$ and Li $1s^22s^1$.

In order to minimise the strain between the TMDCs and graphene, large supercells have been created with anywhere from 4 to 16 MX_2 units, an example of which is shown in Figure 6.1. These supercells have be generated using the ARTEMIS [172] package, which carries out a series of rotation matchings of two layers and produces a unit cell with the minimal strain, alongside estimating the interlayer distances. The supercells were generated with and without lithium ($a = 0$ and $a = 2$) for the 9 different TMDCs investigated, these were then modified to get additional lithium concentrations ($a = 1, 15/16, 17/16$). For such large supercells, the number of configurations for $a = 1$ would result in, for example, 60,000,000 calculations (for one system) and only provide an intermediary voltage. As such, we have only focused on the key points of intercalation ($a = 0, 1, 2$). For $a = 1$, we have chosen 2 configurations based on previous results for TMDCs [289], one with the Li filling every other interlayer region between graphene and the TMDC

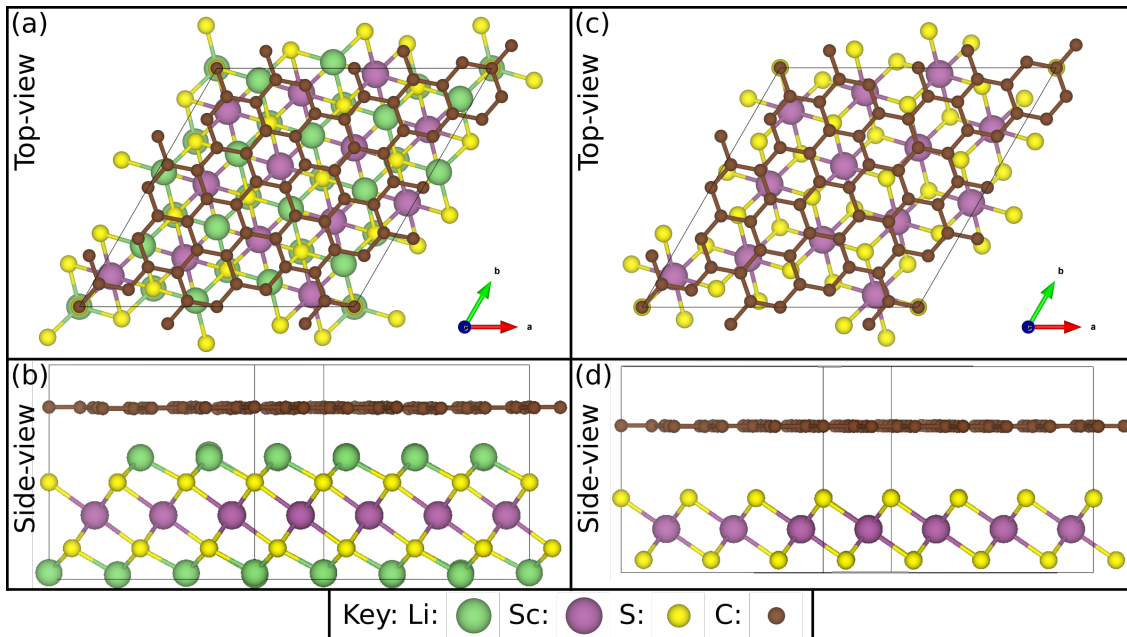


Figure 6.1: Schematic of ScS₂ with graphene with lithium from the top (a) and side (b), and without lithium from the top (c) and the side (d). This has 13 MX₂ units to 56 carbon atoms.

and the second where the lithium is evenly spread between the interlayer regions. Precise geometry of the relevant unit cells and how these additional concentrations were made is provided at the end of this chapter. These were all calculated from a graphene supercell of the same size as in the TMDC-graphene superlattices, the exact sizes of these are given in Table 6.1, and a single unit cell of the TMDCs, the only exception to this is MnS₂ T for which we used a TMDC supercell of the same size, the reason for this is given at the end of this chapter. Volume expansion with increasing lithium content was calculated in the standard method, $\% = \frac{V - V_0}{V_0} \times 100$ where V_0 is the volume of an unintercalated superlattice ($a = 0$).

6.2.2 Voltages and stability

The voltages, V , of these superlattices at different levels of lithium intercalation, can be expressed as

$$\begin{aligned}
V &= -\frac{\Delta G}{\Delta Q} \\
&\approx -\frac{\Delta E}{\Delta Q} \\
&= -\frac{E(\text{Li}_{a_2}\text{MX}_2\text{C}_b) - \left[E(\text{Li}_{a_1}\text{MX}_2\text{C}_b) + (a_2 - a_1)E(\text{Li}) \right]}{(a_2 - a_1)e},
\end{aligned} \tag{6.1}$$

where ΔG is the change in Gibbs free energy, the total lithium content $a_2 > a_1$, $E(\text{Li}_a\text{MX}_2\text{C}_b)$ is the energy of an MX_2 -graphene superlattice with a lithium and b carbon per MX_2 unit and $E(\text{Li})$ is the energy of lithium in its bulk form. The Gibbs free energy can be approximated as the internal energy, as the pressure-volume and vibrational entropy contributions are known to be negligible in TMDCs [319] and graphite/graphene [320].

The thermodynamic stability of these superlattices was assessed by looking at the favourability of the formation the secondary product Li_2X . In Li-ion batteries, the formation of secondary products like Li_2X indicates a loss of the desired layered structure, leading to a loss in capacity. We can determine the maximum lithium intercalation limit by finding a region in phase space where Li_2X is less favourable than an intercalated superlattice, where an unintercalated structure is less favourable and where the elemental bulks are less favourable. These limits are expressed as

$$\Delta\mu_{\text{Li}} \leq \frac{1}{4-a} [2\Delta H(\text{Li}_2\text{X}) - \Delta H(\text{Li}_a\text{MX}_2\text{C}_b) + \Delta\mu_{\text{M}} + b\Delta\mu_{\text{C}}], \tag{6.2}$$

$$\frac{1}{a} [\Delta H(\text{Li}_a\text{MX}_2\text{C}_b) - \Delta H(\text{MX}_2\text{C}_b)] \leq \Delta\mu_{\text{Li}}, \tag{6.3}$$

$$\Delta\mu_{\text{Li},\text{M},\text{X},\text{C}} \leq 0, \tag{6.4}$$

where $\Delta H(\text{A})$ is the enthalpy of formation of compound A with respect to the bulk constituents and $\Delta\mu_{\text{A}}$ is given by $\Delta\mu_{\text{A}} = \mu_{\text{A}} - \mu_{\text{A}}^0$, μ_{A} being the chemical potential of species A when in $\text{Li}_a\text{MX}_2\text{C}_b$, with $\text{A} = \text{Li}, \text{M}, \text{X}, \text{C}$. If we consider the

maximum difference in $\Delta\mu_{Li}$ in equations 6.2 and 6.3 when $\Delta\mu_M = \Delta\mu_C = 0$ we can qualitatively determine if a region of stability exists for $Li_aMX_2C_b$. We define this quantity as E_{IS} and it is given by

$$E_{IS} = \frac{2}{4-a}\Delta H(Li_2X) + \frac{1}{a}\Delta H(MX_2C_b) - \frac{4}{4a-a^2}\Delta H(Li_aMX_2C_b). \quad (6.5)$$

A positive E_{IS} means that $Li_aMX_2C_b$ is thermodynamically favourable and a negative means that that Li intercalated to this capacity is not stable and will result in the formation of Li_2S . Hence, determining the limit of intercalation, a , for when $E_{IS} = 0$ determines that maximum amount of lithium that can be intercalated, and therefore the capacity. For these superlattices we have also considered the formation of LiC_6 from the lithiated superlattices ($a > 0$), and show that this is always unfavourable. The origin the limits that E_{IS} is derived from and the results looking at the formation of LiC_6 can be found at the end of this chapter.

6.3. Results

6.3.1 General properties

To establish the viability of these TMDC-graphene superlattices for the intercalation of Li we first need to examine the resultant strains and formation energies. The exact number of MX_2 units and the carbon to MX_2 ratio (b) is given in Table 6.1 along with the strain associated with each layer and the formation energy per unit area. These are calculated for the TMDCs with no lithium compared with their respective superlattices with no lithium ($a = 0$). Details of this are given at the end of this chapter. As can be seen, the strains are all less than $\pm 0.6\%$ for the graphene and less than $\pm 5\%$ for the TMDCs. All of the formation energies for these structures are less than $\pm 0.02 \text{ eV/\AA}^2$, with the exception of MnS_2 . However, in all cases, these supercells are both energetically viable and have low enough strains to not dramatically affect the resultant properties. In general, the graphene shows minimal strain whereas the TMDCs are more strained, however these are

lower than the expansion that these materials undergo due to lithium intercalation. It is of note that, in all cases, the inclusion of graphene has made these superlattices conductive which is required for these to be used as electrodes.

Table 6.1: The ratios of MX_2 to C along with the strain associated with each layer for the 9 supercells generated using the ARTEMIS [172] package and the formation energies per unit area. The strains are calculated for the TMDCs with no lithium compared with their superlattices with no lithium ($a = 0$).

TMDC	N ^o MX_2	C: MX_2 ratio (b)	Strain on TMDC (%)	Strain on Graphene (%)	Formation energy (meV/Å ²)
MoS ₂ H	16	3.3750	0.98	-0.36	0.86
MoS ₂ T	16	3.3750	-0.59	-0.02	-8.95
WS ₂ H	16	3.3750	0.89	-0.35	0.043
SnS ₂ T	4	4.5000	0.65	-0.15	6.53
ScS ₂ R	13	4.3077	-3.44	0.018	13.38
ScS ₂ T	13	4.3077	-0.24	0.018	19.82
NiS ₂ T	13	3.8462	-3.44	-0.53	5.80
MnS ₂ T	7	3.7143	-4.74	-0.20	64.30
TiS ₂ T	16	3.8750	0.29	-0.27	11.69

6.3.2 Voltages

The voltage is one of the most fundamental properties of an electrode and is used to determine if it is considered as an anode or a cathode. Anodes normally have voltages lower than 2 V vs Li/Li^+ , ideally between 0.5-1.5 V, cathodes normally have voltages higher than 3 V ideally between 3-4.5 V [321]. Figure 6.2 (a) shows how the voltage of the TMDC-graphene superlattices vary as a in $\text{Li}_a\text{MX}_2\text{C}_b$ is increased, calculated using Equation 6.1.

Most of the TMDC-graphene superlattices display voltages which lie in the anode range. MoS₂-H, MoS₂-T, WS₂-H, SnS₂-T, NiS₂-T, MnS₂-T and TiS₂-T all have voltages between ≈ 1.5 and 0 V meaning that these would be suitable as anodes. Despite how similar MoS₂-H and MoS₂-T are in composition, the change in TMDC phase leads to MoS₂-T having a far higher voltage for $a = 0 \rightarrow 1$, this may be caused by the large rearrangement that this system has undergone, having changed from T-phase to T'-phase (a distortion of T-phase with alternating Mo-Mo distances) and back to T-phase for $a = 0 \rightarrow 1 \rightarrow 2$. MoS₂-H has a very flat voltage which is far more preferable when looking for a lithium intercalation battery electrode. SnS₂-T has a flat voltage from $a = 0$ to $a = 2$ as neither of

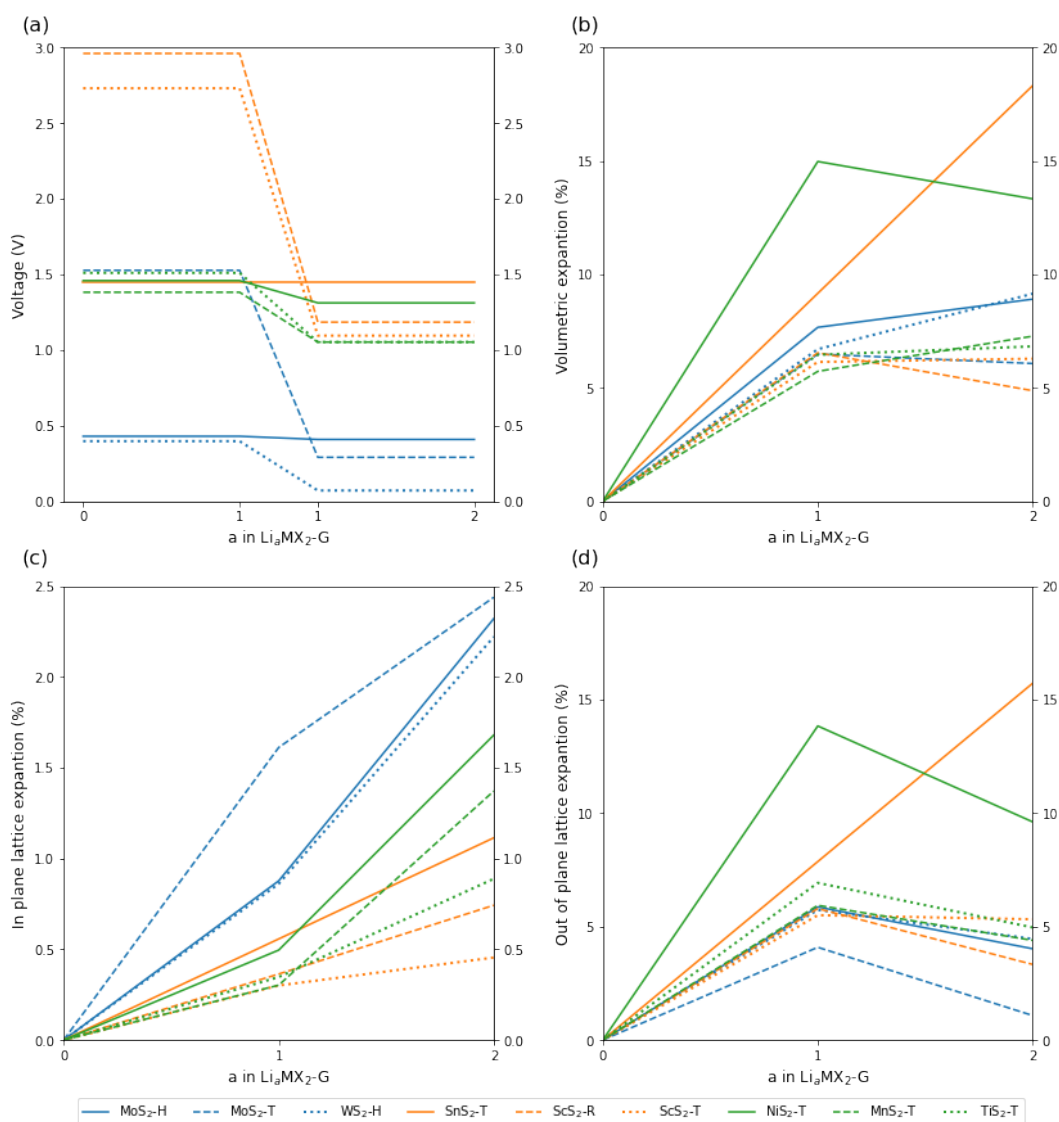


Figure 6.2: Voltages (a), volumetric expansions (b), in plane lattice expansion (c) and out of plane lattice expansion (d) for the TMDC-graphene superlattices as a increases in $\text{Li}_a\text{MX}_2\text{-G}$.

the $a = 1$ configurations were more favourable than a combination of the $a = 0$ and $a = 2$ structures. Our results for $\text{MoS}_2\text{-T}$ with graphene agree with those of experiment where a voltage of ≈ 1.5 V has been seen, as well as irreversible conversion reactions occurring above this voltage [318]. We note that WS_2 , $\text{ScS}_2\text{-R}$ and $\text{ScS}_2\text{-T}$ all show a significant drop in their voltages.

$\text{ScS}_2\text{-R}$ and $\text{ScS}_2\text{-T}$ both start with much higher voltages, closer to 3 V, for $a = 0 \rightarrow 1$, before dropping down to an anode like voltage, around 1.15 V, for $a = 1 \rightarrow 2$. This puts them in an odd situation where they are not quite high enough to be considered a cathode, but starts too high to be considered an anode for its whole intercalation range at this ratio of MX_2 to carbon. This suggests that

ScS₂ based cathodes should have low levels of carbon such that their voltages are not as significantly decreased.

Comparison of the TMDC-graphene voltages with their bulk TMDCs shows that the voltage is generally decreased. The details of this are given at the end of this chapter. The lowest decrease was shown when mixing WS₂-H with graphene which was only decreased by 1.4%. The highest decrease voltage was the mixing of MoS₂-H with graphene which showed a decrease in voltage of 0.72 V without graphene to 0.43 V with graphene. In general, our results show that the addition of graphene decreases the voltages of the TMDCs, with values ranging from from 1.44% to 40.38% in the range of $a = 0 \rightarrow 1$. Clearly the inclusion of graphene increases the effectiveness of these materials as anodes, but is detrimental to the performance of cathodes.

6.3.3 Volumetric Expansion

When investigating Li-ion intercalation electrodes, it is important to look at how the volume of these materials change during cycling, as this can be a cause of degradation of these materials that leads to a loss of usable capacity. Figure 6.2 (b) shows how the volume of the TMDC-graphene superlattices vary as a in Li_aMX₂C_b is increased. As expected, for all superlattices investigated, we can see a general increase in volume when lithium is intercalated. The superlattices at $a = 1$ and $a = 2$ all show smaller volumetric expansions to their respective bulk TMDCs at $a = 1$, with the exception of WS₂-H and SnS₂-T which expand more at $a = 2$, these are given at the end of this chapter. Bulk MnS₂-T has actually shrunk when lithium is intercalated into it, this is due to the aligned spins on the manganese atoms going from 3 up with no lithium to 2 up with lithium, the aligned spins repulse each other leading to a decrease in volume. This is not observed in our MnS₂-T superlattice as the manganese atoms are more spatially separated due to the inclusion of the graphene between the TMDC layers.

The observed expansions of the superlattices can be split into three groups showing slightly different trends. MoS₂-H, WS₂-H, ScS₂-T, MnS₂-T and TiS₂-T

have a large increase in volume for $a = 0 \rightarrow 1$ with a much smaller increase in volume for $a = 1 \rightarrow 2$, this is what we expect to happen for the vast majority of the investigated superlattices as lithium prefers to be split between both sides of the TMDC layer instead of all on one side, meaning that both gaps between the TMDC and graphene layers are spread apart by lithium. Although lithium $\text{ScS}_2\text{-T}$ prefers to all be on one side when $a = 1$, breaking this "trend". $\text{SnS}_2\text{-T}$ has a constant expansion from $a = 0 \rightarrow 2$ due to the $a = 1$ configurations not being favourable. $\text{MoS}_2\text{-T}$, $\text{ScS}_2\text{-R}$ and $\text{NiS}_2\text{-T}$ all show an odd behaviour of contracting when going from $a = 1 \rightarrow 2$, this is also observed experimentally for materials such as NMC which have the largest out of plane lattice constant near 50% Li content [291].

From the lattice constant expansions shown in Figures 6.2 (c) and (d) we can see that the expansion of the out of plane lattice is the biggest contributor to the volumetric expansion. This is due to the Van der Waals gaps between the layers being forced apart by lithium as it is intercalated, this is seen in many other intercalation electrodes [291]. We see volumetric expansions in the range of 5% to 10% for all materials except for $\text{SnS}_2\text{-T}$ and $\text{NiS}_2\text{-T}$. This level of expansion is comparable to that seen in materials used in commercial batteries such as NMC with an expansion of 8% [291]. $\text{SnS}_2\text{-T}$ and $\text{NiS}_2\text{-T}$ both undergo expansion in the range of 10% to 20% which could lead to significant formation of cracks during cycling which accelerate degradation and limit capacity [322].

6.3.4 Thermal Stability and Capacity

We can determine the maximum amount of lithium that the TMDC-graphene superlattices can accommodate by determining when $E_{IS} \approx 0$ by using equation 6.5. Figure 6.3 shows how E_{IS} varies as the level of intercalated lithium, a , is increased. In these structures we investigate strictly one layer of carbon with one layer of TMDC. For all the systems that have positive E_{IS} , a similar or better lithium to carbon ratio than that of graphene on (LiC_6) its own is achieved. This indicates that the capacity of the carbon has been increased. The superlattices

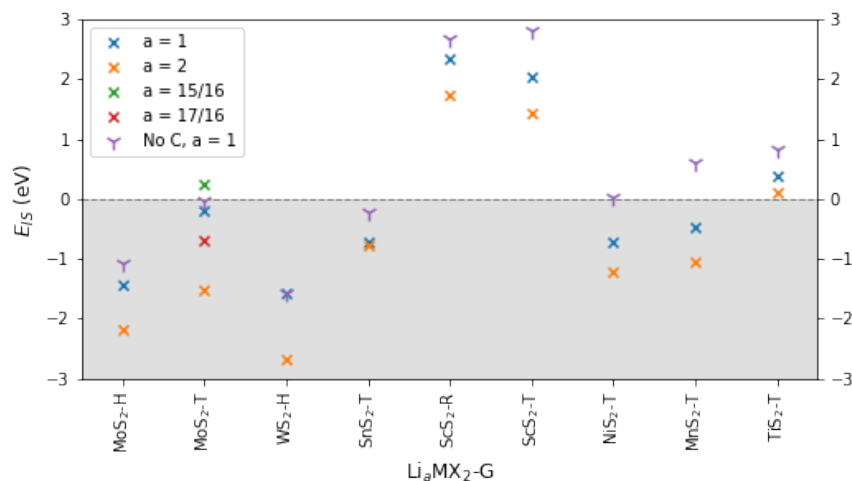


Figure 6.3: E_{IS} for the TMDC-graphene superlattices as the intercalation level, a , increases in $\text{Li}_a\text{MX}_2\text{C}_b$ for $a = 1$ and $a = 2$. The value for E_{IS} has been included for these without graphene as well. For MoS_2 , extra points have been included for $a = 15/16$ and $a = 17/16$.

which show this improvement involve the TMDCs $\text{ScS}_2\text{-R}$, $\text{ScS}_2\text{-T}$, $\text{TiS}_2\text{-T}$ and $\text{MoS}_2\text{-T}$. Conversely, the remaining TMDCs considered readily decompose into Li_2S at $a = 1$. These may still be able to intercalate lithium without undergoing conversion, however, intercalation for $a < 1$ will lead to a low capacities that are not suitable for electrodes.

To further explore the limits of mixing these systems, we expand on the results for $\text{MoS}_2\text{-T}$ with graphene. For $\text{MoS}_2\text{-T}$ at $a = 1$ and $a = 2$ E_{IS} is negative, meaning that it is unfavourable to intercalate this TMDC even to just one lithium per unit. However, the value of E_{IS} at $a = 1$ was very low, equal to -0.191 eV. We have considered lithium concentrations of $a = 15/16$ and $a = 17/16$ (± 1 Li compared to $a = 1$). From this we can confirm that E_{IS} does become positive for $a = 15/16$, equal to 0.242 eV, meaning that $\text{MoS}_2\text{-T}$ with graphene is able to be intercalated and has a capacity equal to 121.29 mAh/g. If we look at the graphene layer, this is roughly equivalent to a limit of LiC_4 . We can also see that the value of E_{IS} at $a = 17/16$ is between the values of E_{IS} at $a = 1$ and $a = 2$. Thus we can state that the MoS_2 -graphene boundary shows a small increase in capacity compared to the pure graphene region, and a slight decrease in performance when compared to pure MoS_2 . This result agrees with Larson *et al.* [316] who showed, for $\text{Li}_a\text{MoS}_2\text{C}_{3.125}$ (50 C: 16 MoS_2), that the limit of intercalation is $a \approx 1$.

ScS₂-R, ScS₂-T and TiS₂-T all are resistant to the formation of Li₂S up to an intercalation of $a = 2$, meaning that these can be intercalated up to at least 2 lithium per MX₂ unit without decomposing. When ScS₂-R and ScS₂-T are compared to graphene, this is almost approaching LiC₂, a large improvement over the LiC₆ limit of graphene. When TiS₂ is compared to graphene, it is the equivalent to going slightly beyond LiC₂. Both ScS₂-R and ScS₂-T have a capacity of 306.77 mAh/g and TiS₂ has a capacity of 310.84 mAh/g.

Comparing the E_{IS} of the TMDC-graphene superlattices to their respective TMDCs at $a = 1$ we can see that the addition of graphene has decreased the stability of the TMDC against intercalation for all systems with the exception of WS₂-H. This is shown by a general decrease in E_{IS} , we find that this decrease compared to the bulk TMDC ranges from 1.09 eV to 0.17 eV, excluding WS₂-H which increases by 0.01 eV.

6.3.5 Changing the ratio of carbon to TMDC

In order to investigate the effect of graphene further, we have looked at what happens when the ratio of graphene to MoS₂-T is increased. This system is of particular relevance as MoS₂ does not conduct without an additive such as hard carbons. We have used MoS₂-T at lithium contents of $a = 0$ and $a = 1$ for this, varying the number of graphene layers between 0 and 3, this is equivalent to $b = 0, 3.375, 6.750$ and 10.125 . For all cases where $b \neq 0$ the same local structure of MoS₂-T and lithium has been used as was found for $a = 1$ and $b = 3.375$, no additional lithium is added as the amount of carbon is increased, a schematic of this is shown in Figure 6.4 (c). From these results we can assess the effect that more carbon has on the local stability, volume expansion and voltage of the MoS₂-T layer. The voltage and E_{IS} change is shown in Figure 6.4 and are given at the end of this chapter.

Our results show that the voltage (from $a = 0$ to $a = 1$) decreases as the amount of carbon, b , is increased. As we have limited our search to just the interface region, this suggests that a truly mixed MoS₂/hard carbon system (which has

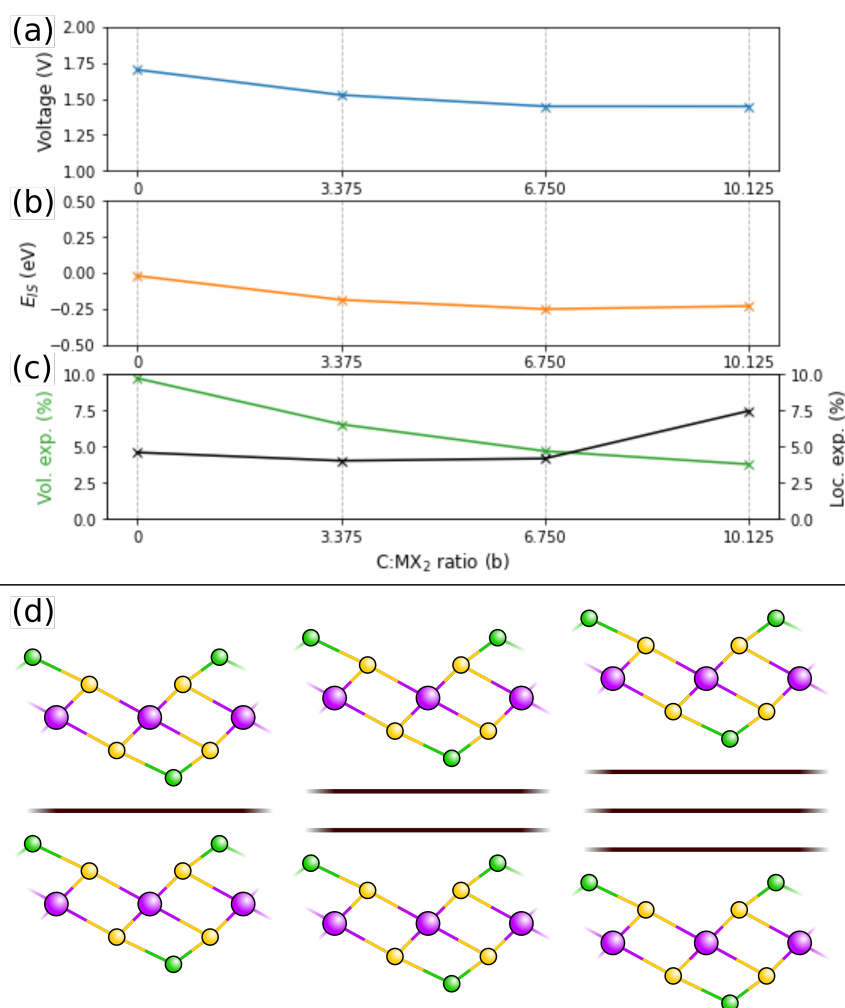


Figure 6.4: (a) The voltage and (b) E_{IS} for MoS₂-T as the number of layers of graphene is increased for a lithium content of $a = 0$ and $a = 1$. (c) shows both the total volumetric expansion in green and the local expansion in the z-axis in black. For the superlattices this is measured from the graphene layer below the TMDC to the graphene layer above, for the TMDC on its own we have used the distance between the closest sulphur atoms in the two neighbouring TMDC layers. (d) is a schematic showing how additional carbon has been added to these systems as additional layers.

bulk regions of both materials) will observe three peaks in its voltage behaviour. The first peak will occur around 1.7 V and be associated with bulk MoS₂ intercalation. The second peak will occur at 1.5 and be associated with the interface and the final much lower peak will be associated with hard carbon (typically of the order of 0.5-1V depending on the carbon). This has been observed in the experiment by Wenelska *et al.* [318] where the interface peak occurs as a shoulder to the main bulk MoS₂ peak with an additional peak at 2.3 V which corresponds to the breakdown into Li₂S.

Looking at the overall expansion of the various carbon superlattices, we can see that the volume expansion decreases with the amount of graphene layers. Given that we are not adding any additional lithium as we increase the number of graphene layers, we need to instead look at how the local environment around the TMDC changes. In order to understand this local environment better, we have also included the local change in the out of plane direction which is measured from the graphene layer just below the TMDC to the graphene layer just above. From this we can actually see that the amount of out of plane space occupied by the TMDC and lithium increases as the number of graphene layers increases. This indicates that the overall decrease in volume expansion as the amount of carbon increases is due to a changes in the in plane lattice expansion.

Our results also show that the local stability of the MoS₂-T layer is also decrease compared to bulk MoS₂-T, with E_{IS} dropping as the amount of carbon, b is increased. We can also see that both the voltage and E_{IS} change in unison, decreasing by roughly the same amount as b is increased. Initially, we see a decrease in E_{IS} . This is due to the donated charge from the Li mainly being absorbed by the TMDC with the graphene not absorbing significant amounts. However, we do see a slight increase in E_{IS} going from $b = 6.750$ to 10.125 where Bader charge analysis [323] indicates that some of the donated charge is now spread to the third graphite layer, which reduces the total charge in the vicinity of the Li-TMDC region and could be responsible for this improvement in stability, details of this are provided at the end of this chapter.

6.4. Conclusion and Chapter Summary

In this work, we have investigated the performance of 9 different TMDC-graphene superlattices for their potential use as Li-ion intercalation electrodes. We have calculated their voltages finding that ScS₂-graphene in both a T- and R-phases possess voltages nearing 3 V, while the other 7 TMDC-graphene superlattices are between 0 V and 1.5 V. The vast majority of these superlattices also show very little volumetric expansion in the range of 5% to 10%, similar to that of NMC

at 8%, the only exceptions to this are SnS₂-T and NiS₂-T which expanded up to nearly 20%.

Looking at the breakdown of these superlattices into Li₂S, LiC₆ and their constituent transition metals, we assess their capacities using a metric of stability, E_{IS} . From all of the superlattices investigated, we found that ScS₂ in both T- and R-phases and TiS₂-T are able to be intercalated up to two Li-ions per MX₂ unit (Li₂MX₂C_b) leading to large capacities of 306.77 mAh/g for both ScS₂ phases and 310.84 mAh/g for TiS₂-T, which were both roughly equivalent to a limit of LiC₂. MoS₂-T was also found to be able to accept lithium up to a limit of $a = 15/16$ in Li_aMoS₂C_b, agreeing with results from see in other studies [316]. This corresponds to a capacity of 121.29 mAh/g, which is equivalent to a limit of LiC₄.

To further explore the effects of graphene in these superlattices, we investigated what would happen to MoS₂-T as additional layers of graphene were added. From this showed that adding more layers of graphene decreased the voltage while our metric of stability, E_{IS} , initially decreased before effectively flat lining. A Bader charge analysis revealed that this may be due to charge being donated to the middle graphene layer, reducing the amount of electrons near the TMDC layer. The overall volume expansion of these superlattices decreases with lithium intercalation as the number of graphene layers is increased, while the local expansion around the TMDC layer increase.

Our results highlights the effects of forming superlattices with TMDCs and graphene for use as Li-ion intercalation electrodes, with low volumetric expansions and high capacities with a wide range of voltages. All of the superlattices investigated have become conductive due to the addition of graphene.

6.5. Supporting Information

6.5.1 Derivation of E_{IS}

The stability of these TMDC-graphene superlattices has been characterised by the formation of Li₂S. When this compound forms in TMDCs it means that a ir-

reversible degradation has occurred, removing both lithium and the chalcogen, which collapses the van der Waals layers that allow for Li-ion intercalation. By assessing the relative stability of these TMDC-graphene superlattices against Li_2S we can construct a phase diagram that indicates when one is more favourable than the other. First we define the enthalpy of formation of relevant products

$$\Delta H(\text{Li}_a\text{MS}_2\text{C}_b) = E(\text{Li}_a\text{MS}_2\text{C}_b) - [a\mu_{\text{Li}}^0 + \mu_{\text{M}}^0 + 2\mu_{\text{S}}^0 + b\mu_{\text{C}}^0], \quad (6.6)$$

$$\Delta H(\text{MS}_2\text{C}_b) = E(\text{MS}_2\text{C}_b) - [\mu_{\text{M}}^0 + 2a\mu_{\text{S}}^0 + b\mu_{\text{C}}^0], \quad (6.7)$$

$$\Delta H(\text{Li}_2\text{S}) = E(\text{Li}_2\text{S}) - [2\mu_{\text{Li}}^0 + \mu_{\text{S}}^0], \quad (6.8)$$

where $\Delta H(\text{A})$ is the enthalpy of formation of compound A, $E(\text{A})$ is the energy of compound A and $\mu_{\text{B}}^0 = E(\text{B})$ is the chemical potential of the element B when it is in its elemental bulk structure and M represents transition metal. Thermodynamic equilibrium requires that

$$\Delta H(\text{Li}_a\text{MS}_2\text{C}_b) = a\Delta\mu_{\text{Li}} + \Delta\mu_{\text{M}} + 2\Delta\mu_{\text{S}} + b\Delta\mu_{\text{C}}, \quad (6.9)$$

where $\Delta\mu_{\text{B}} = \mu_{\text{B}} - \mu_{\text{B}}^0$ with μ_{B} being the chemical potential of the element B in $\text{Li}_a\text{MS}_2\text{C}_b$. This states that the energy of the intercalated superlattice is the sum of the chemical potentials of its constituent atoms. This can be restated as

$$\Delta\mu_{\text{S}} + \frac{b}{2}\Delta\mu_{\text{C}} = \frac{1}{2}[\Delta H(\text{Li}_a\text{MS}_2\text{C}_b) - a\Delta\mu_{\text{Li}} - \Delta\mu_{\text{M}}]. \quad (6.10)$$

We also require that MS_2C_b , Li_2S and the bulk forms of the constituent elements do not form, thus

$$\Delta\mu_{\text{M}} + 2\Delta\mu_{\text{S}} + b\Delta\mu_{\text{C}} \leq \Delta H(\text{MS}_2\text{C}_b) \quad (6.11)$$

$$2\Delta\mu_{\text{Li}} + \Delta\mu_{\text{S}} \leq \Delta H(\text{Li}_2\text{S}), \quad (6.12)$$

$$\Delta\mu_{Li,M,S,C} \leq 0. \quad (6.13)$$

Substituting (6.10) into (6.11) and rearranging

$$\frac{1}{a} [\Delta H(\text{Li}_a\text{MS}_2\text{C}_b) - \Delta H(\text{MS}_2\text{C}_b)] \leq \Delta\mu_{Li}, \quad (6.14)$$

which is our first thermodynamic limit on the chemical potential of lithium that determines when lithium intercalated into MS_2C_b is more favourable than MS_2C_b and bulk lithium. Substituting (6.10) into (6.12) provides

$$\Delta\mu_{Li} \leq \frac{1}{4-a} [2\Delta H(\text{Li}_2\text{S}) - \Delta H(\text{Li}_a\text{MS}_2\text{C}_b) + \Delta\mu_M + b\Delta\mu_C], \quad (6.15)$$

which is our second thermodynamic limit on the chemical potential of lithium that determines when Li_2S does not form. Together these describe the boundary conditions on the chemical potential of lithium based on the formation energies and chemical potentials of relevant products and elements. Given that we have removed all dependence on the chemical potential of the chalcogen (sulphur for all TMDCs investigated), these are dependent only on $\Delta\mu_{Li}$, $\Delta\mu_M$ and $\Delta\mu_C$.

If we consider the relative change in $\Delta\mu_{Li}$ between these two boundaries, Equations(6.14) and (6.15), at $\Delta\mu_M = \Delta\mu_C = 0$, we can quantise a region of stability using a single value E_{IS} . We define this quantity such that a positive value means that there is a region of stability and a negative means there is not, E_{IS} is thus defined as

$$E_{IS} = \frac{2}{4-a} \Delta H(\text{Li}_2\text{S}) + \frac{1}{a} \Delta H(\text{MS}_2\text{C}_b) - \frac{4}{4a-a^2} \Delta H(\text{Li}_a\text{MS}_2\text{C}_b). \quad (6.16)$$

This can also be used for TMDCs without graphene by simply setting $b = 0$.

The values of E_{IS} for the TMDC-graphene superlattices at $a = 1$ and $a = 2$ and the TMDCs without graphene at $a = 1$ are given in Table S 6.2.

Table 6.2: The values of E_{IS} for the TMDC-graphene superlattices at $a = 1$ and $a = 2$ and the bulk TMDCs at $a = 1$.

TMDC	TMDC-graphene		TMDC a = 1
	a = 1	a = 2	
MoS_2 -H	-1.4486	-2.1940	-1.0687
MoS_2 -T	-0.1906	-1.5215	-0.0248
WS_2 -H	-1.5692	-2.6800	-1.5742
SnS_2 -T	-0.7345	-0.7748	-0.2290
ScS_2 -R	2.3434	1.7392	2.6594
ScS_2 -T	2.0365	1.4198	2.8057
NiS_2 -T	-0.7209	-1.2284	0.0136
MnS_2 -T	-0.4807	-1.0503	0.6082
TiS_2 -T	0.3709	0.0994	1.1652

6.5.2 Formation of LiC_6

In addition to the formation of LiS_2 , we have also considered the formation of LiC_6 from the intercalated superlattices. We can state this as



which has limits of

$$\beta \leq \frac{a}{2}, \quad (6.18)$$

$$\beta \geq \frac{6a - b}{12}. \quad (6.19)$$

These represent when there is no LiC_6 formed in the limit there is no additional carbon. Between these limits we found that $Li_aMS_2C_b$ was more favourable for all investigated TMDC-G superlattices. Tables S6.3, S6.4 and S6.5 show the formation energy of $Li_aMS_2C_b$ from all compounds on the right hand side of equation 6.17. A negative formation energy shows that the formation of $Li_aMS_2C_b$ is more favourable, so LiC_6 won't form. All tables show negative formation energies indicating LiC_6 will not form.

Table 6.3: The energetic costs of forming $\text{Li}_{a=1}\text{MS}_2\text{C}_b$ from LiC_6 and various other compounds, based upon equation 6.17.

TMDC	Lower Limit		Upper Limit	
	Form. En. (eV)	β	Form. En. (eV)	β
<i>MoS</i> ₂ -H	-0.8749	0.2188	-1.69	0.5
<i>MoS</i> ₂ -T	-1.9736	0.2188	-2.5676	0.5
<i>WS</i> ₂ -H	-0.8029	0.2188	-1.5488	0.5
<i>SnS</i> ₂ -T	-1.188	0.125	-1.8443	0.5
<i>ScS</i> ₂ -R	-3.1184	0.141	-4.7093	0.5
<i>ScS</i> ₂ -T	-2.7626	0.141	-4.4059	0.5
<i>NiS</i> ₂ -T	-1.3646	0.1795	-1.7052	0.5
<i>MnS</i> ₂ -T	-1.743	0.1905	-2.2955	0.5
<i>TiS</i> ₂ -T	-1.8582	0.1771	-3.2318	0.5

Table 6.4: The energetic costs of forming $\text{Li}_{a=2}\text{MS}_2\text{C}_b$ from LiC_6 and various other compounds, based upon equation 6.17.

TMDC	Lower Limit		Upper Limit	
	Form. En. (eV)	β	Form. En. (eV)	β
<i>MoS</i> ₂ -H	-2.5199	0.7188	-3.3351	1.0
<i>MoS</i> ₂ -T	-3.1075	0.7188	-3.7015	1.0
<i>WS</i> ₂ -H	-1.9872	0.7188	-2.7332	1.0
<i>SnS</i> ₂ -T	-3.461	0.625	-4.1173	1.0
<i>ScS</i> ₂ -R	-6.3053	0.641	-7.8962	1.0
<i>ScS</i> ₂ -T	-5.9334	0.641	-7.5767	1.0
<i>NiS</i> ₂ -T	-2.9944	0.6795	-3.335	1.0
<i>MnS</i> ₂ -T	-3.4747	0.6905	-4.0272	1.0
<i>TiS</i> ₂ -T	-4.8247	0.6771	-6.1982	1.0

6.5.3 Supercells

The in-plane and out of plane lattice constants for the TMDC-graphene superlattices at $a = 0, 1$ and 2 are given in Table S 6.6 and the in plane lattice constant for the bulk TMDCs are given in Table S 6.7. For the TMDC-graphene superlattices these are for the overall supercell and not transition metal to transition metal distances. These values for the superlattices are plotted in the main manuscript in Figures 2(c) and 2(d).

The supercells for $a = 1$ were constructed by taking the fully relaxed supercells for $a = 2$ and uniformly removing lithium. For the $a = 1$ structures where all the lithium was on one side of the TMDC layer this meant that all the lithium on one side was removed. For structures where the lithium is equally spread over both sides of the TMDC layer, lithium from every other lithium site. An example of this is shown in Figure S6.5.

Table 6.5: The energetic costs of forming $\text{Li}_{a=1}\text{MoS}_2\text{C}_b$ from LiC_6 and various other compounds, based upon equation 6.17, for the differing number of graphene layers ($b = 3.375, 6.750$ and 10.125 corresponding to 1, 2 and 3 layers of graphene).

b	Lower Limit		Upper Limit	
	Form. En. (eV)	β	Form. En. (eV)	β
3.375	-1.9736	0.2188	-2.5676	0.5
6.750	-1.5547	0.0	-2.6108	0.5
10.125	-1.6174	0.0	-2.6734	0.5

Table 6.6: In plane and out of plane lattice constants for TMDC-graphene superlattices in Angstroms. These are for the entire superlattice supercells, not the transition metal to transition metal distance.

TMDC	Lat. in plane (Å)			Lat. out of plane (Å)		
	a = 0	a = 1	a = 2	a = 0	a = 1	a = 2
<i>MoS</i> ₂ -H	12.7698	12.8818	13.0662	9.8817	10.4614	10.2790
<i>MoS</i> ₂ -T	12.8141	13.0206	13.1266	9.9824	10.3905	10.0901
<i>WS</i> ₂ -H	12.7725	12.8824	13.0562	9.8576	10.4230	10.2968
<i>SnS</i> ₂ -T	7.3890	N/A	7.4713	9.7767	N/A	11.3144
<i>ScS</i> ₂ -R	13.0551	13.1026	13.1521	9.5638	10.1178	9.8823
<i>ScS</i> ₂ -T	13.0551	13.0944	13.1145	9.5638	10.0900	10.07266
<i>NiS</i> ₂ -T	12.2687	12.3295	12.4748	8.9549	10.1941	9.8154
<i>MnS</i> ₂ -T	8.8761	8.9030	8.9978	9.4412	10.0015	9.8557
<i>TiS</i> ₂ -T	13.6970	13.7446	13.8187	9.5603	10.2224	10.0344

Table S6.8 show the strain on the TMDC and graphene layers in the superlattices along with their respective formation energies. These were all calculated from graphene supercells of the same size as the superlattices and a single unit cell of the TMDCs, the only exception to this is $\text{MnS}_2\text{-T}$. Within the table, $\text{MnS}_2\text{-T}^*$ is the strain and formation energy as calculated with the above method and $\text{MnS}_2\text{-T}$ uses a supercell of the TMDC layer instead. This was done as manganese's potential spin states are complex and numerous. To provide a direct comparison of the spin states, in this case we used the same supercell for the bulk TMDC and the superlattice.

6.5.4 Voltages

The voltages for the TMDC-graphene superlattices for $a = 0 \rightarrow 1$ and $a = 1 \rightarrow 2$ and the TMDCs without graphene for $a = 0 \rightarrow 1$ are given in Table S 6.9. These values for the TMDC-graphene superlattices are plotted in the main manuscript in Figure 2(a).

Table 6.7: The in plane lattice constant for the TMDCs while not in a superlattice and the graphite supercell average carbon-carbon bond lengths in Angstroms.

TMDC	Lat. in plane (Å)		Graphite (Å) C-C dist.
	a = 0	a = 1	
<i>MoS</i> ₂ -H	3.1615	3.1721	1.42407
<i>MoS</i> ₂ -T	3.1821	3.2822	1.42417
<i>WS</i> ₂ -H	3.1650	3.1492	1.42417
<i>SnS</i> ₂ -T	3.6707	3.7772	1.42418
<i>ScS</i> ₂ -R	3.7492	3.6234	1.42417
<i>ScS</i> ₂ -T	3.6291	3.6129	1.42417
<i>NiS</i> ₂ -T	3.3788	3.3945	1.42418
<i>MnS</i> ₂ -T	3.5713	3.3537	1.42424
<i>TiS</i> ₂ -T	3.4136	3.4279	1.42420

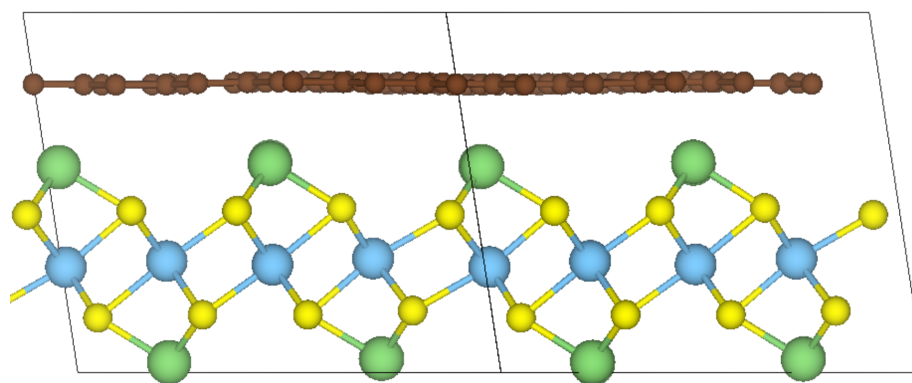


Figure 6.5: The structure of one of the TMDC-graphene superlattices for $a = 1$ where the lithium is spread over both sides of the TMDC.

6.5.5 Volumetric expansion

The volumetric expansion the the TMDC-graphene superlattices for $a = 0 \rightarrow 1$ and $a = 1 \rightarrow 2$ and the TMDCs without graphene for $a = 0 \rightarrow 1$ are given in Table S 6.10. These values for the TMDC-graphene superlattices are plotted in the main manuscript in Figure 2(b).

6.5.6 Effect of additional Graphene

The voltages, E_{IS} , % volumetric expansion and % local expansion for *MoS*₂-T as the number of graphene layers are increased are given in Table S 6.11. These are calculated for lithium contents of $a = 0$ and $a = 1$ in $\text{Li}_a\text{MoS}_2\text{C}_b$ and are plotted in the main manuscript in Figure 4.

The local expansion for bulk *MoS*₂-T is the distance between the closest sulphur atoms in the two neighbouring TMDC layers, this effectively includes the

Table 6.8: The ratios of MX₂ to C along with the strain associated with each layer for the 9 supercells generated using the ARTEMIS [172] package and the formation energies per unit area. The strains are calculated for the TMDCs with no lithium compared with their superlattices with no lithium ($a = 0$).

TMDC	N ^o MX ₂	C:MX ₂ ratio (b)	Strain on TMDC (%)	Strain on Graphene (%)	Formation energy (meV/Å ²)
MoS ₂ H	16	3.3750	0.9794	-0.3630	0.8610
MoS ₂ T	16	3.3750	-0.5935	-0.0253	-8.9538
WS ₂ H	16	3.3750	0.8873	-0.3536	0.04295
SnS ₂ T	4	4.5000	0.6485	-0.1490	6.5286
ScS ₂ R	13	4.3077	-3.4362	0.01825	13.3777
ScS ₂ T	13	4.3077	-0.2399	0.01825	19.8208
NiS ₂ T	13	3.8462	-3.4350	-0.5259	5.8030
MnS ₂ T	7	3.7143	-4.7425	-0.2044	64.2991
MnS ₂ T*	7	3.7143	-7.1114	-0.2044	-10.1196
TiS ₂ T	16	3.8750	0.2909	-0.2700	11.6890

Table 6.9: Voltages for TMDC-Graphene superlattices and their respective TMDCs without graphene.

TMDC	Voltage (eV)		TMDC a = 0 → 1	% decrease a = 0 → 1
	TMDC-Graphene a = 0 → 1	TMDC a = 1 → 2		
MoS ₂ -H	0.4295	0.4085	0.7205	40.3830
MoS ₂ -T	1.5260	0.2905	1.7000	10.2324
WS ₂ -H	0.3971	0.07090	0.4029	1.4442
SnS ₂ -T	1.4470	1.4470	1.6373	11.6228
ScS ₂ -R	2.9596	1.1837	3.1332	5.5409
ScS ₂ -T	2.7294	1.0945	3.2064	14.8762
NiS ₂ -T	1.4581	1.3110	1.9911	26.7691
MnS ₂ -T	1.3812	1.0520	2.2565	38.7901
TiS ₂ -T	1.5092	1.0523	2.0571	26.6346

change in the TMDC layer itself and the change in the van der Waals gap both above and below it as lithium is added. For the superlattices we have used the distance from the graphene layer above the TMDC to the one below, also capturing the change in the TMDC layer and the two van der Waals gaps.

6.5.6.1 Charge Analysis

A Bader charge analysis [324, 325, 326, 323] was carried out on various MoS₂-T systems. Table 6.12 shows the Bader charges of the different species present in MoS₂-T with graphene as the concentration of carbon is increased without any lithium. Also included are the base TMDC without graphene and graphene without the TMDC.

Table 6.10: Volumetric expansion for TMDC-Graphene superlattices and their respective TMDCs without graphene.

TMDC	Volumetric expansion (%)		
	TMDC-Graphene		TMDC
	a = 0 → 1	a = 0 → 2	a = 0 → 1
<i>MoS</i> ₂ -H	7.6632	8.9058	9.4792
<i>MoS</i> ₂ -T	6.4838	6.0682	9.6696
<i>WS</i> ₂ -H	6.6700	9.1470	8.5202
<i>SnS</i> ₂ -T	6.5654	18.3205	16.0291
<i>ScS</i> ₂ -R	6.5399	4.8702	14.5463
<i>ScS</i> ₂ -T	6.1368	6.2799	13.2120
<i>NiS</i> ₂ -T	14.9693	13.3228	24.9218
<i>MnS</i> ₂ -T	5.7221	7.2745	-2.8196
<i>TiS</i> ₂ -T	6.4534	6.8242	15.9876

Table 6.11: The voltage, E_{IS} , % volumetric expansion and % local expansion for *MoS*₂-T as the number of graphene layers are increased.

	Carbon atoms per <i>MX</i> ₂ , b			
	0	3.375	6.750	10.125
Voltage	1.7000	1.5260	1.4475	1.4473
E_{IS}	-0.0248	-0.1906	-0.2548	-0.2341
% expansion	9.6696	6.4838	4.6312	3.7220
% Loc. exp.	4.5396	3.9652	4.1207	7.4130

Table 6.13 shows the Bader charges of the different species present in $\text{Li}_a\text{MoS}_2\text{-T}$ with graphene as the concentration of carbon is increased with lithium at $a = 1$. Also included are the base TMDC without graphene and graphene without the TMDC and 2 Li-ions per 16 carbon atoms.

Table 6.12: The average charge on the different species present in the MoS₂-T graphene superlattices without lithium as b is increased. $b = \infty$ is AA stacked graphite.

Species	N ^o electrons lost				No TMDC ∞
	C:MX ₂ ratio (b)				
	0	3.375	6.750	10.125	
Mo	1.7935	1.7439	1.7012	1.7033	N/A
S	-0.8967	-0.8855	-0.8752	-0.8778	N/A
C1	N/A	0.0080	0.0075	0.0067	N/A
C2	N/A	N/A	0.0071	0.0022	N/A
C3	N/A	N/A	N/A	0.0066	N/A
C Ave.	N/A	0.0080	0.0073	0.0052	0.0000

Table 6.13: The average charge on the different species present in the MoS₂-T graphene superlattices with lithium as b is increased. $b = \infty$ is AA stacked graphite with 2 Li to 16 C.

Species	N ^o electrons lost				No TMDC ∞
	C:MX ₂ ratio (b)				
	0	3.375	6.750	10.125	
Mo	1.6981	1.6198	1.6214	1.6221	N/A
S	-1.2823	-1.1476	-1.1447	-1.1421	N/A
C1	N/A	-0.0591	-0.0306	-0.0281	N/A
C2	N/A	N/A	-0.03092	-0.0070	N/A
C3	N/A	N/A	N/A	-0.0281	N/A
C Ave.	N/A	-0.0591	-0.0307	-0.0211	-0.1068
Li	0.8665	0.8746	0.8757	0.8757	0.8541

Chapter 7

First Principles and Empirical potential

based study of Delithiated

$\text{Ni}_x\text{Mn}_y\text{Co}_{1-x-y}\text{O}_2$ Phase Stability for use in

Li-ion Cathodes

In this chapter, delithiated NMC ($\text{Ni}_x\text{Mn}_y\text{Co}_{1-x-y}\text{O}_2$) has been investigated for its current and further use as a Li-ion battery cathode material. Multiple different stoichiometries and phases of these have been examined to determine when the layered structure, which is key for Li-ion intercalation, is the most favourable. We do this to establish what stoichiometries of NMC, if any, are capable of being completely delithiated. Empirical potentials have been fitted to the data calculated using DFT and convex hulls have been made from both the DFT and the empirical potential data sets. These provide insight into the alloy stability phase space.

7.1. Introduction

The Layered lithium transition metal oxides of the form LiMO_2 ($M = \text{Ni}, \text{Mn}, \text{Co}$) are currently the among most successful group of materials for Li-ion intercalation cathodes in Li-ion batteries. Following the discovery of TiS_2 as a Li-ion intercalation electrode [267, 268, 269], many other layered structures were investigated for this purpose. The first of these to be commercialised was LiCoO_2 which, like TiO_2 , has van der Waals gaps between its CoO_2 layers that can readily accept Li-ion intercalation and extraction [56]. However this material could not be fully deintercalated, becoming unstable at lithium concentration of 0.5 Li per CoO_2 unit. Along side this, it releases oxygen when charged with a high voltage [64]

and has shown capacity fade due to the cobalt dissociation [63]. This led to other layered materials being investigated that could replace LiCoO₂ in commercial applications.

Both LiNiO₂ and LiMnO₂ have been investigated with the same layered structure, showing some benefits and some drawbacks over LiCoO₂. LiNiO₂ suffers from poor thermal stability and breaks down into more favourable Ni-oxides with lithium removal [65], while Spinel phase LiMnO₂ has a lower capacity and undergoes Mn dissociation [67, 270]. An alternative to replacing all the transition metals in LiCoO₂ is a partial substitution leading to the material LiNi_xMn_yCo_{1-x-y}O₂ [280, 281, 282] or LiNi_xCo_yAl_{1-x-y}O₂ [283] (NMC and NCA respectively), which are currently used in commercial batteries. This alloying of transition metals within these layered systems allows for far better control over the materials properties via tuning their exact stoichiometries. While LiCoO₂ has both a high voltage of ≈ 4.25 V and a capacity of 137 mAh/g [56, 327], different stoichiometries of NMC can have both higher voltages and higher capacities, with NMC 111 ($x = y = 1/3$) showing a voltage in the range of 2.5-4.2 V and a capacity of 150 mAh/g [282]. Another stoichiometry shows different properties, with NMC 811 ($x = 0.8, y = 0.1$) having an average voltage of ≈ 3.7 V and a capacity of ≈ 200 mAh/g [328].

However, NMC still suffers from some of the drawbacks of the materials mentioned previously: Mn-rich NMC suffers from greater transition metal dissociation [71], Ni-rich NMC suffers from oxygen release occurring at lower voltages [72], which is related to the coordination of the oxygen atoms [73], as well as Li/Ni disordering [74, 75]. However higher Ni-content does allow for more lithium to be extracted at a set voltage [76]. There are a few methods that can be used to mitigate these problems such as doping [87, 88, 329] and surface modification [330]. Cracks also form during fabrication of Ni-rich NMC [331] which can act as the catalyst for the formation of Li/Ni disordering and phase transitions [332]. On top of all of this, the degradation of NMC releases toxic chemicals into the environment [333, 334, 335, 336]. NiO₂ can be made experimentally completely delithiated. Layered Li_{0.5}NiO₂ can undergo an irreversible phase change

to Spinel $\text{Li}_{0.5}\text{NiO}_2$ which can be intercalated again but can not go back to layered [337, 338]. Finding which stoichiometries of $\text{Ni}_x\text{Mn}_y\text{Co}_{1-x-y}\text{O}_2$ that allows for the full removal of lithium, and thus the greatest capacity, is of utmost importance if NMC is to continue being the primary battery cathode material of the future.

7.2. Method

Figure 7.1 (a) shows a schematic of the overall method followed in this paper. The first step is to investigate multiple transition metal dioxides with density functional theory (DFT) over various $\text{Ni}_x\text{Mn}_y\text{Co}_{1-x-y}\text{O}_2$ stoichiometries in order to find a region in which a layered structure is more preferential, or lower in energy. The layered structure is more optimal for Li-ion batteries than any other phase as the large Van der Waals gap allows for easier Li-ion diffusion within the structure, this is shown in Figure 7.1 (b). Where this layered region exists for NMC, we can move onto the next step: taking the DFT data for only the layered structures and fitting to them empirical potentials: we do this by using the General Utility Lattice Program (GULP) [339, 340]. With this potential we can explore the layered NMC phase space in more depth, faster, and identify stoichiometries that lie on the convex hull. This process is iterated, low points on initial empirical convex hulls are then recalculated within DFT and then used for subsequent empirical potential fits.

The convex hulls used within this work are of a different form to those in previous works. These have three basic compounds, NiO_2 , MnO_2 and CoO_2 , which form the corners with the formation energy of all other mixtures of $\text{Ni}_x\text{Mn}_y\text{Co}_{1-x-y}\text{O}_2$ being calculated with reference to these. This means that all materials investigated have a fixed stoichiometry of two oxygen atoms per transition metal.

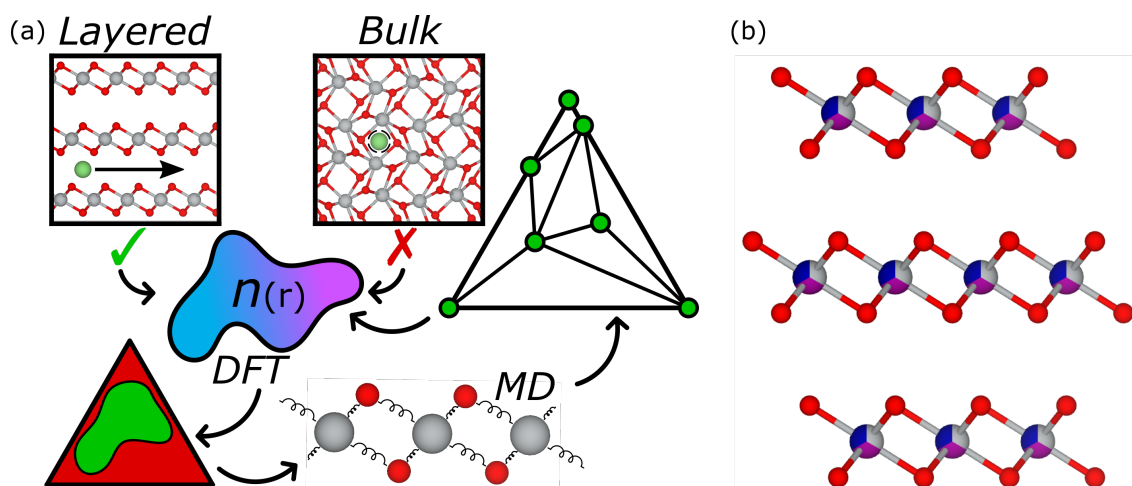


Figure 7.1: (a) A schematic of the workflow followed in this work. A set of $\text{Ni}_x\text{Mn}_y\text{Co}_{1-x-y}\text{O}_2$ structures are put into DFT to explore the phase space, including a layered structure that is preferable for (de)lithiation, a region in which this layered structure is more favourable is found. In order to find the most favourable layered structure, GULP is used to fit potentials to the DFT data and used to generate a convex hull. The most favourable layered structure is put back into DFT to confirm whether or not the search has been successful. (b) The layered structure with R3m symmetry of $\text{Ni}_x\text{Mn}_y\text{Co}_{1-x-y}\text{O}_2$ where each transition metal site can be either Ni, Mn or Co.

7.2.1 Density Functional Theory Parameters

First principles DFT calculations were performed using the Projector augmented wave (PAW) [159, 160] method implemented in the Vienna Ab initio Simulation Package (VASP) [161, 162, 45, 46]. The calculations utilize Perdew-Burke-Ernzerhof electron exchange correlation functions [163, 164]. The plane wave energy cutoff was 500 eV with Γ -centered Monkhorst-Pack grids [165] of $6 \times 6 \times 6$ which were used for the primitive cells, when larger supercells were made, this was reduced such that the reciprocal space k-point density was preserved. Van der Waals interactions were included using the DFT-D3 method of Grimme [53] to account for the weak interactions between the 2D layered materials. The structures were geometrically relaxed until the forces between the atoms were less than $0.01 \text{ eV}/\text{\AA}$ using a combination of the conjugate gradient algorithm [54] and a quasi-Newtonian relaxation algorithm, RMM-DIIS [55]. PAW pseudopotentials were used with the following valence electrons: Ni $3d^8 4s^2$, Mn $3d^5 4s^2$, Co $3d^7 4s^2$ and O $2s^2 2p^4$.

7.2.2 Empirical potentials

DFT calculates the energies for a system from first principles by solving the Schrödinger equation, whereas empirical potentials are simple functions. These are parameterised and fitted to an individual system in order to calculate energetics more efficiently, but less accurately, than DFT. These can take many forms, from simple two-body potentials with very few parameters, such as the Lennard-Jones potential, to three- and four- body potentials each with multiple parameters, angular dependence and separated cores, shells and charges for each atom.

Within these works, we have considered a few different empirical potentials, these were the Lennard-Jones, Morse, Buckingham, coulomb and mixtures of these, before settling on using the Stillinger-Weber potential. The coulomb potential is a simple two-body potential that applies a force depending on the charge of the atoms involved and the distance between them. This has the following form

$$E_{coul,ij} = \frac{1}{4\pi\epsilon_0} \frac{q_i q_j}{r_{ij} \epsilon_{ij}}, \quad (7.1)$$

where q_i is the charge of the i th atom, r_{ij} is the distance between the i th and j th atoms and ϵ_{ij} is the relative permittivity which is a parameter. The total energy of a system of atoms this is calculated with

$$E_{Tot} = \sum_{i,j} E_{coul,ij}, \quad (7.2)$$

where $E_{coul,ij}$ can be replaced with another potential or a sum of multiple different potentials.

The Lennard-Jones potential is an alternative two-body potential of the form

$$E_{Lenn,ij} = 4\epsilon_{ij} \left[\left(\frac{\sigma_{ij}}{r_{ij}} \right)^{12} - \left(\frac{\sigma_{ij}}{r_{ij}} \right)^6 \right], \quad (7.3)$$

which has two fitting parameters, ϵ_{ij} and σ_{ij} . This potential consists of a repulsive and an attractive term, leading to a minima which can be thought of as the equi-

librium bond length between the two atoms being considered. Unlike the coulomb potential, this potential forms a well with a definite minima.

The Buckingham potential was inspired by the Lennard-Jones potential and has the following form

$$E_{Buck,ij} = A_{ij}e^{(-B_{ij}r_{ij})} - \frac{C_{ij}}{r_{ij}^6}. \quad (7.4)$$

This has three fitting parameters, A_{ij} , B_{ij} and C_{ij} . The first term in this expression can be considered as a repulsive term and the second as an attractive term. This was devised as a simplification to the Lennard-Jones potential and has a similar form with a minima.

For the system that was investigated within this piece of work, none of these were found to be sufficient for describing the interactions between the transition metals and oxygen. Instead, a potential with both two-body and three-body terms was used, the Stillinger-Weber potential. The two-body term of this potential is very similar to that of the Lennard-Jones potential but the introduction of a three-body term, that has a dependence on the angle between sets of three atoms, is what differentiates this from the others.

The relaxed geometric and energetic data from the layered (and the planar for reasons that will become clear later) DFT calculations has been used to fit Stillinger-Weber potentials using the General Utility Lattice Program (GULP) [339, 340]. This potential consists of a two-body term

$$E_{SW2,ij} = A_{ij} \cdot \exp\left(\frac{\rho_{ij}}{r_{ij} - r_{Max}}\right) \cdot \left(\frac{B_{ij}}{r_{ij}^4} - 1\right), \quad (7.5)$$

and a three-body term

$$E_{SW3,ijk} = K_{ijk} \cdot \exp\left(\frac{\rho_{ij}}{r_{ij} - r_{Max}}\right) \cdot \exp\left(\frac{\rho_{ik}}{r_{ik} - r_{Max}}\right) \cdot (\cos(\theta_{jik}) - \cos(\theta_0))^2, \quad (7.6)$$

where A_{ij} , ρ_{ij} and B_{ij} are two-body parameters for the potential between atoms i and j with a distance r_{ij} . K_{ijk} is the three body parameter for the atoms i , j

and k which form an angle θ_{jik} with atom i at its centre. r_{Max} is where these terms taper off to zero, having no contributions beyond this distance. Two-body interactions have been used for all O-TM (TM = Ni, Mn, Co) interactions, with $r_{Max} = 3 \text{ \AA}$, all other two-body interactions have been omitted ($A_{ij} = 0$) due to any other "bonds" being over r_{Max} . Three-body interactions have been used for all O-TM-TM interactions with O being the atom at the centre of the bond angle, all other interactions have been omitted ($K_{ijk} = 0$) due to either having more than one bond angle per triplet, such as TM-O-O, or for being over r_{Max} .

To model the molecular dynamic behaviour of these systems, we have made use of the Large-scale Atomic/Molecular Massively Parallel Simulator package (LAMMPS) [15]. Within LAMMPS we have used an energy minimisation routine to find the lowest energy atomic arrangement for each stoichiometry for the layered phase, this is essentially a MD simulation where the kinetic energy of the atoms is fixed to zero. Large supercells of NMC consisting of 81 atoms each have been made over a large range of scales and stoichiometries, while these are of a size that is calculable within DFT, the number of combinations per stoichiometry investigate here would take an unreasonable amount of time. For these systems of 81 atoms, there are 27 transition metal sites to 54 oxygen atoms, every possible stoichiometry between NiO_2 , MnO_2 and CoO_2 of these 27 transition metal sites have been investigated. With 500 random transition metal assignments per stoichiometry for a set scale of the unit cell. These have then been investigated with 7 different scales from 0.995 to 1.025 relative to the size of a pure NiO_2 cell. This leads to 3500 different arrangements being investigated per stoichiometry such that the correct atomic arrangement with the lowest energy is found, these are then used to construct convex hulls.

7.2.3 Phases Investigated

We have investigated eight different transition dioxide phases, these are show in Figure 7.2 (a-h): the layered structure of LiCoO_2 without lithium, the anatase structure of $\beta\text{-TiO}_2$, the rutile structure of $\alpha\text{-TiO}_2$, the distorted structure of ZrO_2

(zirconia), the cubic structure of UO_2 (urania), the planar structure of LiCuO_2 without lithium, the spinel structure of LiMn_2O_4 without lithium and the silica structure of SiO_2 (β -cristobalite). These are used to give a wide range of phases that could potentially be the most favourable for NiO_2 , MnO_2 , CoO_2 and any stoichiometric mix of these three. This should allow us to determine if a layered structure, that is preferable for effective lithium intercalation and deintercalation, is favourable and at what stoichiometries.

The primitive unit cells used for the DFT calculations in this paper have 9, 12, 6, 12, 12, 6, 48 and 24 atoms for the layered, anatase, rutile, distorted, cubic, planar, spinel and silica structures respectively, with one in three of these atoms being the transition metals. Due to the large difference in unit cell sizes, in order to get the same stoichiometries across all the structure, large supercell were often constructed and multiple different arrangements of the transition metals were investigated such that the most favourable configuration at each stoichiometry for each phase was found.

7.3. Results and Discussions

7.3.1 DFT Convex Hull

A convex hull was made using data obtained from DFT for different $\text{Ni}_x\text{Mn}_y\text{Co}_{1-x-y}\text{O}_2$ compositions, this is shown in Figure 7.2 (i). The edges of this convex hull (All single and binary transition metal structures) were investigated using the complete set of eight phases, from this we found that the Cubic and Silica structures were always the least favourable of these, being on average ≈ 0.158 eV per atom less favourable than the third least favourable structure, these were dropped for subsequent stoichiometries investigated. The Anatase structure was also found to be the next least favourable of the remaining structures and was discarded from the search after investigating NMC-111. All of these are shown on the convex hull as coloured triangles as well as any additional stoichiometries that have been investigated with the reduced set of: Layered, Rutile, Distorted,

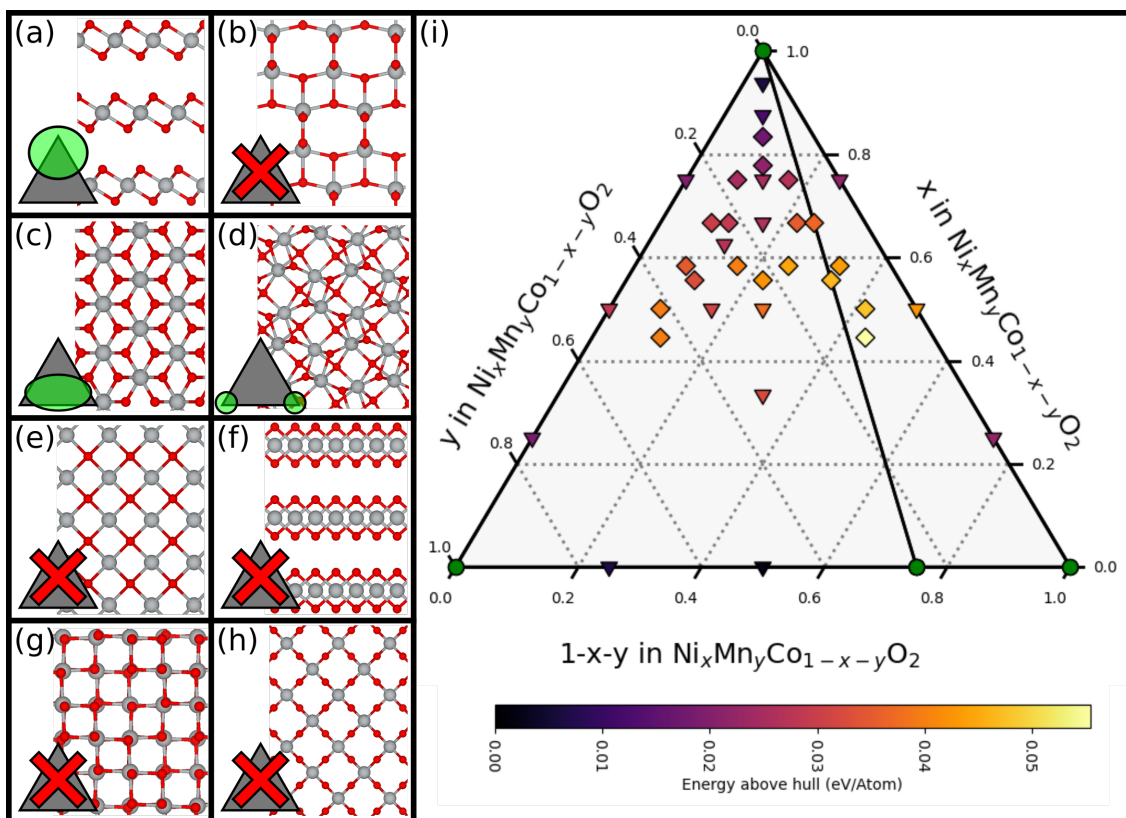


Figure 7.2: All structures considered and where they lie on the Hull. (a) is the layered structure of LiCoO_2 without lithium. (b) is the anatase structure of TiO_2 . (c) is the rutile structure of TiO_2 . (d) is the disordered structure of ZrO_2 (zirconia). (e) is the cubic structure of UO_2 (urania). (f) is the planar structure of LiCuO_2 without lithium. (g) is the spinel structure of LiMn_2O_4 without lithium. (h) is the silica structure of SiO_2 (β -cristobalite). The gray triangles on (a) - (h) show if and where these structures were found to be the most favourable of the set of structures considered. (i) is a convex hull of all the initial structures considered in this study, the green circles are structures that lie on the convex hull, the triangles and squares are for the complete and layered only sets respectively, the colour of which show how far above the convex hull the most stable structure at each stoichiometry is.

Planar and Spinel. It was observed that the Planar structure is unstable without Li for the transition metals Ni, Mn and Co, leading to a phase change to a layered T-phase TMDC structure.

Of the stoichiometries explored, $\text{Ni}_{0.0}\text{Mn}_{0.25}\text{Co}_{0.75}\text{O}_2$ in the Rutile form lies on the convex hull meaning that any other stoichiometry would dissociate into a combination of this, layered NiO_2 , distorted MnO_2 and distorted CoO_2 . For all stoichiometries with less than 50% Ni, a layered structure was always unfavourable, indicating that even if NMC with low Ni content had all its Li removed, it is likely to undergo a phase change to either rutile or zirconia like phases, ignoring any energy cost associated with rearranging the atoms. We emphasise that this would

occur under the conditions where metal/oxygen dissociation is prevented, but dissociation could occur instead. On the other hand, for all stoichiometries above 50% Ni, including NiO₂, the layered phase was found to be more favourable than the other phases.

Given that there is a push for Ni-rich NMC in commercial batteries and that, from our search, we have shown that layered phases are more favourable for these, we have carried out a higher fidelity search of the Ni-rich stoichiometries with only the layered phases (including the planar phase). These layered only additions are shown on the convex hull as coloured diamonds. From this we can see that, in general, structures with more Ni are closer to the hull and stoichiometries with around %50 Ni are the highest above the hull, where as the amount of Mn vs Co has little effect on stability.

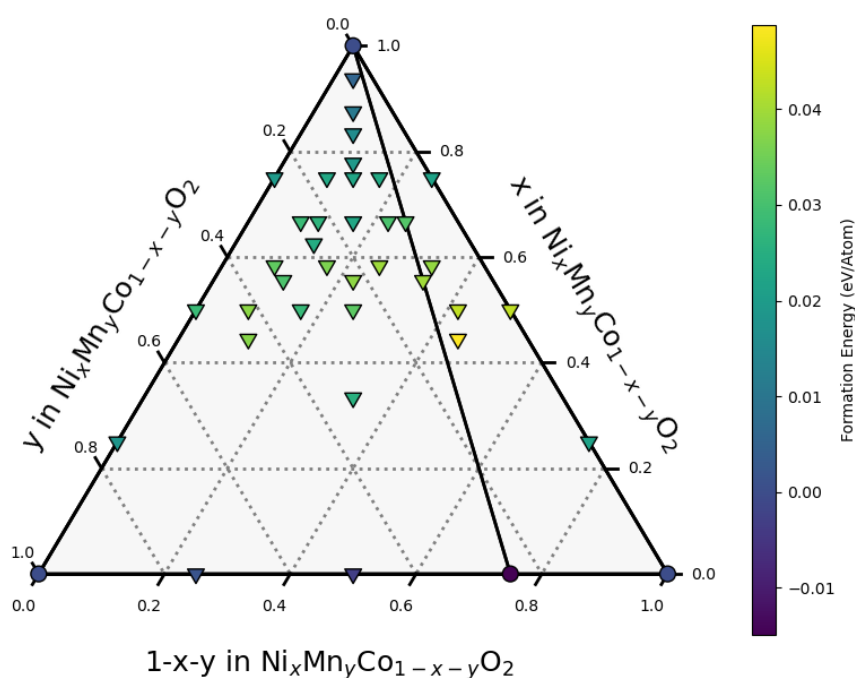


Figure 7.3: DFT calculated convex hull showing the formation energies. The circles are structures that lie on the convex hull, the triangles are for those that do not lie on the convex hull. The colour of these show the formation energies of the most stable structure at each stoichiometry relative to NiO₂, MnO₂ and CoO₂.

There are a few stoichiometries of interest in this set of layered only NMC structures. The stoichiometry that is highest above the convex hull is Ni_{0.4}Mn_{0.1}Co_{0.4}O₂,

shown as a bright yellow diamond on the hull. Shown in Figure 7.3 is the formation energies of these from which we can see that this stoichiometry is extremely unfavourable. The stoichiometries $\text{Ni}_{0.625}\text{Mn}_{0.25}\text{Co}_{0.125}\text{O}_2$, $\text{Ni}_{0.6}\text{Mn}_{0.2}\text{Co}_{0.1}\text{O}_2$ and $\text{Ni}_{0.6}\text{Mn}_{0.25}\text{Co}_{0.083}\text{O}_2$ seem closer to the hull compared to their neighbouring points indicating that there may be a meta stable stoichiometry within this region. For the region where the layered structure was found to be more favourable, as the Ni-content decreases, the formation energy increases (requires more energy to form). If more Co is included than Mn in these layered structures, the formation energy increases at a greater rate. However this can be mitigated by including more Mn than Co. This tells us that for the layered phase, more Ni decreases the formation energy and more Co increases the formation energy meaning that Co-rich stoichiometries will generally be unstable. Within the lower half of the diagram, as Ni content is increased for these, the formation energy increases leading to an overall maximum near $x \approx 0.5$. From all this we can determine that the region of interest, where the layered structure is the most favourable, is the top half of the convex hull with Ni-content above 50%.

7.3.2 Properties of the Layered Materials

A Bader [324, 325, 326, 323] charge analysis of a sub selection of layered NMC structures is shown in Figure 7.4. From this we can see that Manganese donates the most electrons and Nickel donates the least, this lines up with how electro-negative these elements are, with values of 1.91, 1.55 and 1.88 for Nickel, Manganese and Cobalt respectively [341]. The effect of this can be seen in the bader charges of the oxygen as well. Each oxygen is bonded to three transition metals meaning there is a total of eight different bonding environments that oxygen can be in, these eight different environments can be seen in Figure 7.4 as dashed lines. According to bader, the average charge of oxygen atoms with: 3 Ni, 0 Mn and 0 Co is $\approx -0.73 e$, 2 Ni, 0 Mn and 1 Co is $\approx -0.76 e$, 1 Ni, 0 Mn and 2 Co is $\approx -0.78 e$, 0 Ni, 0 Mn and 3 Co is $\approx -0.80 e$, 2 Ni, 1 Mn and 0 Co is $\approx -0.84 e$, 1 Ni,

1 Mn and 1 Co is $\approx -0.86 e$, 1 Ni, 2 Mn and 0 Co is $\approx -0.94 e$ and 0 Ni, 0 Mn and 3 Co is $\approx -1.05 e$.

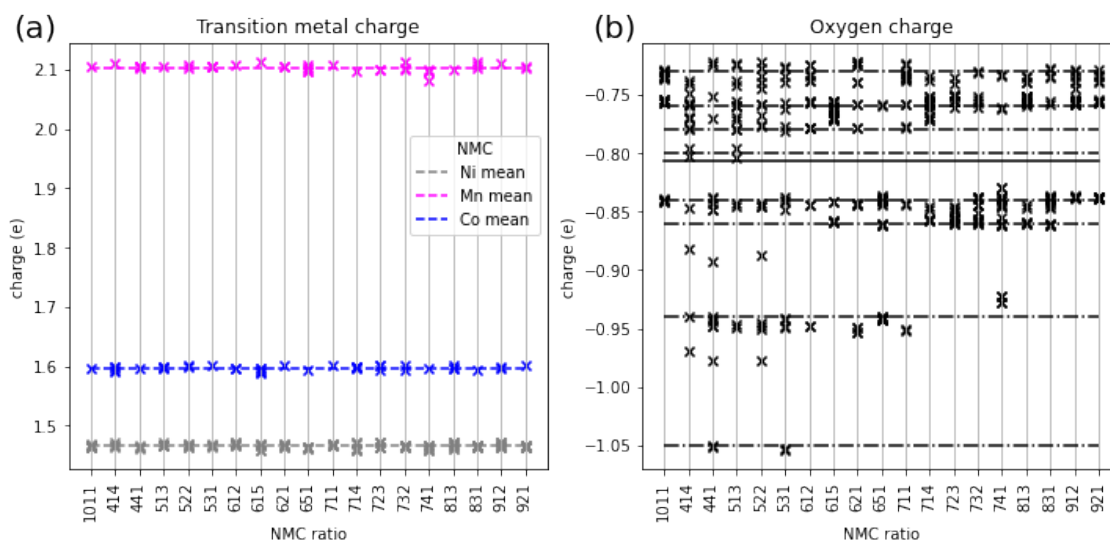


Figure 7.4: A Bader charge analysis of a sub selection of layered NMC structures. (a) shows the charges on the transition metals Ni, Mn and Co with their mean values plotted with dashed lines, (b) shows the charges on the oxygen atoms, the solid black line is the overall average the oxygen atoms while eight additional dashed lines indicate the average charge for oxygen in their eight different bonding situations e.g. what three transition metals they are bonded to.

The transition metal to oxygen bond lengths have also been investigated for use in the empirical potential fitting and these are shown in Figure 7.5. From this we can see that the Ni-O bonds are the most uniform, mainly clustering around the average bond length, while both Mn-O and Co-O show multiple peaks spread across a wider range. This suggests that Jahn-Teller like distortions are occurring in some of these structures for both Mn and Co but not for Ni.

7.3.3 Empirical Convex Hull

A Stillinger-Weber two- and three-body potential was fitted for TM-O (TM = Ni, Mn, Co) and O-TM-TM respectively where O is the atom at the centre of the bond. The energies calculated from DFT and the energies from this fitted potential are shown in Figure 7.6(a) and the form of the two-body parts of the potential is shown in Figure 7.6(b). From the initial fit we can see good agreement with the energies from DFT.

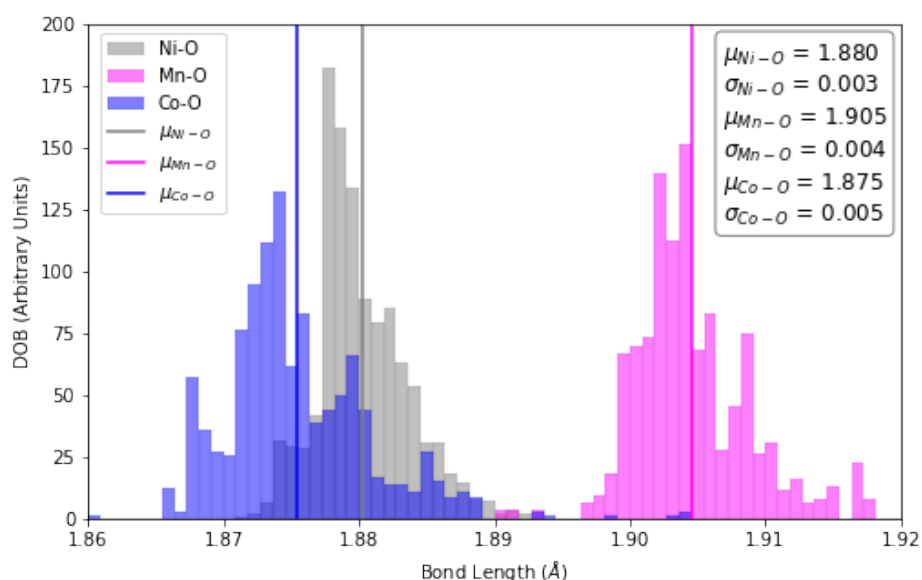


Figure 7.5: Plot of the Bond lengths between each of the transition metals and their neighbouring oxygen atoms. These are from all layered structures that were used in fitting the empirical potential in GULP.

While the two-body potentials here are very shallow, it was found that these agreed more with the DFT energies than steeper potentials, this was due to the wide range of bond lengths found for both Mn-O and Co-O bonds. While both a steep and a shallow potential have a definite minimum, having a shallower potential means that the forces on the atoms will be less powerful with a slight offset from the minima, allowing for slight distortions without too great an increase in energy. This was found to produce a much better fit than a steep Stillinger-Weber potential and the other empirical potentials that have been considered.

From the empirical convex hull we can see that no mixture of NiO₂, MnO₂ and CoO₂ is more favourable than the isolated compounds. The NiO₂ to CoO₂ edge of the hull has 8 points along it that lie on the hull, however it is relatively flat, with all of these having roughly the same energy as NiO₂ to CoO₂ separately. Increasing the amount of MnO₂ increases the formation energy to a maximum around $y \approx 0.625$ before decreasing again down to the MnO₂ corner. Within the middle region of this graph, higher NiO₂ content leads to a slightly higher formation energy than higher CoO₂ content.

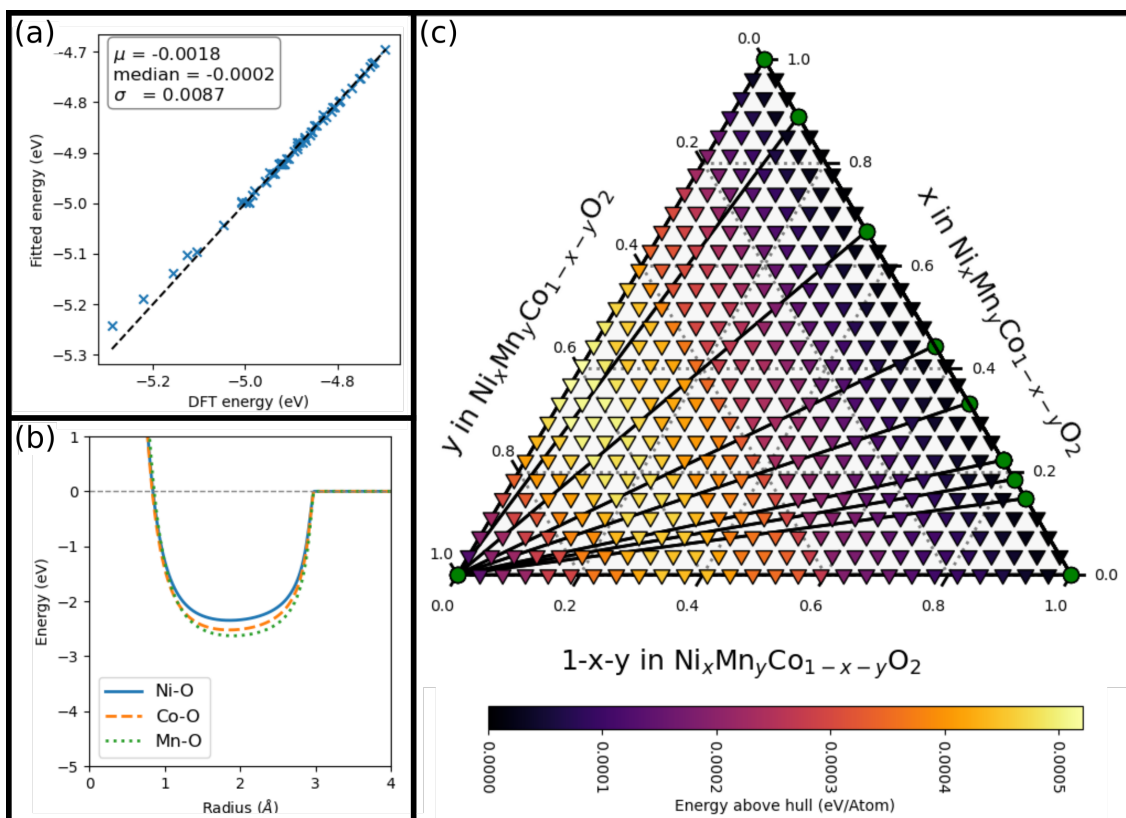


Figure 7.6: (a) Energies of layered structures in DFT vs in GULP. (b) Form of the two-body Stillinger-Weber potentials fitted with GULP. (c) Convex hull for layered NMC from LAMMPS using potentials fitted in GULP, the green circles are structures that lie on the convex hull and the triangles do not lie on the hull, their colour indicates how far above the hull these are.

7.3.4 DFT, GULP and LAMMPS Comparison

Comparing the energies from DFT, GULP and LAMMPS, we can determine how useful these empirical potentials are, this is plotted in Figure 7.7. Both DFT and GULP show good agreement for the Ni-rich layered systems, with the largest error in this region being ≈ 0.01 eV per atom however, the Mn-rich layered systems show larger errors, with the largest being ≈ 0.0464 eV per atom, this is MnO_2 which shows large Jahn-Teller like distortions in its structure. The two-body potentials used within this work have a single minima and, therefore, a single most energetically favourable bond length, whereas structures with Jahn-Teller like distortions will have both elongated and compressed bonds that lie either side of this minima which increases their energies. Many of the Mn-rich structures show some Jahn-Teller distortions leading to these having this greater disparity in energy between DFT and GULP.

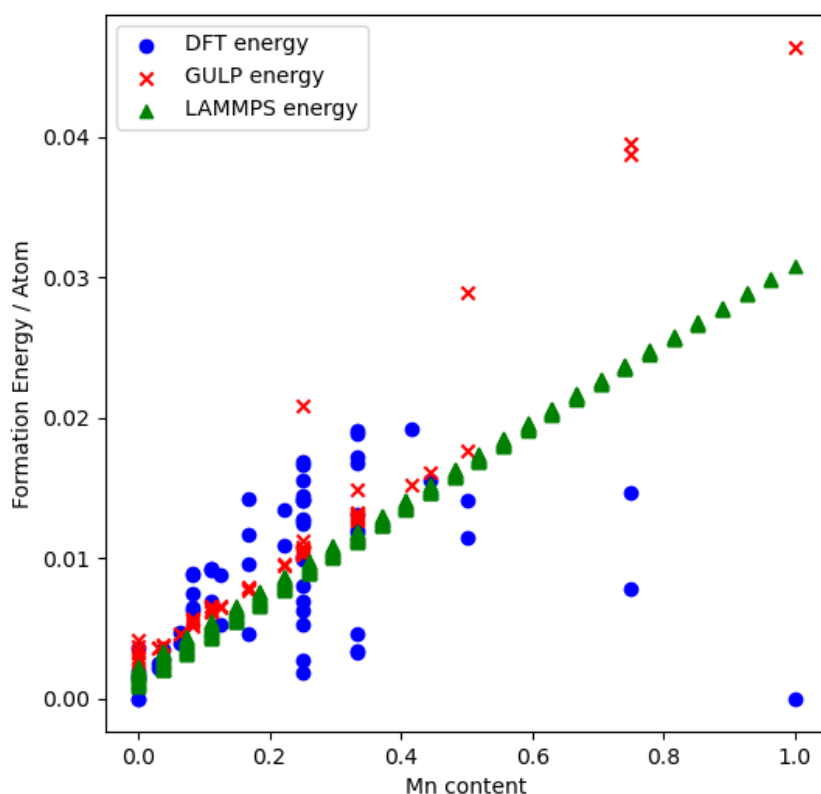


Figure 7.7: A comparison between the energies calculated in DFT, GULP and LAMMPS for the NMC space relative to the formation energies of NiO_2 , MnO_2 and CoO_2 as calculated in DFT.

When these potentials were then used within LAMMPS with an energy minimisation algorithm, the transition metal to oxygen bonds all relaxed towards the minimum energy bond lengths. This means that none of the structures relaxed within LAMMPS show Jahn-Teller like distortions. This has led to the overall LAMMPS energy space being far flatter than that of both DFT and GULP, with variations in the formation energy being on the order of 1×10^{-4} eV per atom in LAMMPS vs 1×10^{-2} eV in DFT. This is a clear indication that these simple empirical potentials are unable to account for the nuances of these layered transition metal dioxide systems, even with the addition of the three-body Stillinger-Weber term. In order to better capture the interactions in these systems, either a four-body term or a more complex two-body term that includes multiple localised minima is required. Thus the empirical potentials investigated here do not provide us with any additional insight that was not already provided by the DFT calculations.

7.4. Conclusion and Chapter summary

In this chapter, eight different transition metal dioxide phases have been investigated using DFT within the $\text{Ni}_x\text{Mn}_y\text{Co}_{1-x-y}\text{O}_2$ space to determine when the layered phase, that is key for the intercalation and deintercalation of Li-ions, is the most favourable. It was found that the layered structure is the most favourable phase of those investigated for Ni-rich NMC, $x > 0.5$, while non-layered phases were more favourable for the Mn- and Co-rich regions. However, of these layered structures, only layered NiO_2 was found to lie on the convex hull. Looking at the properties of the layered structures, it was found that Jahn-Teller like distortions occur for some Mn and Co atoms, leading to a wide range of transition metal to oxygen bond lengths. Taking this DFT data, a two- and three-body Stillinger-Weber potential was fitted using GULP for the layered structures, which was then used within LAMMPS to generate a layered only convex hull with a far larger set of data. From this we found that $\text{Ni}_x\text{Mn}_y\text{Co}_{1-x-y}\text{O}_2$ with high amounts of Mn leads to higher formation energies. However, this energetic space is far flatter than that found using DFT due to the lack of Jahn-Teller like distortions within this data set. This indicates that a far more complex potential is required for this type of system.

Overall, we have found that Ni-rich NMC prefer the layered phase over any other phase that we have investigated. From this we can see that Ni-rich NMCs are able to accommodate the removal of more of their lithium, leading to higher capacities over NMCs with low Ni-content. This indicates that while the stable removal of all lithium from these materials may not be possible, the region $0.6 \leq x \leq 0.625$, $0.2 \leq y \leq 0.25$ and $0.083 \leq 1 - x - y \leq 0.125$ in $\text{Ni}_x\text{Mn}_y\text{Co}_{1-x-y}\text{O}_2$ is the most likely to offer the highest capacities.

Chapter 8

Conclusions and Outlook

8.1. Summary

In this thesis, we have studied many different two-dimensional materials for their use as either devices for photoelectrolysis or as Li-ion battery electrodes. Both of which are key technologies for the future of the human race and the planet as a whole.

Chapter 1 provides insight into the climate crisis, outlining potential solutions, methods for looking into these solutions from a theoretical standpoint and some of the crystalline materials that are investigated within this thesis. Chapter 2 provides an in-depth exploration of Density functional theory and the principles upon which it is built, which serves as the foundation for much of computational materials science. DFT is a powerful tool capable of predicting the electronic structure and properties for systems of atoms that can be described either as an infinitely repeating unit (if planewave wavefunctions are used) or as molecules (if Gaussian wavefunctions are used). The Hohenberg-Kohn theorems eloquently show how all the properties of a system can be functionalised in terms of density while Kohn-Sham built upon this, by reducing the computational cost dramatically by mapping the original interacting system of electrons onto a system of non-interacting electron-like particles. Understanding the founding principles of DFT is paramount to using it to its fullest capabilities.

Chapter 3 covers the intricacies of batteries and photoelectrolysis devices, going over the historical context, theoretical foundations and the current state of the art in both fields. A clear set of challenges has been outlined that need to be overcome in order to advance these fields of research. In the following chapters we hope to address some of these.

In chapter 4, a derivation of phase diagrams and their use was covered, there we then used to show the relative stability of different adsorbed species on monolayer MoS₂ and PdSe₂ and the heterostructure that was constructed from these. The results of this chapter have shown that the energetics of these adsorbed species, and the water splitting reactions that they are involved in, are unaffected by the presence of another material in a heterostructure. This indicates, at least for layered materials that interact *via* van der Waals forces, that materials can be selected for different properties and combined into a heterostructure that would benefit from all these properties. Overall, this means that a material that has a large band gap, large enough for the HER and OER and their overpotentials, can be combined with a material that is more favourable for the energetic steps of the HER and OER in order to make a device that is more efficient than its constituent components. However, further study would be required to confirm this fact.

The surface of T-phase PdSe₂ was shown to require a smaller overpotential for both HER and OER than H-phase MoS₂ in all considered reaction pathways. Whereas H-phase MoS₂ was shown to have superior band alignment with the HER and OER. For all systems investigated, we found that the rate limiting step was always the third step of the OER, where an O* adsorption reacted to become and HOO* adsorption. If the overpotential that is required to overcome this third step was applied, the HER would occur as well, requiring less energy than OER.

In chapter 5, an explanation of convex hulls and their use was covered, these were used to show the relative stability of Sc-S and Sc-O compounds. From these we saw that the layered phase was the most favourable for ScS₂ while this was not the case for ScO₂, however neither of these stoichiometries are on the convex hull. ScS₂ was investigated for use as a Li-ion and beyond Li-ion (Na, K and Mg) battery electrode and showed great potential as a Li-ion cathode. This layered material has a phase change from T- to α -phase as lithium content is increased, however it was found that this material is unstable at low lithium content. Phonon calculations were used to get a lower limit for lithium intercalation and it was found that this occurs at $a = 0.25$ for Li _{a} ScS₂. The upper limit of intercala-

tion was investigated using a new qualitative metric, E_{IS} , based on the formation of Li_2S and ScS_2 from Li_aScS_2 . It was found that this material possesses a remarkably large window of stability when compared to that of other TMDCs, being stable at $a = 1$. From this the overall capacity was shown to be 182.99 mAhg^{-1} .

For Li-ion intercalation, ScS_2 was found to have a high average voltage of 3.977 V and had lower voltages for Na, K and Mg of 3.874 V , 3.799 V and 1.474 V respectively. It was also found that ScS_2 has a Fermi level which lies within an electronic band, indicating that this material is conductive, meaning it does not require the addition of a conductive binder for use. ScS_2 also possesses a remarkable volumetric expansion with lithium that is below 10%, this is similar to that of NMC which is commercially used in the batteries of today. All of this points towards LiScS_2 showing great potential for use as a Li-ion battery cathode.

In chapter 6, nine different TMDC-graphene superlattices have been investigated for their use as Li-ion intercalation electrodes. We have calculated their voltages finding that ScS_2 -graphene in both a T- and R- phases possess voltages nearing 3 V , while the other seven TMDC-graphene superlattices possess voltages in the range of 0 V to 1.5 V . Most of these TMDC-graphene superlattices show very little volumetric expansion in the range of 5% to 10% which is comparable to that of NMC at 8%. Only SnS_2 -T and NiS_2 -T expand more than this, in the range of 10% to 20%. From looking at the potential breakdown of these materials into Li_2S or LiC_6 we have assessed the capacities of these superlattices. For all of these we found that the formation of LiC_6 was never more favourable than the TMDC-graphene superlattice. We found that ScS_2 -T, ScS_2 -R and TiS_2 -T are able to be intercalated up to at least 2 lithium per MX_2 ($\text{Li}_2\text{MX}_2\text{C}_b$) unit without breaking down into Li_2S , showing large capacities of 306.77 mAh/g for both ScS_2 phases and 310.84 mAh/g for TiS_2 -T. This is equivalent to roughly a LiC_2 limit for these three superlattices. MoS_2 -T was also found to be able to accept lithium up to a limit of $a = 15/16$ in $\text{Li}_a\text{MoS}_2\text{C}_b$ which corresponds to a capacity of 121.99 mAh/g and is equivalent to a limit of LiC_4 . The effect of additional graphene was also investigated for the MoS_2 -T system. Adding more layers decreased the voltage

and reduced E_{IS} before it effectively flat lined. The overall volumetric expansion of these also decreased as the number of layers was increased.

These results highlight the effects of forming superlattices with TMDCs and graphene for use as Li-ion intercalation electrodes showing low volumetric expansions, high capacities and a wide range of voltages, while becoming electrically conductive which is something most layered intercalation electrodes are poor at.

In chapter 7, eight different transition metal dioxide phases were investigated using DFT within the $Ni_xMn_yCo_{1-x-y}O_2$ space to determine when the layered phase, that is key for the intercalation and deintercalation of Li-ions, is the most favourable. It was found that the layered structure is the most favourable phase of those investigated for Ni-rich NMC, $x > 0.5$, while non-layered phases were more favourable for the Mn- and Co-rich regions. However, of these layered structures, only layered NiO_2 was found to lie on the convex hull. Looking at the properties of the layered structures, it was found that Jahn-Teller like distortions occur for some Mn and Co atoms, leading to a wide range of transition metal to oxygen bond lengths. Taking this DFT data, a two- and three-body Stillinger-Weber potential was fitted using GULP for the layered structures, which was then used within LAMMPS to generate a layered only convex hull with a far larger set of data. From this we found that $Ni_xMn_yCo_{1-x-y}O_2$ with high amounts of Mn leads to higher formation energies. However, this energetic space is far flatter than that found using DFT due to the lack of Jahn-Teller like distortions within this data set. This indicates that a far more complex potential is required for this type of system.

Overall, we have found that Ni-rich NMC prefer the layered phase over any other phase that we have investigated. From this we can see that Ni-rich NMCs are able to accommodate the removal of more of their lithium, leading to higher capacities over NMCs with low Ni-content. This indicates that while the stable removal of all lithium from these materials may not be possible, the region $0.6 \leq x \leq 0.625$, $0.2 \leq y \leq 0.25$ and $0.083 \leq 1 - x - y \leq 0.125$ in $Ni_xMn_yCo_{1-x-y}O_2$ is the most likely to offer the highest capacities.

8.2. Future Work

Despite the years of work that have gone into this thesis, there is still much work that could be expanded upon and extended. In chapter 4 we explored the use of heterostructuring as a means to create more efficient photoelectrolysis devices, however we only investigated a single combination of TMDCs made of a single layer of the two TMDCs considered. In the conclusion of this piece of work it was determined that a single layer of a TMDC on the surface of many layers of another TMDC could lead to a very efficient device, but we did not test this. A study on other combinations of TMDCs and on a many-layer device would give a deeper understanding of the interactions between the different TMDCs for their use as photoelectrolysis devices.

In chapters 5, the TMDC LiScS_2 was explored for its use as a Li-ion and beyond Li-ion battery electrode. While this was a very in depth theoretical study, a full exploration of the Sc-S-Li phase space could be carried out to determine more about the relative stability of LiScS_2 to Li_2S , Sc and Li formation. This would mean studying additional compounds made up of Li, Sc and S. LiScO_2 was also discarded as a potential battery electrode early on in this work due to the layered phase not being the most favourable form. This material could be further explored to determine whether the layered form of LiScO_2 is dynamically stable, via investigating its phonon modes, as oxides often lead to higher voltage materials than sulphides.

In chapter 6, we investigated the effect of creating superlattices of TMDCs and graphene for use as Li-ion electrodes. Nine different TMDCs were investigated in this, an easy extension to this work would be to investigate more TMDCs so that the exact effect that graphene has on them can be extended more generally. These superlattice also had a plethora of different Li-ion intercalation sites which we explored in a limited manner due to the huge number of potential combinations. One of the smaller superlattices could be further investigated by looking at more combinations and different concentrations of Li-ions to get a more detailed voltage curve and a more exact value for the E_{IS} sign flip.

In chapter 7, we found that simple empirical potentials were able to capture the general energetic trends of layered NMC materials, however, they were unable to show any effect of Jahn-Teller like distortions. Creating a new form of potential that can account for these distortions could lead to a far greater understanding of these materials and allow for more robust conclusions to be drawn about these. This could even be extended further by looking at the effects of adding lithium back into these systems.

8.3. Closing Remarks

The work contained within this thesis has explored many different two-dimensional materials for energy applications. Heterostructuring, superlatticing and alloying show promise for tailoring the properties of two-dimensional materials for both photoelectrolysis and energy storage uses.

Appendix A

Lattice and Basis Vectors for TMDCs

TMDCs have real space lattice vectors of a hexagonal lattice

$$\begin{aligned}\mathbf{a}_1 &= a\hat{x}, \\ \mathbf{a}_2 &= -\frac{1}{2}a\hat{x} + \frac{\sqrt{3}}{2}a\hat{y}, \\ \mathbf{a}_3 &= c\hat{z},\end{aligned}\tag{A.1}$$

where \mathbf{a}_1 and \mathbf{a}_2 have the same length, These have corresponding reciprocal lattice vectors

$$\begin{aligned}\mathbf{b}_1 &= \frac{2\pi}{a} \left(\hat{k}_x + \frac{1}{\sqrt{3}}\hat{k}_y \right), \\ \mathbf{b}_2 &= \frac{2\pi}{a} \left(\frac{2}{\sqrt{3}}\hat{k}_y \right), \\ \mathbf{b}_3 &= \frac{2\pi}{c}\hat{k}_z.\end{aligned}\tag{A.2}$$

The H-phase TMDCs have the following coordinates for the transition metal (M) and chalcogen (X) atoms given in terms of the lattice vectors (crystal coordinates)

$$\begin{aligned}\mathbf{M} &: [0, 0, 0.5], \\ \mathbf{X}_1 &: \left[\frac{1}{3}, \frac{2}{3}, 0.5 + \delta \right], \\ \mathbf{X}_2 &: \left[\frac{1}{3}, \frac{2}{3}, 0.5 - \delta \right].\end{aligned}\tag{A.3}$$

For T-phase TMDCs these are

$$\begin{aligned}
\mathbf{M} &: [0, 0, 0.5], \\
\mathbf{X}_1 &: \left[\frac{1}{3}, \frac{2}{3}, 0.5 + \delta \right], \\
\mathbf{X}_2 &: \left[\frac{2}{3}, \frac{1}{3}, 0.5 - \delta \right].
\end{aligned}
\tag{A.4}$$

In both of these the distance between the M and X atoms along the \mathbf{a}_3 real lattice direction is given as $0.5 \pm \delta$ to indicate that both X layers are equal distance from the M layer with one being above and one being below.

Appendix B

Jahn-Teller Distortions

The d -shell electrons around transition metals are made up of five orbitals labelled d_{xy} , d_{xz} , d_{yz} , $d_{x^2-y^2}$ and d_{z^2} . For an octahedral complex (6 bonds), these orbitals are split into two degenerate sets, the first is called the t_{2g} and consists of the d_{xy} , d_{xz} and d_{yz} orbitals, this is lower in energy than the second, which is called the e_g and consists of the $d_{x^2-y^2}$ and d_{z^2} orbitals. The t_{2g} are lower in energy than the e_g within these complexes as the e_g orbitals lie along the bonds where the negative charge of electrons also lies, whereas the t_{2g} are in between these bonds.

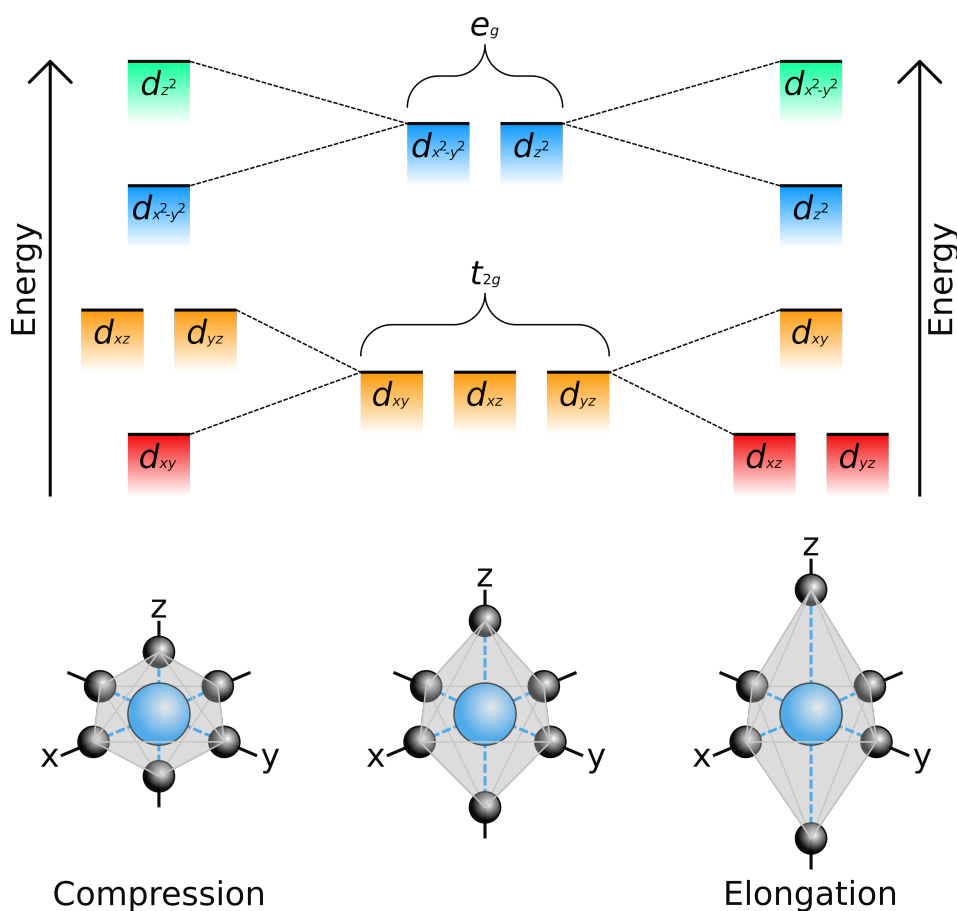


Figure B.1: A schematic of Jahn-Teller distortions showing how the degenerate t_{2g} and e_g states split causing compression or elongation along the z-direction.

When these orbitals are filled they become lower in energy and the unfilled orbitals become higher in energy. Due to their alignments relative to the x , y and z directions, orbitals that are oriented similarly will become shifted if another is filled or unfilled, meaning if the t_{2g} states with z -components become filled and lower in energy, the unfilled e_g state with a z -component will also become lower in energy, this is shown in Figure B.1.

This shift in the energy of the states also changes the relative lengths of the octahedral bonds, when t_{2g} and e_g are degenerate all the bonds in the octahedral complex are of equal length. When the z -component orbitals become lower in energy, the bonds along the z -direction become elongated relative to the bonds in the x - y plane, and when the z -component orbitals become higher in energy, the bonds along the z -direction become compressed relative to the bonds in the x - y plane. These are called Jahn-Teller distortions and while we have outlined how this can occur in d -orbitals here, it can also occur in other bonding arrangements for other orbitals.

The exact filling of the t_{2g} and e_g states can lead to both strong and weak Jahn-Teller distortions, with unevenly occupied e_g orbitals leading to a strong distortion and unevenly occupied t_{2g} orbitals leading to a weak distortion. The filling and Jahn-Teller distortion strength and type for $d1$ to $d5$ are shown in Figure B.2 and for $d6$ to $d10$ in Figure B.3.

While this is mainly observed in almost fully ionic systems, where the transition metals lose an integer amount of electrons to the octahedrally bonded ligands, it can still be observed in more covalent like octahedral complexes even when the orbitals are not "filled" simply due to orbital overlap between the transition metal and the ligands.

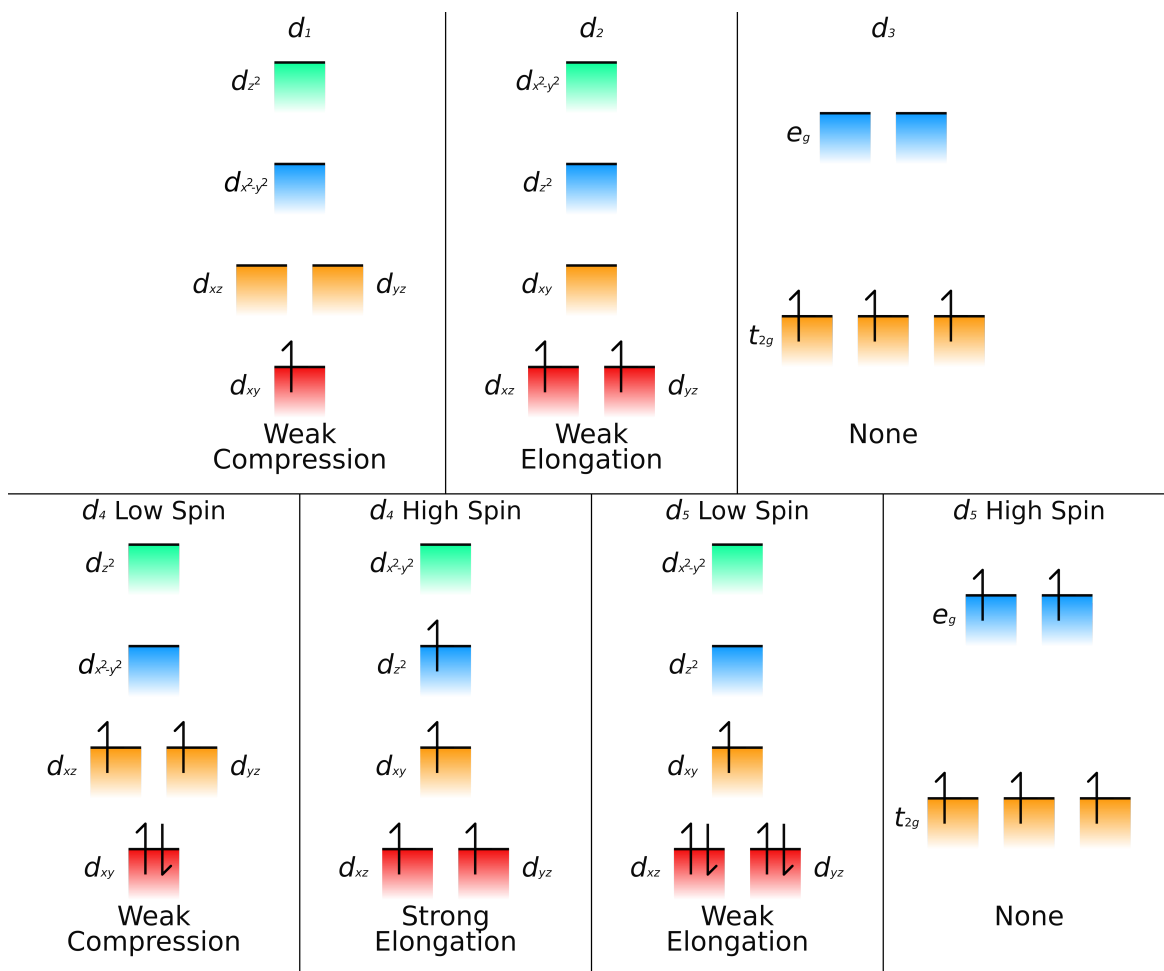


Figure B.2: The filling of the d -shell orbitals for d_1 to d_5 with the strength and type of the Jahn-Teller distortion.

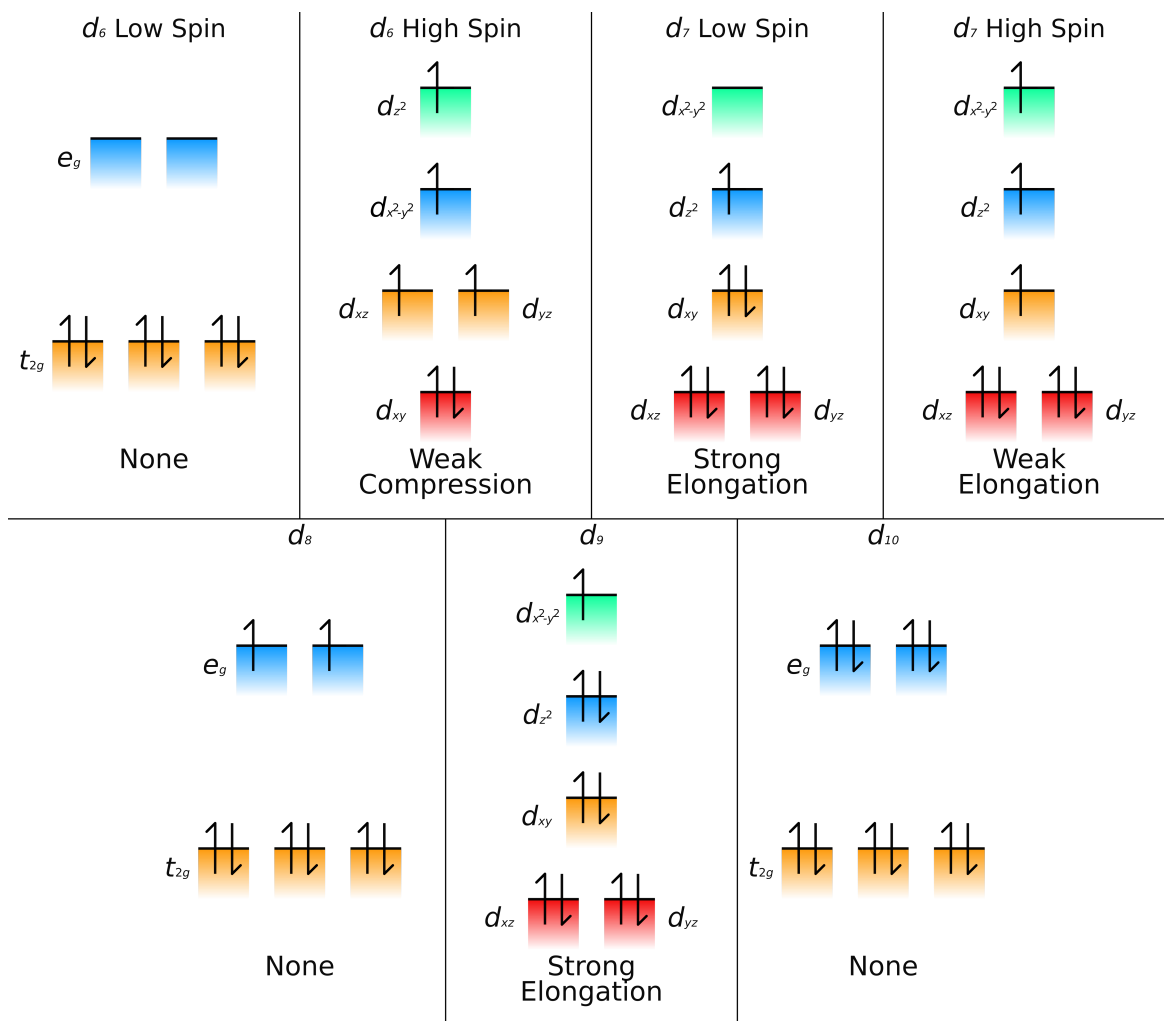


Figure B.3: The filling of the d -shell orbitals for d_6 to d_{10} with the strength and type of the Jahn-Teller distortion.

Bibliography

- [1] BP statistical review of world energy 2020.
- [2] Rebecca Lindsey. Climate change: Atmospheric carbon dioxide. 2021.
- [3] Global monitoring laboratory - carbon cycle greenhouse gases.
- [4] Pierre Friedlingstein, Michael O'Sullivan, Matthew W. Jones, Robbie M. Andrew, Judith Hauck, Are Olsen, Glen P. Peters, Wouter Peters, Julia Pongratz, and Stephen et al. Sitch. Global carbon budget 2020. *Earth System Science Data*, 12(4):3269–3340, 2020.
- [5] Germain Vallverdu, Marie Minvielle, Nathalie Andreu, Danielle Gonbeau, and Isabelle Baraille. First principle study of the surface reactivity of layered lithium oxides LiMO_2 (M = Ni, Mn, Co). *Surface Science*, 649:46–55, 2016.
- [6] Naoaki Yabuuchi and Tsutomu Ohzuku. Novel lithium insertion material of $\text{LiCo}_{1/3}\text{Ni}_{1/3}\text{Mn}_{1/3}\text{O}_2$ for advanced lithium-ion batteries. *Journal of Power Sources*, 119-121:171–174, 2003.
- [7] Chen-Xi Zu and Hong Li. Thermodynamic analysis on energy densities of batteries. *Energy and Environmental Science*, 4:2614–2624, 2011.
- [8] Liangxu Lin, Shaowei Zhang, Yuqing Liu, Gordon G. Wallace, and Jun Chen. Two-dimensional transition metal dichalcogenides in supercapacitors and secondary batteries. *Energy Storage Materials*, 19:408–423, 2019.
- [9] DOE technical targets for hydrogen production from electrolysis, 2021.
- [10] DOE hydrogen production: natural gas reforming, 2021.
- [11] Kazuhiko Maeda. Photocatalytic water splitting using semiconductor particles: History and recent developments. *Journal of Photochemistry and Photobiology C: Photochemistry Reviews*, 12(4):237–268, 2011.
- [12] Jingrun Ran, Jun Zhang, Jiaguo Yu, Mietek Jaroniec, and Shi Zhang Qiao. Earth-abundant cocatalysts for semiconductor-based photocatalytic water splitting. *Chem. Soc. Rev.*, 43:7787–7812, 2014.
- [13] Axel D. Becke. Perspective: Fifty years of density-functional theory in chemical physics. *The Journal of Chemical Physics*, 140(18):18A301, 2014.

- [14] Peter Y Yu and Manuel Cardona. *Fundamentals of semiconductors*. Springer, 2005.
- [15] A. P. Thompson, H. M. Aktulga, R. Berger, D. S. Bolintineanu, W. M. Brown, P. S. Crozier, P. J. in 't Veld, A. Kohlmeyer, S. G. Moore, T. D. Nguyen, R. Shan, M. J. Stevens, J. Tranchida, C. Trott, and S. J. Plimpton. LAMMPS - a flexible simulation tool for particle-based materials modeling at the atomic, meso, and continuum scales. *Comp. Phys. Comm.*, 271:108171, 2022.
- [16] Stephen J. McDonnell and Robert M. Wallace. Atomically-thin layered films for device applications based upon 2D TMDC materials. *Thin Solid Films*, 616:482–501, 2016.
- [17] E Benavente. Intercalation chemistry of molybdenum disulfide. *Coordination Chemistry Reviews*, 224(1–2):87–109, May 2002.
- [18] Lifan Wang, Zhi Xu, Wenlong Wang, and Xuedong Bai. Atomic mechanism of dynamic electrochemical lithiation processes of MoS_2 nanosheets. *Journal of the American Chemical Society*, 136(18):6693–6697, Apr 2014.
- [19] Liang Zhang, Dan Sun, Jun Kang, Jun Feng, Hans A. Bechtel, Lin-Wang Wang, Elton J. Cairns, and Jinghua Guo. Electrochemical reaction mechanism of the MoS_2 electrode in a lithium-ion cell revealed by in situ and operando x-ray absorption spectroscopy. *Nano Letters*, 18(2):1466–1475, Jan 2018.
- [20] M.R. Hilton, R. Bauer, and P.D. Fleischauer. Tribological performance and deformation of sputter-deposited MoS_2 solid lubricant films during sliding wear and indentation contact. *Thin Solid Films*, 188(2):219–236, 1990.
- [21] H. Topsøe, B.S. Clausen, and F.E. Massoth. *Hydrotreating Catalysis*, volume 11. 1996.
- [22] Per Joensen, R. F. Frindt, and S. Roy Morrison. Single-layer MoS_2 . *Mat. Res. Bull.*, 21:457–461, 1986.
- [23] Qing Hua Wang, Kouros Kalantar-Zadeh, Andras Kis, Jonathan N. Coleman, and Michael S. Strano. Electronics and optoelectronics of two-dimensional transition metal dichalcogenides. *Nature Nanotechnology*, 7(11):699–712, Nov 2012.
- [24] Manish Chhowalla, Hyeon Suk Shin, Goki Eda, Lain-Jong Li, Kian Ping Loh, and Hua Zhang. The chemistry of two-dimensional layered transition metal dichalcogenide nanosheets. *Nature Chemistry*, 5:263–275, 2013.
- [25] Francis H. Davies, Conor J. Price, Ned T. Taylor, Shane G. Davies, and Steven P. Hepplestone. Band alignment of transition metal dichalcogenide heterostructures. *Physical Review B*, 103(4), 2021.

- [26] A. G. Thomas, W. R. Flavell, A. K. Mallick, A. R. Kumarasinghe, D. Tsoutsou, N. Khan, C. Chatwin, S. Ryner, and G. C. Smith. Comparison of the electronic structure of anatase and rutile TiO₂ single-crystal surfaces using resonant photoemission and x-ray absorption spectroscopy. *PHYSICAL REVIEW B*, 75:035105–1–035105–12, 2007.
- [27] M. E. Arroyo-de Dompablo, A. Morales-Gracia, and M. Taravillo. DFT+U calculations of crystal lattice, electronic structure, and phase stability under pressure of TiO₂ polymorphs. *The Journal of Chemical Physics*, 135:054503, 2011.
- [28] M. Molenda, R. Dziembaj, E. Podstawka, and L. M. Proniewicz. Changes in local structure of lithium manganese spinels (Li:Mn=1:2) characterised by XRD, DSC, TGA, IR, and Raman spectroscopy. *Journal of Physical and Chemistry of Solids*, 66:1761–1768, 2005.
- [29] Haowei Peng, Jingbo Li, Shu-Shen Li, and Jian-Bai Xia. First-principles study of the electronic structures and magnetic properties of 3d transition metal-doped anatase TiO₂. *Journal of Physics Condensed Matter*, 20(12):125207, 2008.
- [30] Steven H. Simon. *The Oxford Solid State Basics*. Oxford University Press, 1 edition, 2013.
- [31] Harald Ibach and Hans Lüth. *Solid-State Physics*. Springer Berlin, Heidelberg, 4 edition, 2009.
- [32] Steven M. Girvin and Kun Yang. *Modern Condensed Matter Physics*. Cambridge University Press, 2019.
- [33] M. Born and T. von Karman. On the theory of specific heat. *Physikalische Zeitschrift*, 14:15–19, Jan 1913.
- [34] M. Born and T. von Karman. On the distribution of natural vibrations of spot-lattices. *Physikalische Zeitschrift*, 14:65–71, Jan 1913.
- [35] Charles Kittel. *Introduction to solid state physics*. John Wiley & Sons, 8 edition, 2004.
- [36] Felix Bloch. Über die quantenmechanik der elektronen in kristallgittern. *Zeitschrift für Physik*, 52(7–8):555–600, Jul 1929.
- [37] Richard M. Martin. *Electronic Structure: Basic Theory and Practical Methods*. Cambridge University Press, 2 edition, 2020.
- [38] M. Born and R. Oppenheimer. Zur quantentheorie der molekeln. *Annalen der Physik*, 389(20):457–484, Aug 1927.

- [39] D. R. Hartree. The wave mechanics of an atom with a non-coulomb central field. part i. theory and methods. *Mathematical Proceedings of the Cambridge Philosophical Society*, 24(1):89–110, Jan 1928.
- [40] D. R. Hartree. The wave mechanics of an atom with a non-coulomb central field. part ii. some results and discussion. *Mathematical Proceedings of the Cambridge Philosophical Society*, 24(1):111–132, Jan 1928.
- [41] P. Hohenberg and W. Kohn. Inhomogeneous electron gas. *Physical Review*, 136(3B), Nov 1964.
- [42] W. Kohn and L. J. Sham. Self-consistent equations including exchange and correlation effects. *Physical Review*, 140(4A):1133–1138, Nov 1965.
- [43] Paul Bendt and Alex Zunger. New approach for solving the density-functional self-consistent-field problem. *Physical Review B*, 26(6):3114–3137, Sep 1982.
- [44] G P Srivastava. Broyden’s method for self-consistent field convergence acceleration. *Journal of Physics A: Mathematical and General*, 17(6), Apr 1984.
- [45] G. Kresse and J. Furthmüller. Efficiency of ab-initio total energy calculations for metals and semiconductors using a plane-wave basis set. *Computational Materials Science*, 6(1):15 – 50, 1996.
- [46] G. Kresse and J. Furthmüller. Efficient iterative schemes for ab initio total-energy calculations using a plane-wave basis set. *Phys. Rev. B*, 54:11169–11186, 1996.
- [47] John P. Perdew, Kieron Burke, and Matthias Ernzerhof. Generalized gradient approximation made simple. *Physical Review Letters*, 77(18):3865–3868, Oct 1996.
- [48] Jochen Heyd, Gustavo E. Scuseria, and Matthias Ernzerhof. Hybrid functionals based on a screened Coulomb potential. *Journal of Chemical Physics*, 118(18):8207–8215, May 2003.
- [49] Jochen Heyd, Gustavo E. Scuseria, and Matthias Ernzerhof. Erratum: Hybrid functionals based on a screened Coulomb potential (*Journal of Chemical Physics* (2003) 118 (8207)), Jun 2006.
- [50] P. E. Blöchl. Projector augmented-wave method. *Physical Review B*, 50(24):17953–17979, Dec 1994.
- [51] P. P. Ewald. Die berechnung optischer und elektrostatischer gitterpotentiale. *Annalen der Physik*, 369(3):253–287, 1921.
- [52] Hendrik J. Monkhorst and James D. Pack. Special points for brillouin-zone integrations. *Physical Review B*, 13(12):5188–5192, Jun 1976.

- [53] Stefan Grimme, Jens Antony, Stephan Ehrlich, and Helge Krieg. A consistent and accurate ab initio parametrization of density functional dispersion correction (DFT-D) for the 94 elements H-Pu. *The Journal of Chemical Physics*, 132(15):154104, 2010.
- [54] Will Tribbey. Numerical recipes. *ACM SIGSOFT Software Engineering Notes*, 35(6):30–31, Nov 2010.
- [55] Péter Pulay. Convergence acceleration of iterative sequences. the case of scf iteration. *Chemical Physics Letters*, 73(2):393 – 398, 1980.
- [56] K. Mizushima, P.C. Jones, P.J. Wiseman, and J.B. Goodenough. Li_xCoO_2 ($0 < x \leq 1$): A new cathode material for batteries of high energy density. *Materials Research Bulletin*, 15(6):783–789, Apr 1980.
- [57] R. Yazami and Ph. Touzain. A reversible graphite-lithium negative electrode for electrochemical generators. *Journal of Power Sources*, 9(3):365–371, Jan 1983.
- [58] Bruno Scrosati. History of lithium batteries. *J Solid State Electrochem*, 15:1623–1630, 2011.
- [59] Chaofeng Liu, Zachary G. Naele, and Guozhong Cao. Understanding electrochemical potentials of cathode materials in rechargeable batteries. *Materials Today*, 19(2):109–123, 2016.
- [60] John B. Goodenough and Kyu-Sung Park. The Li-ion rechargeable battery: A perspective. *Journal of the American Chemical Society*, 135:1167–1176, 2013.
- [61] Partha Saha, Moni Kanchan Datta, Oleg I. Velikokhatnyi, Ayyakkannu Manivannan, David Alman, and Prashant N. Kumta. Rechargeable magnesium battery: Current status and key challenges for the future. *Progress in Materials Science*, 66:1–86, 2014.
- [62] B. J. Hwang, Y. W. Tsai, D. Carlier, and G. Ceder. A combined computational/experimental study on $\text{LiNi}_{1/3}\text{Co}_{1/3}\text{Mn}_{1/3}\text{O}_2$. *Chem. Mater.*, 15:3676–3682, 2003.
- [63] G Amatucci. Cobalt dissolution in LiCoO_2 -based non-aqueous rechargeable batteries. *Solid State Ionics*, 83(1-2):167–173, Jan 1996.
- [64] Arumugam Manthiram. A reflection on lithium-ion battery cathode chemistry. *Nature Communications*, 11(1), 2020.
- [65] Tsutomu Ohzuku, Atsushi Ueda, and Masatoshi Nagayama. Electrochemistry and structural chemistry of LiNiO_2 (R3M) for 4 volt secondary lithium cells. *Journal of The Electrochemical Society*, 140(7):1862–1870, 1993.

- [66] J. Reed, G. Ceder, and A. Van Der Ven. Layered-to-spinel phase transition in Li_xMnO_2 . *Electrochemical and Solid-State Letters*, 4:A78–A81, 2001.
- [67] R. J. Gummow and M. M. Thackeray. An investigation of spinel-related and orthorhombic LiMnO_2 cathodes for rechargeable lithium batteries. *Journal of The Electrochemical Society*, 141(5):1178–1182, 1994.
- [68] Yukinori Koyama, Isao Tanaka, Yang-SooKim Nishitani, and HirohikoAdachi HirohikoAdachi. First principles study on factors determining battery voltages of LiMO_2 ($M=\text{Ti-Ni}$). *Japanese Journal of Applied Physics*, 38(8R):4804, Aug 1999.
- [69] Tsutomu Ohzuku and Yoshinari Makimura. Layered lithium insertion material of $\text{Li}(\text{Ni}_{1/3}\text{Co}_{1/3}\text{Mn}_{1/3})\text{O}_2$ for lithium-ion batteries. *Chemistry Letters*, 30(7):642–643, Feb 2001.
- [70] K.M Shaju, G.V Subba Rao, and B.V.R Chowdari. Performance of layered $\text{Li}(\text{Ni}_{1/3}\text{Co}_{1/3}\text{Mn}_{1/3})\text{O}_2$ as cathode for Li-ion batteries. *Electrochimica Acta*, 48(2):145–151, Nov 2002.
- [71] Joseph W. Bennett, Diamond T. Jones, Robert J. Hamers, and Sara E. Mason. First-principles and thermodynamics study of compositionally tuned complex metal oxides: Cation release from the (001) surface of Mn-rich lithium nickel manganese cobalt oxide. *Inorganic Chemistry*, 57(21):13300–13311, 2018.
- [72] Roland Jung, Michael Metzger, Filippo Maglia, Christoph Stinner, and Hubert A. Gasteiger. Oxygen release and its effect on the cycling stability of $\text{LiNi}_x\text{Mn}_y\text{Co}_z\text{O}_2$ (NMC) cathode materials for Li-ion batteries. *Journal of The Electrochemical Society*, 164(7), May 2017.
- [73] Jiaxin Zheng, Tongchao Liu, Zongxiang Hu, Yi Wei, Xiaohe Song, Yang Ren, Weidong Wang, Mumin Rao, Yuan Lin, Zonghai Chen, and et al. Tuning of thermal stability in layered $\text{Li}(\text{Ni}_x\text{Mn}_y\text{Co}_z)\text{O}_2$. *Journal of the American Chemical Society*, 138(40):13326–13334, 2016.
- [74] Enyue Zhao, Lincan Fang, Minmin Chen, Dongfeng Chen, Qingzhen Huang, Zhongbo Hu, Qing-bo Yan, Meimei Wu, and Xiaoling Xiao. New insight into Li/Ni disorder in layered cathode materials for lithium ion batteries: A joint study of neutron diffraction, electrochemical kinetic analysis and first-principles calculations. *Journal of Materials Chemistry A*, 5(4):1679–1686, Dec 2016.
- [75] E. Rossen, C.D.W. Jones, and J.R. Dahn. Structure and electrochemistry of $\text{Li}_x\text{Mn}_y\text{Ni}_{1-y}\text{O}_2$. *Solid State Ionics*, 57(3-4):311–318, Apr 1992.
- [76] Johannes Kasnatscheew, Stephan Röser, Markus Börner, and Martin Winter. Do increased Ni contents in $\text{LiNi}_x\text{Mn}_y\text{Co}_z\text{O}_2$ (NMC) electrodes de-

crease structural and thermal stability of Li ion batteries? a thorough look by consideration of the Li⁺ extraction ratio. *ACS Applied Energy Materials*, 2(11):7733–7737, 2019.

- [77] Dave Andre, Sung-Jin Kim, Peter Lamp, Simon Franz Lux, Filippo Maglia, Odysseas Paschos, and Barbara Stiaszny. Future generations of cathode materials: An automotive industry perspective. *Journal of Materials Chemistry A*, 3(13):6709–6732, Feb 2015.
- [78] Patrick Rozier and Jean Marie Tarascon. Review—Li-rich layered oxide cathodes for next-generation Li-ion batteries: Chances and challenges. *Journal of The Electrochemical Society*, 162(14), Oct 2015.
- [79] Gang Wang, Liling Yi, Ruizhi Yu, Xianyou Wang, Yu Wang, Zhongshu Liu, Bing Wu, Min Liu, Xiaohui Zhang, Xiukang Yang, and et al. Li_{1.2}Ni_{0.13}Co_{0.13}Mn_{0.54}O₂ with controllable morphology and size for high performance lithium-ion batteries. *ACS Applied Materials & Interfaces*, 9(30):25358–25368, Jul 2017.
- [80] Arefeh Kazzazi, Dominic Bresser, Agnese Birrozzi, Jan von Zamory, Maral Hekmatfar, and Stefano Passerini. Comparative analysis of aqueous binders for high-energy Li-rich NMC as a lithium-ion cathode and the impact of adding phosphoric acid. *ACS Applied Materials & Interfaces*, 10(20):17214–17222, 2018.
- [81] Mylène Hendrickx, Andreas Paulus, Maria A. Kirsanova, Marlies K. Van Bael, Artem M. Abakumov, An Hardy, and Joke Hadermann. The influence of synthesis method on the local structure and electrochemical properties of Li-rich/Mn-rich NMC cathode materials for Li-ion batteries. *Nanomaterials*, 12(13):2269, Jun 2022.
- [82] Wei Yin, Alexis Grimaud, Gwenaëlle Rouse, Artem M. Abakumov, Anatoliy Senyshyn, Leiting Zhang, Sigita Trabesinger, Antonella Iadecola, Dominique Foix, Domitille Giaume, and et al. Structural evolution at the oxidative and reductive limits in the first electrochemical cycle of Li_{1.2}Ni_{0.13}Mn_{0.54}Co_{0.13}O₂. *Nature Communications*, 11(1), Mar 2020.
- [83] Jun Wang, Xin He, Elie Paillard, Nina Laszczynski, Jie Li, and Stefano Passerini. Lithium- and manganese-rich oxide cathode materials for high-energy lithium ion batteries. *Advanced Energy Materials*, 6(21):1600906, Aug 2016.
- [84] Juan An, Liyi Shi, Guorong Chen, Musen Li, Hongjiang Liu, Shuai Yuan, Shimou Chen, and Dengsong Zhang. Insights into the stable layered structure of a Li-rich cathode material for lithium-ion batteries. *Journal of Materials Chemistry A*, 5:19738–19744, 2017.

- [85] C.H. Chen, J. Liu, M.E. Stoll, G. Henriksen, D.R. Vissers, and K. Amine. Aluminum-doped lithium nickel cobalt oxide electrodes for high-power lithium-ion batteries. *Journal of Power Sources*, 128(2):278–285, Dec 2004.
- [86] Wangda Li, Steven Lee, and Arumugam Manthiram. High-nickel NMA: A cobalt-free alternative to NMC and NCA cathodes for lithium-ion batteries. *Advanced Materials*, page 2002718, 2020.
- [87] Muhd Firdaus Kasim, Wan Aida Azizan, Kelimah Anak Elong, Norashikin Kamarudin, Muhamad Kamil Yaakob, and Nurhanna Badar. Enhancing the structural stability and capacity retention of Ni-rich $\text{LiNi}_{0.7}\text{Co}_{0.3}\text{O}_2$ cathode materials via Ti doping for rechargeable Li-ion batteries: Experimental and computational approaches. *Journal of Alloys and Compounds*, 888:161559, Dec 2021.
- [88] Yehonatan Levartovsky, Arup Chakraborty, Sooraj Kunnikuruvan, Sandipan Maiti, Judith Grinblat, Michael Talianker, Dan Thomas Major, and Doron Aurbach. Enhancement of structural, electrochemical, and thermal properties of high-energy density Ni-rich $\text{LiNi}_{0.85}\text{Co}_{0.1}\text{Mn}_{0.05}\text{O}_2$ cathode materials for Li-ion batteries by niobium doping. *ACS Applied Materials & Interfaces*, 13(29):34145–34156, 2021.
- [89] Berke Pişkin, Cansu Savaş Uygur, and M. Kadri Aydınol. Morphology effect on electrochemical properties of doped (W and Mo) 622NMC, 111NMC, and 226NMC cathode materials. *International Journal of Hydrogen Energy*, 45(14):7874–7880, Aug 2019.
- [90] Ngoc Thanh Tran, Che-an Lin, and Shih-kang Lin. Insights into the structural and thermodynamic instability of Ni-rich NMC cathode. *ACS Sustainable Chemistry & Engineering*, 11(18):6978–6987, 2023.
- [91] Hyung-Joo Noh, Sungjune Youn, Chong Seung Yoon, and Yang-Kook Sun. Comparison of the structural and electrochemical properties of layered $\text{Li}[\text{Ni}_x\text{Co}_y\text{Mn}_z]\text{O}_2$ ($x=1/3, 0.5, 0.6, 0.7, 0.8$ and 0.85) cathode material for lithium-ion batteries. *Journal of Power Sources*, 233:121–130, Jan 2013.
- [92] Muhammad Mominur Rahman and Feng Lin. Oxygen redox chemistry in rechargeable Li-ion and Na-ion batteries. *Matter*, 4(2):490–527, Feb 2021.
- [93] Annalena R. Genreith-Schriever, Hrishit Banerjee, Ashok S. Menon, Euan N. Basseby, Louis F.J. Piper, Clare P. Grey, and Andrew J. Morris. Oxygen hole formation controls stability in LiNiO_2 cathodes. *Joule*, 7(7):1623–1640, Jul 2023.
- [94] Shenzhen Xu, Guangfu Luo, Ryan Jacobs, Shuyu Fang, Mahesh K. Mahanthappa, Robert J. Hamers, and Dane Morgan. Ab initio model-

- ing of electrolyte molecule ethylene carbonate decomposition reaction on Li(Ni,Mn,Co)O₂ cathode surface. *ACS Applied Materials and Interfaces*, 9:20545–20553, 2017.
- [95] Ana Cristina Martinez, Sylvie Grugeon, Dominique Cailieu, Matthieu Courty, Pierre Tran-Van, Bruno Delobel, and Stephane Laruelle. High reactivity of the nickel-rich LiNi_{1-x-y}Mn_xCo_yO₂ layered materials surface towards H₂O/CO₂ atmosphere and LiPF₆-based electrolyte. *Journal of Power Sources*, 468:228204, 2020.
- [96] Juan C. Garcia, Javier Bareño, Jianhua Yan, Guoying Chen, Andrew Hauser, Jason R. Croy, and Hakim Iddir. Surface structure, morphology, and stability of Li(Ni_{1/3}Mn_{1/3}Co_{1/3})O₂ cathode material. *Journal of Physical Chemistry C*, 121:8290–8299, 2017.
- [97] Peter W. Atkins, Julio de Paula, and James J. Keeler. *Atkins' physical chemistry*. Oxford University Press, 2023.
- [98] Seungho Cho, Ji-Wook Jang, Kun-Hong Lee, and Jae Sung Lee. Research update: Strategies for efficient photoelectrochemical water splitting using metal oxide photoanodes. *APL Materials*, 2(1):010703, Jan 2014.
- [99] Yi Yang, Shuwen Niu, Dongdong Han, Tianyu Liu, Gongming Wang, and Yat Li. Progress in developing metal oxide nanomaterials for photoelectrochemical water splitting. *Advanced Energy Materials*, 7(19):1700555, Jun 2017.
- [100] Detlef Bahnemann, Peter Robertson, Chuanyi Wang, Wonyong Choi, Helen Daly, Mohtaram Danish, Hugo de Lasa, Salvador Escobedo, Christopher Hardacre, Tae Hwa Jeon, and et al. 2023 roadmap on photocatalytic water splitting. *Journal of Physics: Energy*, 5(1):012004, 2023.
- [101] Ju-Hyeon Kim, Sehun Seo, Jong-Hoon Lee, Hojoong Choi, Seungkyu Kim, Guangxia Piao, Yong Ryun Kim, Byoungwook Park, Jongmin Lee, Yoonsung Jung, and et al. Perovskite-based photocathodes: Efficient and stable perovskite-based photocathode for photoelectrochemical hydrogen production (adv. funct. mater. 17/2021). *Advanced Functional Materials*, 31(17):2170119, Jan 2021.
- [102] Changli Li, Jingfu He, Yequan Xiao, Yanbo Li, and Jean-Jacques Delaunay. Earth-abundant cu-based metal oxide photocathodes for photoelectrochemical water splitting. *Energy & Environmental Science*, 13(10):3269–3306, Sep 2020.
- [103] Takashi Hisatomi, Jun Kubota, and Kazunari Domen. Recent advances in semiconductors for photocatalytic and photoelectrochemical water splitting. *Chem. Soc. Rev.*, 43(22):7520–7535, Jan 2014.

- [104] Akihiko Kudo and Yugo Miseki. Heterogeneous photocatalyst materials for water splitting. *Chem. Soc. Rev.*, 38(1):253–278, Nov 2008.
- [105] Xiaobo Chen, Shaohua Shen, Liejin Guo, and Samuel S. Mao. Semiconductor-based photocatalytic hydrogen generation. *Chemical Reviews*, 110(11):6503–6570, Nov 2010.
- [106] R. J. Andres, J. S. Gregg, L. Losey, G. Marland, and T. A. Boden. Monthly, global emissions of carbon dioxide from fossil fuel consumption. *Tellus, Series B: Chemical and Physical Meteorology*, 63(3):309–327, 2011.
- [107] A. Evans, V. Strezov, and T. J. Evans. Assessment of utility energy storage options for increased renewable energy penetration. *Renewable and Sustainable Energy Reviews*, 16:4141–4147, 2012.
- [108] Qing Tang and De-en Jiang. Mechanism of hydrogen evolution reaction on 1T-MoS₂ from first principles. *ACS Catalysis*, 6(8):4953–4961, 2016.
- [109] B. Amin, N. Singh, and U. Schwingenschlögl. Heterostructures of transition metal dichalcogenides. *Phys. Rev. B*, 92:075439, 2015.
- [110] Agnieszka Kuc, Thomas Heine, and Andras Kis. Electronic properties of transition-metal dichalcogenides. *MRS Bulletin*, 40(7):577–584, 2015.
- [111] Francis H. Davies, Conor J. Price, Ned T. Taylor, Shane G. Davies, and Steven P. Hepplestone. Band alignment of transition metal dichalcogenide heterostructures. *Physical Review B*, 103(4), 2021.
- [112] Julia Gusakova, Xingli Wang, Li Lynn Shiau, Anna Krivosheeva, Victor Shaposhnikov, Victor Borisenko, Vasilii Gusakov, and Beng Kang Tay. Electronic properties of bulk and monolayer TMDs: Theoretical study within DFT framework (GVJ-2e method). *physica status solidi (a)*, 214(12):1700218, 2017.
- [113] Wen Lei, Shengli Zhang, Gunter Heymann, Xin Tang, Jianfeng Wen, Xiaojun Zheng, Guanghui Hu, and Xing Ming. A new 2D high-pressure phase of PdSe₂ with high-mobility transport anisotropy for photovoltaic applications. *J. Mater. Chem. C*, 7:2096–2105, 2019.
- [114] Mukesh Jakhar, Jaspreet Singh, Ashok Kumar, and Ravindra Pandey. First-principles study of the hexagonal T-phase PdSe₂ monolayer and its application in solar cells. *The Journal of Physical Chemistry C*, 124(49):26565–26571, 2020.
- [115] Dan Qin, Peng Yan, Guangqian Ding, Xujin Ge, Hongyue Song, and Guoying Gao. Monolayer PdSe₂: A promising two-dimensional thermoelectric material. *Scientific Reports*, 8(1):2764, 2018.
- [116] Wei Sheng, Ying Xu, Mingwei Liu, Guozheng Nie, Junnian Wang, and Shijing Gong. The InSe/SiH type-II van der waals heterostructure as a promis-

- ing water splitting photocatalyst: a first-principles study. *Phys. Chem. Chem. Phys.*, 22:21436–21444, 2020.
- [117] Yu-Peng Yuan, Lin-Wei Ruan, James Barber, Say Chye Joachim Loo, and Can Xue. Hetero-nanostructured suspended photocatalysts for solar-to-fuel conversion. *Energy Environ. Sci.*, 7:3934–3951, 2014.
- [118] Wei Chen, Guo-Bo Huang, Hao Song, and Jian Zhang. Efficient and stable charge transfer channels for photocatalytic water splitting activity of CdS without sacrificial agents. *J. Mater. Chem. A*, 8:20963–20969, 2020.
- [119] Withana Siripala, Anna Ivanovskaya, Thomas F. Jaramillo, Sung-Hyeon Baeck, and Eric W. McFarland. A $\text{Cu}_2\text{O}/\text{TiO}_2$ heterojunction thin film cathode for photoelectrocatalysis. *Solar Energy Materials and Solar Cells*, 77(3):229–237, 2003.
- [120] Hongtao Yu, Shuo Chen, Xie Quan, Huimin Zhao, and Yaobin Zhang. Silicon nanowire/ TiO_2 heterojunction arrays for effective photoelectrocatalysis under simulated solar light irradiation. *Applied Catalysis B: Environmental*, 90(1):242–248, 2009.
- [121] Jin Li, Xianming Liu, and Jian Zhang. Smart assembly of sulfide heterojunction photocatalysts with well-defined interfaces for direct Z-scheme water splitting under visible light. *ChemSusChem*, 13(11):2996–3004, 2020.
- [122] Manish Kumar Mohanta, Ashima Rawat, Nityasagar Jena, Raihan Ahammed, Abir De Sarkar, et al. Superhigh out-of-plane piezoelectricity, low thermal conductivity and photocatalytic abilities in ultrathin 2d van der waals heterostructures of boron monophosphide and gallium nitride. *Nanoscale*, 11(45):21880–21890, 2019.
- [123] Jun Zhao and Hui Zeng. Type-II AsP/As van der waals heterostructures: Tunable anisotropic electronic structures and optical properties. *Advanced Materials Interfaces*, 8(6):2001555, 2021.
- [124] Jingliang Chen, Xing Wei, Ru Zhang, Jian Liu, Ye Tian, Yan Zhang, Tingting Guo, Jibin Fan, Lei Ni, Mingshuo Zhang, and Li Duan. Type-II $\text{C}_2\text{N}/\text{ZnTe}$ van der waals heterostructure: A promising photocatalyst for water splitting. *Advanced Materials Interfaces*, 8(9):2002068, 2021.
- [125] Jiewen Min, Mengshi Zhou, Chunxiao Zhang, Chao Tang, Xiangyang Peng, and Jianxin Zhong. Type-II vdW heterojunction $\text{SeGa}_2\text{Te}/\text{SeIn}_2\text{Se}$ as a high-efficiency visible-light-driven water-splitting photocatalyst. *Physics Letters A*, 413:127594, 2021.
- [126] Xiangzheng Jia, Qian Shao, Yongchun Xu, Ruishan Li, Kai Huang, Yongzhe Guo, Cangyu Qu, and Enlai Gao. Elasticity-based-exfoliability measure for

high-throughput computational exfoliation of two-dimensional materials. *npj Computational Materials*, 7(1), 2021.

- [127] Darren Nutting, Jorlandio F. Felix, Evan Tillotson, Dong-Wook Shin, Adolfo De Sanctis, Hong Chang, Nick Cole, Saverio Russo, Adam Woodgate, Ioannis Leontis, Henery A Fernandez, Monica F. Craciun, Sarah J. Haigh, and Freddie Withers. Heterostructures formed through abraded van der waals materials. *Nature Communications*, 11(1):3047, 2020.
- [128] Ashima Rawat, Raihan Ahammed, Dimple, Nityasagar Jena, Manish Kumar Mohanta, and Abir De Sarkar. Solar energy harvesting in type II van der waals heterostructures of semiconducting group III monochalcogenide monolayers. *The Journal of Physical Chemistry C*, 123(20):12666–12675, 2019.
- [129] Manish Kumar Mohanta, Ashima Rawat, Nityasagar Jena, Dimple, Raihan Ahammed, and Abir De Sarkar. Interfacing boron monophosphide with molybdenum disulfide for an ultrahigh performance in thermoelectrics, two-dimensional excitonic solar cells, and nanopiezotronics. *ACS Applied Materials & Interfaces*, 12(2):3114–3126, 2020. PMID: 31904214.
- [130] Jialuo Ren, Chunxiao Zhang, Chaoyu He, Tao Ouyang, Jin Li, Chao Tang, and Jianxin Zhong. Optoelectronic properties of type-II SePtTe/InS van der waals heterojunction. *Journal of Applied Physics*, 128(4):043103, Jul 2020.
- [131] Raihan Ahammed, Ashima Rawat, Nityasagar Jena, Dimple, Manish Kumar Mohanta, and Abir De Sarkar. ZrS₃/MS₂ and ZrS₃/MXY (M = Mo, W; X, Y = S, Se, Te; X≠Y) type-II van der waals hetero-bilayers: Prospective candidates in 2D excitonic solar cells. *Applied Surface Science*, 499:143894, 2020.
- [132] Yuan Guo, Jingjing Min, Xiaolin Cai, Liying Zhang, Chengyan Liu, and Yu Jia. Two-dimensional type-II BP/MoSi₂P₄ vdw heterostructures for high-performance solar cells. *The Journal of Physical Chemistry C*, 126(9):4677–4683, 2022.
- [133] Jingxiang Low, Jiaguo Yu, Mietek Jaroniec, Swelm Wageh, and Ahmed A. Al-Ghamdi. Heterojunction photocatalysts. *Advanced Materials*, 29(20):1601694.
- [134] Wee-Jun Ong, Lutfi Kurnianditia Putri, Lling-Lling Tan, Siang-Piao Chai, and Siek-Ting Yong. Heterostructured AgX/g-C₃N₄ (X=Cl and Br) nanocomposites via a sonication-assisted deposition-precipitation approach: Emerging role of halide ions in the synergistic photocatalytic reduction of carbon dioxide. *Applied Catalysis B: Environmental*, 180:530–543, 2016.

- [135] B. Archana, Nagaraju Kottam, Sanjay Nayak, K. B. Chandrasekhar, and M. B. Sreedhara. Superior photocatalytic hydrogen evolution performances of WS₂ over MoS₂ integrated with CdS nanorods. *The Journal of Physical Chemistry C*, 124(27):14485–14495, 2020.
- [136] Ruru Song, Lu Wang, and Youyong Li. Improving the electrochemical activity of PdSe₂ by constructing P/T structural interfaces. *Applied Surface Science*, 597:153626, May 2022.
- [137] Akinola D. Oyedele, Shize Yang, Liangbo Liang, Alexander A. Puzetzy, Kai Wang, Jingjie Zhang, Peng Yu, Pushpa R. Pudasaini, Avik W. Ghosh, Zheng Liu, Christopher M. Rouleau, Bobby G. Sumpter, Matthew F. Chisholm, Wu Zhou, Philip D. Rack, David B. Geohegan, and Kai Xiao. PdSe₂: Pentagonal two-dimensional layers with high air stability for electronics. *Journal of the American Chemical Society*, 139(40):14090–14097, 2017.
- [138] Eugene S. Kadantsev and Pawel Hawrylak. Electronic structure of a single MoS₂ monolayer. *Solid State Communications*, 152(10):909–913, 2012.
- [139] Xu Zhao, Qianyi Zhao, Binru Zhao, Xianqi Dai, Shuyi Wei, and Yaqiang Ma. Electronic and optical properties of PdSe₂ from monolayer to trilayer. *Superlattices and Microstructures*, 142:106514, 2020.
- [140] Danyun Xu, Yuanzhi Zhu, Jiapeng Liu, Yang Li, Wenchao Peng, Guoliang Zhang, Fengbao Zhang, and Xiaobin Fan. Microwave-assisted 1T to 2H phase reversion of MoS₂ in solution: a fast route to processable dispersions of 2H-MoS₂ nanosheets and nanocomposites. *Nanotechnology*, 27:385604, 2016.
- [141] Xiaorong Gan, Lawrence Yoon Suk Lee, and Kwok yin Wong. 2H/1T phase transition of multilayer MoS₂ by electrochemical incorporation of S vacancies. *ACS Applied Energy Materials*, 9:4754–4765, 2018.
- [142] Zhenhua Wu, Lei Lu, Xiaochong Liang, Chaochao Dun, Shicheng Yan, Erzhen Mu, Yang Liu, and Zhiyu Hu. Formation of hexagonal PdSe₂ for electronics and catalysis. *The Journal of Physical Chemistry C*, 124(20):10935–10940, 2020.
- [143] Jifeng Sun, Hongliang Shi, Theo Siegrist, and David J. Singh. Electronic, transport, and optical properties of bulk and mono-layer PdSe₂. *Applied Physics Letters*, 107(15):153902, 2015.
- [144] Uttam Gupta and C.N.R. Rao. Hydrogen generation by water splitting using MoS₂ and other transition metal dichalcogenides. *Nano Energy*, 41:49–65, 2017.

- [145] Wingkei Ho, Jimmy C. Yu, Jun Lin, Jiaguo Yu, and Puishan Li. Preparation and photocatalytic behavior of MoS₂ and WS₂ nanocluster sensitized TiO₂. *Langmuir*, 20(14):5865–5869, 2004.
- [146] Xuebin Hou, Huimin Zhou, Min Zhao, Yibing Cai, and Qufu Wei. MoS₂ nanoplates embedded in Co–N-doped carbon nanocages as efficient catalyst for HER and OER. *ACS Sustainable Chemistry & Engineering*, 8(14):5724–5733, 2020.
- [147] Jiajun Wang, Wei Wang, Zongyuan Wang, Jingguang G. Chen, and Changjun Liu. Porous MS₂/MO₂ (M = W, Mo) nanorods as efficient hydrogen evolution reaction catalysts. *ACS Catalysis*, 6(10):6585–6590, 2016.
- [148] Dongdong Zhu, Jinlong Liu, Yongqiang Zhao, Yao Zheng, and Shi-Zhang Qiao. Engineering 2D metal-organic framework/MoS₂ interface for enhanced alkaline. *Small*, 15(14):1613–6829, 2019.
- [149] Lei Li, Zhaodan Qin, Lucie Ries, Song Hong, Thierry Michel, Jieun Yang, Chrystelle Salameh, Mikhael Bechelany, Philippe Miele, Daniel Kaplan, Manish Chhowalla, and Damien Voiry. Role of sulfur vacancies and undercoordinated Mo regions in MoS₂ nanosheets toward the evolution of hydrogen. *ACS Nano*, 13(6):6824–6834, 2019.
- [150] Hui Xu, Jianjian Yi, Xiaojie She, Qin Liu, Li Song, Shuangming Chen, Yingchao Yang, Yanhua Song, Robert Vajtai, Jun Lou, Huaming Li, Shouqi Yuan, Jingjie Wu, and Pulickel M. Ajayan. 2D heterostructure comprised of metallic 1T-MoS₂/monolayer O-g-C₃N₄ towards efficient photocatalytic hydrogen evolution. *Applied Catalysis B: Environmental*, 220:379–385, 2018.
- [151] Quanjun Xiang, Jiaguo Yu, and Mietek Jaroniec. Synergetic effect of MoS₂ and graphene as cocatalysts for enhanced photocatalytic H₂ production activity of TiO₂ nanoparticles. *Journal of the American Chemical Society*, 134(15):6575–6578, 2012.
- [152] Jian Zhang, Fang Feng, Yong Pu, Xing’ao Li, Cher Hon Lau, and Wei Huang. Tailoring the porosity in iron phosphosulfide nanosheets to improve the performance of photocatalytic hydrogen evolution. *ChemSusChem*, 12(12):2651–2659, 2019.
- [153] Wen Lei, Wei Wang, Xing Ming, Shengli Zhang, Gang Tang, Xiaojun Zheng, Huan Li, and Carmine Autieri. Structural transition, metallization, and superconductivity in quasi-two-dimensional layered PdS₂ under compression. *Phys. Rev. B*, 101:205149, 2020.
- [154] Chen Long, Yan Liang, Hao Jin, Baibiao Huang, and Ying Dai. PdSe₂: Flexible two-dimensional transition metal dichalcogenides monolayer for water

- splitting photocatalyst with extremely low recombination rate. *ACS Applied Energy Materials*, 2(1):513–520, 2018.
- [155] Mukesh Jakhar and Ashok Kumar. Tunable photocatalytic water splitting and solar-to-hydrogen efficiency in beta-PdSe₂ monolayer. *Catal. Sci. Technol.*, 11:6445–6454, 2021.
- [156] Laurence M Peter. *Photoelectrochemistry: from basic principles to photocatalysis*. Royal Society of Chemistry, 2016.
- [157] Quanlong Xu, Liuyang Zhang, Bei Cheng, Jiajie Fan, and Jiaguo Yu. S-scheme heterojunction photocatalyst. *Chem*, 6(7):1543–1559, 2020.
- [158] Tsuyoshi Takata, Junzhe Jiang, Yoshihisa Sakata, Mamiko Nakabayashi, Naoya Shibata, Vikas Nandal, Kazuhiko Seki, Takashi Hisatomi, and Kazunari Domen. Photocatalytic water splitting with a quantum efficiency of almost unity. *Nature*, 581(7809):411–414, 2020.
- [159] Peter E Blöchl. Projector augmented-wave method. *Physical review B*, 50(24):17953, 1994.
- [160] Georg Kresse and Daniel Joubert. From ultrasoft pseudopotentials to the projector augmented-wave method. *Physical Review B*, 59(3):1758, 1999.
- [161] G. Kresse and J. Hafner. Ab initio molecular dynamics for liquid metals. *Physical Review B*, 47:558–561, 1993.
- [162] G. Kresse and J. Hafner. Ab initio molecular-dynamics simulation of the liquid-metal–amorphous-semiconductor transition in germanium. *Physical Review B*, 49:14251–14269, 1994.
- [163] John P Perdew, Kieron Burke, and Matthias Ernzerhof. Generalized gradient approximation made simple. *Physical Review Letters*, 77(18):3865, 1996.
- [164] John P. Perdew, Kieron Burke, and Matthias Ernzerhof. Generalized gradient approximation made simple. *Physical Review Letters*, 78:1396–1396, 1997.
- [165] Hendrik J. Monkhorst and James D. Pack. Special points for brillouin-zone integrations. *Phys. Rev. B*, 13:5188–5192, 1976.
- [166] Xujing Ji, Degong Ding, Xiaoxiao Guan, Chunyang Wu, Haofu Qian, Juexian Cao, Jixue Li, and Chuanhong Jin. Interlayer coupling dependent discrete H - T' phase transition in lithium intercalated bilayer molybdenum disulfide. *ACS Nano*, 15(9):15039–15046, 2021.
- [167] Chin-Yi Tsai. Absorption coefficients of silicon: A theoretical treatment. *Journal of Applied Physics*, 123:183103, 2018.

- [168] K. Setayeshmehr, M. Hashemi, and N. Ansari. Photoconversion efficiency in atomically thin tmdc-based heterostructures. *Optics Express*, 29(21):32910, 2021.
- [169] D.P. Rai, Tuan V. Vu, Amel Laref, H. Joshi, and P.K. Patra. Promising optoelectronic response of 2D monolayer MoS₂: A first principles study. *Chemical Physics*, 538:110824, 2020.
- [170] Qu Yue, Jun Kang, Zhengzheng Shao, Xueao Zhang, Shengli Chang, Guang Wang, Shiqiao Qin, and Jingbo Li. Mechanical and electronic properties of monolayer MoS₂ under elastic strain. *Physics Letters A*, 376(12-13):1166–1170, 2012.
- [171] M. Bajdich, J. Nørskov, and A. Vojvodic. surface energetics of alkaline-earth metal oxides: Trends in stability and adsorption of small molecules. *Physical Review B*, 15, 2015.
- [172] Ned Thaddeus Taylor, Francis Huw Davies, Isiah Edward Mikel Rudkin, Conor Jason Price, Tsz Hin Chan, and Steven Paul Hepplestone. Artemis: Ab initio restructuring tool enabling the modelling of interface structures. *Computer Physics Communications*, 257:107515, 2020.
- [173] Isabela C. Man, Hai Yan Su, Federico Calle-Vallejo, Heine A. Hansen, José I. Martínez, Nilay G. Inoglu, John Kitchin, Thomas F. Jaramillo, Jens K. Nørskov, and Jan Rossmeisl. Universality in oxygen evolution electrocatalysis on oxide surfaces. *ChemCatChem*, 3(7):1159–1165, 2011.
- [174] Qing Tang and De-en Jiang. Mechanism of hydrogen evolution reaction on 1T-MoS₂ from first principles. *ACS Catalysis*, 6(8):4953–4961, 2016.
- [175] Joseph H. Montoya, Monica Garcia-Mota, Jens K. Nørskov, and Aleksandra Vojvodic. Theoretical evaluation of the surface electrochemistry of perovskites with promising photon absorption properties for solar water splitting. *Physical Chemistry Chemical Physics*, 17(4):2634–2640, 2015.
- [176] Ned Thaddeus Taylor, Conor Jason Price, Alexander Petkov, Marcus Ian Romanis Carr, Jason Charles Hale, and Steven Paul Hepplestone. The potential of overlayers on tin-based perovskites for water splitting. *The Journal of Physical Chemistry Letters*, 11(10):4124–4130, 2020.
- [177] M. Born and R. Oppenheimer. Zur quantentheorie der molekeln. *Annalen der Physik*, 389(20):457–484, 1927.
- [178] A. D. McNaught and A. Wilkinson. *Compendium of Chemical Terminology 2nd ed.* IUPAC, 2006.
- [179] Michael G. Walter, Emily L. Warren, James R. McKone, Shannon W. Boettcher, Qixi Mi, Elizabeth A. Santori, and Nathan S. Lewis. Solar water splitting cells. *Chemical Reviews*, 110(11):6446–6473, 2010.

- [180] Allen J. Bard. R. Memming in "Electroanalytical Chemistry. Technical Report 2, 1982.
- [181] Mahmoud G. Ahmed, Imme E. Kretschmer, Tarek A. Kandiel, Amira Y. Ahmed, Farouk A. Rashwan, and Detlef W. Bahnemann. A facile surface passivation of hematite photoanodes with TiO₂ overlayers for efficient solar water splitting. *ACS Applied Materials & Interfaces*, 7(43):24053–24062, 2015.
- [182] Eugene Heifets, Justin Ho, and Boris Merinov. Density functional simulation of BaZrO₃ (011) surface structure. *Physical Review B*, 75:155431, 2007.
- [183] Jacob M. Clary, Aaron M. Holder, and Charles B. Musgrave. Computationally predicted high-throughput free-energy phase diagrams for the discovery of solid-state hydrogen storage reactions. *ACS Applied Materials & Interfaces*, 12(43):48553–48564, 2020.
- [184] K.T. Jacob and Srilekshmi Muraleedharan. Phase diagram of the system Ce-Rh-O. *Calphad*, 65:171–176, 2019.
- [185] Sven A.E. Johansson and G. Wahnström. First-principles derived complexion diagrams for phase boundaries in doped cemented carbides. *Current Opinion in Solid State and Materials Science*, 20(5):299–307, 2016.
- [186] R. C. Longo, F. T. Kong, Santosh KC, M. S. Park, J. Yoon, D.-H. Yeon, J.-H. Park, S.-G. Doo, and K. Cho. Phase stability of Li-Mn-O oxides as cathode materials for Li-ion batteries: insights from ab initio calculations. *Phys. Chem. Chem. Phys.*, 16(23):11233–11242, 2014.
- [187] Yuri A. Mastrikov, Rotraut Merkle, Eugene Heifets, Eugene A. Kotomin, and Joachim Maier. Pathways for oxygen incorporation in mixed conducting perovskites: A DFT-based mechanistic analysis for (La, Sr)MnO₃ - δ . *The Journal of Physical Chemistry C*, 114(7):3017–3027, 2010.
- [188] Toshiyasu Nishimura and Toshiaki Kodama. Analysis of chemical state for alloying elements in iron rust. *Tetsu-to-Hagane*, 88(6):320–325, 2002.
- [189] Atchara Punya Jaroenjittichai. Formation energies and chemical potential diagrams of II-Ge-N₂ semiconductors. *Integrated Ferroelectrics*, 175(1):186–192, 2016.
- [190] M. Selleby, M. Hillert, and J. Ågren. Use of chemical potential of a compound in potential phase diagrams. *Calphad*, 35(3):342–345, 2011.
- [191] Harumi Yokokawa, Katsuhiko Yamaji, Teruhisa Horita, and Natsuko Sakai. A convex polyhedron approach of constructing chemical potential diagrams for multicomponent systems. *Calphad*, 24(4):435–448, 2000.

- [192] Scott A. Chambers and Peter V. Sushko. Probing energy landscapes in multilayer heterostructures: Challenges and opportunities. *APL Materials*, 7(11):110904, 2019.
- [193] Kris T. Delaney, Nicola A. Spaldin, and Chris G. Van de Walle. Theoretical study of schottky-barrier formation at epitaxial rare-earth-metal/semiconductor interfaces. *Physical Review B*, 81(16), 2010.
- [194] S. J. Sque, R. Jones, and P. R. Briddon. Structure, electronics, and interaction of hydrogen and oxygen on diamond surfaces. *Physical Review B*, 73(8), 2006.
- [195] S. P. Hepplestone and P. V. Sushko. Effect of metal intermixing on the schottky barriers of Mo(100)/GaAs(100) interfaces. *Journal of Applied Physics*, 116(19):193703, 2014.
- [196] Richard F. Bader. A quantum theory of molecular structure and its applications. *Chemical Reviews*, 91(5):893–928, 1991.
- [197] M.R.Gennero de Chialvo and A.C. Chialvo. Hydrogen evolution reaction: Analysis of the volmer-heyrovsky-tafel mechanism with a generalized adsorption model. *Journal of Electroanalytical Chemistry*, 372(1):209 – 223, 1994.
- [198] Anna S Andersson. Thermal Stability of LiFePO₄-Based Cathodes. *Electrochemical and Solid-State Letters*, 3(2):66, 2000.
- [199] Lixia Liao, Pengjian Zuo, Yulin Ma, Xinqun Chen, Yongxin An, Yunzhi Gao, and Geping Yin. Effects of temperature on charge/discharge behaviors of LiFePO₄ cathode for Li-ion batteries. *Electrochimica Acta*, 60:269–273, 2012.
- [200] By Lung-Hao Hu, Feng Yu Wu, Cheng Te Lin, Andrei N. Khlobystov, and Lain Jong Li. Graphene-modified LiFePO₄ cathode for lithium ion battery beyond theoretical capacity. *Nature Communications*, 4(1):1–7, 2013.
- [201] Dao Yong Wan, Zhi Yu Fan, Yong Xiang Dong, Erdenebayar Baasanjav, Hang-Bae Jun, Bo Jin, En Mei Jin, and Sang Mun Jeong. Effect of Metal (Mn, Ti) Doping on NCA Cathode Materials for Lithium Ion Batteries. *Journal of Nanomaterials*, 2018:1–9, 2018.
- [202] Gyeong Won Nam, Nam Yung Park, Kang Joon Park, Jihui Yang, Jun Liu, S. Chong Yoon, and Kook-Yang Sun. Capacity Fading of Ni-Rich NCA Cathodes: Effect of Microcracking Extent. *ACS Energy Letters*, 4(12):2995–3001, 2019.
- [203] Wangda Li, Steven Lee, and Arumugam Manthiram. High-Nickel NMA: A Cobalt-Free Alternative to NMC and NCA Cathodes for Lithium-Ion Batteries. *Advanced Materials*, 32(33):2002718, aug 2020.

- [204] Nathan D. Phillip, Andrew S. Westover, Claus Daniel, and Gabriel M. Veith. Structural Degradation of High Voltage Lithium Nickel Manganese Cobalt Oxide (NMC) Cathodes in Solid-State Batteries and Implications for Next Generation Energy Storage. *ACS Applied Energy Materials*, 3(2):1768–1774, 2020.
- [205] R. N. Ramesha, Dasari Bosubabu, M. G. Karthick Babu, and K. Ramesha. Tuning of Ni, Mn, and Co (NMC) content in $0.4(\text{LiNi}_x\text{Mn}_y\text{Co}_z\text{O}_2) \cdot 0.4(\text{Li}_2\text{MnO}_3)$ toward stable high-capacity lithium-rich cathode materials. *ACS Applied Energy Materials*, 3(11):10872–10881, 2020.
- [206] Xifei Li and Youlong Xu. Spinel LiMn_2O_4 active material with high capacity retention. *Applied Surface Science*, 253(21):8592–8596, aug 2007.
- [207] Xifei Li, Youlong Xu, and Chunlei Wang. Suppression of Jahn–Teller distortion of spinel LiMn_2O_4 cathode. *Journal of Alloys and Compounds*, 479(1-2):310–313, jun 2009.
- [208] Yunjian Liu, Jun Lv, Yang Fei, Xiangdong Huo, and Yuezhong Zhu. Improvement of storage performance of LiMn_2O_4 /graphite battery with AlF_3 -coated LiMn_2O_4 . *Ionics*, 19(9):1241–1246, sep 2013.
- [209] Huiwen Ji, Jinpeng Wu, Zijian Cai, Jue Liu, Deok Hwang Kwon, Hyunchul Kim, Alexander Urban, Joseph K. Papp, Emily Foley, Yaosen Tian, Mahalingam Balasubramanian, Haegyeom Kim, Raphaële J. Clément, Bryan D. McCloskey, Wanli Yang, and Gerbrand Ceder. Ultrahigh power and energy density in partially ordered lithium-ion cathode materials. *Nature Energy*, 5(3):213–221, 2020.
- [210] Yingchun Ding, Qijiu Deng, Caiyin You, Yunhua Xu, Jilin Li, and Bing Xiao. Assessing electrochemical properties and diffusion dynamics of metal ions (Na, K, Ca, Mg, Al and Zn) on a C_2N monolayer as an anode material for non-lithium ion batteries. *Physical Chemistry Chemical Physics*, 22(37):21208–21221, 2020.
- [211] Vadym V. Kulish, Oleksandr I. Malyi, Clas Persson, and Ping Wu. Phosphorene as an anode material for Na-ion batteries: a first-principles study. *Physical Chemistry Chemical Physics*, 17(21):13921–13928, 2015.
- [212] Xiaoxi Zou, Peixun Xiong, Jin Zhao, Jimin Hu, Zhitian Liu, and Yunhua Xu. Recent research progress in non-aqueous potassium-ion batteries. *Phys. Chem. Chem. Phys.*, 19(39):26495–26506, 2017.
- [213] Dashuai Wang, Yingying Zhao, Ruqian Lian, Di Yang, Dong Zhang, Xing Meng, Yanhui Liu, Yingjin Wei, and Gang Chen. Atomic insight into the structural transformation and anionic/cationic redox reactions of VS_2

- nanosheets in sodium-ion batteries. *Journal of Materials Chemistry A*, 6(33):15985–15992, 2018.
- [214] Bo Zhou, Hui Shi, Rongfang Cao, Xiaodong Zhang, and Zhenyi Jiang. Theoretical study on the initial stage of a magnesium battery based on a V_2O_5 cathode. *Phys. Chem. Chem. Phys.*, 16(34):18578–18585, 2014.
- [215] Jiandong Wu and Guohua Gao. First-principles study of VPO 4 O as a cathode material for rechargeable Mg batteries. *Physical Chemistry Chemical Physics*, 21:4947–4952, 2019.
- [216] Dixing Ni, Jing Shi, Wan Xiong, Shuying Zhong, Bo Xu, and Chuying Ouyang. The effect of protons on the Mg^{2+} migration in an α - V_2O_5 cathode for magnesium batteries: a first-principles investigation. *Physical Chemistry Chemical Physics*, 21(14):7406–7411, 2019.
- [217] Manish Chhowalla, Hyeon Suk Shin, Goki Eda, Lain-jong Li, Kian Ping Loh, and Hua Zhang. The chemistry of two-dimensional layered transition metal dichalcogenide nanosheets. *Nature Chemistry*, 5(4):263–275, apr 2013.
- [218] Stephen J. McDonnell and Robert M Wallace. Atomically-thin layered films for device applications based upon 2D TMDC materials. *Thin Solid Films*, 616:482–501, oct 2016.
- [219] Shaoxun Fan, Xiaolong Zou, Hongda Du, Lin Gan, Chengjun Xu, Wei Lv, Yan Bing He, Quan Hong Yang, Feiyu Kang, and Jia Li. Theoretical Investigation of the Intercalation Chemistry of Lithium/Sodium Ions in Transition Metal Dichalcogenides. *Journal of Physical Chemistry C*, 121(25):13599–13605, jun 2017.
- [220] Yi Wei, Jiaxin Zheng, Suihan Cui, Xiaohe Song, Yantao Su, Wenjun Deng, Zhongzhen Wu, Xinwei Wang, Weidong Wang, Mumin Rao, Yuan Lin, Chongmin Wang, Khalil Amine, and Feng Pan. Kinetics Tuning of Li-Ion Diffusion in Layered $Li(Ni_xMn_yCo_z)O_2$. *Journal of the American Chemical Society*, 137(26):8364–8367, jul 2015.
- [221] Q. D. Chen, S. F. Yuan, J. H. Dai, and Y. Song. Functionalized $M_2TiC_2 T x$ MXenes ($M = Cr$ and Mo ; $T = F, O,$ and OH) as high performance electrode materials for sodium ion batteries. *Physical Chemistry Chemical Physics*, 23(2):1038–1049, 2021.
- [222] Peifang Luo and Zan Huang. Fabrication of scandium-doped lithium manganese oxide as a high-rate capability cathode material for lithium energy storage. *Solid State Ionics*, 338(May):20–24, 2019.
- [223] Subramani Bhuvaneshwari, U.V. Varadaraju, R. Gopalan, and Raju Prakash. Structural stability and superior electrochemical performance of Sc-doped

- LiMn₂O₄ spinel as cathode for lithium ion batteries. *Electrochimica Acta*, 301:342–351, apr 2019.
- [224] Kimiko Nakajima, Flavio L. Souza, Andre L.M. Freitas, Andrew Thron, and Ricardo H.R. Castro. Improving Thermodynamic Stability of nano-LiMn₂O₄ for Li-Ion Battery Cathode. *Chemistry of Materials*, 33(11):3915–3925, 2021.
- [225] C. J. M. Rooymans. The Crystal Structure of LiScO₂. *Zeitschrift fuer Anorganische und Allgemeine Chemie*, 2(1844):234–235, 1961.
- [226] Guowei Zhao, Iqbal Muhammad, Kota Suzuki, Masaaki Hirayama, and Ryoji Kanno. Synthesis, crystal structure, and the ionic conductivity of new lithium ion conductors, M-doped LiScO₂ (M= Zr, Nb, Ta). *Materials Transactions*, 57(8):1370–1373, 2016.
- [227] Zhixiao Liu, Huiqiu Deng, Shiguo Zhang, Wangyu Hu, and Fei Gao. A first-principles investigation of the ScO₂ monolayer as the cathode material for alkali metal-ion batteries. *Journal of Materials Chemistry A*, 6(7):3171–3180, 2018.
- [228] Zhixiao Liu, Huiqiu Deng, Shiguo Zhang, Wangyu Hu, and Fei Gao. Theoretical prediction of LiScO₂ nanosheets as a cathode material for Li–O₂ batteries. *Physical Chemistry Chemical Physics*, 20(34):22351–22358, 2018.
- [229] Zhen Ming Xu, Shou Hang Bo, and Hong Zhu. LiCrS₂ and LiMnS₂ Cathodes with Extraordinary Mixed Electron-Ion Conductivities and Favorable Interfacial Compatibilities with Sulfide Electrolyte. *ACS Applied Materials and Interfaces*, 10(43):36941–36953, 2018.
- [230] Hui Zhang, Xinyue Lin, and Zhen-Kun Tang. Stable ScS₂ nanostructures with tunable electronic and magnetic properties. *Solid State Communications*, 220:12–16, oct 2015.
- [231] C. Ataca, H. Şahin, and S. Ciraci. Stable, single-layer MX₂ transition-metal oxides and dichalcogenides in a honeycomb-like structure. *Journal of Physical Chemistry C*, 116(16):8983–8999, 2012.
- [232] J. A. Reyes-Retana and F. Cervantes-Sodi. Spin-orbital effects in metal-dichalcogenide semiconducting monolayers. *Scientific Reports*, 6(1):24093, apr 2016.
- [233] M van Dijk and C.M. Plug. The crystal structure of LiScS₂ and NaScS₂. *Materials Research Bulletin*, 15(1):103–106, jan 1980.
- [234] Lubomír Havlák, Jan Fábry, Margarida Henriques, and Michal Dušek. Structure determination of KScS₂, RbScS₂ and KLnS₂ (Ln = Nd, Sm, Tb, Dy, Ho, Er, Tm and Yb) and crystal–chemical discussion. *Acta Crystallographica Section C Structural Chemistry*, 71(7):623–630, jul 2015.

- [235] Dwaipayan Chakraborty, Madhu Pandey, and Priya Johari. ScS₂ Monolayer as a Potential Cathode Material for Alkali-ion Batteries and Beyond. pages 1–25, jan 2022.
- [236] Abdullah Al Roman, M. Mahbubur Rahman, Kamal Hossain, Sudipto Das, and Farid Ahmed. Development of high-performance ScS₂ monolayer as cathode material: A DFT analysis. *Solid State Communications*, 352:114828, sep 2022.
- [237] H. Katzke, P. Tolédano, and W. Depmeier. Phase transitions between polytypes and intralayer superstructures in transition metal dichalcogenides. *Physical Review B - Condensed Matter and Materials Physics*, 69(13):1–8, 2004.
- [238] J. Ribeiro-Soares, R. M. Almeida, E. B. Barros, P. T. Araujo, M. S. Dresselhaus, L. G. Cançado, and A. Jorio. Group theory analysis of phonons in two-dimensional transition metal dichalcogenides. *Physical Review B*, 90(11):115438, sep 2014.
- [239] J. Paier, M. Marsman, K. Hummer, G. Kresse, I. C. Gerber, and J. G. Angyán. Screened hybrid density functionals applied to solids. *Journal of Chemical Physics*, 124(15):154709, apr 2006.
- [240] Atsushi Togo and Isao Tanaka. First principles phonon calculations in materials science. *Scripta Materialia*, 108:1–5, nov 2015.
- [241] Aiswarya Bhaskar, Daria Mikhailova, Nilüfer Kiziltas-Yavuz, Kristian Nikolowski, Steffen Oswald, Natalia N. Bramnik, and Helmut Ehrenberg. 3d-Transition metal doped spinels as high-voltage cathode materials for rechargeable lithium-ion batteries. *Progress in Solid State Chemistry*, 42(4):128–148, 2014.
- [242] H. Hohyun Sun, Un Hyuck Kim, Jeong Hyeon Park, Sang Wook Park, Dong Hwa Seo, Adam Heller, C. Buddie Mullins, Chong S. Yoon, and Yang Kook Sun. Transition metal-doped Ni-rich layered cathode materials for durable Li-ion batteries. *Nature Communications*, 12(1):1–11, 2021.
- [243] Piaopiao Wen, Huangkai Wang, Xianyou Wang, Haibo Wang, Yansong Bai, and Zhenhua Yang. Exploring the physicochemical role of Pd dopant in promoting Li-ion diffusion dynamics and storage performance of NbS₂ at the atomic scale. *Physical Chemistry Chemical Physics*, 24:14877–14885, 2022.
- [244] M. K. Aydinol, A. F. Kohan, G. Ceder, K. Cho, and J. Joannopoulos. Ab initio study of lithium intercalation in metal oxides and metal dichalcogenides. *Physical Review B*, 56(3):1354–1365, jul 1997.

- [245] Martin Mayo, Kent J. Griffith, Chris J. Pickard, and Andrew J. Morris. Ab Initio Study of Phosphorus Anodes for Lithium- and Sodium-Ion Batteries. *Chemistry of Materials*, 28(7):2011–2021, apr 2016.
- [246] Andrey N. Enyashin and Gotthard Seifert. Density-functional study of Li_xMoS_2 intercalates ($0 \leq x \leq 1$). *Computational and Theoretical Chemistry*, 999:13–20, nov 2012.
- [247] Qingqing Zhang, Rong Li, Mengmeng Zhang, Bianli Zhang, and Xinglong Gou. SnS_2 /reduced graphene oxide nanocomposites with superior lithium storage performance. *Electrochimica Acta*, 115:425–433, Jan 2014.
- [248] Peng Gao, Liping Wang, Yu-Yang Zhang, Yuan Huang, Lei Liao, Peter Sutter, Kaihui Liu, Dapeng Yu, and En-Ge Wang. High-resolution tracking asymmetric lithium insertion and extraction and local structure ordering in SnS_2 . *Nano Letters*, 16(9):5582–5588, Aug 2016.
- [249] Yukinori Koyama, Hajime Arai, Isao Tanaka, Yoshiharu Uchimoto, and Zempachi Ogumi. First principles study of dopant solubility and defect chemistry in LiCoO_2 . *J. Mater. Chem. A*, 2(29):11235–11245, 2014.
- [250] Zhixiao Liu, Huiqiu Deng, and Partha P. Mukherjee. Evaluating pristine and modified SnS_2 as a lithium-ion battery anode: A first-principles study. *ACS Applied Materials and Interfaces*, 7(7):4000–4009, 2015.
- [251] Anubhav Jain, Shyue Ping Ong, Geoffroy Hautier, Wei Chen, William Davidson Richards, Stephen Dacek, Shreyas Cholia, Dan Gunter, David Skinner, Gerbrand Ceder, and Kristin A. Persson. Commentary: The Materials Project: A materials genome approach to accelerating materials innovation. *APL Materials*, 1(1):011002, jul 2013.
- [252] B. Amin, N. Singh, and U. Schwingenschlögl. Heterostructures of transition metal dichalcogenides. *Physical Review B - Condensed Matter and Materials Physics*, 92(7):1–6, 2015.
- [253] Fawad Khan, M. Idrees, C. Nguyen, Iftikhar Ahmad, and Bin Amin. A first-principles study of electronic structure and photocatalytic performance of GaN-MX_2 ($M = \text{Mo}, \text{W}$; $X = \text{S}, \text{Se}$) van der Waals heterostructures. *RSC Advances*, 10(41):24683–24690, 2020.
- [254] Francis H. Davies, Conor J. Price, Ned T. Taylor, Shane G. Davies, and Steven P. Hepplestone. Band alignment of transition metal dichalcogenide heterostructures. *Physical Review B*, 103(4):1–10, 2021.
- [255] F. Zhou, M. Cococcioni, C. A. Marianetti, D. Morgan, and G. Ceder. First-principles prediction of redox potentials in transition-metal compounds with LDA + U. *Physical Review B - Condensed Matter and Materials Physics*, 70(23):1–8, 2004.

- [256] F. Zhou, C. A. Marianetti, M. Cococcioni, D. Morgan, and G. Ceder. Phase separation in Li_xFePO_4 induced by correlation effects. *Physical Review B - Condensed Matter and Materials Physics*, 69(20):1–4, 2004.
- [257] V. L. Chevrier, S. P. Ong, R. Armiento, M. K.Y. Chan, and G. Ceder. Hybrid density functional calculations of redox potentials and formation energies of transition metal compounds. *Physical Review B - Condensed Matter and Materials Physics*, 82(7):1–11, 2010.
- [258] Michael Woodcox, Robert Shepard, and Manuel Smeu. First principles investigation into the interwoven nature of voltage and mechanical properties of the Li_xNMC -811 cathode. *Journal of Power Sources*, 516(June):230620, dec 2021.
- [259] ShunLi Shang, Yi Wang, Pinwen Guan, William Y. Wang, Huazhi Fang, Tim Anderson, and Zi-Kui Liu. Insight into structural, elastic, phonon, and thermodynamic properties of α -sulfur and energy-related sulfides: a comprehensive first-principles study. *Journal of Materials Chemistry A*, 3(15):8002–8014, 2015.
- [260] Yue Qi, Louis G. Hector, Christine James, and Kwang Jin Kim. Lithium Concentration Dependent Elastic Properties of Battery Electrode Materials from First Principles Calculations. *Journal of The Electrochemical Society*, 161(11):F3010–F3018, aug 2014.
- [261] Félix Mouhat and François-Xavier Coudert. Necessary and sufficient elastic stability conditions in various crystal systems. *Physical Review B*, 90(22):224104, dec 2014.
- [262] Edward A D Baker, Joe Pitfield, Conor J. Price, and Steven P. Hepplestone. Computational analysis of the enhancement of photoelectrolysis using transition metal dichalcogenide heterostructures. *Journal of Physics: Condensed Matter*, 34(37):375001, sep 2022.
- [263] Yingchun Lyu, Xia Wu, Kai Wang, Zhijie Feng, Tao Cheng, Yang Liu, Meng Wang, Riming Chen, Leimin Xu, Jingjing Zhou, Yuhao Lu, and Bingkun Guo. An Overview on the Advances of LiCoO_2 Cathodes for Lithium-Ion Batteries. *Advanced Energy Materials*, 11(2):2000982, jan 2021.
- [264] J. Luo, C.Y. Dai, Z. Wang, K. Liu, W.G. Mao, D.N. Fang, and X. Chen. In-situ measurements of mechanical and volume change of LiCoO_2 lithium-ion batteries during repeated charge–discharge cycling by using digital image correlation. *Measurement*, 94:759–770, dec 2016.
- [265] A. Yamada, S. C. Chung, and K. Hinokuma. Optimized LiFePO_4 for Lithium Battery Cathodes. *Journal of The Electrochemical Society*, 148(3):A224, 2001.

- [266] J. Barker. In-situ measurement of the thickness changes associated with cycling of prismatic lithium ion batteries based on LiMn_2O_4 and LiCoO_2 . *Electrochimica Acta*, 45(1-2):235–242, sep 1999.
- [267] M. S. Whittingham. Electrical energy storage and intercalation chemistry. *Science*, 192(4244):1126–1127, Jun 1976.
- [268] A. H. Thompson. Lithium ordering in Li_xTiS_2 . *Physical Review Letters*, 40(23):1511–1514, Jun 1978.
- [269] Cyrus Umrigar, D. E. Ellis, Ding-Sheng Wang, H. Krakauer, and M. Posternak. Band structure, intercalation, and interlayer interactions of transition-metal dichalcogenides: TiS_2 and LiTiS_2 . *Physical Review B*, 26(9):4935–4950, Nov 1982.
- [270] M. Yoshio, S. Inoue, M. Hyakutake, G. Piao, and H. Nakamura. New lithium manganese composite oxide for the cathode of rechargeable lithium batteries. *Journal of Power Sources*, 34(2):147–152, Jan 1991.
- [271] Hui Li, Weijun Li, Lin Ma, Weixiang Chen, and Jianming Wang. Electrochemical lithiation/delithiation performances of 3d flowerlike MoS_2 powders prepared by ionic liquid assisted hydrothermal route. *Journal of Alloys and Compounds*, 471(1–2):442–447, Mar 2009.
- [272] Xiangpeng Fang, Chunxiu Hua, Xianwei Guo, Yongsheng Hu, Zhaoxiang Wang, Xueping Gao, Feng Wu, Jiazhao Wang, and Liquan Chen. Lithium storage in commercial MoS_2 in different potential ranges. *Electrochimica Acta*, 81:155–160, Oct 2012.
- [273] Tyler Stephenson, Zhi Li, Brian Olsen, and David Mitlin. Lithium ion battery applications of molybdenum disulfide (MoS_2) nanocomposites. *Energy Environ. Sci.*, 7(1):209–231, Oct 2013.
- [274] Juan Xia, Jin Wang, Dongliang Chao, Zhen Chen, Zheng Liu, Jer-Lai Kuo, Jiayu Yan, and Ze Xiang Shen. Phase evolution of lithium intercalation dynamics in 2h- MoS_2 . *Nanoscale*, 9(22):7533–7540, May 2017.
- [275] Liang Zhang, Dan Sun, Jun Kang, Jun Feng, Hans A. Bechtel, Lin-Wang Wang, Elton J. Cairns, and Jinghua Guo. Electrochemical reaction mechanism of the MoS_2 electrode in a lithium-ion cell revealed by in situ and operando X-ray absorption spectroscopy. *Nano Letters*, 18(2):1466–1475, Jan 2018.
- [276] N IMANISHI, M TOYODA, Y TAKEDA, and O YAMAMOTO. Study on lithium intercalation into MoS_2 . *Solid State Ionics*, 58(3–4):333–338, Dec 1992.
- [277] Chandramohan George, Andrew J. Morris, Mohammad H. Modarres, and Michael De Volder. Structural evolution of electrochemically lithiated MoS_2

- nanosheets and the role of carbon additive in Li-Ion batteries. *Chemistry of Materials*, 28(20):7304–7310, Oct 2016.
- [278] Yutao Lu, Xiayin Yao, Jingyun Yin, Gang Peng, Ping Cui, and Xiaoxiong Xu. MoS₂ nanoflowers consisting of nanosheets with a controllable interlayer distance as high-performance lithium ion battery anodes. *RSC Advances*, 5(11):7938–7943, Dec 2014.
- [279] Ashish Nadar, Yukti Arora, Pallavi Thakur, T.N. Narayanan, Arnab Bhattacharya, and Deepa Khushalani. ReS₂ vs MoS₂: Viable electrodes for batteries and capacitors. *Electrochemistry Communications*, 139:107313, Jul 2022.
- [280] Zhaolin Liu, Aishui Yu, and Jim Y Lee. Synthesis and characterization of LiNi_{1-x-y}Co_xMn_yO₂ as the cathode materials of secondary lithium batteries. *Journal of Power Sources*, 81–82:416–419, Sep 1999.
- [281] Masaki Yoshio, Hideyuki Noguchi, Jun-ichi Itoh, Masaki Okada, and Takashi Mouri. Preparation and properties of LiCo_yMn_xNi_{1-x-y}O₂ as a cathode for lithium ion batteries. *Journal of Power Sources*, 90(2):176–181, Oct 2000.
- [282] S.H. Park, C.S. Yoon, S.G. Kang, H.-S. Kim, S.-I. Moon, and Y.-K. Sun. Synthesis and structural characterization of layered Li[Ni_{1/3}Co_{1/3}Mn_{1/3}]O₂ cathode materials by ultrasonic spray pyrolysis method. *Electrochimica Acta*, 49(4):557–563, Feb 2004.
- [283] Yadong Wang, Junwei Jiang, and J.R. Dahn. The reactivity of delithiated Li(Ni_{1/3}Co_{1/3}Mn_{1/3})O₂, Li(Ni_{0.8}Co_{0.15}Al_{0.05})O₂ or LiCoO₂ with non-aqueous electrolyte. *Electrochemistry Communications*, 9(10):2534–2540, Aug 2007.
- [284] Manish Chhowalla, Hyeon Suk Shin, Goki Eda, Lain-Jong Li, Kian Ping Loh, and Hua Zhang. The chemistry of two-dimensional layered transition metal dichalcogenide nanosheets. *Nature Chemistry*, 5(4):263–275, Mar 2013.
- [285] M. Stanley Whittingham. The role of ternary phases in cathode reactions. *Journal of The Electrochemical Society*, 123(3):315–320, Mar 1976.
- [286] M. Stanley Whittingham. Chemistry of intercalation compounds: Metal guests in chalcogenide hosts. *Progress in Solid State Chemistry*, 12(1):41–99, Jan 1978.
- [287] Yong-Ping Gao, Xu Wu, Ke-Jing Huang, Ling-Li Xing, Ying-Ying Zhang, and Lu Liu. Two-dimensional transition metal diseleniums for energy storage application: A review of recent developments. *CrystEngComm*, 19(3):404–418, Dec 2016.

- [288] Yong-Ping Gao, Jing Xu, Ke-Jing Huang, Hui Lu, Ya-Xi Pang, and Guo-qiang Li. An overview of the current status and prospects of cathode materials based on transition metal sulfides for magnesium-ion batteries. *CrytEngComm*, 23(43):7546–7564, Oct 2021.
- [289] Conor Jason Price, Edward Allery Baker, and Steven Paul Hepplestone. First principles study of layered transition metal dichalcogenides for use as electrodes in Li-ion and Mg-ion batteries. *Journal of Materials Chemistry A*, 11(23):12354–12372, May 2023.
- [290] Haimei Qi, Lina Wang, Tiantian Zuo, Shunlan Deng, Qi Li, Zong-Huai Liu, Peng Hu, and Xuexia He. Hollow structure VS₂@reduced graphene oxide (RGO) architecture for enhanced sodium-ion battery performance. *Chem-ElectroChem*, 7(1):78–85, Nov 2019.
- [291] Michael Woodcox, Robert Shepard, and Manuel Smeu. First principles investigation into the interwoven nature of voltage and mechanical properties of the Li_xNMC-811 cathode. *Journal of Power Sources*, 516:230620, Oct 2021.
- [292] Dip K. Nandi, Uttam K. Sen, Arpan Dhara, Sagar Mitra, and Shaibal K. Sarkar. Intercalation based tungsten disulfide (WS₂) Li-ion battery anode grown by atomic layer deposition. *RSC Advances*, 6(44):38024–38032, Apr 2016.
- [293] Emily Hitz, Jiayu Wan, Anand Patel, Yue Xu, Louisa Meshi, Jiaqi Dai, Yanan Chen, Aijiang Lu, Albert V. Davydov, Liangbing Hu, and et al. Electrochemical intercalation of lithium ions into NbSe₂ nanosheets. *ACS Applied Materials & Interfaces*, 8(18):11390–11395, Apr 2016.
- [294] Conor Jason Price, Joe Pitfield, Edward Allery Baker, and Steven Paul Hepplestone. First principles study of layered scandium disulfide for use as Li-ion and beyond-Li-ion batteries. *Physical Chemistry Chemical Physics*, 25(3):2167–2178, Jan 2023.
- [295] Donald W. Murphy, Francis J. Di Salvo, George W. Hull, and Joseph V. Waszczak. Convenient preparation and physical properties of lithium intercalation compounds of group 4b and 5b layered transition metal dichalcogenides. *Inorganic Chemistry*, 15(1):17–21, Jan 1976.
- [296] J MORALES, C PEREZVICENTE, and J TIRADO. Chemical and electrochemical lithium intercalation and staging in 2H-SnS₂. *Solid State Ionics*, 51(3–4):133–138, Feb 1992.
- [297] Jung-wook Seo, Jung-tak Jang, Seung-won Park, Chunjoong Kim, Byung-woo Park, and Jinwoo Cheon. Two-dimensional SnS₂ nanoplates with ex-

- traordinary high discharge capacity for lithium ion batteries. *Advanced Materials*, 20(22):4269–4273, Nov 2008.
- [298] Jiantao Zai, Kaixue Wang, Yuezeng Su, Xuefeng Qian, and Jiesheng Chen. High stability and superior rate capability of three-dimensional hierarchical SnS₂ microspheres as anode material in lithium ion batteries. *Journal of Power Sources*, 196(7):3650–3654, Apr 2011.
- [299] Bin Luo, Yan Fang, Bin Wang, Jisheng Zhou, Huaihe Song, and Linjie Zhi. Two dimensional graphene–SnS₂ hybrids with superior rate capability for lithium ion storage. *Energy Environ. Sci.*, 5(1):5226–5230, Nov 2011.
- [300] Mingyue Wang, Ying Huang, Yade Zhu, Xing Wu, Na Zhang, and Hongming Zhang. Binder-free flower-like SnS₂ nanoplates decorated on the graphene as a flexible anode for high-performance lithium-ion batteries. *Journal of Alloys and Compounds*, 774:601–609, Oct 2018.
- [301] Rui Li, Chang Miao, Mengqiao Zhang, and Wei Xiao. Novel hierarchical structural SnS₂ composite supported by biochar carbonized from chewed sugarcane as enhanced anodes for lithium ion batteries. *Ionics*, 26(3):1239–1247, Nov 2019.
- [302] Qinghong Wang, Lifang Jiao, Yan Han, Hongmei Du, Wenxiu Peng, Qingna Huan, Dawei Song, Yuchang Si, Yijing Wang, and Huatang Yuan. CoS₂ hollow spheres: Fabrication and their application in lithium-ion batteries. *The Journal of Physical Chemistry C*, 115(16):8300–8304, Apr 2011.
- [303] Yaochen Song, Jiaxuan Liao, Cheng Chen, Jian Yang, Jinchen Chen, Feng Gong, Sizhe Wang, Ziqiang Xu, and Mengqiang Wu. Controllable morphologies and electrochemical performances of self-assembled nano-honeycomb WS₂ anodes modified by graphene doping for lithium and sodium ion batteries. *Carbon*, 142:697–706, Jul 2018.
- [304] Xiaodong Xu, Chandra Sekhar Rout, Jieun Yang, Ruiguo Cao, Pilgun Oh, Hyeon Suk Shin, and Jaephil Cho. Freeze-dried WS₂ composites with low content of graphene as high-rate lithium storage materials. *Journal of Materials Chemistry A*, 1(46):14548, Oct 2013.
- [305] Yuan Liu, Minqiang Zhu, and Di Chen. Sheet-like MoSe₂/C composites with enhanced Li-ion storage properties. *Journal of Materials Chemistry A*, 3(22):11857–11862, Apr 2015.
- [306] Geon-Kyu Sung, Ki-Joon Jeon, and Cheol-Min Park. Highly reversible and superior Li-storage characteristics of layered GeS₂ and its amorphous composites. *ACS Applied Materials & Interfaces*, 8(43):29543–29550, Oct 2016.

- [307] Ekaterina Pomerantseva and Yury Gogotsi. Two-dimensional heterostructures for energy storage. *Nature Energy*, 2(7), Jun 2017.
- [308] D. Kwabena Bediako, Mehdi Rezaee, Hyobin Yoo, Daniel T. Larson, S. Y. Zhao, Takashi Taniguchi, Kenji Watanabe, Tina L. Brower-Thomas, Efthimios Kaxiras, and Philip Kim. Heterointerface effects in the electrointercalation of van der waals heterostructures. *Nature*, 558(7710):425–429, Jun 2018.
- [309] Zhi Xiang Huang, Bo Liu, Dezhi Kong, Ye Wang, and Hui Ying Yang. SnSe₂ quantum dot/RGO composite as high performing lithium anode. *Energy Storage Materials*, 10:92–101, Aug 2017.
- [310] Jake Entwistle, Ruihuan Ge, Kunal Pardikar, Rachel Smith, and Denis Cumming. Carbon binder domain networks and electrical conductivity in lithium-ion battery electrodes: A critical review. *Renewable and Sustainable Energy Reviews*, 166:112624, Jun 2022.
- [311] Xin Qi, Berislav Blizanac, Aurelien DuPasquier, Archit Lal, Philip Niehoff, Tobias Placke, Miodrag Oljaca, Jie Li, and Martin Winter. Influence of thermal treated carbon black conductive additive on the performance of high voltage spinel Cr-doped LiNi_{0.5}Mn_{1.5}O₄ composite cathode electrode. *Journal of The Electrochemical Society*, 162(3), Dec 2014.
- [312] Nitin A. Kaskhedikar and Joachim Maier. Lithium storage in carbon nanostructures. *Advanced Materials*, 21(25-26):2664–2680, Jul 2009.
- [313] EunJoo Yoo, Jedeok Kim, Eiji Hosono, Hao-shen Zhou, Tetsuichi Kudo, and Itaru Honma. Large reversible Li storage of graphene nanosheet families for use in rechargeable lithium ion batteries. *Nano Letters*, 8(8):2277–2282, Jul 2008.
- [314] Manish Kumar Mohanta, Ashima Rawat, Nityasagar Jena, Dimple Sharma, Raihan Ahammed, and Abir De Sarkar. Interfacing boron monophosphide with molybdenum disulfide for an ultrahigh performance in thermoelectrics, two-dimensional excitonic solar cells, and nanopiezotronics. *ACS Applied Materials & Interfaces*, 12(2):3114–3126, Dec 2019.
- [315] Raihan Ahammed, Ashima Rawat, Nityasagar Jena, Dimple Sharma, Manish Kumar Mohanta, and Abir De Sarkar. ZrS₃/MS₂ and ZrS₃/MXY (M = Mo, W; X, y = S, Se, Te; x≠y) type-II van der waals hetero-bilayers: Prospective candidates in 2D excitonic solar cells. *Applied Surface Science*, 499:143894, Sep 2019.
- [316] Daniel T. Larson, Ioanna Fampiou, Gunn Kim, and Efthimios Kaxiras. Lithium intercalation in graphene–MoS₂ heterostructures. *The Journal of Physical Chemistry C*, 122(43):24535–24541, Oct 2018.

- [317] Muhammad Yousaf, Yunsong Wang, Yijun Chen, Zhipeng Wang, Attia Firdous, Zeeshan Ali, Nasir Mahmood, Ruqiang Zou, Shaojun Guo, Ray P. Han, and et al. A 3D trilayered CNT/MoS₂/C heterostructure with an expanded MoS₂ interlayer spacing for an efficient sodium storage. *Advanced Energy Materials*, 9(30):1900567, Jul 2019.
- [318] K. Wenelska, V. Adam, E. Thauer, L. Singer, R. Klingeler, X. Chen, and E. Mijowska. Fabrication of 3D graphene/MoS₂ spherical heterostructure as anode material in Li-Ion battery. *Frontiers in Energy Research*, 10, Aug 2022.
- [319] M.K. Aydinol, A.F. Kohan, and G. Ceder. Ab initio calculation of the intercalation voltage of lithium-transition-metal oxide electrodes for rechargeable batteries. *Journal of Power Sources*, 68(2):664–668, Oct 1997.
- [320] Kristin Persson, Yoyo Hinuma, Ying Shirley Meng, Anton Van der Ven, and Gerbrand Ceder. Thermodynamic and kinetic properties of the Li-graphite system from first-principles calculations. *Physical Review B*, 82(12), 2010.
- [321] Ali Eftekhari. Low voltage anode materials for lithium-ion batteries. *Energy Storage Materials*, 7:157–180, Jan 2017.
- [322] R. Hausbrand, G. Cherkashinin, H. Ehrenberg, M. Groeting, K. Albe, C. Hess, and W. Jaegermann. Cheminform abstract: Fundamental degradation mechanisms of layered oxide Li-ion battery cathode materials: Methodology, insights and novel approaches. *ChemInform*, 46(12), Feb 2015.
- [323] Min Yu and Dallas R. Trinkle. Accurate and efficient algorithm for bader charge integration. *The Journal of Chemical Physics*, 134(6):064111, Feb 2011.
- [324] W Tang, E Sanville, and G Henkelman. A grid-based bader analysis algorithm without lattice bias. *Journal of Physics: Condensed Matter*, 21(8):084204, Jan 2009.
- [325] Edward Sanville, Steven D. Kenny, Roger Smith, and Graeme Henkelman. Improved grid-based algorithm for bader charge allocation. *Journal of Computational Chemistry*, 28(5):899–908, Jan 2007.
- [326] Graeme Henkelman, Andri Arnaldsson, and Hannes Jónsson. A fast and robust algorithm for bader decomposition of charge density. *Computational Materials Science*, 36(3):354–360, Jun 2006.
- [327] Da Deng. Li-ion batteries: Basics, progress, and challenges. *Energy Science & Engineering*, 3(5):385–418, Sep 2015.
- [328] Katharina Märker, Philip J. Reeves, Chao Xu, Kent J. Griffith, and Clare P. Grey. Evolution of structure and lithium dynamics in LiNi_{0.8}Mn_{0.1}Co_{0.1}O₂

- (NMC811) cathodes during electrochemical cycling. *Chemistry of Materials*, 31(7):2545–2554, Mar 2019.
- [329] Juan An, Liyi Shi, Guorong Chen, Musen Li, Hongjiang Liu, Shuai Yuan, Shimou Chen, and Dengsong Zhang. Insights into the stable layered structure of a Li-rich cathode material for lithium-ion batteries. *Journal of Materials Chemistry A*, 5(37):19738–19744, Aug 2017.
- [330] Hyejung Kim, Min Gyu Kim, Hu Young Jeong, Haisol Nam, and Jaephil Cho. A new coating method for alleviating surface degradation of $\text{LiNi}_{0.6}\text{Co}_{0.2}\text{Mn}_{0.2}\text{O}_2$ cathode material: Nanoscale surface treatment of primary particles. *Nano Letters*, 15(3):2111–2119, 2015.
- [331] Thomas M. Heenan, Aaron Wade, Chun Tan, Julia E. Parker, Dorota Matras, Andrew S. Leach, James B. Robinson, Alice Llewellyn, Alexander Dimitrijevic, Rhodri Jervis, and et al. Identifying the origins of microstructural defects such as cracking within Ni-rich nmc811 cathode particles for lithium-ion batteries. *Advanced Energy Materials*, 10(47):2002655, 2020.
- [332] Shuang Li, Zhenpeng Yao, Jianming Zheng, Maosen Fu, Jiajie Cen, Sooyeon Hwang, Huile Jin, Alexander Orlov, Lin Gu, Shun Wang, and et al. Direct observation of defect-aided structural evolution in a nickel-rich layered cathode. *Angewandte Chemie International Edition*, 59(49):22092–22099, 2020.
- [333] Jared Bozich, Mimi Hang, Robert Hamers, and Rebecca Klaper. Core chemistry influences the toxicity of multicomponent metal oxide nanomaterials, lithium nickel manganese cobalt oxide, and lithium cobalt oxide to daphnia magna. *Environmental Toxicology and Chemistry*, 36(9):2493–2502, 2017.
- [334] Ian L. Gunsolus, Mimi N. Hang, Natalie V. Hudson-Smith, Joseph T. Buchman, Joseph W. Bennett, Daniel Conroy, Sara E. Mason, Robert J. Hamers, and Christy L. Haynes. Influence of nickel manganese cobalt oxide nanoparticle composition on toxicity toward shewanella oneidensis mr-1: Redesigning for reduced biological impact. *Environmental Science: Nano*, 4(3):636–646, Jan 2017.
- [335] Mimi N. Hang, Ian L. Gunsolus, Hunter Wayland, Eric S. Melby, Arielle C. Mensch, Katie R. Hurley, Joel A. Pedersen, Christy L. Haynes, and Robert J. Hamers. Impact of nanoscale lithium nickel manganese cobalt oxide (nmc) on the bacterium shewanella oneidensis mr-1. *Chemistry of Materials*, 28(4):1092–1100, 2016.
- [336] Mimi N. Hang, Natalie V. Hudson-Smith, Peter L. Clement, Yongqian Zhang, Chenyu Wang, Christy L. Haynes, and Robert J. Hamers. Influence of nanoparticle morphology on ion release and biological impact of

- nickel manganese cobalt oxide (nmc) complex oxide nanomaterials. *ACS Applied Nano Materials*, 1(4):1721–1730, 2018.
- [337] J.M. Tarascon, G. Vaughan, Y. Chabre, L. Seguin, M. Anne, P. Strobel, and G. Amatucci. In situ structural and electrochemical study of $\text{Ni}_{1-x}\text{Co}_x\text{O}_2$ metastable oxides prepared by soft chemistry. *Journal of Solid State Chemistry*, 147(1):410–420, Jul 1999.
- [338] Matteo Bianchini, Maria Roca-Ayats, Pascal Hartmann, Torsten Brezesinski, and Jürgen Janek. There and back again—the journey of LiNiO_2 as a cathode active material. *Angewandte Chemie International Edition*, 58(31):10434–10458, Jul 2019.
- [339] Julian D. Gale. Gulp: A computer program for the symmetry-adapted simulation of solids. *Journal of the Chemical Society, Faraday Transactions*, 93(4):629–637, Feb 1997.
- [340] Julian D. Gale and Andrew L. Rohl. The general utility lattice program (gulp). *Molecular Simulation*, 29(5):291–341, Feb 2003.
- [341] Alan D. McNaught, Andrew Wilkinson, and A. D. Jenkins. *IUPAC compendium of Chemical Terminology: The gold book*. International Union of Pure and Applied Chemistry, 2006.